FY 2016 Annual Report

Site-Directed Research & Development

Strategic Opportunity Research
Exploratory Research

NEVADA NATIONAL
NNSS
SECURITY SITE

Nevada National Security Site

Site-Directed Research and Development

Fiscal Year 2016 Annual Report

Report Date: April 2017

Disclaimer

This report was prepared as an account of work by an agency of the United States Government. Neither the United States Government nor any agency thereof, nor any of their employees, nor any of their contractors, subcontractors, or their employees, makes any warranty, express or implied, or assumes any legal liability or responsibility for the accuracy, completeness or any third party's use or the results of such use of any information, apparatus, product, or process disclosed, or represents that its use would not infringe privately owned rights. Reference herein to any specific commercial product, process, or service trade name, trademark, manufacturer, or otherwise, does not necessarily constitute or imply its endorsement, recommendation, or favoring by the United States Government or any agency thereof or its contractors or subcontractors. The views and opinions of authors expressed herein do not necessarily state or reflect those of the United States Government or any agency thereof.

Availability Statement

Available for sale to the public from:

U.S. Department of Commerce
National Technical Information Service
5301 Shawnee Road
Alexandria, VA 22312
Telephone: 800.553.6847
Fax: 703.605.6900
E-mail: orders@ntis.gov
Online ordering: http://www.ntis.gov/help/ordermethods.aspx

Available electronically at http://www.osti.gov/bridge

Available for a processing fee to the U.S. Department of Energy and its contractors in paper, from:

U.S. Department of Energy
Office of Scientific and Technical Information
P.O. Box 62
Oak Ridge, TN 37831-0062
Telephone: 865.576.6401
Fax: 865.576.5728
E-mail: reports@adonis.osti.gov
Online ordering: http://www.osti.gov/reportform.html

Contents

I was recently asked to peer into my "crystal ball" to glean insight on near-term strategic R&D thrusts for our mission needs. It doesn't take much insight to quickly perceive how dramatically the geopolitical landscape can engulf planned initiatives. One need only spend a few minutes watching world news to see the significant events across the globe that are driven by disparate situations, such as:

- Non-state actors and the threat they present to our nation (e.g., ISIL)

- State actors and their motivation to be considered as significant global players (e.g., North Korea)

- Tensions that have been emerging from expansionism in Eastern Europe (e.g., Crimea)

- Continuing nuclear power plant design flaws and their long-term impacts to the uncontrolled environment (e.g., Fukushima)

These are just a few examples of global conflict that can fundamentally impact initiatives and should, in principle, drive our investment strategies for our Site-Directed Research and Development program. In terms of pressing national interest, we are challenged by new subcritical experiments and integrating them with seismic experiments, as well as achieving a high level of efficiency across our major divisions. Of particular importance to achieving effective implementation is the development of remote technologies as opposed to human-intensive onsite-captured data. From its inception, every organizational element of the NNSS has been addressing and solving complex problems with elegant and implementable solutions. Our diagnostic forte, coupled with our ability to capture and process complex data, has become the norm for most of our programs.

The past decade has continued a proud and scientifically challenging SDRD Program. SDRD initiatives have reaped phenomenal returns on minor financial investments, and some have been characterized as not only evolutionary but also revolutionary. As we face the unknown future, I am certain that SDRD will continue to lead our effort to produce scientific discoveries across our program in support of national security. SDRD will continue to flourish, paving the path for future mission success.

Raffi Papazian
Vice President for Program Integration

This page left blank intentionally

The Next "Tri-Decade" for the Nevada National Security Site

As the Nevada National Security Site (NNSS) continues to evolve and transition its mission to a broader scope, significant challenges lie ahead that present unique opportunities for our research and development (R&D) enterprise. At this juncture, we are poised to create a different future investment strategy. Our decisions at the beginning of a new tri-decade span must be guided as expertly as possible given the greater complexity and multifaceted nature of our work.

Much of our past history can be found elsewhere; however, it can be broadly categorized into two tri-decade generations—the 1950s–1980s Legacy and the 1990s–2020s Stewardship. Now, we begin to ponder a third generation, the 2030s–2060s. We conducted many technical discussions over the past few years that will help us navigate our path to 2030 and beyond. In one such dialogue, we examined our history, noted current trends, and imagined the Site-Directed Research and Development (SDRD) program in the far future, looking back at the end of the coming tri-decade. We asked our future selves: How did we do? What were the hallmarks of this generation? Based on our assessments, what emerged was the prevalence of man–machine intelligence; in this sense SDRD is similar to other entities and enterprises who are seeing this in their future. Core to our mission is the development of robust, autonomous, smart systems that operate in highly complex situations where high-value data are collected. While the next generation of strategic investment may be yet unnamed, we are consciously moving toward it, shaping our best prediction and vision of the future. In 2016 we instituted a number of in-depth technical "deep dives" to conceive of how we might incorporate this vision into our R&D approach and realize this future. We will be starting to make some of these decisions in early 2017 as this report goes to publication.

"Ground Truth and Discovery IV"

The 4th annual year-end review of SDRD projects was held in September 2016. Once again the review showcased the various efforts and results achieved to a growing audience. The event began with a special plenary session on whether scientists and engineers can impact national security decision-making by Dr. Gerry Yonas. Our new format to include strategic opportunity research projects and two parallel concurrent sessions in the afternoon rounded out the day. We believe this venue for presenting and discussing R&D results has become indispensably important given the complexity of projects, the extended collaborations, and geographic separation between some of our sites. In addition, members of our advisory board were in attendance to review and assess projects as part of our ongoing advisory activities.

Gerry Yonas delivers a plenary session, "The Science Advisor's Dilemma," at the FY 2016 SDRD Annual Review

At the close of the 1950s–1980s Legacy era, we entered the period of Stewardship. In the last decade of stewardship, we have already begun to envision what will characterize the next generation of R&D strategic investment.

Strategic Opportunity Research Continues, Exploratory Research Remains Strong

As planned, over the previous few fiscal years of SDRD, we have systematically implemented our strategy to fund longer-term, higher-impact R&D investments. We have described the process and methodology employed to implement strategic opportunity R&D and have seen the first fruits of the labor involved. Fiscal year (FY) 2016 was the second full year of funding of strategic opportunity projects, and these have had measurable success. Reports summarizing the FY 2016 efforts of these projects are featured in the first section of this annual report. While these projects will essentially be complete in FY 2017, it was imperative to explore our strategic investments at this juncture and determine the best path forward. Although this seemed a straightforward task, it became clear it would be more difficult than we initially thought.

Our portfolio of exploratory research (featured in the second section of this report) continues to be a powerful pipeline for new innovations that form the cornerstone of the program. Many of our prior projects have progressed along the technical readiness timeline, having been adopted by programs and developed into field-ready devices, systems, and techniques. For instance, the optical ranging diagnostic (see FY 2014 annual report introduction) is now routinely used on a wide range of hydrodynamic experiments for the stockpile stewardship program. Other projects continue to close the knowledge gaps and reduce uncertainty in key areas of physics (see "SDRD to Stockpile Stewardship Success: A Perspective on Dynamic Temperature," page viii). In global security we have developed prior SDRD work in communications into special systems built around software-defined radio concepts (see "SDRD to Global Security Success: Software Defined Radio," page xi).

Karen McCall Named FY 2016 MVPI!

In FY 2015, the SDRD program embarked upon strategic initiatives—projects selected for their potential to bring transformative, substantive, long-term impact to our national security science mission. Unmanned aerial systems (UASs) were the focus of one of two inaugural projects. Early in the effort, it became clear that in order to realize the strategic potential of UASs to our mission and rapidly produce leading edge developments, we needed to embrace a bold and aggressive approach. With creative thinking and strategic aplomb, Karen McCall quickly rose to the challenge, bringing the first wholly owned, payload-capable UASs into the aviation assets of the NNSS. Karen orchestrated delivery of our first UAVs in September 2015, just six months into our accelerated UAS development plan.

Karen has also established protocols and procedures that are allowing us to move forward in developing and operating advanced sensors and other technology for UASs. She has proven a pioneer in advanced aviation operations and has laid the groundwork for long-term support for unmanned aerial technology R&D at the NNSS. The combination of Karen's insight, diligence, and support to the SDRD strategic initiative has already made a tremendous impact to our national security missions and will undoubtedly position the NNSS for future far-reaching outcomes in unmanned systems.

Karen McCall, Nevada National Security Site (NNSS), receives the 2016 Most Valuable Principal Investigator award from SDRD program manager, Howard Bender

Program Highlights and Project Selection

In the next few years, SDRD will reach another milestone, logging 20 years in supporting the NNSS national security missions. The program has made an indelible impact on science and technology—and perhaps, more importantly, the people who have contributed to this endeavor. From modest beginnings, a potent force for impacting our missions has evolved. As planned, we introduced major elements that have made SDRD an indispensable enterprise: multi-year lifecycles in 2009, "work for others" added to the portfolio in 2010, increased investment rate in 2014, and strategic opportunity projects in 2015. With these significant improvements in place, we have the proven infrastructure of a highly effective program. We continue to invest 2.5% of the NNSS overall budget, or about $9.2M, to fund SDRD. However, future plans call for increasing our investment percentage to nearly 3.5%, close to our Congressional authorization limit. Delineating a small fraction for strategic opportunity research and a larger for exploratory projects has been effective, and we anticipate continuing this as we gauge outcomes across our R&D portfolio.

SDRD to Stockpile Stewardship Success: A Perspective on Dynamic Temperature

Dynamic temperature is important in the understanding of a shocked metal, primarily because the temperature constrains equation-of-state models, but it also affects the phase and strength of the metal and therefore its shape when imploded. Unfortunately, dynamic temperature measurements, especially measurements of a metal's melt curve, are very difficult to make with useful accuracy. Several years ago SDRD began a systematic study of the issues affecting optical pyrometry. Our first success involved design and fabrication of an early version of an integrating sphere (IS) to measure the emissivity before, during, and after shock loading. White light is introduced to the IS, where it scatters many times before reflecting from the sample surface to a set of detectors with varying wavelength filters. In a series of publications in the *Journal of Applied Physics* beginning in 2009, we described first pyrometry with estimates for the emissivity limits (Seifter 2009), then an IS and its performance with a bare shocked metal (Seifter 2011), then the IS with a window between it and the sample to measure the dynamic emissivity in the infrared (Turley 2011), and finally the IS with a flash-lamp illumination scheme for visible light (La Lone 2013). (Visible wavelength radiance measurements are preferred to IR, as they are more constraining on the temperature results.) To determine dynamic temperature, we perform a pair of experiments with similar shock conditions. On one shot we measure the dynamic reflectance, R, and derive the emissivity, ε. (For metals, where there is no optical transmission, $\varepsilon = 1 - R$.) On the other shot we measure the shocked sample radiance. From Planck's law we can derive the temperature knowing the wavelengths of the measurements. By measuring the sample-window interface velocity to determine the stress or pressure on each shot, we also derive the shock stress.

We have done these temperature measurements with both high explosive (HE) and gun drives at our shock facility at the Special Technologies Laboratory. Both methods are restricted, however. With HE we have a very limited ability to vary the shock conditions, in part because we cannot safely exceed 10 g HE loads. The light gas gun is unable to reach the shock pressures of HE, where much of our applied interest lies. Consequently, we have purchased and are installing a propellant launcher to complement the present gas gun. Meanwhile, we have begun a new set of experiments in a collaboration with Caltech, using their powder gun. In this work we obtain the temperature over a range of conditions in a single shot by causing the shock stress to release slowly enough that we can determine the emissivity, radiance, and stress, all with nearly nanosecond time resolution during the entire shock release. Using this technique we conducted a series of experiments on tin with different drive conditions to verify that the release curves overlap properly. Samples were shocked on the Hugoniot to a state not far below melt, but far above the 9 GPa solid-solid phase change from β to body-centered tetragonal (bct). When the shock front reaches the window, the impedance mismatch between a tin sample and a LiF window causes an immediate release to a bct state between the Hugoniot and the melt curve. As shown in the figure, these points are marked 1R, 2R, and 3R, the names of the three shots. After a few hundred nanoseconds, when the beginning of the release fan from the shock reflected from the back of the impactor arrives at the tin-LiF interface, the slower release begins. In our experiments we followed the temperature and pressure to well beyond the onset of melt (colored curves in the figure). Upon reaching the solid-liquid boundary, the slope of the release temperature versus shock pressure changed suddenly, and after that point the temperature followed the calculated melt curve.
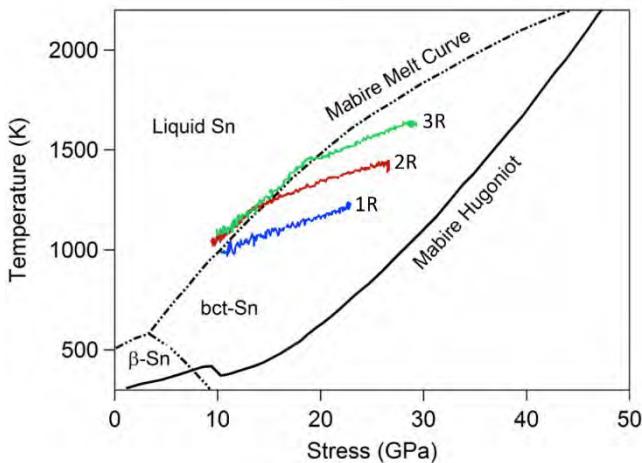
Calculated phase diagram (black) of Mabire (2000) and measured temperature versus stress release paths (color, right to left) for three shots on tin. The abrupt change in slope (steepening) at the dash-dot line indicates the intersection with the melt boundary as the release begins to follow the melt curve. The two highest-stress shots are slightly above the calculated melt curve from 19 GPa down to 9 GPa, but the disagreement is within the uncertainties. The lowest curve beginning at 1R is from an experiment that was too low in stress to release to melt.

Contributed by L. Veeser

La Lone, B. M., G. D. Stevens, W. D. Turley, D. B. Holtkamp, A. J. Iverson, R. S. Hixson, L. R. Veeser, *J. Appl. Phys.* **114** (2013) 063506.

C. Mabire and P. L. Héreil, *AIP Conf. Proc.* **505** (2000) 93.

Seifter, A., et al., *J. Appl. Phys.* **105** (2009) 123526.

Seifter, A., M. Grover, D. B. Holtkamp, A. J. Iverson, G. D. Stevens, W. D. Turley, L. R. Veeser, M. D. Wilke, J. A. Young , *J. Appl Phys.* **110** (2011) 093508.

Turley, W. D., D. B. Holtkamp, L. R. Veeser, G. D. Stevens, B. R. Marshall, A. Seifter, R. B. Corrow, J. B. Stone, J. A. Young, M. Grover, *J. Appl. Phys.* **110** (2011) 103510.

An efficient SDRD program is of the utmost importance, and we are actively involved in continuous improvement to achieve optimal results of our limited resources. The FY 2017 proposal call utilized the same two-phase proposal process we conceived in 2015. The process consists of a streamlined idea phase, followed by an invited full proposal, and was described in detail in the FY 2015 annual report. Proposal submissions were up 12% in the first year of implementation and again 7% for FY 2017. We also invited 70 full proposals in FY 2017, up slightly from FY 2016, further indication that a robust mix of high-quality pre-proposals were submitted. Three new technical review teams (subcommittees) performed FY 2017 proposal evaluation formed around key mission focus areas: (1) stockpile stewardship, (2) global security, and (3) emerging science and technology and new strategic ventures. This structure was highly effective in providing robust technical review of proposals. Further review was provided by our advisory level committee, thus completing a comprehensive evaluation yielding another strong project selection process.

FY 2016 Annual Report Synopsis

The reports that follow are for project activities that occurred from October 2015 through September 2016. Project lifecycle is indicated under the title as well as the original proposal number (in the following format: site abbreviation--ID #--originating fiscal year, e.g., STL-###-YR).

Disruptive Technology: Bringing the Makerspace Environment to SDRD

The concept of a "hackerspace" started in Europe around 1995, where a collective of computer enthusiasts would congregate, share experience, and transform ideas into reality. In 2005, American hackers brought hackerspaces to the U.S., changing the name to "Makerspace" and starting a technology innovation revolution. Since then, thousands of makerspaces opened, giving entrepreneurs, students, hackers, investors, and patent attorneys a clearinghouse to build the future. The positive energy level in a makerspace is infectious.
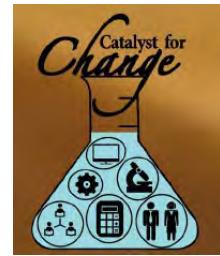
Meanwhile, in 1991, a Finnish student named Torvalds wrote and gave away a Unix clone operating system called Linux. He licensed it using a "free" model. Anyone was free to use Linux, however they wanted, for free. This single event lit the fire that has become the open-source software movement. Now millions of programs with billions of lines of source code are available for students, hobbyists, entrepreneurs, researchers, commercial businesses, and governments.

Hardware development, capabilities, and price have made major strides in the past 20 years as well. When makers couple open-source software to low-cost high-performance hardware, we have rapid, low-risk, highly productive development cycles. This is a most exciting time in the tech world, and developments are only appearing faster.

Today, forward-thinking businesses are using the tremendously successful makerspace model and are creating internal makerspaces for their employees. These spaces are filled with tools like 3-D printers, desktop milling machines, Raspberry Pis, robotics, and virtual reality headsets. Employers expect that makerspaces will grow new employee interactions, teamwork, and enthusiasm. And they will.

In October 2016, National Security Technologies, LLC (NSTec), launched its own internal makerspace initiative called the Catalyst Lab with several objectives. As an SDRD offshoot, our lab will take full advantage of the open-source movement and low-cost hardware. It will function with separate tools/gadgets/toys and accelerated purchasing turnaround with minimal oversight and restrictions. NSTec is following a skunk, phantom, scorpion, fablab, techshop, and millions of other makerspace models inside its Catalyst Lab.

Contributed by C. Hollabaugh

Each of the reports describe the discoveries, achievements, and challenges encountered by the researchers and their teams. SDRD, by definition, invests in high-risk and high-payoff research and the element of uncertainty is implicit. While many of our efforts are successful and result in positive outcomes or technology utilization, some fall short of expectations but cannot be construed as failure in the negative sense. The latter result is a natural and valid part of the process of advanced research and often leads to unforeseen new pathways to future discovery. Regardless, either result advances our knowledge base and increases our ability to identify solutions and/or avoid costly and unwarranted paths for future challenges.

In summary, the SDRD program continues to provide an unfettered mechanism for innovation that returns multi-fold to our customers, to national security, and to the general public. The program is a vibrant R&D innovation engine, empowered by its discretionary pedigree, important mission spectrum, dedicated resources, and sound

SDRD to Global Security Success: Software-Defined Radio

The term software-defined radio (SDR) first appeared in the early 1980s when it was coined by Raytheon E-Systems to describe an early software-configurable radio design. In 2009, a major breakthrough with regard to small, embedded SDRs occurred with the advent of the first commercial single-chip RF front-end designed by Lime Microsystems. The LMS6002D was the first true RF-to-bits and bits-to-RF single-chip device, enabling miniature SDRs on a single printed circuit board.

In FY 2010, an engineering team led by Martin Fay at NSTec's Special Technologies Laboratory (STL) used an LMS6002D for the first time on an SDRD project ("Search Device"). Due to the highly complex nature of these devices, it was critical to gain experience with this type of device before proposing work to prospective sponsors. In FY 2012, STL secured a $1.2M project to develop a miniature SDR transceiver based on the LMS6002D and a Xilinx Spartan 6 field-programmable gate array.

During the development of the aforementioned FY 2012 SDR project, the team began to gain interest from additional sponsors in the area of high data rate SDR transmitters. This work, coupled with additional SDRD projects, has dramatically bolstered NSTec's ability to deliver unique SDRs to the government.

Utilizing a Xilinx Zynq system-on-chip as the core processor, Fay's team was able to combine all of the required digital and microwave circuitry for the high data rate transmitter design onto a single printed circuit board measuring only 1" × 3" in size.

Advanced SDR test platform developed for an FY 2013 SDRD project (Fay 2014)

In FY 2017, STL's current state-of-the-art design will be able to change waveforms on the fly during a single mission. This is the true realization of SDR, where the "personality" of the radio can be substantially changed without changing any hardware. By May 2017, STL will have executed $10M in government sponsor funding on SDR projects. All of those projects have a direct lineage to or benefited from the experience gained on the original FY 2010 SDRD project.

Contributed by M. Fay

Fay, M., K. Painter, S. Gordoni, S. Lyon, "Secure sensor networks using direct-sequence spread-spectrum," in *Site-Directed Research and Development*, FY 2013, National Security Technologies, LLC, Las Vegas, Nevada, 2014, 79–84.

competitiveness, which yields maximum taxpayer benefit. The 26 projects described exemplify the creativity and ability of a diverse scientific and engineering talent base. The efforts also showcase an impressive capability and resource that can be brought to find solutions to a broad array of technology needs and applications relevant to the NNSS mission and national security.

Acknowledgments

Howard A. Bender III
SDRD Program Manager
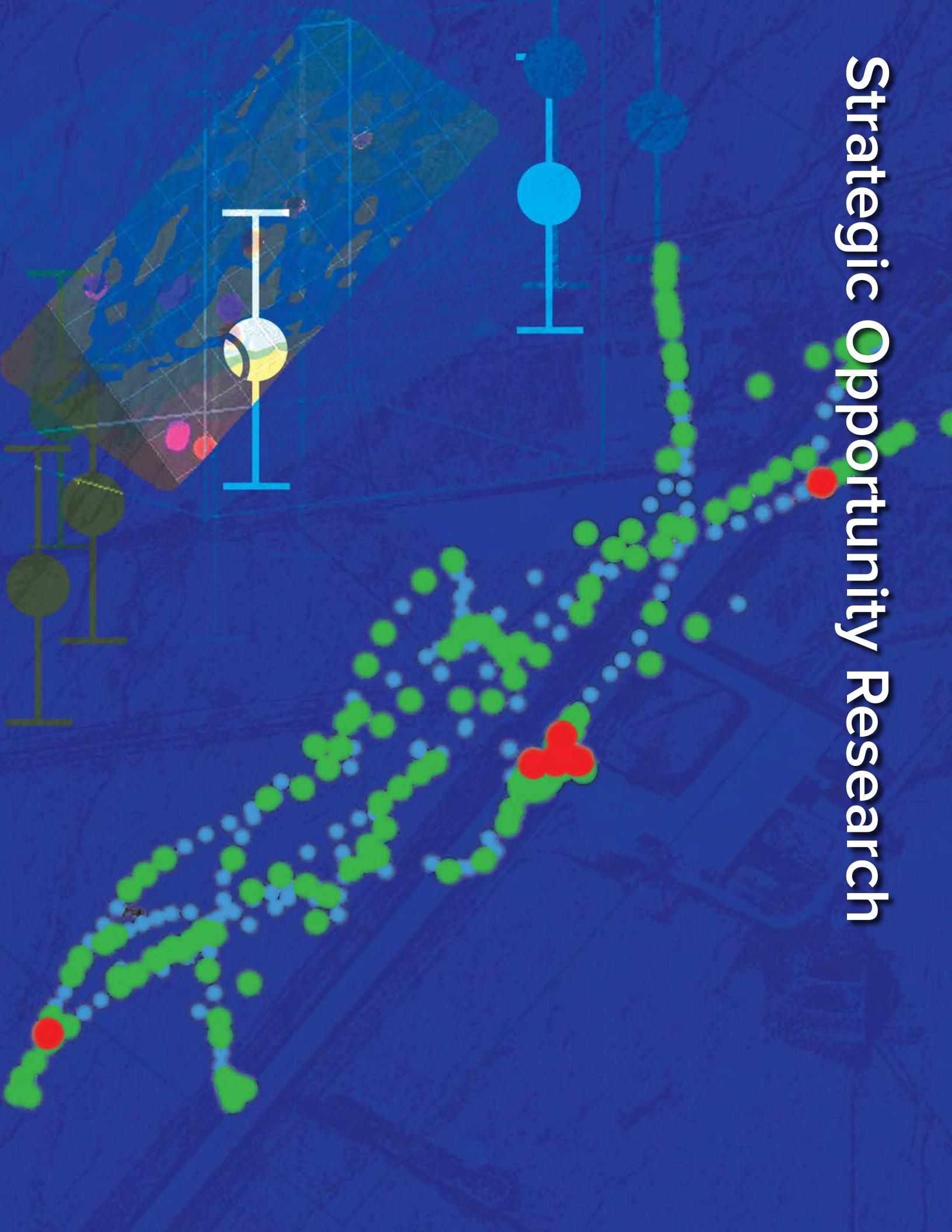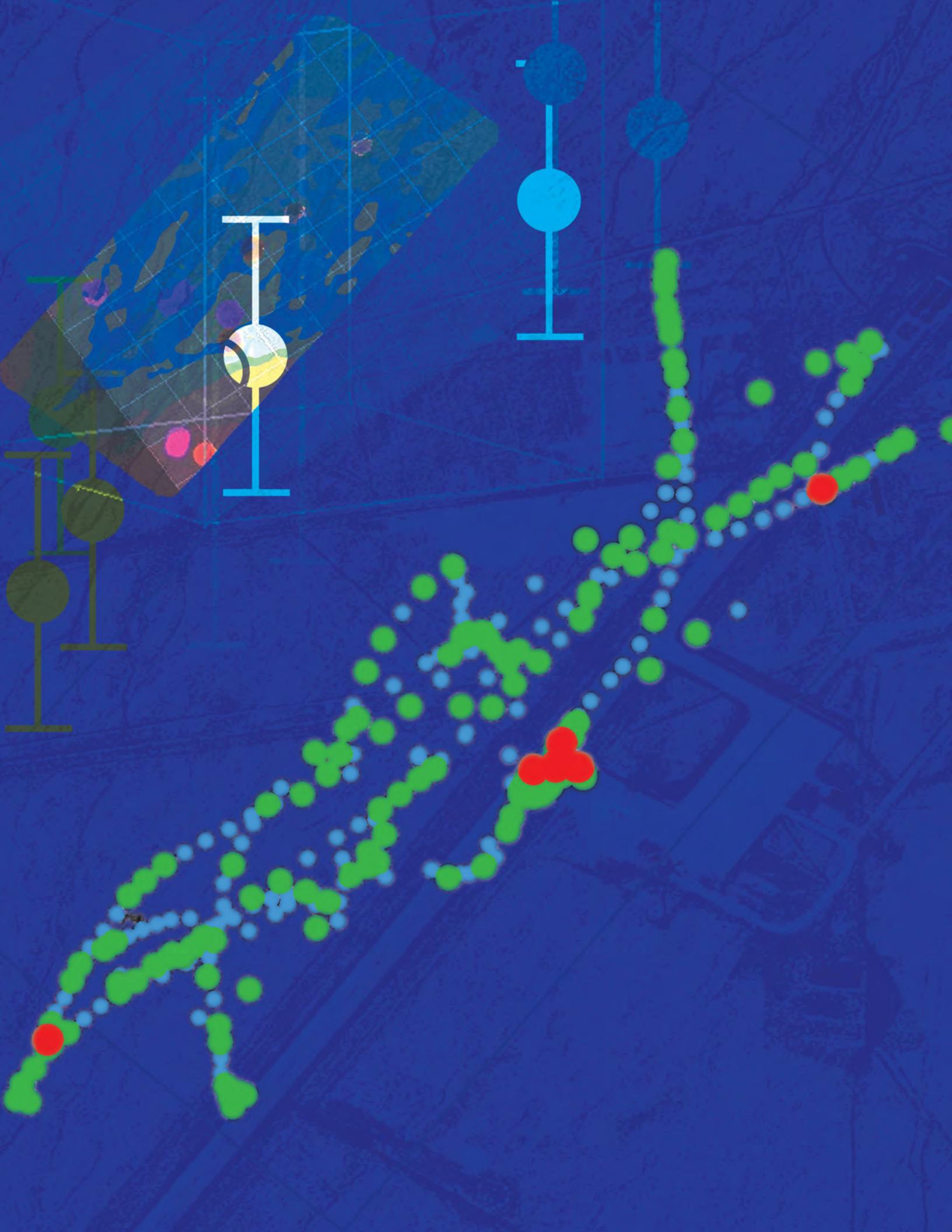
Enhanced Dynamic Materials Research
LAO-19-15 | Continued from FY 2015, Continuing in FY 2017 | Year 2 of 3

Brandon La Lone,[1,a] Gerald D. Stevens,[a] Dale Turley,[a] Lynn R. Veeser,[b] and Robert S. Hixson[b]

We have initiated a research program in dynamic materials properties to address some key outstanding shock physics issues. To do this we have acquired a new research-quality propellant launcher, which was installed at the NSTec Special Technologies Laboratory (STL) gas gun and small-scale explosives campus; the launcher will be operational in FY 2017. This new launcher is the same bore diameter as the existing STL light gas gun (40 mm) but triples the maximum velocity (2.5 km/s) achievable. With this new capability we will initiate new dynamic materials research directions that are first and foremost rigorous, but that also are needed to improve diagnostic capability to determine the fundamental physics models used in large hydrodynamic codes. Such codes are routinely used to simulate dynamic events, but results are only as good as the input physics models. We have investigated the spall strength of copper single crystals, and have begun making careful measurements of wave propagation speeds. We have also initiated research into pressure and temperature melt boundary measurements of shocked tin in a collaboration with the California Institute of Technology. In FY 2017, we will continue these efforts and will also begin a new investigation that will determine whether or not a metal that melts upon shock loading can resolidify upon subsequent compression.

[1] lalonebm@nv.doe.gov, 805-681-2046
[a] Special Technologies Laboratory; [b] New Mexico Operations–Los Alamos

Background

This strategic SDRD project has several focus areas. In Year 2 of this project, significant advancements were made in the following three areas, which are the focus of this report: (1) obtaining a 40 mm bore propellant launcher to allow us to reach higher shock pressures, (2) understanding the properties of single-crystal metals and how their response as a function of crystalline orientation contributes to polycrystalline response, and (3) improving temperature measurements sufficiently to begin to measure the melt curve of tin.

Project

Propellant Launcher Initiative

The 40 mm bore light gas gun at the Special Technologies Laboratory (STL) is routinely used for shock wave studies and diagnostic development. However, this gun has an upper velocity limit of approximately 800 m/s. One of our key capability goals is to reach shock wave stresses that are roughly equivalent to those occurring in high-explosive detonation, which can drive shock wave stresses as high as ~50 GPa in some metals. To reach this performance requires higher impact speeds than our gas gun. We therefore looked in detail at propellant launcher systems that were roughly equivalent in launch tube bore but had a much higher impact speed capability. We decided upon and acquired a 40 mm propellant launcher from Physics Applications,

Inc., as a "turnkey" system. The launch tube is 5.5 m in length and 146 mm in outer diameter; the target chamber and catch tank are a combined 2.6 m long and are 0.9 m in diameter. The launcher is designed to use up to 700 g of smokeless propellant for launching 40 mm diameter projectiles between 0.5 and 2.5 km/s, greatly expanding our velocity range for performing shock compression studies. This launcher has been delivered and installed in Building 229 at STL, which is the same building that houses the light gas gun. A photograph of the installed gun is shown in Figure 1.

Figure 1. The new propellant launcher, installed in Building 229 at STL, is capable of launching projectiles at 0.5 to 2.5 km/s, which expands the velocity range considerably for shock compression experiments

We are presently awaiting site plan approval before the training and test shots can be performed in FY 2017, after which full operations will commence.

Single-Crystal Metal Physics

Metals used in engineering applications are made from polycrystalline materials, where the sample is composed of small "grains" of single-crystal metal. If such materials are not made correctly, it is possible to have grains oriented in a way that is not purely random. This can lead to anisotropic mechanical response of the metal, where the properties depend on the orientation of the sample relative to the stresses applied. In the first year of this project, we performed scoping studies on three different orientations of single-crystal copper to explore elastic and plastic

wave speed and spall strength anisotropies. Based on those results (Hixson 2016), we decided to examine in detail the spall strength of [100] oriented copper crystals in this work.

Metals are put under tension when release waves collide during high-explosive and gas gun–driven shock wave experiments. When the tensile stress exceeds the tensile strength of the metal, it will spall—meaning the sample will tear itself apart. The spall strength for polycrystalline metals has been reported to depend on the peak compressive stress prior to tension, the tensile strain rate as tension is applied, and the dwell time, defined as the time between the compressive and tensile pulses. The variables that affect the spall strength of single-crystal copper have not been thoroughly investigated. Minich (2004) reported a peak compressive stress dependence; however, the tensile strain rate also varied in their experiments, so it is not possible to untangle the two effects from their data alone. Our initial results from FY 2015 indicated the strain rate had at least some effect on the spall stress (Hixson 2016).

We designed and executed a series of plate impact experiments to begin to look for dependencies of spall strength upon the various parameters. This led us to do a carefully designed series of experiments where the goal was to hold the tensile strain rate more or less constant and vary the peak stress for copper crystals. We did this by changing the sample thicknesses and the impact velocity for each experiment. Thicker samples result in lower tensile strain rates, whereas higher impact velocities increase the peak stress and the strain rate. Table 1 shows the experimental parameters used in our experiments and is a combination of data from Years 1 (only the [100] orientation data are shown) and 2 of this project.

All experiments used impactors that were half the thickness of the target. Both the targets and impactors were made from [100] oriented copper crystals (99.99%) purchased from MTI Corporation that were polished to a specular finish and were flat and parallel to within 10 microns. The surface normal was always within ±2 degrees of the [100] crystal orientation

Table 1. Experimental parameters for the [100] copper spall experiments

[100] Experiment No.	Impactor Thickness (mm)	Target Thickness (mm)	Deceleration Rate (m/s/s)	Free Surface Velocity (m/s)	Pullback Velocity $\Delta u_{pullback}$ (m/s)	Peak Stress (GPa)	Spall Strength (GPa)
150818-2	2	4	5.47×10^8	279.3	96.1	5.172	1.690
150819-1	2	4	5.53×10^8	295.2	95.1	5.483	1.674
150820-2	1	2	1.21×10^9	297.2	120.8	5.522	2.124
160524-1	1.5	3	8.25×10^8	453.9	109.9	8.670	1.934
150819-2	1	2	1.83×10^9	594.6	145.3	11.635	2.556
150820-1	2	4	9.17×10^8	597.1	119.6	11.689	2.104
160524-2	2.5	5	6.84×10^8	700.9	117.8	13.963	2.072

according to vendor specifications. Impactors were launched using the STL light gas gun. The free surface velocity was recorded using standard photonic Doppler velocimetry (PDV) techniques with two-fiber PDV probes.

One of the free surface velocity records is shown in Figure 2. The spall signature of the copper crystals is unique in that there is a high-frequency oscillation associated with the compression pulse that follows the pullback signal. A detailed study of this signature will be performed in future work. Of interest to the present study are the free surface velocity plateau (0–350 ns), the deceleration after the plateau (related to the tensile strain rate), and the total velocity depth or pullback velocity that is a measure of the spall stress. The free surface velocity and deceleration are determined from a fit to separate linear segments (red curves in Figure 2), and the pullback velocity is determined by inspection. These values are listed in Table 1. The free surface velocities and pullback velocities were converted to peak stress and approximate spall strength using standard impedance matching methods. We performed the same analysis to the published data from Minich (2004) to determine the peak stress, deceleration rate, and spall strength from their experiments. Figure 3 shows a 3-D plot of the spall strength as a function of peak compressive stress and deceleration from our experiments and the Minich (2004) experiments. Surprisingly, all data are well fit by a single plane, indicating that the spall strength, in the ranges evaluated, is linearly dependent on both the
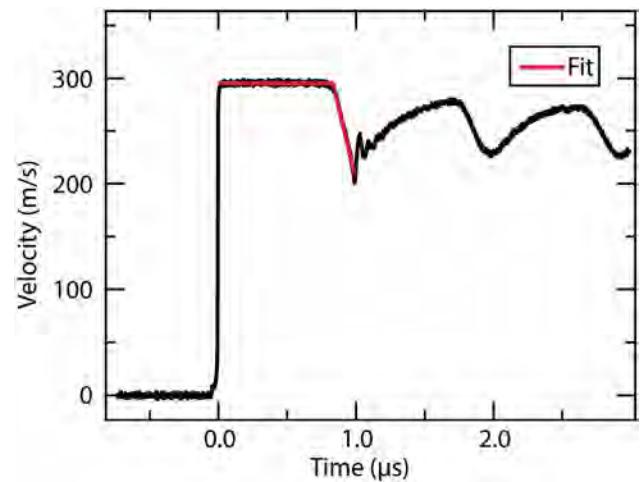
Figure 2. Free surface velocity record for spall along [100] oriented copper crystals, Experiment No. 150819-1 (black curve). We determine the peak velocity and the deceleration by fitting two linear segments (red curve) to the measured velocity.

peak compressive stress and the deceleration rate. The fit parameters are given by spall stress [GPa] = 1.5(1) + 0.46(11) × Decel [mm/(μs)2] + 0.014(3) × P [GPa].

Inspection of Figure 3 indicates that more data are needed to increase confidence in the planar fit, as most of the high stress work by Minich (2004) was performed at nominally the same deceleration rate. Next year, we plan to further this investigation by performing experiments with various deceleration rates at higher stresses. We also intend to perform similar parameter studies on other copper orientations, [110] and [111].
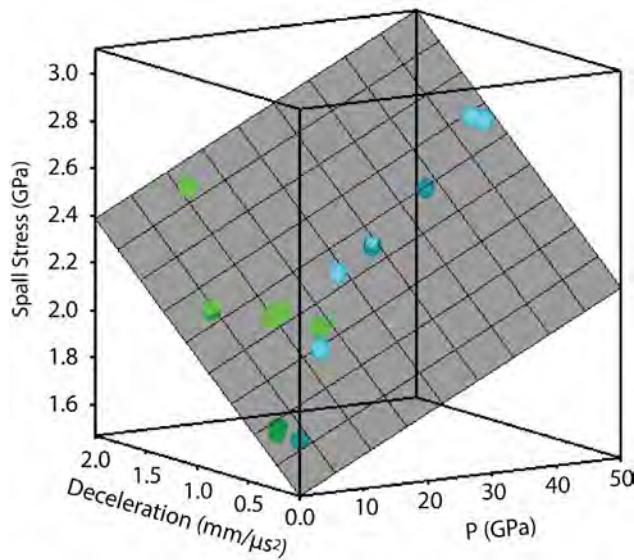
Figure 3. [100] oriented copper spall stress as a function of peak compressive stress (P) and the measured deceleration rate in the pullback signal. The green spheres are our data and the blue spheres are data from Minich (2004). A single plane accurately fits all of the data.

Figure 4. Static (diamond anvil cells [DAC]) melt curves for several metals (Errandonea 2001). These tend to be relatively flat with increasing pressure. Theoretical models and dynamic melt data are generally much higher at high pressures.

We performed initial work to determine if there are anisotropies in either elastic or plastic wave speeds. We expect elastic wave speeds to be 10%–15% different depending upon orientation, but directional dependency of plastic (shock) speeds is more uncertain. Early methods for measuring wave speeds suffered from large uncertainties, so we have developed a new experimental technique using a "top hat" design and multiple channels of velocimetry. Early results show promise, and we will report results in the future.

Tin Temperature Measurements

The measurement of phase transition boundaries is an important aspect of equations of state development for weapons physics because the way a material responds under dynamic loading depends on its phase and its strength in that phase. The locations of solid-solid and melt phase boundaries are important to capture accurately for developing phase-aware physics models. Dynamic melt determinations for metals have most frequently been done using the rarefaction overtake method (McQueen 1982), in which the sound speed is measured as a function

of shock stress, and the change in sound speed that accompanies the loss of shear strength upon melt is observed. This method requires experiments over a relatively large range of shock states to determine the point where the shock Hugoniot and melt curve cross, and it does not provide a direct measurement of the melt temperature. This has driven the dynamic materials community to look for more simple and cost-effective methods for measuring where materials melt both on and off the principal Hugoniot. Other dynamic melt diagnostics (x-ray diffraction [Morgan 2010, Gorman 2015], velocimetry [Mabire 2000], and reflectivity [Elias 1988]) also lack a way to measure temperatures, with one exception. Researchers led by Partouche-Sebban (2005) made dynamic pyrometric measurements on lead using samples shocked to near melt (either 49 or 57 GPa) and reflected from windows of different shock impedance. They obtained temperature-pressure points around 12 (polymethyl methacrylate), 30 (lithium fluoride [LiF]), and 50 GPa (sapphire) from the radiance and reflectance after the
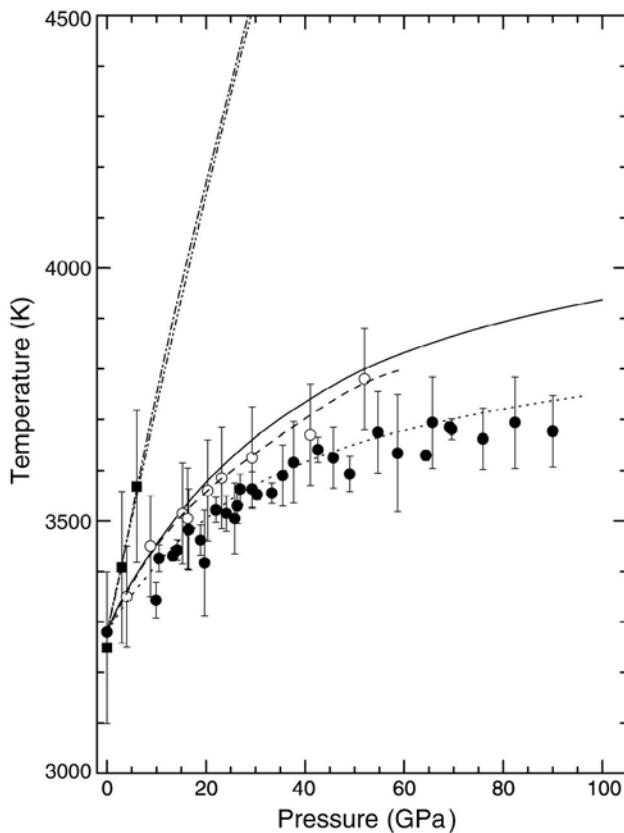
Figure 5. Static melt curve measurements for tantalum (Errandonea 2003). Open circles and the dashed curve represent their most recent work. The double-dot-dash curve going off the top of the graph is a calculation (Lindemann criterion) that is consistent with the dynamic sound speed measurements (Dai 2009) at 9700 K and 300 GPa (off scale in this figure).

Figure 6. A modified graph from Dewaele (2010) showing recent static DAC melt data (color), dynamic sound speed data (Dai 2009) (black square), and theoretical models (curves) for melting of tantalum. These DAC data are closer to theory and dynamic data than Errandonea's (2003), but a significant discrepancy still exists.

shocks reflected from the various windows. They also included one point for tin with melt at T = 1400 ±50 K and 14.4 GPa.

Melt curves have also been measured statically using diamond anvil cells (DAC), laser heating, and x-ray diffraction (see Figure 4 [Errandonea 2001]). Although DAC temperature data at melt (from pyrometry and using ambient emissivity values) are often relatively flat with increasing pressure, as seen in Figure 4, both theoretical models and dynamic measurements tend to show a steep increase in the melt curve with increasing stress. For metals at high pressures, there is often a serious disagreement, sometimes thousands of degrees, between DAC data and both theory

and dynamic measurements. Figure 5 shows more recent tantalum (Ta) data (open circles) along with some fits to the measurements (Errandonea 2003). A subsequent sound speed measurement (Dai 2009) observed a temperature of 9700 ±1000 K at ~300 GPa. While the uncertainty is large, the measurement is not even close to an extrapolation of the DAC data, which would be around 4000 K at this pressure. Figure 6 displays more recent DAC Ta data (Dewaele 2010) in which the authors tried to reconcile the discrepancy. Finding errors in the melt signature and pyrometry in the DAC, they improved the diagnostic. The new DAC temperature data are indeed higher than the earlier measurements, but they still lie well below the dynamic measurement. Similar large disagreements exist for molybdenum (Mo), tungsten (W), vanadium (V), and other metals. It is obvious that a new melt-temperature diagnostic would be very useful.

In the first year of this project, in collaboration with the California Institute of Technology (Caltech), we demonstrated a melt boundary identification technique using radiometry, integrating sphere (IS) reflectometry, and velocimetry to measure the temperature, emissivity, and stress histories of shocked compressed tin with few-nanosecond time resolution. The sample is shocked to an elevated temperature and pressure in

Table 2. Shock parameters for radiance and emissivity experiments on shocked tin at the Caltech powder gun

Shot Number	Copper Projectile Velocity (km/s)	Impact Stress (GPa)	Interface Velocity (km/s)	Stress at Interface (GPa)
1R	1.727	31.0	1.258	22.7
2R	1.965	36.7	1.424	26.6
3R	2.108	40.3	1.516	28.8
1E	1.829	33.4	1.319	24.1
2E	1.961	36.6	1.413	26.3
3E	1.973	36.9	1.427	26.6
4E	2.042	38.6	1.475	27.8

its solid phase, and as the pressure is released, the sample melts; this technique provides a continuous, highly accurate melt boundary measurement. This year, using the same technique, we performed additional experiments at higher and lower peak stresses to provide a more comprehensive measurement of the tin melt boundary.

The experimental technique is detailed in last year's SDRD report (Hixson 2016) and is briefly summarized here. A 1.3 mm thick copper impactor, backed by syntactic foam (a low wave impedance material), is launched to velocities ranging from 1.7 to 2.1 km/s using the 40 mm diameter single-stage powder gun at Caltech's laboratory for experimental geophysics. The target is a 3 mm thick tin sample, diamond turned on both sides, and backed by either a 5 or 10 mm thick LiF window. Loctite 326 is used to bond the tin sample to the window, with bond thicknesses typically in the 1–4 μm range. All measurements are made at the tin-glue-LiF interface when it is under a condition of uniaxial strain. At impact a shock wave is launched into the tin sample, which partially releases upon reflection with the LiF window. The tin at the interface is initially compressed to the high-pressure solid body-centered tetragonal (BCT) phase at an elevated temperature. A shock wave is also launched into the copper flyer upon impact; when the shock in the copper reflects off the syntactic foam, it sends a ramped release wave into the tin. This release wave reaches the interface about 300 ns after the initial shock wave. The release wave lowers the interface stress at a rate of approximately 75 GPa/μs, and the release path intersects the melt boundary. Reflectance and radiometry shots were

performed independently to diagnose this process. Our flash lamp illuminating IS reflectance diagnostic (La Lone 2013) was used to collect dynamic reflectance of the tin-LiF interface at six different wavelengths, 500, 700, 850, 1100, 1300, and 1550 nm, and the velocity at the interface was measured with PDV using a laser wavelength of 1565.1 nm. The reflectance is converted to emissivity using Kirchhoff's law. For the radiometry shots, we collect thermal radiance in two spectral channels, 1300 and 1600 nm, using a similar diagnostic. The thermal radiance measurement is combined with the emissivity measurement to obtain the temperature history using the Planck equation as described in La Lone (2013).

Table 2 lists the shock parameters for three radiance (R) and four reflectance-emissivity (E) shots. Figure 7 shows the dynamic reflectance normalized to the ambient reflectance, along with the stress derived from the PDV measurement of the tin-LiF interface velocity, for Shot 4E at six wavelengths. When the shock reaches the window interface, the tin transforms almost immediately to the BCT phase, and its reflectance increases by 5%–15%. About 600 ns later there is a subsequent drop in reflectance when the release path intersects the tin melt boundary. These sudden emissivity changes indicate that, at least for tin, the reflectance alone is a good phase-change indicator.

To obtain dynamic temperature measurements, radiance from Experiment 1R was paired with emissivities from Experiment 1E, 2R was paired with 3E, and 3R was paired with 4E. The emissivities at 1100 nm and 1300 nm were averaged for the 1300 nm temperature
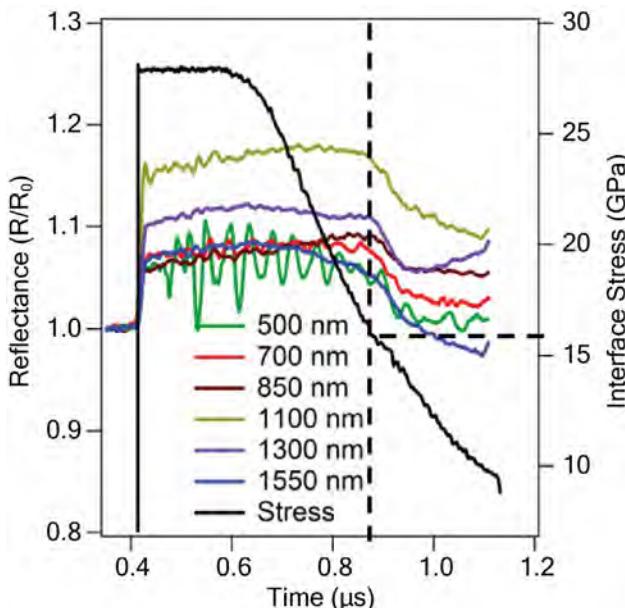
Figure 7. Reflectance divided by ambient reflectance for six wavelengths (color) and shock stress (black) measured by PDV versus time on Shot 3E at the Caltech gun. The vertical dashed line shows where the reflectance begins to drop due to intersection with the melt boundary, and the horizontal dashed line indicates the stress at which this occurs.

calculations, and the 1550 nm emissivity was used for the 1600 nm temperature calculations. The temperature and interface velocity histories for Shots 2R and 3R are shown in Figure 8. We combine the temperature curves for the two detectors and merge the result with the stress curve to obtain a temperature versus stress release path for each radiance experiment. The temperature-stress curves appear in Figure 9 superimposed upon the calculated phase diagram of Mabire (2000). Our measured temperature curves release from right to left in the figure. The release curves begin at a partially released state, lower than the Hugoniot, from the shock reflecting off the lower impedance LiF window. The release curves follow an isentrope and therefore unload along the melt curve after intersecting it. Melt is indicated by an abrupt change in the slope (steepening) of the release curves as they transition from releasing in the solid phase to releasing along the melt boundary. The steeper portion of the release, where the curves are on the melt boundary, is in good agreement with the calculated melt curve
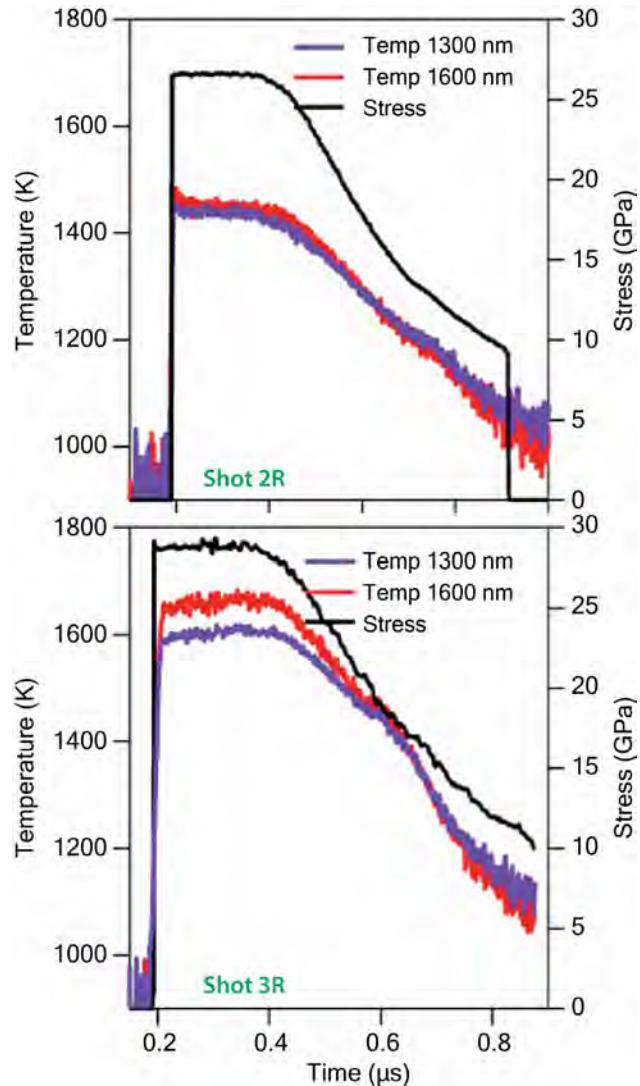
Figure 8. Shock stress (black) and temperature *T* (color) for radiance detectors at 1300 and 1600 nm wavelengths for Shots 2R and 3R at the Caltech gun. After shock breakout into the window, *T* is roughly constant until the stress begins to release around 0.4 μs. We see slight disagreement between the two detectors for Shot 3R, and this affects the uncertainty. However, the agreement appears to be quite good on the lower portion of the release, where the release is on the melt boundary, so the melt temperatures are accurate.

of Mabire (2000). The slight disagreement with the calculations is within our measurement uncertainties of about ±3%.
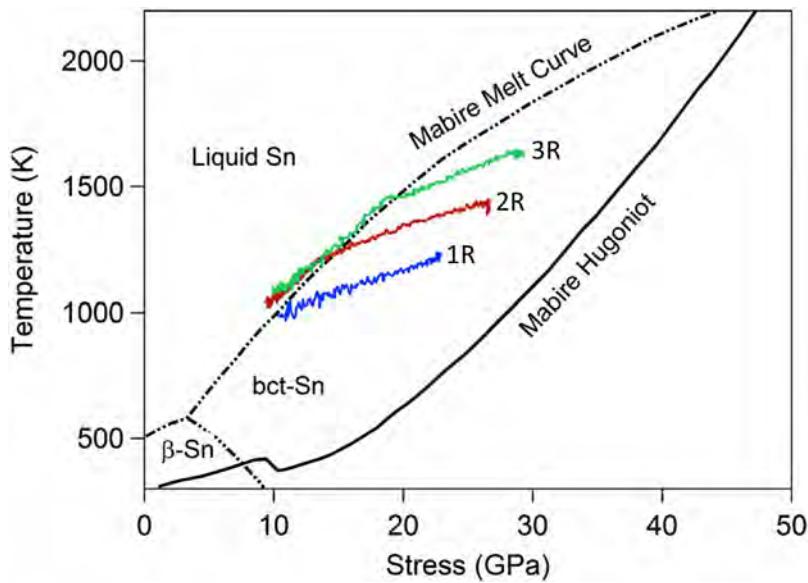
Figure 9. Measured temperature versus stress release paths for tin (color) and the calculated phase diagram (black) of Mabire (2000). Initial shock is to a point on the Hugoniot curve. Immediately the wave partially reflects from the window because of impedance mismatch; the measurements begin at this partially released state, at the far right end of each curve. After about 300 ns, a release wave from the back of the impactor arrives at the window and begins the slower release along the colored curves. The abrupt change in slope (steepening) indicates the intersection with the melt boundary as the release begins to follow the melt curve. The two highest-stress shots agree well with the calculated melt curve. The lowest curve is from an experiment that did not release quite to melt.

In FY 2017 we plan to perform experiments at higher stresses to explore more of the melt curve for tin. Starting from higher shock stresses, we expect the release curve to eventually deviate from the melt curve and continue to release purely in the liquid phase. Our new propellant launcher should allow us to shock tin to about 50 GPa, which will be near or above the point where the Hugoniot and melt curve cross. Once we establish the pure liquid phase, we will attempt to recompress the interface and look for signs of resolidification. At present, it is unknown if recompressed liquid metal will solidify on the timescales of these experiments, even if it is thermodynamically favorable to do so.

Conclusion

A new propellant launcher has been acquired and installed at STL. We expect this instrument to be fully operational in mid-FY 2017.

Initial results on the spall properties of single-crystal copper have been obtained on the 40 mm bore gas gun at STL. Our results indicate that the spall strength of [100] copper is linearly dependent on both the peak compressive stress and the release rate as the sample goes into tension. More work is needed to better define these dependencies and develop a theoretical framework for our measurements.

We have obtained very good temperature data on tin across the center of the Mabire (2000) phase diagram— temperatures from 1000 to 1400 K and stress from about 9 to 27 GPa. We have directly observed the melt boundary. We plan to continue this work in FY 2017 to map out more of this calculated equation of state. The resulting techniques will enable similar temperature measurements in the phase change regime for other metals.

Acknowledgments

References

Dai, C., J. Hu, H. Tan, "Hugoniot temperatures and melting of tantalum under shock compression determined by optical pyrometry," *J. Appl. Phys.* **106** (2009) 043519.

Dewaele, A., M. Mezouar, N. Guignot, P. Loubeyre, "High melting points of tantalum in a laser-heated diamond anvil cell," *Phys. Rev. Lett.* **104** (2010) 255701.

Elias, P., P. Chapron, B. Laurent, "Detection of melting in release for a shock-loaded tin sample using the reflectivity measurement method," *Opt. Commun.* **66** (1988) 100–106.

Errandonea, D., B. Schwager, R. Ditz, C. Gessmann, R. Boehler, M. Ross, "Systematics of transition-metal melting," *Phys. Rev. B* **63** (2001) 132104.

Errandonea, D., M. Somayazulu, D. Häusermann, H. K. Mao, "Melting of tantalum at high pressure determined by angle dispersive x-ray diffraction in a double-sided laser-heated diamond-anvil cell," *J. Phys. Condens. Matter* **15**, 45 (2003) 7635.

Gorman, M. G., et al., "Direct observation of melting in shock-compressed bismuth with femtosecond x-ray diffraction," *Phys. Rev. Lett.* **115**, 9 (2015) 095701.

Hixson, R. S., B. La Lone, G. D. Stevens, W. D. Turley, L. R. Veeser, "Enhanced dynamic materials research," in *Site-Directed Research and Development*, FY 2015, National Security Technologies, LLC, Las Vegas, Nevada, 2016, 15–29.

La Lone, B. M., G. D. Stevens, W. D. Turley, D. B. Holtkamp, A. J. Iverson, R. S. Hixson, L. R. Veeser, "Release path temperatures of shock-compressed tin from dynamic reflectance and radiance measurements," *J. Appl. Phys.* **114** (2013) 063506.

Mabire, C., P. L. Héreil, "Shock induced polymorphic transition and melting of tin," *AIP Conf. Proc.* **505** (2000) 93–96.

McQueen, R. G., J. W. Hopson, J. N. Fritz, "Optical technique for determining rarefaction wave velocities at very high pressures," *Rev. Sci. Instrum.* **53** (1982) 245.

Minich, R. W., J. U. Cazamias, M. Kumar, A. J. Schwartz, "Effect of microstructural length scales on spall behavior," *Metallurgical and Materials Transactions A* **35A**, 9 (2004) 2663–2673.

Morgan, D. V., M. Grover, D. Macy, M. Madlener, G. Stevens, W. D. Turley, "Observations of shock-loaded tin and zirconium surfaces with single-pulse x-ray diffraction," *Powder Diffr.* **25** (2010) 138–142.

Partouche-Sebban, D., et al., "Measurement of the shock-heated melt curve of lead using pyrometry and reflectometry," *J. Appl. Phys.* **97** (2005) 043521.

This page left blank intentionally

Unmanned Aircraft System for Remote Contour Mapping of a Nuclear Radiation Field
RSLN-15-15 | Continued from FY 2015, Continuing in FY 2017 | Year 2 of 3

Karen McCall,[1,a] Russell Malchow,[a] Paul Guss,[a] Rick Fischer,[b] Michael Lukens,[a] Mark Adan,[a] Michael Howard,[a] Eric Wagner,[a] Ki Park,[a] Rusty Trainham,[c] Paul Oh,[d] and Pareshkumar Brahmbratt[d]

Nuclear radiation detection and monitoring are very important to public safety, particularly for nuclear disasters involving radioactive contamination. Among the advantages an unmanned aerial system (UAS) has are quick deployment, low-altitude flying that enhances sensitivity, no radiation exposure health safety restriction, and the ability to access highly hazardous or radioactive areas. Additionally, the UAS can be configured with nuclear detecting sensors optimized to measure the hazard associated with the event. For this project, small UAS (sUAS) platforms were obtained for sensor payloads for radiation detection and electro-optical systems that were specifically developed for UAS research, development, and operational testing. The sensor payloads will be optimized for future contour mapping of a nuclear radiation field, which will result in a formula for low-cost UAS platform operations with built-in formation flight control. The focus of the FY 2016 work was to initiate the sUAS comprehensive testing using the Sandstorm and other acquired platforms, acquire sensors for detection and localization, and continue the development of algorithms. In FY 2017, we will conduct a series of UAS flights to collect data to better define and inform future UAS endeavors. The data collections will include a variety of radiological, optical, and imagery data. The collection of data will be made available to interested parties to conduct in-depth analysis and investigation. The flights will include near real–time and real-time data from autonomous flights including beyond the visual line of sight.

[1] mccallka@nv.doe.gov, 702-295-8089
[a] Remote Sensing Laboratory–Nellis; [b] Remote Sensing Laboratory–Andrews; [c] Special Technologies Laboratory;
[d] University of Nevada, Las Vegas

Background

Unmanned aircraft systems (UASs) have many advantages and provide significant operational benefits. It is a common argument that UASs are better suited for "4D" tasks: dull, dirty, dangerous, and deep (Barnhart 2012a). The "dull" aspect refers to repetitive missions. "Dirty" refers to environments in which there are nuclear, biological, and chemical threats. The tasks deemed "dangerous" are those in which there is a high risk to the aircraft and aircrew. "Deep" tasks are those that are beyond the range of current manned aircraft (Franklin 2008). Low-cost UASs (Di 2011a) are becoming increasingly popular in both research and practical applications. Lately, UAS research is becoming a notable area with a growing number of papers focused on system modeling, navigation, flight control, path planning, and other topics. With the rapid development of electronics and wireless communication technology, civilian remote sensing becomes practical by installing inexpensive sensors on UASs.

UASs, which are governed by FAA rules (FAA 2015), are used for remote sensing applications in many different areas, such as water management, forest fire detection, wetland monitoring, and crop identification (Chao 2009). Compared with a single UAS, the cooperative UAS platforms provide more safety and efficiency (Geramifard 2011, Han 2013a, 2014a). Multiple UASs can share information with each other by wireless communication (Abdessameud 2010), so optimal algorithms like gradient searching can be implemented (Gan 2011).

The central tenet of the UAS is that the cockpit does not have an operator onboard the aircraft; therefore, control of the aircraft must take place by other means. The approach to command and control can be separated into three distinct forms: (1) ground control or remote piloting, (2) semi-autonomous control, and (3) autonomous control.

A small UAS (sUAS) (maximum weight of 55 lb) can employ sensors to not only perform remote sensing, but also to assist with the autonomous or semi-autonomous navigation and operation of the sUAS (Beard 2012). Under autonomous control, the on-board computer is in control—not a human being (Gupta 2013). Goplen (2015) has enumerated the types of data that UASs collect for U.S. Geological Survey use and archives: 3-D modeling, color infrared orthophotography, contour map generation, digital surface models, feature extraction, keyhole markup language, normalized difference vegetation index, orthophotography point cloud generation, and volumetric measurements.

UAS designs are usually one of two types: fixed-wing (Di 2011a) or rotary-wing, which are also called vertical takeoff and landing (VTOL) UASs. Fixed-wing UASs can cooperate (Di 2011b) to fulfill the requirements of many practical applications (Han 2013b, 2014b, 2014c) and are popular for tasks requiring endurance (Chao 2010). Compared to fixed-wing UASs, VTOL UASs have particular advantages, such as hovering capabilities and little space restriction for takeoff and landing, which are beneficial for applications in search and surveillance as well as static image capturing or remote sensing.

UAS payloads may be either sensors or cargo (Barnhart 2012b). For sUASs, typically, the payloads are sensors. Designers of electro-optical sensor payloads for sUASs are under intense pressure to evolve their technologies to keep pace with the fast-moving trends in the sUAS industry. Perhaps in no other market is there a need for smaller, lighter, and less expensive payloads as in the sUAS industry.

Project

The motivation of this work is to detect the level of nuclear radiation in a timely way through efficient use of low-cost UASs. Table 1 outlines the project mission statement and objectives to accomplish the mission. The status column summarizes progress during FY 2016.

Over the past two years, the project has acquired two fixed-wing Sandstorm UASs in FY 2015, and two small fixed-wing T-28s, two rotary-wing 3DR quadcopters, and one rotary-wing octocopter in FY 2016 (Figure 1). The systems are capable of performing normal and operational scenario flight maneuvers. The systems are self-contained, have an independent capability to control or terminate the flight, use autonomous waypoint navigation, support line-of-sight and beyond-line-of-sight operations, and have the flexibility to integrate commercially available off-the-shelf and government-furnished sensors.

The systems' control, telemetry, and subsystems meet minimum federal requirements for aerial flight missions. The system will be further tested to provide real-time sensor data and metadata for processing and recording.

NNSS UAS Training, Testing, and Data Collection

Multiple tasks and efforts were conducted throughout FY 2016, including training for UAS operators, testing of sensors, and demonstration flights over radiological sources while streaming data in real time (Figures 2 and 3). The demonstration flights allowed the team to discover the benefits and issues with integrating sensors into small platforms. With discovery comes opportunity for improvement.

Table 1. UAS project mission and progress for FY 2016

Domain	SDRD UAS Strategic Initiative—Phase A	Status
Mission Statement	By FY 2018, NNSS will operate an unmanned aerial system (UAS) with a detector, returning data relevant to determining radiological hazards on the ground, demonstrating the ability to integrate systems and detectors into the system.	Infrastructure established.
Environment	The UAS will fly low and slow to allow for radiological detection but above or around obstacles.	Training flights conducted and continuing.
Awareness and Navigation	The UAS will be programmed using standard autopilot waypoints and will be actively monitored.	Reviewing flight management systems for incorporating onto the various platforms.
Sensors	The UAS will incorporate a radiological and other sensor for reporting on the presence of and identification of radiological hazards and other hazards.	Infrastructure established. Integrating sensors.
Communication	The UAS will communicate in real time or near-real time relevant navigation and detection information. Information will be formatted and relayed so as to be useful for currently used software systems or platforms.	Infrastructure established. Data telemetry tested.
Architecture	The UAS will implement an up-to-date architecture or architectures.	Team established to develop standards for sensor integration.

Figure 1. NNSS UAS platforms: (a) Sandstorm fixed wing, heavy payload; (b) 3DR Solo, very small payload; (c) Tarot Octocopter, heavy payload and multi-sensor capable; and (d) T-28 Aircraft, a training aircraft
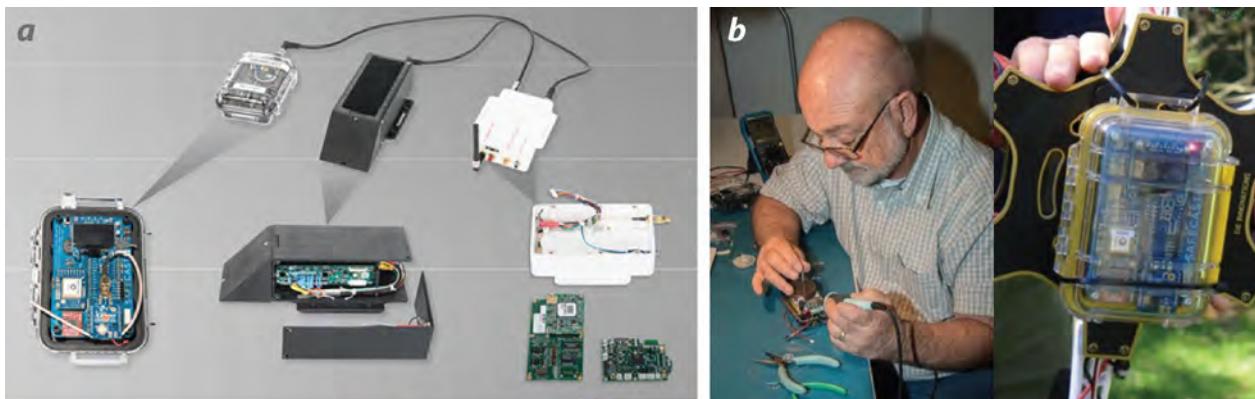
Figure 2. NNSS UAS (a) small radiological sensors and (b) sensor integration efforts for small platforms

Figure 3. NNSS UAS training flights conducted using the different platforms

Data Collection

During the radiation detection tests with the Sandstorm fixed-wing aircraft, the Safecast and Desert Eagle radiation detectors were mounted inside the platform with the components of the digital video camera. All the sensors were individually battery powered, and the data from the sensors were sent to ground stations situated nearby.

The Safecast's bGeigie Nano is a mobile radiation detector that uses a pancake Geiger-Müeller tube to measure alpha, beta, and gamma radiation. With the addition of an XBee module from Digi Corporation, the bGeigie Nano's GPS receiver can send data wirelessly over Wi-Fi, Bluetooth, and other protocols. For use on the Sandstorm, we acquired the transmitter/receiver hardware and successfully demonstrated its performance with the Special Technologies Laboratory (STL)

RaptorX software (RaptorX 2015). After the real-time system was demonstrated, we began to integrate it with the Remote Sensing Laboratory (RSL) Advanced Visualization and Integration of Data (AVID) acquisition and analysis system.

The Desert Eagle is a low-power multichannel analyzer/spectra transmitter device, which when combined with the 1" × 1" thallium-doped sodium iodide (NaI:Tl) detector enables a sUAS to collect and transmit real-time isotopic gamma ray spectra. The government off-the-shelf radiation detection system not only integrates into the STL RaptorX package, but it also interfaces with the AVID system. This is a critical milestone on the proof-of-concept pathway to demonstrate and to achieve the technology to autonomously perform a radiological survey using a sUAS. The Desert Eagle collects a 1024-channel spectra at 0–3 MeV and sends the spectra acquired at 1 Hz to a ground station for real-time mapping, breadcrumb tracking, or isotope identification (Figure 4).

The UAS platforms, equipped with radiation detectors, will also be outfitted and tested with complementary optical systems, such as hyperspectral, thermal, and visual cameras, or chemical sensors. During the radiation detection mission, a digital camera was mounted on the bottom of the front of the Sandstorm (Figure 5). Data from the camera were streamed in real-time to a ground station. The data were taken in conjunction with the radiation data, but the two data streams were recorded on separate ground units. A goal in the future would be to have an integrated system for recording, displaying, and analysis of multiple sensor data types.

In addition to the digital video camera, the project acquired a high-definition still digital camera and a lidar camera for data collection on the Sandstorm and octocopter platforms (Figure 6). These sensors will be researched for terrain reconstruction, obstacle sensing, and developing 3-D maps.

Data Analysis Results

Safecast and Desert Eagle radiation measurement data were collected during the UAS flight mission to locate two sources placed near the Desert Rock Airport runway. The sources were a small ^{137}Cs source and a smaller ^{60}Co source. Due to the small sizes of the sources, only the cesium source was detected. These results led us to conduct additional tests with the Safecast and Desert Eagle detectors to characterize their detection capability in relationship to distance.

Readings from the Safecast and Desert Eagle detectors were analyzed. The difference in count rates was plotted against distance to show that the count rates change inversely to the square of the distance between the source and the counters (Figure 7). A
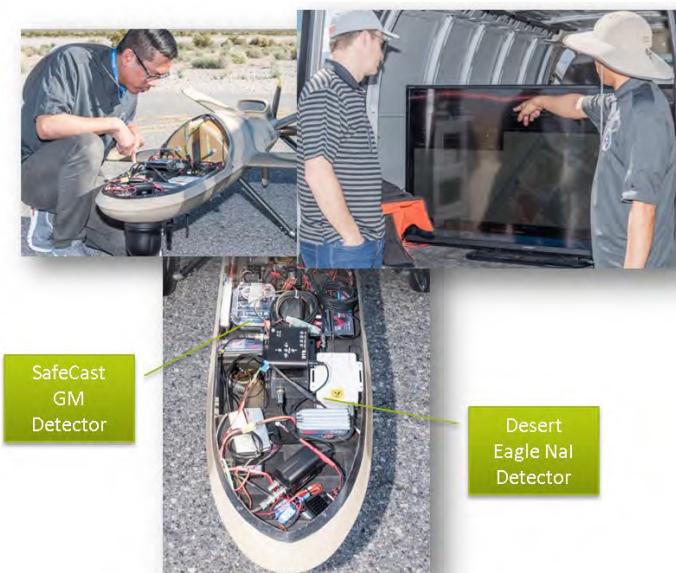
Figure 4. Safecast and Desert Eagle mounted inside the Sandstorm UAS, sending data in real time to a ground monitoring station

SafeCast GM Detector

Desert Eagle NaI Detector

Figure 5. UAS digital video camera and ground monitoring system showing real-time data

Figure 6. Additional UAS optical sensors for UAS platforms

power expression was fitted to the plot and a function developed. The average values fell remarkably close to an R^2 value of 1. Error bars represent the variability of each counting period and uncertainty in measuring accuracy. The source distances were measured to an accuracy of ±0.5 feet.

During the collection flights the UAS platform flew between 100 and 400 feet above the sources. As indicated in the graph in Figure 8, using the equation derived in Figure 7 for a ^{137}Cs 16.2 mCi source, the flight altitude is expected to inversely impact the measurements from the detectors onboard. The flight
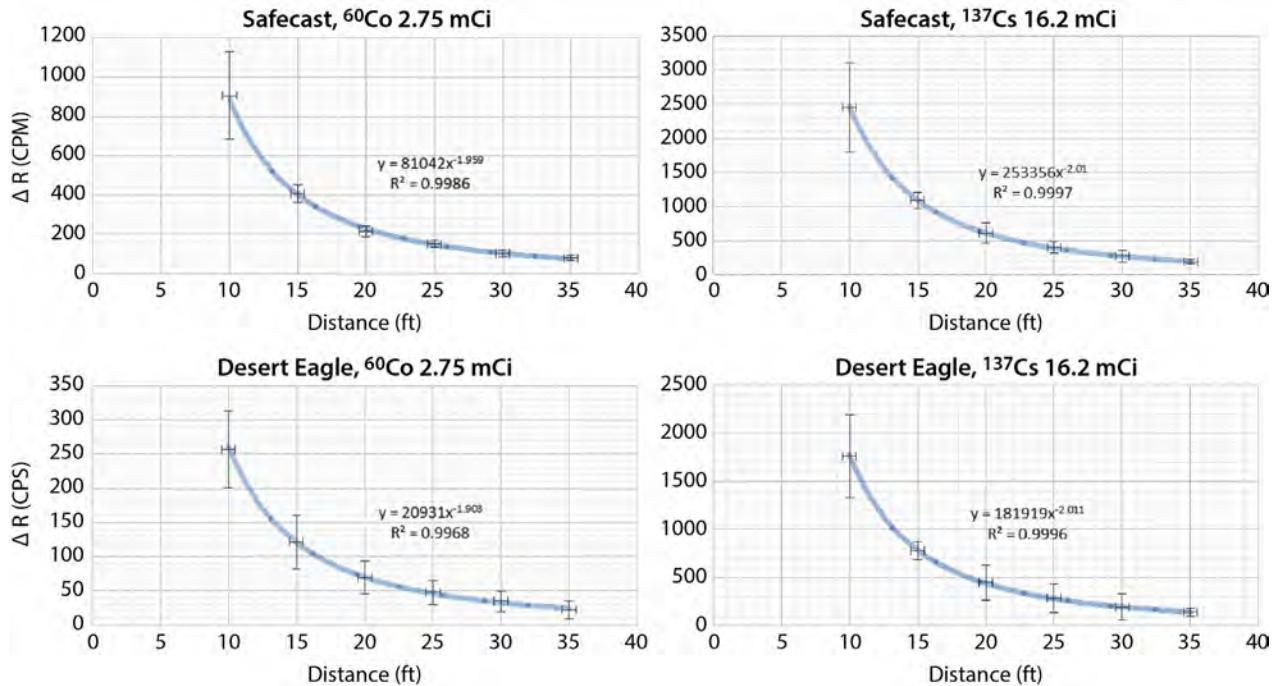
Figure 7. Counts vs. distance plots for Safecast and Desert Eagle detectors

altitude would provide measured counts of around 25 for 100 feet and reduce to 1 count for altitudes above 350 feet. The highest reading would be measured on the ground with the UAS taxiing past the source at a distance of less than 50 feet.

In normal aerial data collection efforts, the data collected are subjected to several corrections and quality assurance tests to ensure the resulting maps represent the terrestrial radiation environment as accurately as possible. During early UAS data collection efforts, it was discovered the equipment had

positioning errors. This issue resulted in inaccuracies in the data plotted on the maps. To ensure the data were not in error, a low-level aerial radiological survey using the Aerial Measuring System (AMS) helicopter was performed to collect radiation background measurements at Desert Rock Airport (Figure 9). Despite the position errors, the data were analyzed to produce gross count maps for the Safecast (Figure 10) and Desert Eagle (Figure 11), and a cesium extraction for the Desert Eagle spectral data was collected (Figure 12).
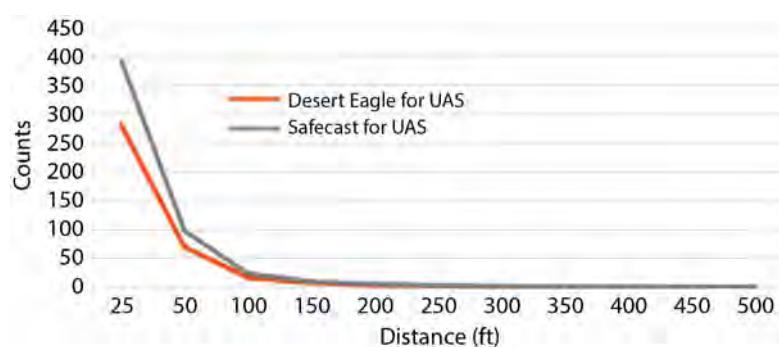
Figure 8. Expected counts vs. distance plot for the Safecast and Desert Eagle detectors
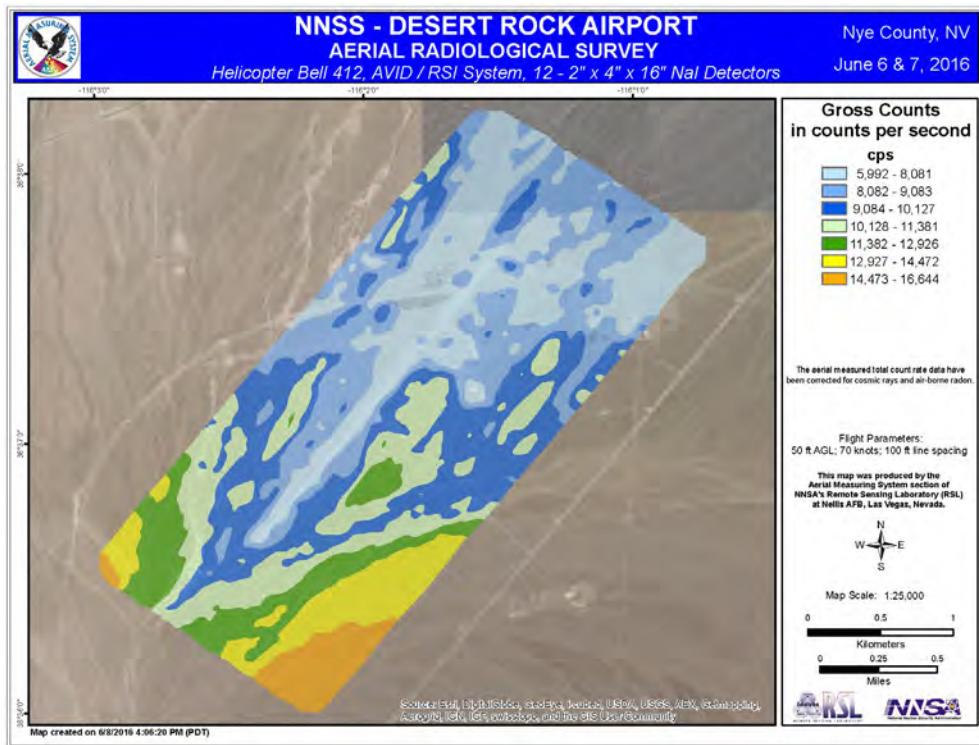
Figure 9. AMS helicopter background survey gross count
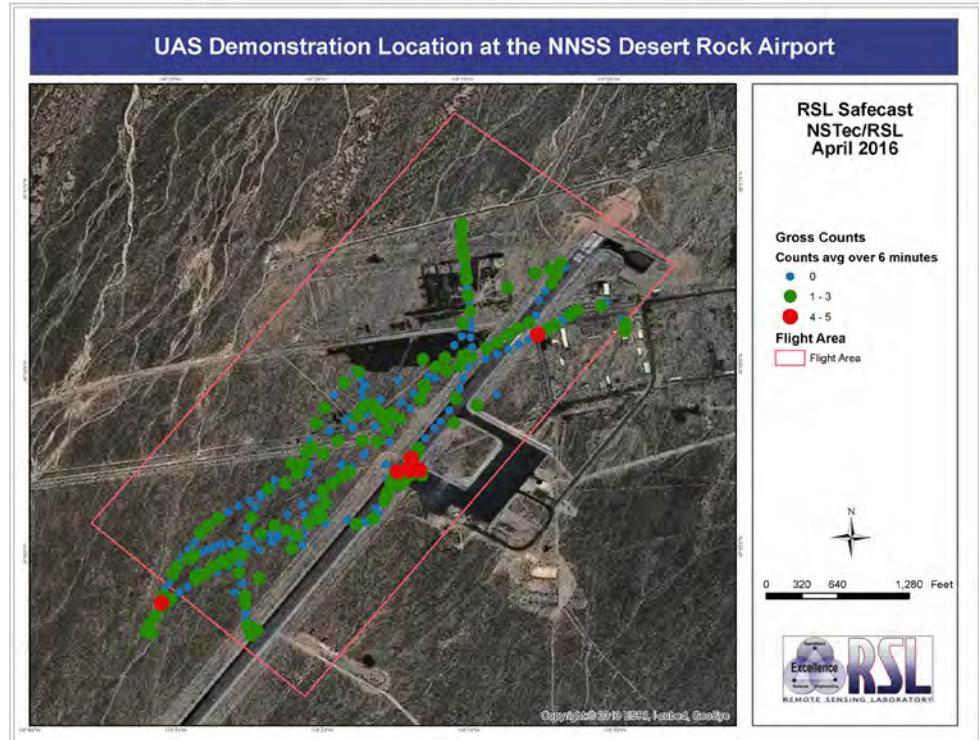
Figure 10. Safecast gross count data from source flight at Desert Rock Airport
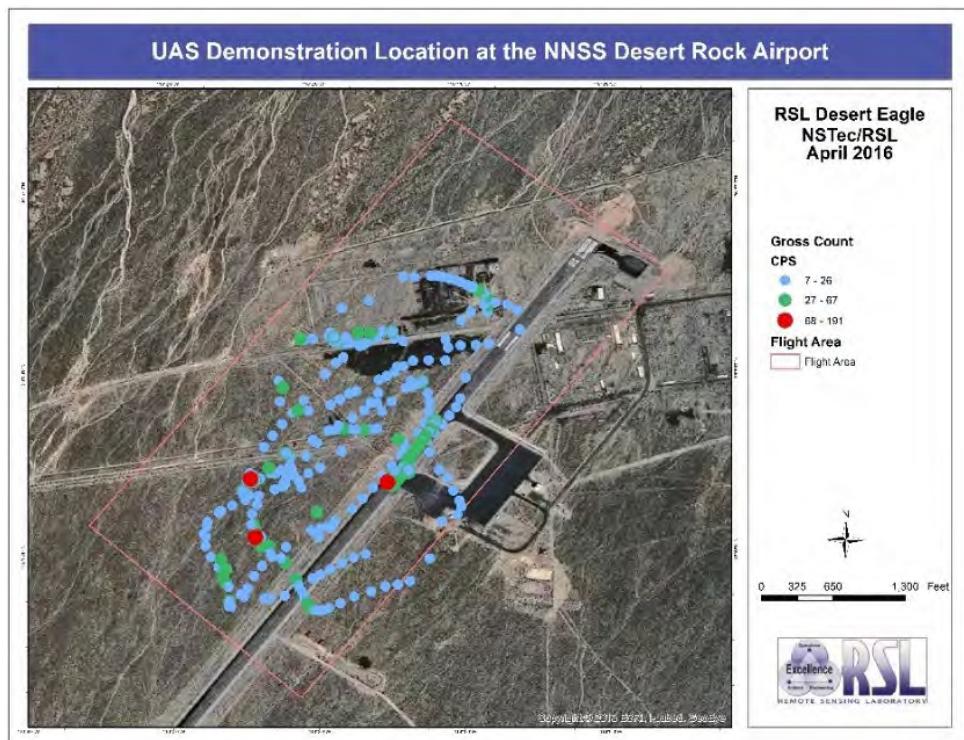
Figure 11. Desert Eagle gross count data from source flight at Desert Rock Airport
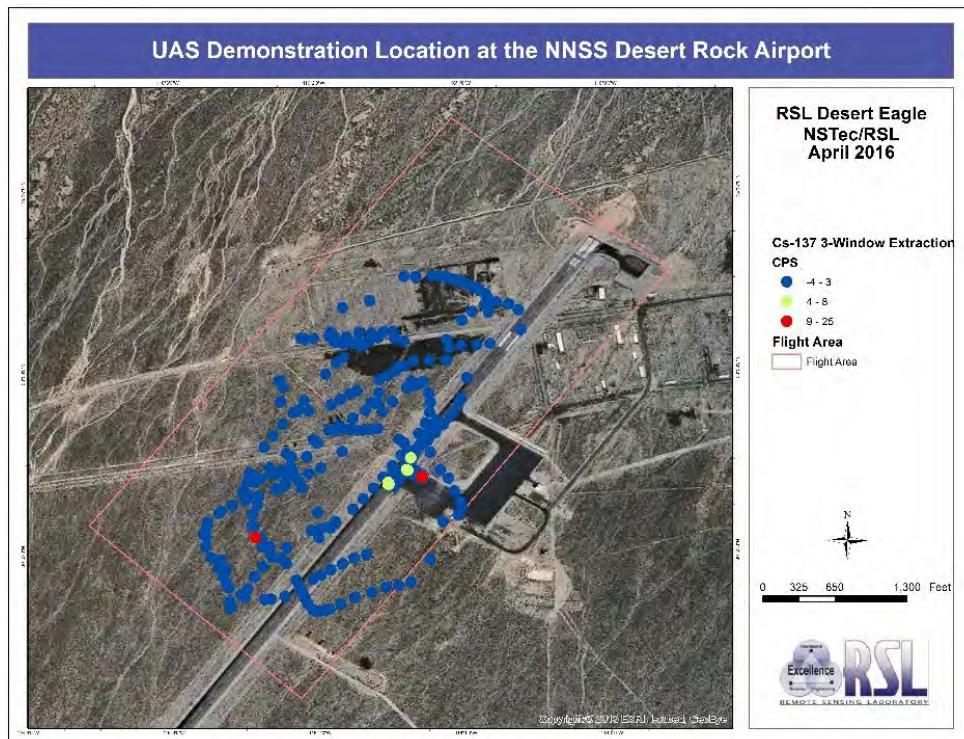
Figure 12. Desert Eagle 3-window cesium extraction map from Desert Rock Airport

Gross Count Maps

To obtain a gross count, the count data that were collected by the equipment were integrated between 24 and 3,027 keV by

$$C_G = \Big|_{E=24}^{3027} c(E) \tag{1}$$

where C_G is gross count rate (counts per second [cps]), E is photon energy in keV, and $c(E)$ is count rate in the energy spectrum at energy E (cps).

Cesium 3-Window Algorithm

The 3-window algorithm employs a narrow window centered on the energy of the specific photopeak of the isotope of concern. The algorithm assumes that the background counts in the photopeak window are proportional to the counts recorded in the two background windows. The algorithm employs a background window on each side of the photopeak window. This algorithm assumes that for any spectrum, the number of background counts in the photopeak window is linearly related to the counts in the two background windows:

$$C_3 = \left. \left\{ \Big|_{E=E_2}^{E_3} c(E) - B_{3P} \right\} \right.$$
$$-K_3 \left\{ \left[\Big|_{E=E_1}^{E_2} c(E) - B_{3L} \right] + \left[\Big|_{E=E_3}^{E_4} c(E) - B_{3H} \right] \right\} \tag{2}$$

with

$$K_3 = \frac{\Big|_{E=E_2}^{E_3} c_{ref}(E) - B_{3P}}{\Big|_{E=E_1}^{E_2} c_{ref}(E) - B_{3L} + \Big|_{E=E_3}^{E_4} c_{ref}(E) - B_{3H}}, \tag{3}$$

where C_3 is the count rate from the 3-window algorithm, E_n are the limiting energies of the windows ($E_1 < E_2 < E_3 < E_4$), B_{3P} is the average background count rate in the 3-window photopeak window (cps), B_{3L} is the average background count rate in the 3-window low-energy window (cps), B_{3H} is the average background count rate in the 3-window high-energy window (cps), and K_3 is the ratio of the count rate in the primary window to the count rates in the two background windows in a reference region of the survey area.

UNLV Formation Flights

An objective of the UAS project, in collaboration with the University of Nevada, Las Vegas (UNLV), is to explore the use of formation flights using multiple UASs and algorithms to search for a source. UNLV acquired three hexacopter UAVs and demonstrated flying them in formation based on a set flight pattern using a single ground control station (Figure 13). In addition to the formation flight, UNLV equipped the UASs with Safecast detectors. In FY 2017, UNLV will demonstrate formation flights over a source with the Safecast detectors. The demonstration will also show real-time contouring of data.

Figure 13. UNLV UAS formation flights

Poisson Clutter Split (PCS) Algorithms for Unmanned Aircraft

There is a desire to improve the analysis and interpretation of radiation data collected by these multiple UASs by using advanced data processing algorithms. We are investigating the effectiveness of the Poisson Clutter Split (PCS) algorithm, developed by Physical Sciences, Inc. (PSI) (Cosofret 2014), which determines a statistical estimation of the background for sparse data acquisitions, thus being an ideal tool for our UAS environments. We plan to collaborate with PSI to implement the PCS algorithm to UAS-collected data and then adjust it based on data collection findings. This algorithm will be used to analyze and interpret the data collected by the onboard radiation detectors in real time. The algorithm is well tested and executed, so the implementation of the PCS algorithm for improved detection and discrimination capabilities of the UAS collected data within this SDRD project is relatively straightforward. It does involve collection of detector response data, which we plan to do in FY 2017. Implementation of the PCS algorithm is in its earliest stages, and we expect to improve the sensitivity of our sUAS-based detector system with its employment.

Conclusion

In this project we are engineering a UAS concept for remote sensing with several UASs. In FY 2015 (Guss 2016), we received authorization to acquire two UAS platforms and subsequently acquired five additional platforms in FY 2016. The preliminary field missions described above look promising and illustrate the potential to make significant remote sensing radiological measurements using sUAS platforms. We are also in the process of incorporating algorithms to improve real-time data analysis. In FY 2016, we continued development of the algorithms and initiated a comprehensive sUAS remote sensing operations program using the acquired seven UAS platforms. In FY 2017, we will conduct a series of UAS flights to collect data to better define and inform future UAS endeavors and incorporate near real-time data from autonomous flights including beyond the visual line of sight. In addition, we will implement formation flights and algorithms for improved detection and discrimination.

Acknowledgments

References

Abdessameud, A., A. Tayebi, "Formation stabilization of VTOL UASs subject to communication delays," 49th IEEE Conference on Decision and Control, Atlanta, Georgia, December 15–17, 2010, 4547–4552.

Barnhart, R. K., B. Hottman, D. M. Marshall, E. Shappee, *Introduction to Unmanned Aircraft Systems*, RCR Press, Boca Raton, Florida, 2012a, 2.

Barnhart, R. K., B. Hottman, D. M. Marshall, E. Shappee, *Introduction to Unmanned Aircraft Systems*, RCR Press, Boca Raton, Florida, 2012b, 24.

Beard, R. W., T. W. McLain, *Small Unmanned Aircraft Theory and Practice*, Princeton University Press, Princeton, New Jersey, 2012, 288.

Chao, H., A. M. Jensen, Y. Han, Y. Chen, "AggieAir: Towards low-cost cooperative multispectral remote sensing using small unmanned aircraft systems," in *Advances in Geoscience and Remote Sensing*, G. Jedlovec, ed., InTech, Vukovar, Croatia, 2009, 463–490, https://www.researchgate.net/publication/221905354_AggieAir_Towards_Low-cost_Cooperative_Multispectral_Remote_Sensing_Using_Small_Unmanned_Aircraft_Systems, accessed January 5, 2016.

Chao, H. Y., Y. C. Cao, Y. Q. Chen, "Autopilots for small unmanned aerial vehicles: A survey," *International Journal of Control, Automation, and Systems* **8**, 1 (2010) 36–44.

Cosofret, B. R., K. Shokhirev, P. Mulhall, D. Payne, B. Harris, "Utilization of advanced clutter suppression algorithms for improved standoff detection and identification of radionuclide threats," *Proc. SPIE* **9073** (2014) 907316.

Di, L., Y. Chen, "Autonomous flying under 500 USD based on RC aircraft," *Proc. of 2011 ASME/IEEE International Conference on Mechatronic and Embedded Systems and Applications*, Washington, D.C. (2011a).

Di, L., H. Chao, J. Han, Y. Chen, "Cognitive multi-UAV formation flight: Principle, low-cost UAV testbed, controller tuning and experiments," *Proc. of 2011 ASME/IEEE International Conference on Mechatronic and Embedded Systems and Applications*, Washington, D.C. (2011b).

FAA, "Operation and Certification of Small Unmanned Aircraft Systems," Small UAS Notice of Proposed Rulemaking, Billing Code 4910-13-P, Department of Transportation, Federal Aviation Administration, 14 CFR Parts 21, 43, 45, 47, 61, 91, 101, 107, and 183, FAA Federal Register 80, 35, Monday, February 23, 2015, Proposed Rules (February 23, 2015), http://www.gpo.gov/fdsys/pkg/FR-2015-02-23/pdf/2015-03544.pdf, accessed May 5, 2015.

Franklin, M., "Unmanned combat air vehicles: Opportunities for the guided weapons industry?" Royal United Services Institute for Defence and Security Studies (2008), https://rusi.org/sites/default/files/200808_op_unmanned_combat_air_vehicles.pdf, accessed January 6, 2016.

Gan, S. K., S. Sukkarieh, "Multi-UAS target search using explicit decentralized gradient-based negotiation," IEEE International Conference on Robotics and Automation, Shanghai, China, May 9–13, 2011.

Geramifard, A., J. Redding, N. Roy, J. P. How, "UAS cooperative control with stochastic risk models," American Control Conference, San Francisco, California, June 29–July 1, 2011.

Goplen, S. E., J. L. Sloan, "National unmanned aircraft systems project office," U.S. Geological Survey Fact Sheet, FS-2015–3013, 2015.

Gupta, S. G., M. M. Ghonge, P. M. Jawandhiya, "Review of unmanned aircraft system (UAS)," *International Journal of Advanced Research in Computer Engineering and Technology* **2**, 4 (2013) 1646–1658, http://www.uxvuniversity.com/wp-content/uploads/2014/04/Review-of-Unmanned-Aircraft-System-UAS.pdf, accessed January 6, 2016.

Guss, P., et al., "Multiple unmanned aircraft system for remote contour mapping of a nuclear radiation field," in *Site-Directed Research and Development*, FY 2015, National Security Technologies, LLC, Las Vegas, Nevada, 2016, 1–13.

Han, J., Y. Q. Chen, "Cooperative source seeking and contour mapping of a diffusive signal field by formations of multiple UAVs," *Proc. IEEE 2013 International Conference on Unmanned Aircraft Systems*, Atlanta, Georgia, 2013a.

Han, J., Y. Xu, L. Di, Y. Q. Chen, "Low-cost multi-UAS technologies for contour mapping of a nuclear radiation field," *J. Intell. Robot. Syst.* **70** (2013b) 401–410.

Han, J., Y. Q. Chen, "Multiple UAV formations for cooperative source seeking and contour mapping of a radiative signal field," *J. Intell. Robot. Syst.* **74** (2014a) 323–332.

Han, J., L. Di, C. Coopmans, Y. Q. Chen, "Pitch loop control of a VTOL UAS using fractional order controller," *J. Intell. Robot. Syst.* **73** (2014b) 187–195.

Han, J., "Cyber-physical systems with multi-unmanned aerial vehicle-based cooperative source seeking and contour mapping," Doctoral Thesis, Utah State University, 2014c.

RaptorX, https://raptorx.org, 2015, accessed September 30, 2015.
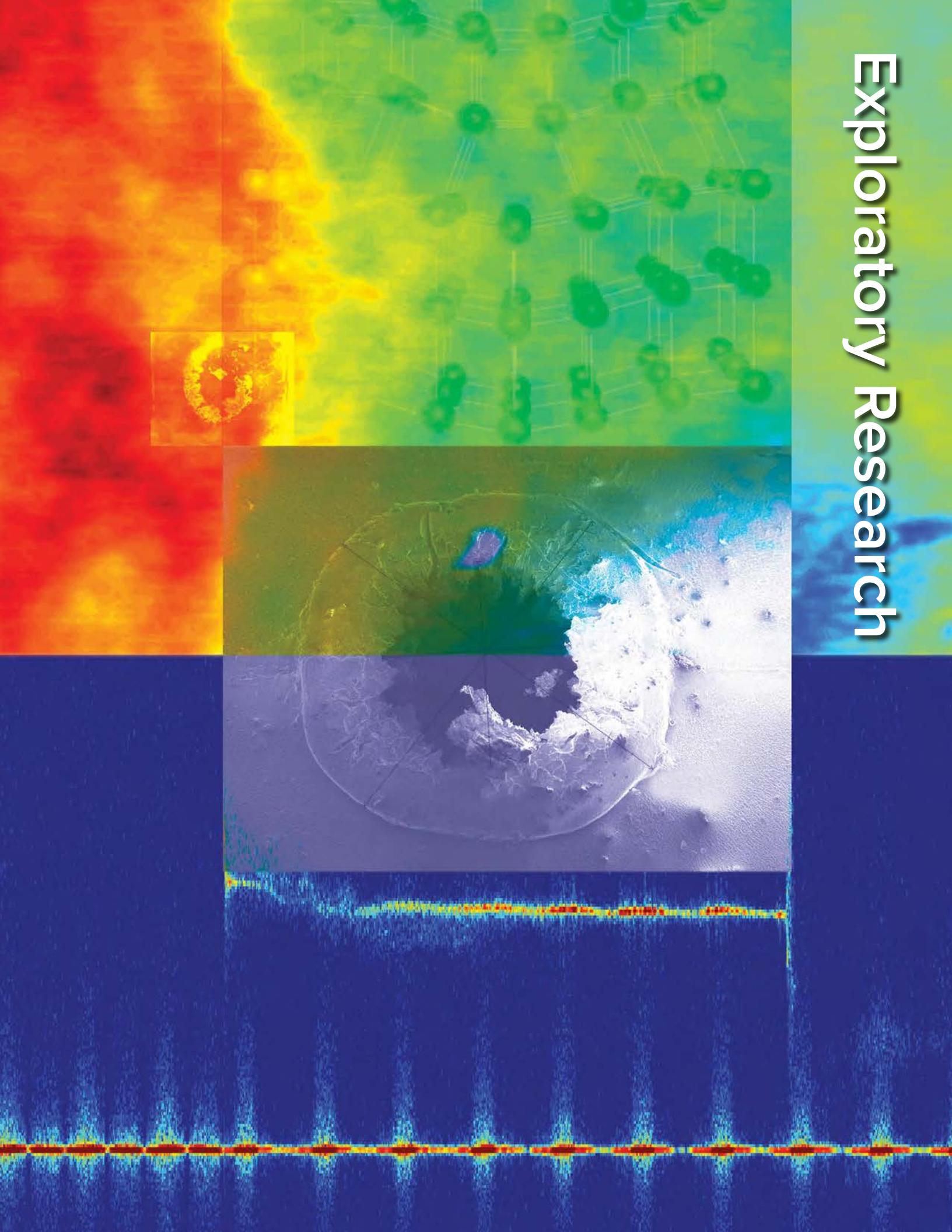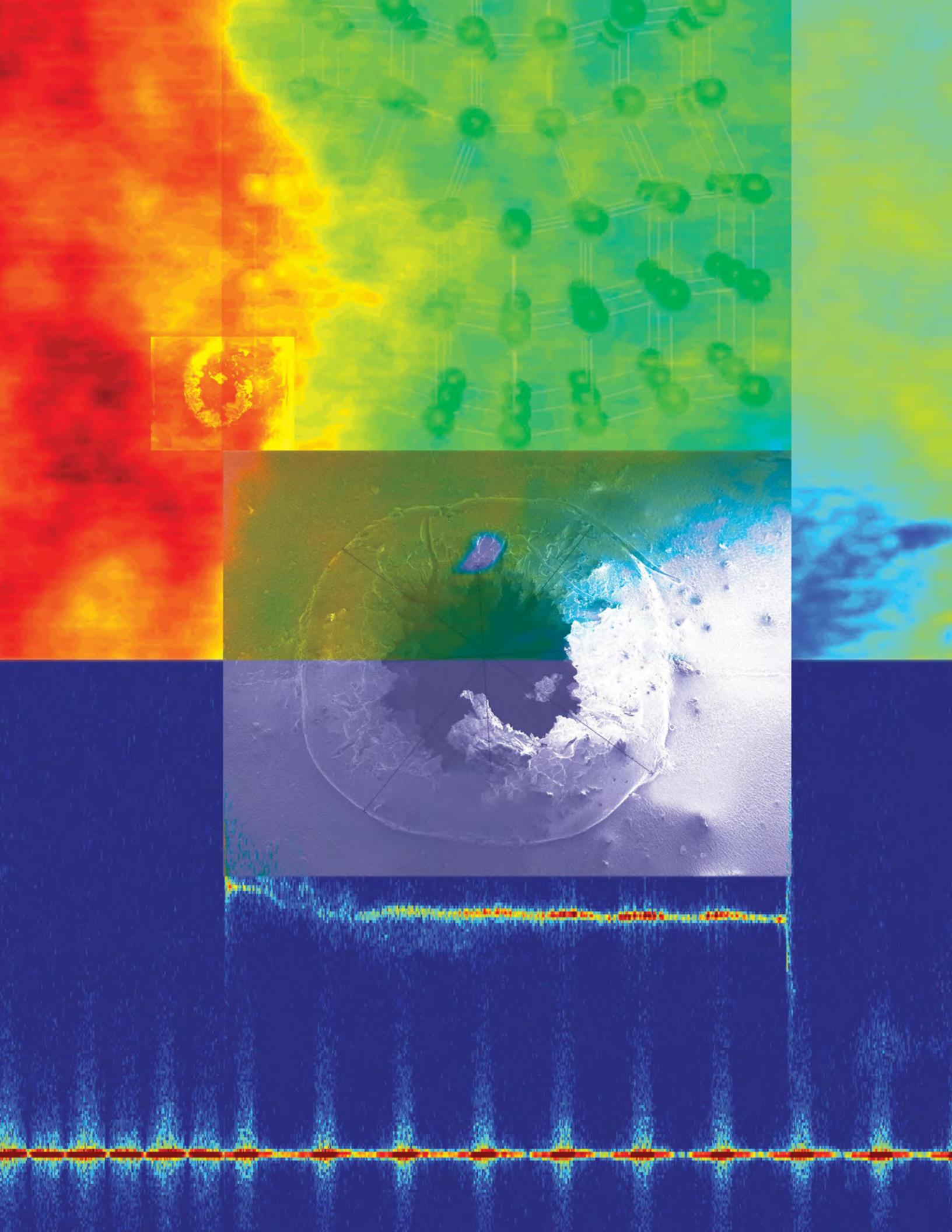
A Multi-Axial Time-Resolved Spectroscopic Technique for Magnetic Field, Electron Density, and Temperature Measurements in Dense Magnetized Plasmas

LO-001-16 | Continuing in FY 2017 | Year 1 of 3

Eric C. Dutra,[1,a] Jeffrey A. Koch,[a] Radu Presura,[b] William Angermeier,[c] Timothy Darling,[c] Roberto Mancini,[c] and Aaron Covington[c]

The scope of this three-year project is to develop a multi-axial time-resolved spectroscopic technique for simultaneous measurement of magnetic field strengths, electron densities, and temperatures of dense magnetized plasmas for Z-pinch and dense plasma focus applications. These plasma properties are quantified by using emission spectra to measure the Zeeman splitting and Stark and Doppler broadening. At high electron densities and temperatures, Stark and Doppler broadening dominate the line profiles, making it difficult to measure the Zeeman component. Two approaches can be used to make Zeeman splitting measurements under such conditions: the first employs a polarization technique to separate out the circularly and linearly polarized components, where the circular component is more affected by Zeeman splitting (Rochau 2010); the second is the technique used in this work, and it is based on the different widths of Zeeman-split fine structure components (Gomez 2014). In this first year, we have characterized a streaked spectroscopy system and recorded initial time-resolved emission spectra from dense magnetized plasma. These measurements were coupled with spectral emission modeling from the University of Nevada, Reno, and used to develop an analysis procedure for estimating magnetic field strength, electron densities, and temperatures. In the future, we plan to refine this technique and collect data at higher plasma temperatures.

[1] dutraec@nv.doe.gov, 925-960-2584
[a] Livermore Operations; [b] New Mexico Operations–Sandia; [c] University of Nevada, Reno

Background

Spectroscopic techniques in the visible range are often used in plasma experiments to measure magnetic field–induced Zeeman splitting, electron densities via collisional broadening, and temperatures from Doppler broadening. Pulsed power research Z-pinch machines, such as the Sandia National Laboratories Z machine, the NSTec dense plasma focus (DPF), and the University of Nevada, Reno (UNR) Zebra, produce dense magnetized plasmas using a Marx bank to drive current through a wire or gas. These machines can have an electric current rise time on the order of hundreds of nanoseconds with target performance that is magnetically driven and dependent on the current that travels along the outer sheath of the plasma column formation. This current induces a magnetic field that compresses the plasma, thereby increasing plasma electron density and temperature. Spectroscopy provides a noninvasive way to make these measurements. The characterization of magnetic fields, field symmetries, and electron densities and temperatures provides information about the current distribution and current loss across the anode-cathode (A-K) gap. These plasma parameters can be used to validate modeling codes in the design of new pulsed power Z-pinch machines.

The spectral line emission from the plasma sheath can be measured using time-resolved spectroscopy. However, when plasma temperatures and densities are high, collisional and Doppler broadenings dominate line profiles, making it difficult to measure the Zeeman component. In general, two techniques provide a measurement of both the collisional and the Doppler and Zeeman components. The first method measures both the linearly polarized components of the spectra, which are dominated by collisional and Doppler broadening, and the circularly polarized components, which are more affected by Zeeman broadening. Measurement of the circularly polarized emission spectra allows a deconvolution of the collisional and Doppler broadening from the Zeeman broadening, enabling a measurement of the magnetic fields, electron densities, and temperatures (Rochau 2010, Gomez 2014).

The second approach investigates the fine structure components of a given multiplet, which are split differently due to the magnetic field. In the linear regime, the splitting is determined by the change in energy as defined by

$$\Delta E = g_{LSJ}\mu_B M B, \tag{1}$$

where μ_B is the Bohr magneton; M is the projection of the total angular momentum, J, onto the given state in the direction for B; and g_{LSJ} is Landé g factor, given by

$$g_{LSJ} = 1 + \frac{J(J+1) + S(S+1) + L(L+1)}{2J(J+1)}, \tag{2}$$

where J is the total angular momentum, L is the orbital angular momentum, and S is the electron spin angular momentum.

L and S represent the total spin of the orbital momentum of the radiator, where the change in energy defines the broadening of the Zeeman splitting. Because the doublet components have similar collisional and Doppler broadening in the same plasma, the difference in the line broadening of the two doublets depends solely on the magnetic field, along with the L and S components of the Landé g factor (Stambulchik 2007, Tessarin 2011, Blesener 2012).

Project

In experiments conducted at UNR at the Nevada Terawatt Facility (NTF) using the 1 MA Z-pinch (Zebra), we explored the response of Al III doublet, 4P ^{2}P$_{3/2}$ to 4S ^{2}S$_{1/2}$ and 4P ^{2}P$_{1/2}$ to 4S ^{2}S$_{1/2}$, transitions. Optical light emitted from the pinch was fiber-coupled to high-resolution spectrometers. The dual spectrometers were coupled to two high-speed visible streak cameras to capture time-resolved emission spectra from the plasma. The data reflect emission spectra from 120 ns before the current peak to 100 ns after the current peak, where the current peak is approximately the time at which the pinch occurs. The Al III doublet was used to measure Zeeman, collisional, and Doppler-broadened emission with the method described in the second approach. The modeling, experimental method, data analysis, and results obtained during the first year of the project are described below.

Spectral Modeling

The spectral line emission modeling of collisional and Doppler broadening is available from Prism Computational Science in two software packages, PrismSPECT and SPECT3D. PrismSPECT is a basic geometrical radiation transport code, whereas SPECT3D can incorporate complex geometries, electron density, and temperature distribution. SPECT3D can also use magneto-hydrodynamic (MHD) output files as input files for simulating radiation transport. SPECT3D will become useful in follow-on years of the project. However, radiation transport codes that include Zeeman splitting are not available. In the first year of the project, we worked on developing a spectral line emission code for Zeeman splitting, particularly focusing on the P → S transition, 4P ^{2}P$_{3/2}$ to 4S ^{2}S$_{1/2}$ and 4P ^{2}P$_{1/2}$ to 4S ^{2}S$_{1/2}$, for the Al III and Na II doublets. Zeeman splitting occurs due to weak interaction of these transitions and is illustrated in a schematic energy-level diagram in Figure 1a; the graph in Figure 2a shows the P → S transition-modeled emission spectra. The model is created by first calculating the Landé g factor from the J, L, and S components and their coefficients, then using the
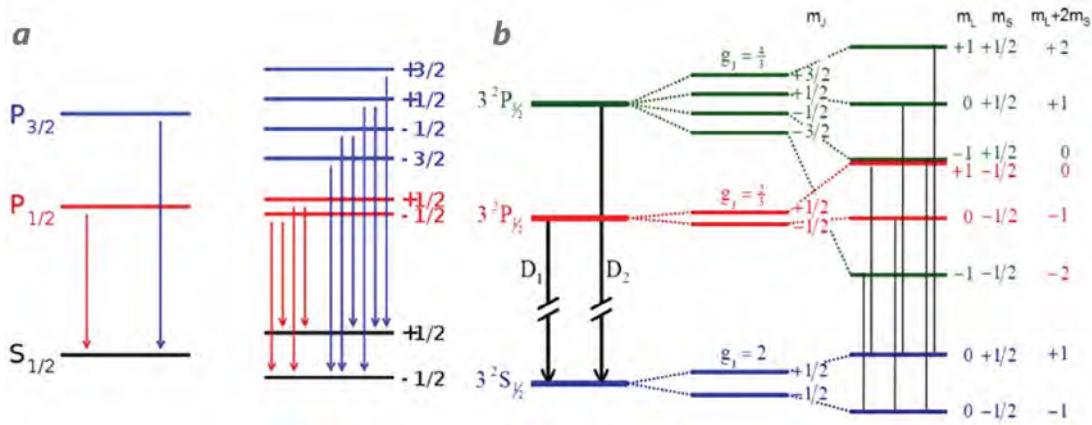
Figure 1. (a) The transition of 4P $^2P_{3/2}$ to 4S $^2S_{1/2}$ and 4P $^2P_{1/2}$ to 4S $^2S_{1/2}$ in the typical Zeeman effect and (b) the Paschen-Back transition of the 4P $^2P_{3/2}$ to 4S $^2S_{1/2}$ and 4P $^2P_{1/2}$ to 4S $^2S_{1/2}$
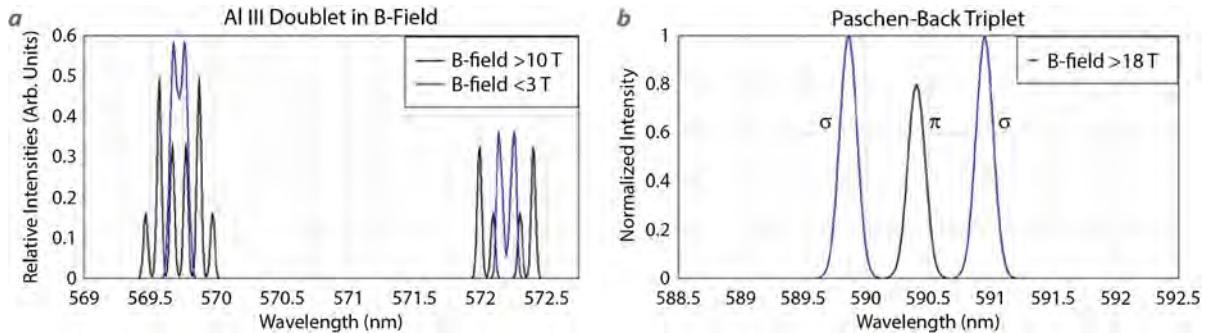
Figure 2. (a) The Zeeman modeled spectrum of the 4P $^2P_{3/2}$ to 4S $^2S_{1/2}$ and 4P $^2P_{1/2}$ to 4S $^2S_{1/2}$ transition, and (b) the Paschen-Back modeled spectrum of the 4P $^2P_{3/2}$ to 4S $^2S_{1/2}$ and 4P $^2P_{1/2}$ to 4S $^2S_{1/2}$ transition

Bohr magneton, Landé g factor, and the magnetic field strengths to calculate the energy shifts, the polarization states, and the spectral line emissions.

In stronger magnetic fields, when the energy shift induced by the magnetic field is greater than the energy shift induced by the angular momentum and spin coupling, the splitting of the line emission is dominated by the Paschen-Back effect. The Paschen-Back splitting of these two lines, of the 4P $^2P_{3/2}$ to 4S $^2S_{1/2}$ and 4P $^2P_{1/2}$ to 4S $^2S_{1/2}$ transitions, is illustrated in the energy level diagram of Figure 1b. In this regime, the field-induced precessions are so rapid that we must think of the L and S as individually precessing around the B-field rather than the precession of J, as in the case of the linear Zeeman splitting. The degree of splitting is determined by the change in energy as defined by $\Delta E = \mu_B(m_l + 2m_s)B$, where μ_B is the Bohr magneton; m_l and m_s are the magnetic moments of L and S, respectively; and B is the magnetic field strength. This

formula is used to calculate energy shifts, polarization states, and spectral line emissions for the model, as seen in Figure 2b.

Experimentally, the magnetic field can be determined by comparing measured data against a simulation. For example, the magnetic field was estimated by first modeling the P → S transition of the Al III doublet or Na II doublet (4P $^2P_{3/2}$ to 4S $^2S_{1/2}$ and 4P $^2P_{1/2}$ to 4S $^2S_{1/2}$) and then plotting the collected data against the model. The Zeeman splitting or Paschen-Back model is combined with the collisional and Doppler-broadened spectrum FWHM simulated in PrismSPECT and used to fit the experimental data. The experimentally observed polarization components, degree of linear and circular polarization, and intensities were plotted along with the results of the simulated spectra. An iterative approach was used to minimize fitting uncertainty until a best fit was achieved.

Equipment Characterization

Two Acton SpectraPro SP-2750 spectrometers from Princeton Instruments were purchased for this project. These spectrometers were coupled to an NSTec L-CA-24 medium-speed streak camera and were imaged with an SI-1000 CCD camera. Each spectrometer came with a rotatable turret for three different gratings, 150, 1800, and 2400 lines/mm, all blazed in the visible spectrum. The sweep window of the streak cameras was configured to be 480 ns, giving a sweep speed of 12 ns/mm. The slit on the spectrometers was set to 50 µm. The output of the spectrometer was aligned to the slit of the streak camera. We used an Oriel Instruments 6035 Hg(Ar) calibration lamp with known spectral emission lines (435.8, 546.1, 577, and 579 nm) for measuring the linear dispersion of the spectrometer systems for all gratings. For the 150 lines/mm grating, linear dispersion was calculated using the four Hg lines stated above. The emission lines are imaged across the slit of the streak camera. The linear dispersion of the system was calculated to be 8.86 nm/mm, with a spectral resolution of 6.7 ±0.25 Å.

The linear dispersion and spectral resolution of the remaining two gratings were characterized in two ways. First, we set the monochromator's center wavelength to 578 nm, then we imaged the 577 and 579 nm Hg lines onto the streak camera slit. However, this only provides a 2 nm linear dispersion relation. To verify the linear dispersion across the entire slit, we fixed a single wavelength (546.1 nm Hg line) onto the slit of the camera and centered this to the middle row pixel of the CCD camera. Then we varied the center wavelength set point of the spectrometer by increments of 1 nm across the field of view (FOV) of the CCD camera. This projected the 546.1 nm Hg line separated by 1 nm increments across the CCD camera onto set pixel locations. The linear dispersion calculated using both methods described above yielded the same results. The linear dispersion of the 1800 lines/mm grating was calculated to be 0.61 nm/mm with a spectral resolution of 0.47 ±0.025 Å. The linear dispersion of the 2400 lines/mm grating was calculated to be 0.38 nm/mm with a spectral resolution of 0.31 ±0.025 Å.

For the experiment, the spectrometer center wavelength was set to 570 nm, with an approximate spectral window of 11 nm. Data were collected 250 ns before the peak current. Visible light was captured from the wire ablation stage to stagnation and recorded on the streak camera. An initial survey of visible spectra was done using the 150 lines/mm grating. The Al III doublet (596.6 and 572.2 nm) was identified. Following identification, high-resolution gratings (1800 and 2400 lines/mm) were used to determine the broadened spectra. Figure 3 shows these systems set up on the experimental floor of the Zebra bay inside a large Faraday cage.

Figure 3. Acton SpectraPro SP-2750 spectrometers coupled to NSTec L-CA-24 optical streak camera

Wire Array Experiments

The experiments were conducted at the NTF on the 1 MA Zebra Z-pinch pulsed power generator. Figure 4 illustrates the experimental setup. Two optical probes collected visible light emitted from the plasma source. The probes were aligned to two different plasma regions and were oriented perpendicular to each other at a radial distance of 13.3 cm from the pinch. Probes 1 and 2 used an F220SMA-532 fiber collimator to collect light emitted from the wire array. The wire array loads used for this experiment were 15 μm thick aluminum alloy (Al-5056) wires mounted in a 1.2 cm diameter cylindrical configuration. Being the standard wire configuration at the facility, it was chosen because the width of the load would be within the FOV of the optical probes. The optical probe was aligned to a single wire. Also shown in Figure 4 is a side view diagram of the Zebra cylindrical wire array load located at the center of the chamber. In the figure, a B-dot probe is located 14 cm from the center chamber. The FOV of the optical probe is 0.6 cm, illustrated by the side view, and 0.15 cm, illustrated by the top view. The cylindrical wire arrays have a diameter of 1.2 cm. The optical probe was aligned to a single wire in such a way that the slit of the spectrometer acted as an aperture, imaging 1.5 mm wide by 6 mm high light parallel to the wire, just to the right of the center of the wire, onto the Acton SpectraPro SP-2750 spectrometer and compressing the height to 200 μm, which is the diameter of the core of the fiber.

Data Analysis

Data discussed are those collected from a cylindrical aluminum wire array. The data of the Al III doublet (569.6 and 572.2 nm) with a temporal fiducial on the far right of the image are shown in Figure 5. The lineouts were taken at multiple intervals along the Al III doublet emission. The doublet emission lasts approximately 70 ns. The streaked data were processed by applying the wavelength characterization data to map the wavelength (nm) across the pixels. Intensity characterization has not been implemented at this time but will be used in the future. Because the overall line intensity was low, several lines within a specified time window were averaged to ensure a good signal-to-noise ratio. However, we had to limit the width of the time window so that important line features did not change appreciably with current. The lineout was taken at the start of the current rise, 120 ns before the current peak. The lineout was averaged over a 20 ns wide window and was retaken every 20 ns for the entire sweep record of the emission.

The collected datasets are compared to a line emission PrismSPECT model that allows us to vary the electron
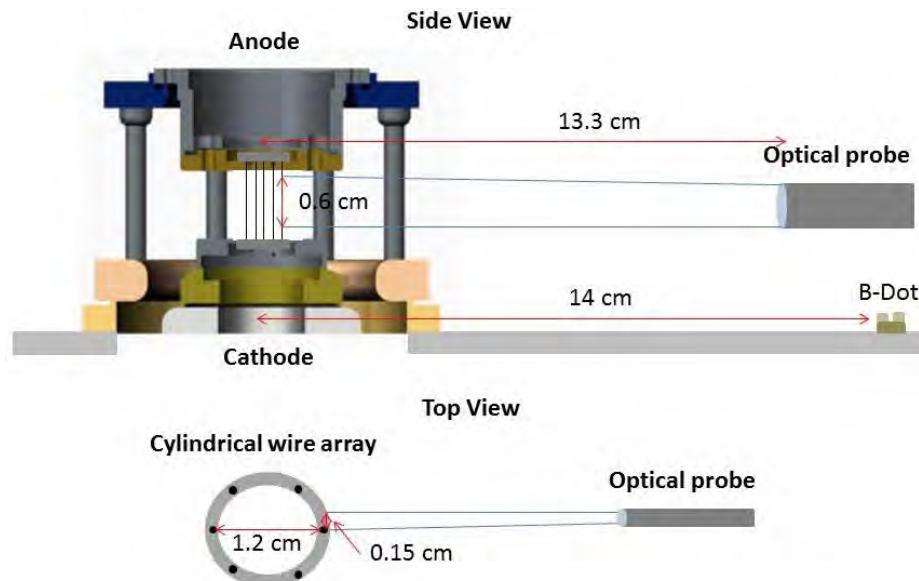

Figure 4. Side view diagram of the Zebra cylindrical wire array load, located at the center of the chamber, and locations of the B-dot and optical probes in relation to the center chamber. The FOV of the optical probe is 0.6 cm, as illustrated by the side view, and 0.15 cm, as illustrated by the top view. The cylindrical wire arrays have a diameter of 1.2 cm.
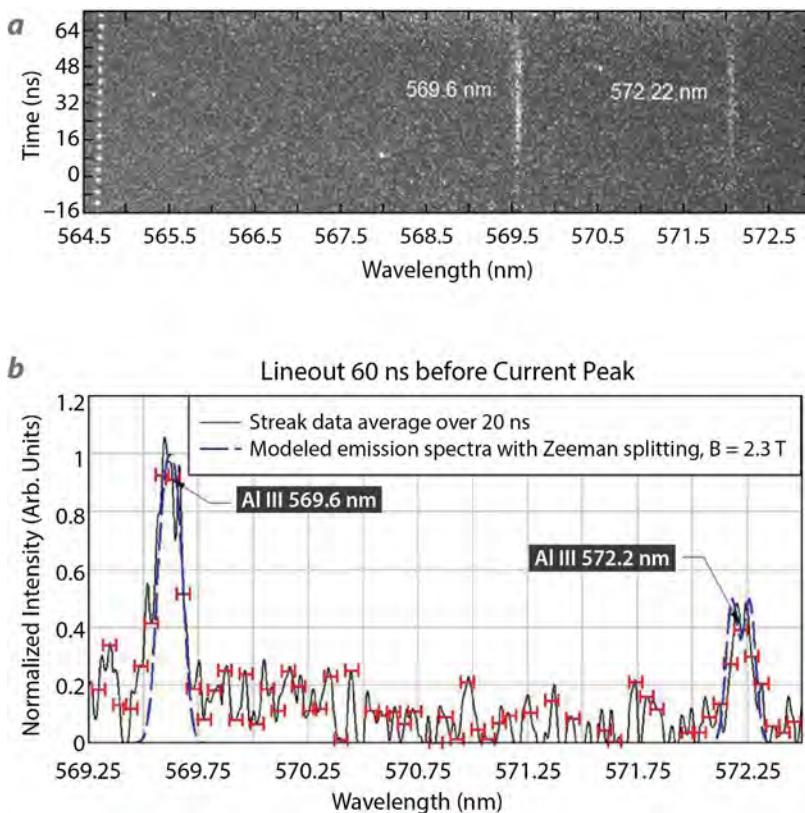
Figure 5. (a) The streak emission spectra of the Al III doublet captured during the wire ablation stage of a Z-pinch. (b) A lineout, averaged over 20 ns, of an Al III doublet 120 ns before the current peak.

density and temperature parameters. These parameters affect the line width and the predicted broadening of the line spectra and are used to fit the streak data. Once an approximate fit is achieved, the output line width from PrismSPECT is used as an input parameter in a Zeeman splitting code. The Zeeman code models the 4P $^2P_{3/2}$ to 4S $^2S_{1/2}$ and 4P $^2P_{1/2}$ to 4S $^2S_{1/2}$ transitions, and then calculates the energy shift due to the magnetic field. Then the code applies the energy shift to the spectrum and models the polarized components, both linear and circular. The code also calculates the convolved spectrum of the polarized components. The output spectrum includes a broadening mechanism from electron density, ion temperature, and magnetic field. This process is iterated, varying the electron density, ion temperature, and magnetic field, until an approximate fit is found. The best fit is achieved when modeled spectra of both transitions fall within the systematic error of the system. This model is applied to several points in time within the streaked spectrum. The magnetic field is then plotted as a function of time and compared to the magnetic

field that was calculated using B-dot probes. A similar technique could be utilized to plot both the electron density and temperature as a function of time.

The spectra shown in Figure 5 were modeled using optically thin values of 10 eV and 1×10^{16} cm^{-3}, for the electron temperature and density, respectively. The magnetic field strength at 60 ns before the current peak is found to be 2.3 Tesla, 1 Tesla at 80 ns before current peak, and 0.5 Tesla at 100 ns before the current peak. Shown in Figure 6 is a comparison of the magnetic field strength as a function of time for B-dot (solid line) and Zeeman spectroscopy (solid dots). The B-dot measures electric current as a function of time as well as the total current through the anode and cathode gap. At the time of the measurements, the total current through the anode and cathode gap was measured to be 0.0006, 0.0066, and 0.104 MA; divided among six wires this yields an individual wire current of 0.1, 1.1, and 17.4 kA, respectively. Assuming cylindrical geometry, we can calculate the magnetic field by

$$B = \mu I/2\pi r, \tag{3}$$
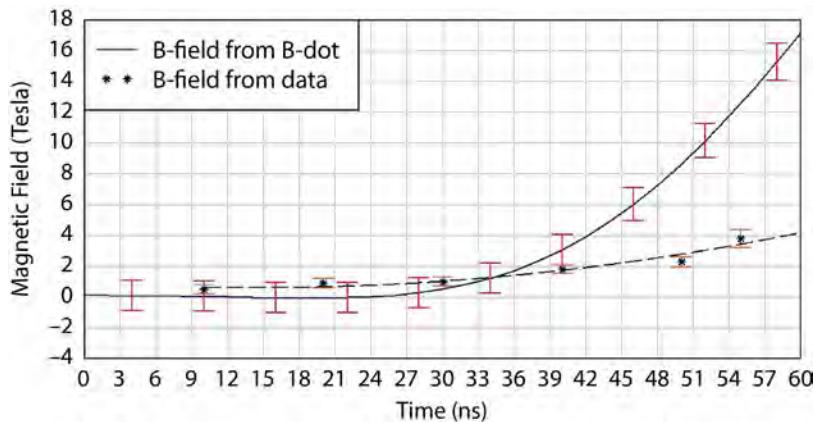
Figure 6. The magnetic field as a function of time from spectroscopy data and magnetic field calculated using the B-dot probe data average over the FOV of the spectrometer, 1.5 mm, parallel to the wire

where I is the current passing axially through the conducting cylinder, μ is the permeability of the material between the conductors, and r is the radius of the conductor (Tessarin 2011). This yields the magnetic field

$$B[T] = 200\ I[MA]/r[mm]. \qquad (4)$$

The B-dot–generated plot shows an increasing trend in the magnetic field, which is consistent with the spectroscopic measurement. However, there is a discrepancy in the magnetic field measurements between the B-dot and the measured magnetic field from the optical measurements at later times. At this point in the ablation stage of the wire, current is not only flowing through the coronal plasma of the wire but also moving away from the wire to form the precursor centered at the z-axis. The B-dot probes measure the total current passing through the anode-cathode plate and, therefore, are not spatially resolved to measure when current starts flowing along the precursor. Future experiments and MHD modeling along with radiation transport will be employed to verify this result. The error bars associated with the spectroscopic measurements are based on the spectral resolution of the system. We are currently working on a more careful analysis of these errors.

Laser Ablation Experiments

Laser ablation experiments were conducted at the NTF with the Zebra pulsed power generator coupled to the Leopard laser. The Leopard laser has an energy of up to 30 J with a 0.8 ns pulse width at a wavelength of 1057 nm. In this configuration, the laser ablates a target, creating an ionized plasma plume. The plasma plume expands across the anode-cathode gap, creating a load or a path on which the Zebra's 1 MA current travels. The current flows through the outer shell of the ablation plume, along the z-axis, producing a magnetic field in the azimuthal direction. The magnetic field is indicated by the arrows around the plasma column in Figure 7. The current and magnetic field form the J × B force that compresses the plasma and produces a Z-pinch. Two optical probes collect visible light emitted from the plasma source. The setup is illustrated in Figure 7. The side view diagram of the anode-cathode assembly in Figure 7 is similar to the cylindrical wire array load in Figure 4. A B-dot probe is located 14 cm from center chamber, and optical probes are located 13.3 cm from the center chamber. The top view of Figure 7 illustrates the FOV of the optical probes. An optical plano-convex lens is used in conjunction with the fiber collimator adapter to focus on the location identified in the diagram of Figure 7. One of the optical probes was aligned radially to the center of the plasma column, normal to the magnetic field. The other was aligned slightly shifted from the radially optical probe, aligning to the FOV parallel to the magnetic field.

One of the benefits of the laser ablation experiments is load fabrication. The wire array configurations are limited to the availability of the wire material and thickness. Building the loads can be challenging and time-consuming, but in our case the process went quickly and so we were able to change material rapidly. In the laser ablation experiments, we tested Al, copper
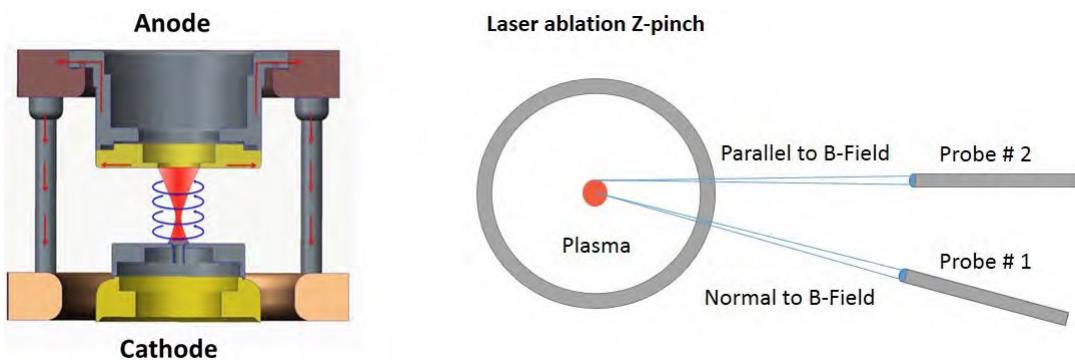
Figure 7. The laser is focused through the top of the anode plate onto the sample target on top of the cathode; when Zebra is turned on, a current travels though the plasma that creates the J × B force radially inward toward the z-axis

(Cu), polyethylene (C_2H_4), deuterated polyethylene (CD_2), and sodium chloride (NaCl). For Al, C_2H_4, and CD_2, the Al III and C IV P → S transitions were identified through modeling as possible emission lines that could be used for the spectroscopic broadening measurements. However, initial experiments showed that only the Al III emission lines were visible. The experiments with Cu loads were conducted to try to identify a suitable transition in Cu that could be used for future experiments at the Gemini DPF. Again, experiments found no useful visible emission line that could be used for spectroscopic measurements as outlined above. It should be noted that a dielectric breakdown in the vertical transition line was discovered after our experiments. This could have been limiting the current to the load. This issue has been resolved, and these experiments will be revisited in spring of 2017.

Next, we focused on a viable transition in NaCl, specifically the Na I P → S transition, which was found to have a very prominent absorption line in the visible spectrum. Further experiments were conducted using NaCl as a dopant for targets previously used in the ablation experiments (Al, Cu, C_2H_4, and CD_2). A 6 mol NaCl solution was made for the dopant. A small sample of the NaCl solution was placed onto the target material and allowed to dry. The target was then loaded into the chamber for the laser ablation experiments. We found that the Na I P → S transition was prominent in all spectra collected for the various tested target materials. This spectrum was used to make preliminary spectroscopic measurements of the magnetic field.

Preliminary Data Analysis

The preliminary data collected from laser ablation Z-pinch experiments are discussed. A single lineout from shot 4450 is shown in Figure 8 for the Na I doublet (589 and 589.6 nm). This shot used an Al target doped with NaCl in a boron nitride target holder. The target was ablated using 23.3 J of energy from the Leopard laser. A lineout was taken at the peak current, approximately 0.8 MA. The optical emission was collected from the probe aligned parallel to the magnetic field. As mentioned in the **Background** section, the contributions from collisional and Doppler broadening are minimized for the optical light collected parallel to the magnetic field due to the polarization of the light emitted from that region. In a strong magnetic field, the Na I doublet forms a triplet out of the circularly and linearly polarized components. As discussed in the ***Spectral Modeling*** section of this report, in strong magnetic fields when the energy shift induced by the magnetic field is greater than the energy shift induced by the angular momentum and spin coupling, the splitting (energy shifts) of the line emission is now dominated by the Paschen-Back effect. Here the change in energy is directly related to the magnetic field, as shown in Equation 5.

$$\Delta\lambda[\text{Å}] = 0.32 * B[T] \tag{5}$$

Figure 8 shows the lineout from the peak current plotted with a theoretical spectrum, which assumed a magnetic field strength of 33.5 Tesla. Assuming cylindrical geometry and using Equation 4, we can calculate
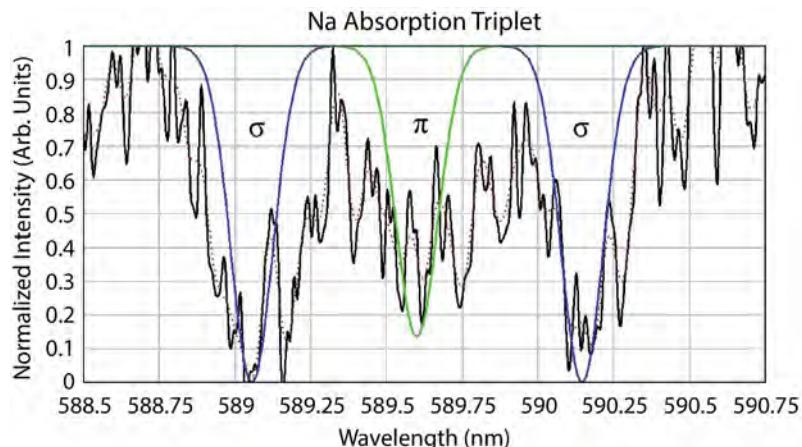
Figure 8. A lineout taken at peak current from the Al laser ablation load. Data are fitted with a theoretical Paschen-Back model of the Al III doublet 4P $^2P_{3/2}$ to 4S $^2S_{1/2}$ and 4P $^2P_{1/2}$ to 4S $^2S_{1/2}$ transition simulated with a 33.5 Tesla magnetic field.

the magnetic field at the radius of the FOV of the probe. This calculation yields a magnetic field strength of 36 ±4 Tesla.

Conclusion

Spectroscopic measurements of aluminum wire arrays have been made using the Al III doublet, 4P $^2P_{3/2}$ to 4S $^2S_{1/2}$ and 4P $^2P_{1/2}$ to 4S $^2S_{1/2}$ transitions. Using PrismSPECT in conjunction with a model that has been developed at UNR for Zeeman splitting, we have measured temperatures, electron densities, and magnetic fields. The spectroscopic magnetic field measurements show consistent trends to B-dot measurements. The results from the wire array experiments were published in *Review of Scientific Instruments* (Dutra 2016). However, in the near future MHD modeling and radiation transport will be included in the code to obtain a complete description of optical emission from the evolving plasma distribution. In the next two years of the SDRD project, we plan to make measurements at higher temperatures (>15 eV) and electron densities (>1 × 10^{17} cm^{-2}). This will require additional modeling and the use of other materials or dopants. Preliminary magnetic field measurements of laser ablation targets, doped with NaCl, have been made near peak current.

Acknowledgments

References

Blesener, K. S., S. A. Pikuz, T. A. Shelkovenko, I. C. Blesener, D. A. Hammer, Y. Maron, V. Bernshtam, R. Doron, L. Weingarten, Y. Zarnitsky, "Measuring magnetic fields in single aluminum wire plasmas with time-resolved optical spectroscopy," *High Energy Density Physics* **8**, 3 (2012) 224–226.

Dutra, E. C., J. A. Koch, R. Presura, W. A. Angermeier, T. Darling, S. Haque, R. C. Mancini, A. M. Covington, "Development of a spectroscopic technique for simultaneous magnetic field, electron density, and temperature measurements in ICF-relevant plasmas," *Rev. Sci. Instrum.* **87**, 11 (2016) 11E558.

Gomez, M. R., S. B. Hansen, K. J. Peterson, D. E. Bliss, A. L. Carlson, D. C. Lamppa, D. G. Schroen, G. A. Rochau, "Magnetic field measurements via visible spectroscopy on the Z machine," *Rev. Sci. Instrum.* **85**, 11 (2014) 11E609.

Rochau, G. A., J. E. Bailey, Y. Maron, "Applied spectroscopy in pulsed power plasmas," *Physics of Plasmas* **17**, 5 (2010) 055501.

Stambulchik, E., K. Tsigutkin, Y. Maron, "Spectroscopic method for measuring plasma magnetic fields having arbitrary distributions of direction and amplitude," *Phys. Rev. Lett.* **98**, 22 (2007) 225001.

Tessarin, S., et al., "Beyond Zeeman spectroscopy: Magnetic-field diagnostics with Stark-dominated line shapes," *Physics of Plasma* **18**, 9 (2011) 093301-1–093301-9, http://plasma-gate.weizmann.ac.il/uploads/bibman/tessarin:2011a.pdf, accessed January 18, 2017.

Correlation between Hot Spots and 3-D Defect Structure in Single and Polycrystalline High-Explosive Materials

NLV-035-16 | Continuing in FY 2017 | Year 1 of 3

Cameron Hawkins,[1,a] Oliver Tschauner,[b] Zachary Fussell,[a.b] Jason McClure,[b] Seth Root,[c] Eric Machorro,[a] and Edward Daykin[a]

A novel approach that spatially identifies inhomogeneities in high-explosive (HE) materials from microscale (defects, conformational disorder) to mesoscale (voids, inclusions) is being developed using two synchrotron x-ray methods: tomography and Lang topography. These techniques provide a nondestructive method for characterization of millimeter-sized samples prior to shock experiments. These characterization maps can be used to correlate continuum-level measurements in shock compression experiments to the mesoscale and microscale structure. The unified diagnostic tool being developed can be used to correlate pre-shot inhomogeneities with in situ shock diagnostics in future research. This provides a way to determine which type of heterogeneity, or combination thereof, in the sample contributes most to hot spot formation. Thus, for HE materials, variability in the detonation response can be correlated with characteristic features in the sample that existed prior to shock compression. Correlating these inhomogeneities to hot spot formation will assist with understanding the performance of HEs and allow them to become more reproducible, reliable, and safer. In the first year of this work, HE analogous materials were studied as a precursor to studying HE materials directly. In year two we will apply these methods to a suite of HE samples. After pre-shot characterization of defects, the samples will be subjected to shock to establish the correlation between defects on different length scales with hot spot formation.

[1] hawkinmc@nv.doe.gov, 702-295-9807
[a] North Las Vegas; [b] University of Nevada, Las Vegas; [c] Sandia National Laboratories

Background

The formation of hot spots in highly energetic materials during the initial stages of detonation is one of the key components in understanding the detonation process. High-explosive (HE) materials are usually not refined single crystals but compounds of HE crystallites and binders. Impedance mismatch between binder and crystallites can influence the response of a material to shock. In addition, accidental but unavoidable inhomogeneities such as cracks, voids, grain boundaries, inclusions of fluid or solid phases in the crystallites, and crystal lattice defects, can affect the initial response of the material to shock and can become locations where

hot spots form. Thus, correlating the inhomogeneities to hot spot formations is key to understanding the initial stages of detonation (Cawkwell 2008, Kuklja 2014). Such correlation, quantitatively established, helps to provide an understanding of the performance of HEs, therefore allowing them to become more reproducible, more reliable, and safer.

Understanding HE detonation is largely empirical, and a need exists to develop predictive capabilities. While hot spots are suspected to play a crucial role during the onset of detonation, the conditions that generate
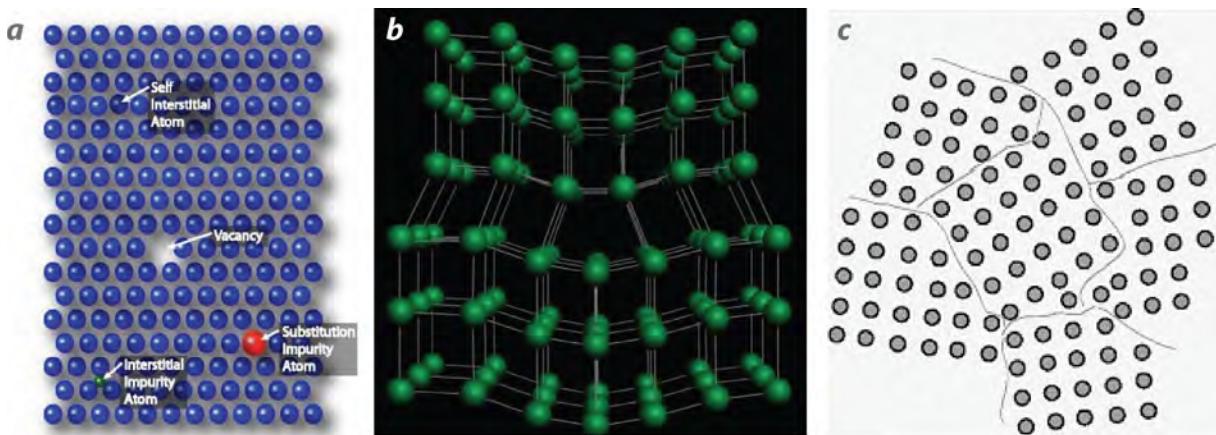
Figure 1. Defects may be (a) point defects such as voids and inclusions (NDT 2016), (b) linear defects such as dislocations, or (c) planar defects such as stacking faults, twin boundaries, or grain boundaries (Utah 2016)

these hot spots and the initial stages of their evolution in terms of stress, temperature, and chemical reactions are poorly understood (Cawkwell 2008, Kuklja 2014). HE response is typically measured and modeled at a continuum level without regard to internal structure and heterogeneity (Shan 2014). Mesoscale modeling is an emerging field with a large need to compare experimental data to simulations (Baer 2012, Shan 2014). Measurements that examine mesoscale (atomic level) and microscale (molecular level) effects are needed to understand the variability observed in HE and to help tie the actual spatially variable onset of chemical reaction to the evolution of the reaction wave front on a fluid-dynamic scale.

During dynamic compression, localized stress and temperature in aggregate samples are affected by defects, voids, impurities, and other heterogeneities that exist prior to shock (Figure 1). These affect lattice structure and produce weak points by inducing lattice strain. In a solid without internal structural degrees of freedom, such as an FCC (face-centered cubic) metal, such local strain would induce small-scale reverberations. In molecular solids, such as most HE materials, the local strain around the defects can be relaxed by changes in the conformational state of the molecules. In other words, the excess free energy from induced strain will be converted in part into an increase in internal energy. In HE materials, different conformational states of molecules have different sensitivities to shock (Tsyshevsky 2016). Thus, defects induce local

strain, which then induce changes in sensitivities. We are examining the extent of such changes of conformation around defects in HE materials as well as the nature of these conformational changes in terms of sensitivity.

Local changes in the molecule structure that have higher sensitivity to shock can therefore lend themselves to detonation (Figure 1). Surber (2007), Chen (2014), and You (2015) have examined the surface of beta-HMX (octahydro-1,3,5,7-tetranitro-1,3,5,7-tetrazocine) crystallites and found that the presence of a layer of delta-HMX, which is highly sensitive, as well as the thickness of this layer, controls the bulk sensitivity of HMX. Current techniques of spatially resolved defect characterization (transmission electron microscopy [TEM] darkfield, LEEDS) are destructive and cannot be applied to samples prior to shock experiments. Furthermore, these methods are restricted to very small length scales (nanometers), whereas characterization of samples prior to shock needs to extend to a millimeter scale or beyond. Characterization of voids and impurities in HE samples is presently restricted to sub-millimeter length scale and lacks correlation of impurity location with impurity phase identification. There is a need for nondestructive characterization techniques that cover the mesoscale (millimeter to micron) and microscale (micron to nanometer) to provide a way to understand the stress and temperate evolution upon shock loading.
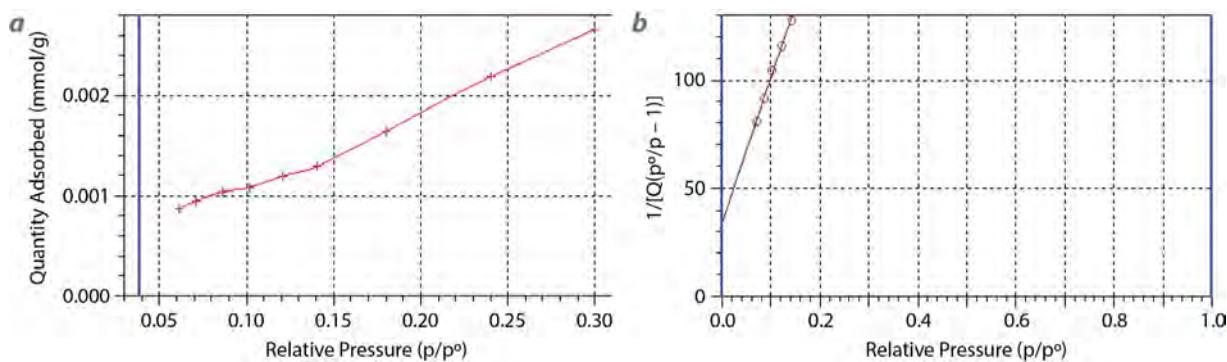
Figure 2. Brunauer-Emmett-Teller (BET) for aluminum boron carbide (AlB$_4$C) (a) isotherm plot and (b) surface area plot

Project

In this first year, data of HE analog materials were collected and utilized to develop the pre-shock diagnostic software that will ultimately provide a way to tie pre-shock characteristics to HE detonation. Measurements of samples were taken using Brunauer-Emmett-Teller (BET) surface analysis, tomography, and Lang topography with the developed and tested compressed sensing software. The same sample was then shocked using a gas gun and analyzed post-shock. The main result is a nondestructive 3-D characterization of defects and crystal orientation of polycrystalline and heterogeneous materials prior to shock experiments, which in the future can be compared to in situ shock to provide a connection between pre-shock characteristics and hot spot formation. The x-ray characterization maps, combined with shock compression experiments, will correlate the internal structure with the continuum-level response. The software being developed provides a way to establish this method for routine sample characterization prior to shock experiments.

BET Experiments

BET analysis was performed to quantify bulk density, total surface area, and pore size in the samples examined (DallaValle 1948). These parameters are useful in estimating shock travel time in samples before shock and in assessing the overall excess heat produced by void collapse. Detonation is largely affected by temperature, and voided regions in a sample can drive up the temperature. Upon shock, void

collapse will occur, and with the knowledge of pore size and average density, a better understanding of the material is gained, as porosity alters the Hugoniot (Hixson 2012). It is postulated that the voids produce an area of increased energy that when shocked has a temperature higher than the surrounding area; this condition creates a hot spot.

Two samples (provided by collaborator S. Root from Sandia National Laboratories), which included aluminum tantalum carbide (AlTaC) and aluminum boron carbide (AlB$_4$C), were tested using BET. Each sample was individually placed into a test tube and then loaded into the Micromeritics equipment for testing. The gas used during the experiment was Krypton at a temperature of 77.35 K. Shown in Figure 2 are isotherm and surface area plots produced by the experiment, from which the bulk density, total surface area, and pore size can be extracted.

Tomography and Topography Experiments

A combination of x-ray tomographic and topographic techniques along with a highly spatially resolved structure analysis was utilized to map mesoscale and microscale structure and defects, such as voids and inclusions. These techniques use the high-energy micro-focused synchrotron beam line 16-IDB at Carnegie Science's High Pressure Collaborative Access Team (HPCAT) at the Advanced Photon Source (APS), Argonne National Laboratory. Available energies beyond 30 keV provide full transmission of the x-rays through samples of centimeter-scale thickness and radial extension.
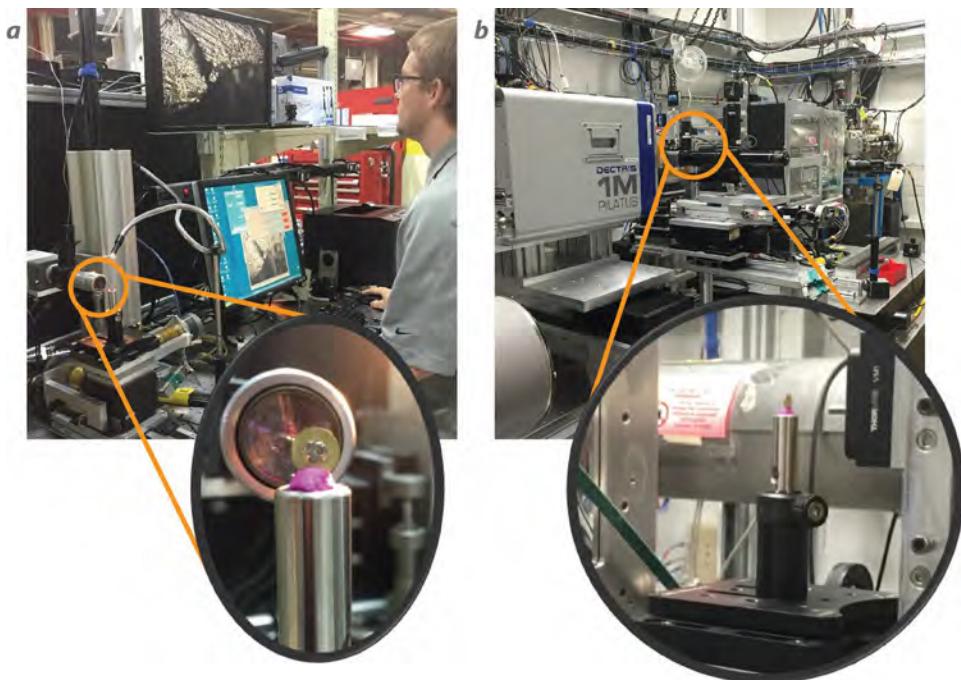
Figure 3. Tomography and topography at APS/HPCAT: (a) camera setup and (b) beam line setup

X-ray tomography provides a 2-D electron density distribution (micron-resolution) that can be applied to single-crystal, polycrystalline, and/or powdered samples. This method detects voids and cracks on the mesoscale as well as density differences in polycrystalline aggregates of single or multiple phases. The 2-D tomography map can be used to identify regions that could generate local temperature or stress excursion during shock.

Individual samples were pressed into a ring and mounted onto a post. Each sample was approximately 3 mm in diameter and 0.5 mm in thickness. A camera system shown in Figure 3a was used to test for tilt to ensure the sample was flat with respect to the camera. The center of the sample was also calculated to center it with respect to the beam. The post was then positioned onto a motorized stage as shown in the test setup in Figure 3b. This provided a way to position the sample so images could be collected on the entire surface. The tomograms were collected with a beam of 0.3738 Å wavelength that was focused to 1×2 μm^2 to 2×4 μm^2 with a diode located behind the sample.

Bismuth (Bi), ammonium nitrate (NH_4NO_3), aluminum tantalum carbide (AlTaC), aluminum (Al), and silica (SiO_2), the materials analyzed, are shown in Figure 4. These specific samples were chosen purposely to provide a variety of grain sizes and to characterize heterogeneities on different length scales. Dense regions and voids can be easily distinguished in the tomograms. For the AlTaC sample shown, it is interesting that despite extensive mechanical mixing, the TaC is not homogeneously distributed, as evidenced by the differences in the density seen on the tomogram. The Al sample provides a good indication that void distribution is possible to discern on even a small grainsize sample. These samples demonstrate the capabilities of measuring voids and crystal boundaries in samples with spatial resolutions in the 10 μm range using intensified CCD detectors for tomography.

We used a topography technique based on Lang topography, which is a single-crystal diffraction method in which images are taken over a range of angles; this approach provides variations in intensity that can be used to identify strain (Klapper 2000, Giacovazzo 2002). The Lang method shows the spatial distribution
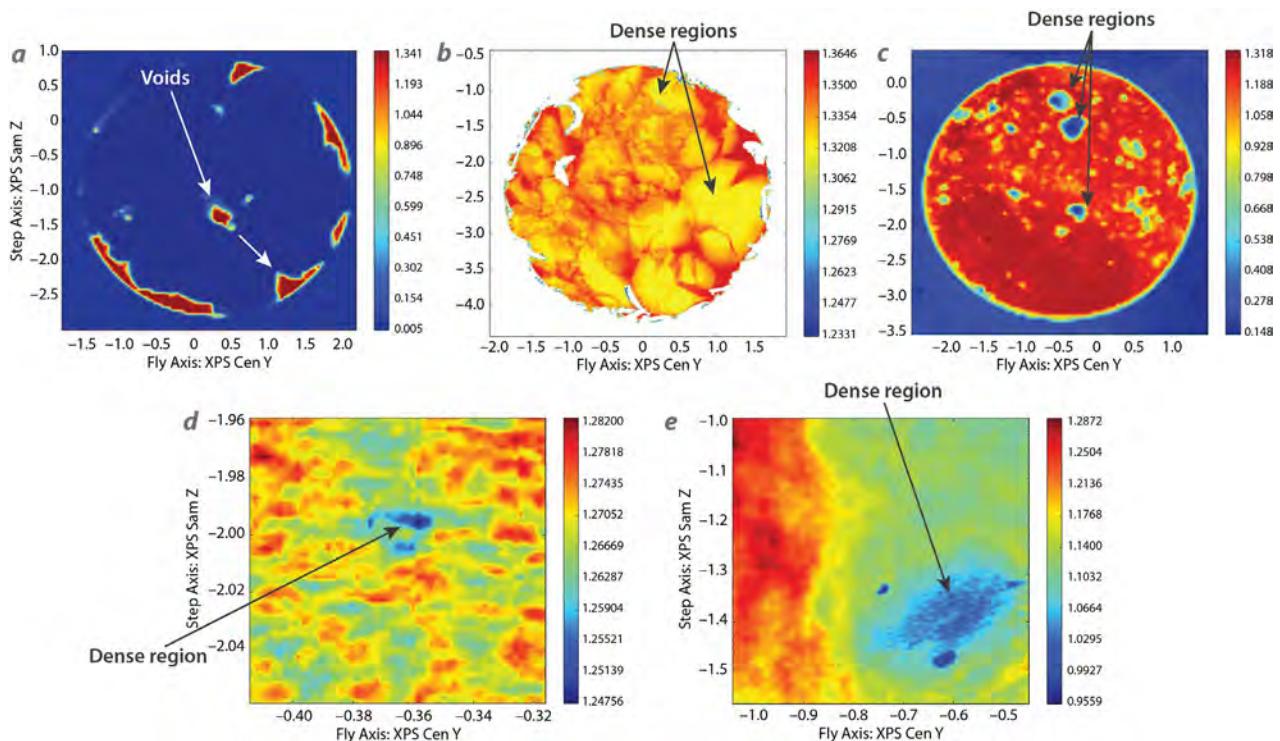
Figure 4. Tomography samples included (a) Bi, (b) NH_4NO_3, (c) AlTaC, (d) Al, and (e) SiO_2. Dense regions and voids are evident.

of crystal defects (point defects, dislocations, domain walls) through the strain that these defects induce in a particular crystal lattice plane. The sample is oriented such that a Bragg diffraction peak of a certain lattice plane is observed on an x-ray-sensitive area detector. Defects deform the lattice plane and thereby tilt the plane slightly out of optimal Bragg diffraction conditions. Thus, at any location of a defect, the Bragg signal will be reduced. In the Lang approach, the Bragg intensity is mapped as a function of the location in a crystal; thus, the distribution of defects in the crystal becomes visible without damaging the crystal.

This year we significantly improved the Lang method by (a) using fast x-ray area detectors instead of conventional image plates and collecting Lang maps in time series rather than by correlated sample detector motion; (b) using a strongly focused, high-energy synchrotron x-ray beam instead of a collimated in-house x-ray source; and (c) developing software for fast processing of the time-series Lang maps. Our improvements have resulted in an increase of spatial resolution of Lang defect mapping by three orders of

magnitude, as well as the first examination of crystallites as small as 50 μm in diameter and the first simultaneous Lang topographic mapping of several Bragg reflections, which allows determination of the Burgers vectors of dislocations. This ultimately leads to a reconstruction of the 3-D defect structure in a crystal, which is the next step of data analysis and has yet to be implemented in the software.

In the Lang topograms, dislocation kernels are marked by shifts of the phase factor or the Bragg intensity. The micro-focus hard x-rays are focused to 1×2 μm^2 at monochromatic x-ray energies typically between 30 and 40 keV. This technique provides a fully 3-D quantitative assessment of defect structure, orientation, and induced strain in polycrystalline aggregates.

The Lang topography technique was performed on one sample of ammonium nitrate as an available, structurally simple, low-sensitivity HE material. On-the-flight capture of frames was used with micron-sized frame rates that provided ~100 times higher spatial resolution than the conventional approach with detector
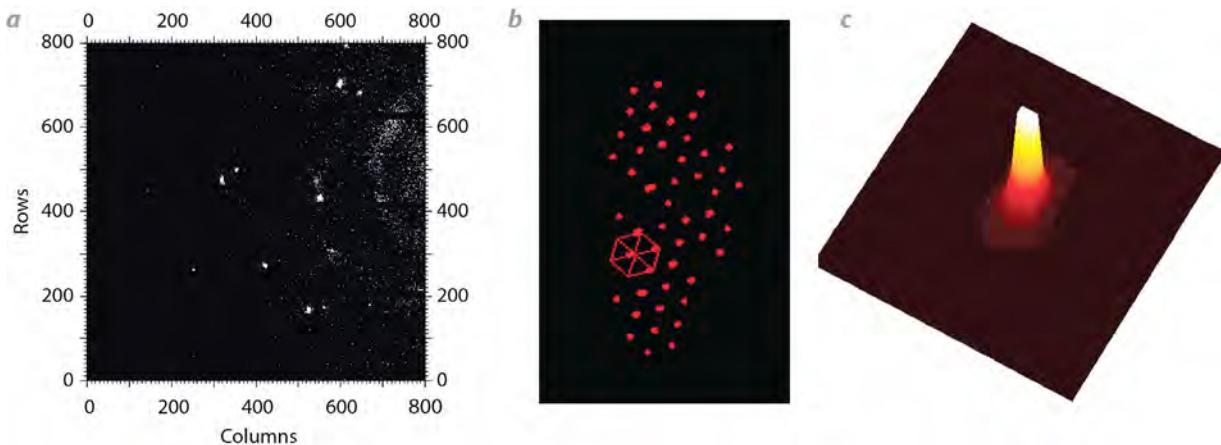
Figure 5. Topography of NH_4NO_3 multiple peak intensities, (b) reciprocal space projection of the crystal grain, and (c) peak intensity distribution of one reflection at a certain 1×2 µm increment

translation. Shown in Figure 5 are several peak intensities, the reciprocal space projection of the crystal grain, and the peak intensity distribution of one reflection at a certain 1×2 µm increment. The Lang map is constructed out of the integrated intensities of the reflection at all sample locations (1×2 mm pixels) as outlined in the next section and shown in Figure 6.

Software Development

2-D tomographic maps were collected with a compressed sensing–based approach that provides sub-micrometer spatial resolution of density contrasts (voids, cracks, inclusions). Compressed sensing applied to the tomogram technique improved the efficiency of collection by a factor of 10 to 50 without compromising the spatial resolution. This provided a more time-efficient method for tomographic imaging, which allows much larger-sized samples to be characterized.

Lang topograms provide characterization of crystal internal defects (dislocations, domain walls, point defect clusters) and were collected using a fast area detector. A series of frames were collected, each attached to one spatial coordinate. The Bragg peak in each frame is fitted and integrated, and these become pixels of a new image where 2-D coordinates are the spatial coordinates from the scan log. To examine the effect of defects on the structure, the Bragg intensity is converted into an electron density. Local optimization is used in lieu of conventional structure analysis, since the latter is significantly more time intensive.

Figure 6 shows a Lang topogram reconstruction using the developed analysis software. This topogram includes 961 raw diffraction images from which Lang topograms having a dimension of 31×31 pixels (each pixel is 2×2 µm^2) are created, as shown by Figure 6b. The red points within the large set of images (Figure 6a) are the peak intensities of reflections and indicate defects. Figure 6c shows a line defect and clusters of point defects.

Gas Launcher Experiments

Upon shock loading, it is expected that void collapse will generate a high heat region/hot spot (Shan 2014) causing local melting and transformation to high pressure-temperature phases in the area around the hot spot. Prior to shock, the voids, defects, and crystal boundaries can be measured in the sample using tomography and topography as outlined in the previous subsections. Shock experiments on those same samples can induce hot spot formation. Then in situ or recovery analysis can verify whether hot spots form around voids and can possibly help determine temperature evolution around crystal defects and grain boundaries when compared to the pre-shock tomography/topography of the sample.

Experiments were performed on Bi samples using the single-stage gas launcher at the University of Nevada, Las Vegas (UNLV) shock lab (Figure 7a). Lexan projectiles (8 mm diameter) with stainless steel flyer plates (5.5 mm diameter) impacted samples encased in a
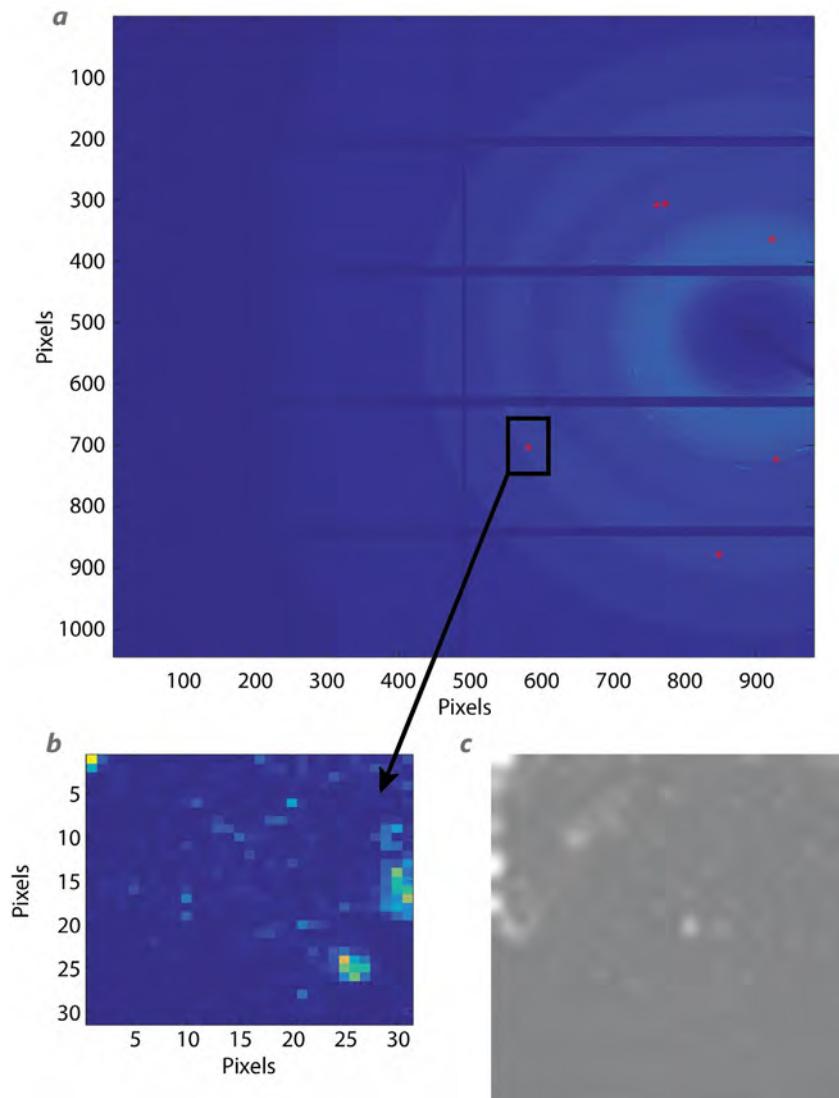
Figure 6. Lang topography reconstruction showing (a) 961 raw diffraction images, (b) computer-generated topogram based on raw data, and (c) a 16-bit tiff image showing a line defect and clusters of point defects
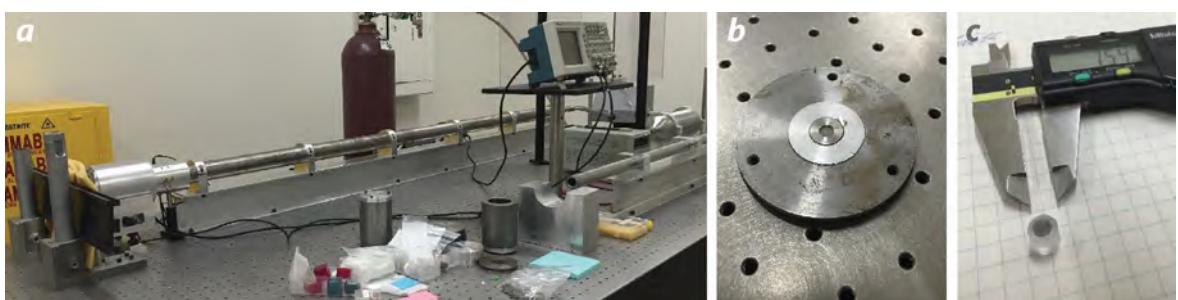
Figure 7. UNLV (a) gas launcher setup, (b) Bi sample in holder, and (c) Lexan projectile with flyer plate

holder, as shown in Figure 7b. Once the sample was shocked, it was recovered, polished, and microscopy was performed.

Post-Shock Recovery Analysis with Microscopy

Scanning electron microscopy (SEM) of the Bi sample is shown in Figure 8. Backscatter electron and secondary electron techniques were used to examine the sample topography on a sub-micron scale as well as to examine regions of possible transformation of Bi to high pressure phases through increased electron density. Shock-induced melting is shown to occur in these SEM images based on three observations, (1) melt droplets, (2) Bi recrystallized (crystallite regrowth in absence of a phase change) around voids, and (3) absence of Bi-III in recrystallized regions (temperature of release above melt line or at least above Bi-III back transformation temperature). Backscatter electron microscopy on well-polished surfaces shows relative electron density differences, which could indicate different phases or crystal orientations, as shown in Figure 8c.

Conclusion

This work advances the creation of a diagnostic to understand mesoscale and microscale defect effects during extreme dynamic compression. The crystal structure around voids, defects, and inclusions were examined, and distribution maps of phases of different sensitivity were generated. This novel diagnostic can link defect and void identification with local structural changes. The technique provides the groundwork for distinguishing whether the onset of detonation in hot spots is generated by local high-temperature-upon-void collapse or by the presence of more shock-sensitive conformational states and phases in the location surrounding the defect.

This year concluded in successfully testing the feasibility of these diagnostic methods and their relevance for characterizing mesoscale and microscale defects. Compressed sensing approaches were developed for more time-efficient tomographic imaging (larger samples, shorter time). Tomographic imagining has
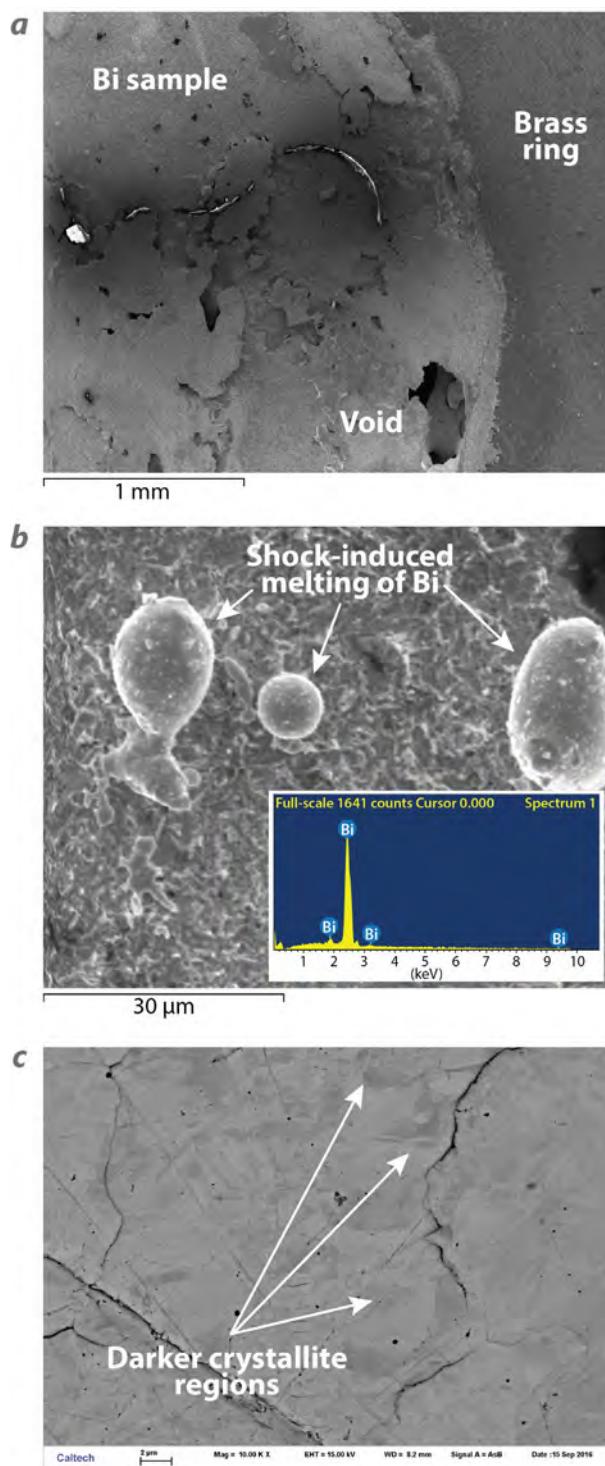
Figure 8. SEM images of a Bi sample showing (a) sample with ring, (b) melted regions, and (c) crystallite differences

been combined with single-crystal micro-diffraction for obtaining crystal orientation grain by grain. This information is then used for fast-mapping Lang topography (that is, spatially resolved measurements of Bragg intensity as a function of local lattice strain induced by crystal defects). The UNLV shock lab was utilized to conduct shock experiments on characterized samples. Post-shock recovery SEM analysis showed shock-induced melting and different crystallite regions in the examined sample.

In FY 2017 we will apply these methods to a suite of HE samples. After characterizing pre-shot defects, samples will be subjected to shock to establish the correlation between defects on different length scales with hot spot formation.

Acknowledgments

References

Baer, M. R., D. K. Gartling, P. E. DesJardin, "Probabilistic models for reactive behavior in heterogeneous condensed phase media," *Combustion Theory and Modelling* **16**, 1 (2012) 76–106.

Cawkwell, M. J., T. D. Sewell, L. Zheng, D. L. Thompson, "Shock-induced shear bands in an energetic molecular crystal: Application of shock-front absorbing boundary conditions to molecular dynamics simulations," *Phys. Rev. B* **78** (2008) 014107.

Chen, M.-W., S. You, K. S. Suslick, D. D. Dlott, "Hot spots in energetic materials generated by infrared and ultrasound, detected by thermal imaging microscopy," *Rev. Sci. Instrum.* **85** (2014) 023705.

DallaValle, J. M., et al., *Micromeritics: The Technology of Fine Particles*, 2nd edition, Pitman Publishing Corporation, 1948.

Giacovazzo, C., *Fundamentals of Crystallography*, 2nd edition, Oxford University Press, New York, 2002, 793; 799–801.

Hixson, R., "Shock and Detonation Physics, and Some Applications," course materials, Naval Postgraduate School, Monterey, Caifornia, Spring 2012.

Klapper, H., "Generation and propagation of dislocations during crystal growth," *Mater. Chem. Phys.* **66**, 2–3 (2000) 101–109.

Kuklja M. M., "Quantum-chemical modeling of energetic materials: Chemical reactions triggered by defects, deformations, and electronic excitations," in *Advances in Quantum Chemistry*, J. R. Sabin, E. Brändas, eds., Academic Press, 2014, 71–146.

NDT Resource Center, "Property modification," https://www.nde-ed.org/EducationResources/CommunityCollege/Materials/Structure/property.htm, accessed September 7, 2016.

Shan, T. R., A. P. Thompson, "Shock-induced hotspot formation and chemical reaction initiation in PETN containing a spherical void," *J. Phys. Conf. Ser.* **500** (2014) 172009, http://iopscience.iop.org/article/10.1088/1742-6596/500/17/172009/pdf, accessed October 25, 2016.

Surber, E., A. Lozano, A. Lagutchev, H. Kim, D. D. Dlott, "Surface nonlinear vibrational spectroscopy of energetic materials: HMX," *J. Phys. Chem. C* **111**, 5 (2007) 2235–2241.

Tsyshevsky, R., O. Sharia, M. Kuklja, "Molecular Theory of Detonation Initiation: Insight from First Principles Modeling of the Decomposition Mechanisms of Organic Nitro Energetic Materials," *Molecules* **21**, 2 (2016) 236.

Utah Engineering, "Planar defects: Grain boundaries," https://www.google.com/#q=http://www.eng.utah,edu/~zhang/images/lecture-6-grain-boundary-dislocation-defects-vacancy.pdf, accessed September 7, 2016.

You, S., M.-W. Chen, D. D. Dlott, K. S. Suslick, "Ultrasonic hammer produces hot spots in solids," *Nat. Comm.* **6** (2015).

This page left blank intentionally

Surface Waves in Brittle Materials: Experiments and Simulations
NLV-014-16 | Year 1 of 1

Michael Pena,[1,a] Jason McDonald,[b] Sikhanda Satapathy,[b] Brendan O'Toole,[c] Mohamed Trabia,[c] Mathew Boswell,[c] and Richard Jennings[c]

The objective of this project was to investigate the role of impact-generated surface waves on fracture initiation in brittle materials to gain insight into how these materials fail. Ballistic impact experiments using a single-stage gas gun were conducted to observe surface waves traversing across the impact surface. Cylindrical polycarbonate projectiles were fired at borosilicate glass at nominal velocities of 400 and 800 m/s. Surface velocity profiles were recorded using a multiplexed photon Doppler velocimetry system at several lateral distances from impact. Simulations were conducted of the experiments and the results compared to the experiments. In the course of this study, it was also discovered that another velocity signal could be consistently detected beneath the impact site. This velocity signal is presumably due to the propagation of an interface marking a sharp change in either refractive index or absorption at 1550 nm. The magnitude of the velocity appears to depend on the stress state (it was observed to increase with increasing impact velocity), does not correspond to any intrinsic wave velocity of the material, and its temporal dependence exhibits a rich structure. The exact origin of this signal is yet to be determined; however, it does not appear to be due to a failure wave.

[1] penamt@nv.doe.gov, 702-295-3242
[a] North Las Vegas; [b] U.S. Army Research Laboratory, Aberdeen Proving Ground, Maryland; [c] University of Nevada, Las Vegas

Background

The effectiveness of armor-grade ceramics has been demonstrated through their use in body armor and ground vehicle protection systems. Ceramic armor systems outperform similar steel-based systems while significantly reducing weight. Ceramics are, however, brittle materials exhibiting high compressive strength and rather low tensile strength. A detailed understanding of the mechanisms of failure and inelasticity in brittle materials is still lacking.

It is suspected that surface defects and flaws play an important role in the impact response of brittle materials, such as ceramics and glass. High-speed projectile impact induces complex surface waves that generate multi-stress loading in the target. Presumably the interaction of surface flaws with these waves can contribute significantly to crack initiation and failure. Prior experimental studies (Sarva 2007, Reddy 2008, Samiee 2010) have shown substantial benefit of surface treatment of ceramics on the ballistic performance. The correlation between layer material properties and degree of ballistic improvement, however, is not well understood.

Previous attempts using existing ceramics models have proved unsuccessful in reproducing the results of these experiments (McDonald unpublished). One possible explanation for this lack of success could be

that surface waves of combined dilatational and verti-cal shearing motion, often referred to as Rayleigh-type waves, are contributing significantly to cracking and failure in ceramics. Waves of this type have been studied extensively by seismologists over the years in both single half space and layered systems (Rayleigh 1885, Love 1911, Stoneley 1924). Some notable findings are the range of existence of such modes (as a function of material properties) in two-layered systems (Sezawa 1939, Scholte 1947, Bolt 1960) and the dependence of their amplitude on material properties and layer thickness (Sezawa 1935, 1937). Extension of these methods to problems of interest in ballistics and impact, using modern computational techniques, could shed light on surface layer effects in ceramics. Experimental techniques that can accurately measure surface motion for brittle materials such as ceramics and glass will also be necessary to gain a better understanding of the role of surface waves. The objective of this project was to investigate the role of impact-generated surface waves on fracture initia-tion in brittle materials. This was accomplished using multiplexed photonic Doppler velocimetry (MPDV) in a novel configuration to measure transverse movement combined with high-speed camera imagery to record crack propagation.
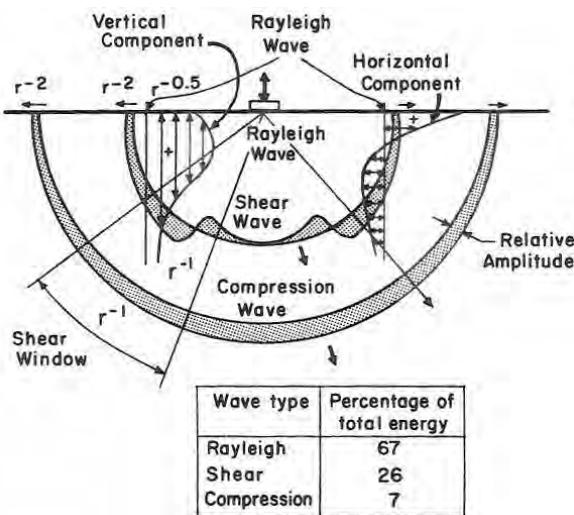
When the surface of an elastic material is dynamically loaded, various waves are generated and propagate away from the source. The different wave types and their properties are summarized in Figure 1 (Woods 1968). The interaction of these various waves with surface defects probably leads to the initiation of the failure process in brittle materials. Of the three funda-mental wave types, the Rayleigh or R waves are proba-bly the most detrimental because they carry more energy and tend to cause more violent surface motion, as demonstrated in Figure 2 (Lamb 1904), which shows the horizontal and vertical surface motion caused by a point load with an impulse-like time response. It has also been shown that the R waves can cause very large tensile stresses for high-rate loading (McDonald 2016). It is possible that the reported improvement in ballis-tic behavior of brittle materials after surface coating could be due to modification of surface waves by the coatings. If this is the case, then a careful study of the surface waves may shed light on the initial failure process and how it can be manipulated.

Project

Experiments

Borosilicate glass targets used in these experiments were 152.4 mm long, 152.4 mm wide, and 24.5 mm deep. Four target plates were stacked to form a thick block. Optical epoxy or optical index coupling gel was applied between plates to reduce reflections at the interfaces as employed previously by Tsai and Kolsky (1967). It was found, however, that shots performed


Figure 1. Distribution of displacement and energy for dilatational (P), shear (S), and Rayleigh (R) waves from a normal load on a surface (Woods 1968). The R wave carries a majority of the energy and falls off more slowly with distance from the source.
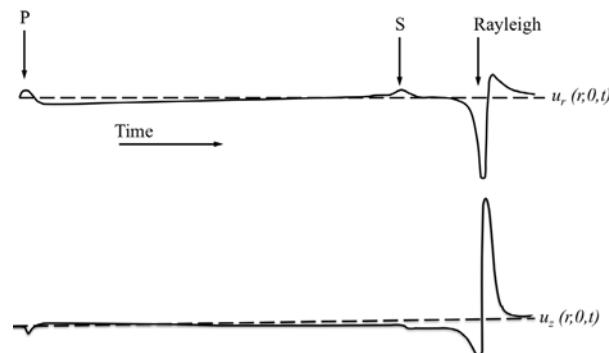

Figure 2. Horizontal and vertical displacements from an impulse load applied at a point (Lamb 1904)
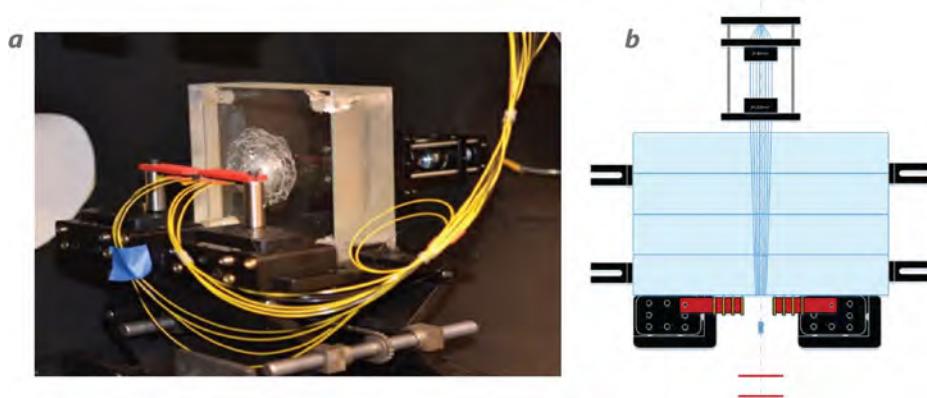
Figure 3. The target setup configuration: (a) dual-fiber probes are positioned at the impact surface and a relay lens images an MT-connector from the rear, and (b) a diagram of the top view. For redundancy, two optical beam breaks (shown at top of diagram) measure projectile velocity at the exit of the gas gun barrel. Due to limited MPDV channels, not all front surface wave and rear-placed probes could be fielded concurrently.

without this media showed no difference in the velocity wave forms, and its use was abandoned in later experiments.

The specific glass used was Schott Borofloat 33. The mechanical properties given in the technical brochure are Young's modulus of 64 GPa, Poisson's ratio of 0.2, and density of 2.2 g/cm³. Other sources vary slightly, namely Anderson (2013, 2014). The longitudinal and transverse wave speeds are 5.69 km/s and 3.48 km/s, respectively. The Hugoniot elastic limit reported by Bourne (1998) is 8 GPa, and Alexander et al. (2008) determined a similar value of 8.7 GPa.

The diameter and length of the polycarbonate projectiles were nominally 5.5 and 8.0 mm, respectively. Eight AC Photonics dual-fiber pigtail probes were placed ~1 mm from the impact surface, aligned to the horizontal target center axis, and positioned so that their lateral distance was staggered from the impact center. Probes on the impact-side recorded the surface velocity as a Rayleigh wave crossed in front of the probe and displaced the material in the direction normal to the probe long axis.

At the rear of the target, a relay lens system imaged the front of a 48-fiber MT-connector onto the impact area. The relay lens produced a 5x magnification so that individual fiber images were equally spaced

1.25 mm apart and had a diameter of 45 µm. Using small angle approximations, the maximum pointing errors from the outside fibers were less than 1° from normal and were neglected. Figure 3 shows the target/probe setup. Probe positions were determined by using burn paper to mark relative interrogation points. The burn paper's position relative to target was noted, giving an overall accuracy of ±0.25 mm.

The original intent for interrogating the surface from the rear was to measure the projectile velocity as it impacts the glass target and, possibly, observe the glass surface directly under the projectile as it indents into the target. Due to limited MPDV channels, the full complement of interrogation points could not be fielded concurrently with the front surface wave probes. On separate shots, 24 probes were used to record the impact location from the rear. A redundant measurement of the projectile velocity was carried out using two optical beam breaks separated by 304.8 mm (12") and located at the exit of the launch barrel. Our system triggers were also initiated by these beam breaks.

The MPDV system is an adaptation of traditional photonic Doppler velocimetry (PDV) where the number of velocity records per recording channel is increased by utilizing common wavelength multiplexing and fiber delay techniques. The system used in these

experiments has the capability to record 32 velocity records on four oscilloscope channels. However, the interrogation count was reduced due to using dual-fiber probes in a send-transmit configuration.

Simulations

Finite element simulations of the shots were performed using the EPIC code from Southwest Research Institute. Axisymmetry was assumed in all the simulations. The mesh size used was 0.05 mm. The glass was assumed to behave as a linear elastic material with mass density of 2.23 g/cm^3, shear modulus of 26.7 GPa, and bulk modulus of 35.6 GPa. The polycarbonate was modeled as an elastic-plastic material with a tensile-failure criteria (tensile strength = 70 MPa). The mass density

was 1.22 g/cm^3, the shear modulus 0.93 GPa, the bulk modulus 8.9 GPa, and the elastic-plastic response was treated using a Johnson-Cook model:

$$\sigma = \left(A + B\varepsilon^n \right)\left(1 + C \ln \tilde{\varepsilon} \right), \tag{1}$$

where A = 80 MPa, B = 75 MPa, C = 0.052, and n = 2.0.

Results

Waves Along the Impact Surface: Failure Initiation

Presented here are the results of two experiments conducted using a projectile with a diameter of 5.588 mm with nominal impact velocities of 400 and 800 m/s. Figures 4 and 5 show surface velocity and displacement versus time for a point 13.3 mm and
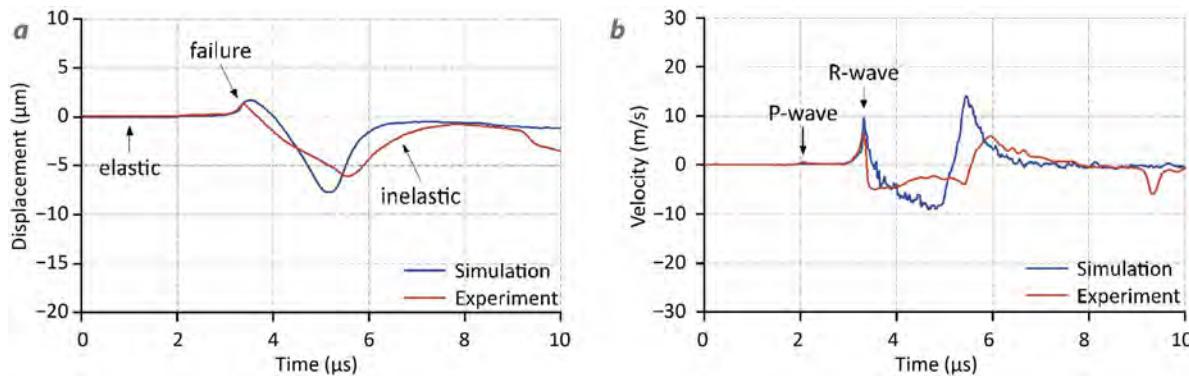
Figure 4. Comparison of simulated and measured (a) vertical displacement and (b) velocity versus time at 13.3 mm from the impact site. The nominal impact velocity for this shot was 400 m/s. The measured signal follows the linear elastic result until fracture initiates and local unloading of the stress state occurs. This initial failure appears to occur during the ramp up of the Rayleigh wave.
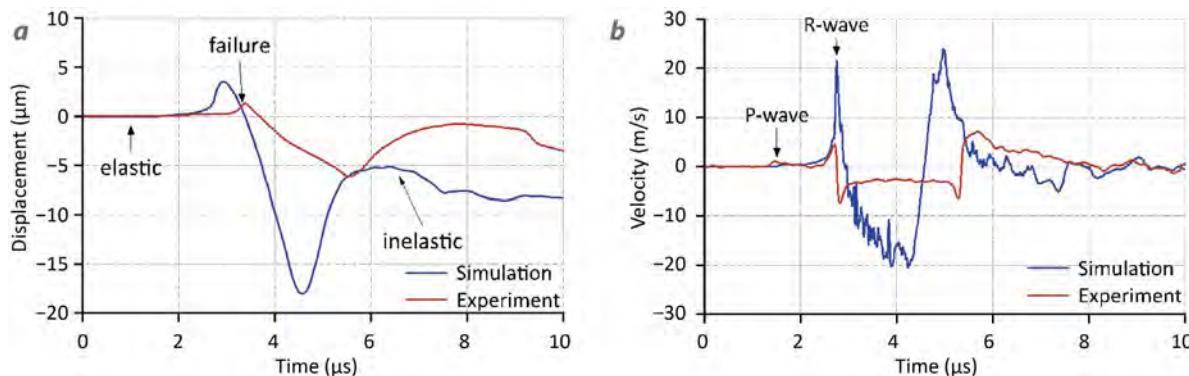

Figure 5. Comparison of simulated and measured (a) vertical displacement and (b) velocity versus time at 11.5 mm from the impact site. The nominal impact velocity for this shot was 800 m/s. The measured signal follows the linear elastic result until fracture initiates and local unloading of the stress state occurs. This initial failure appears to occur as the Rayleigh wave is building.
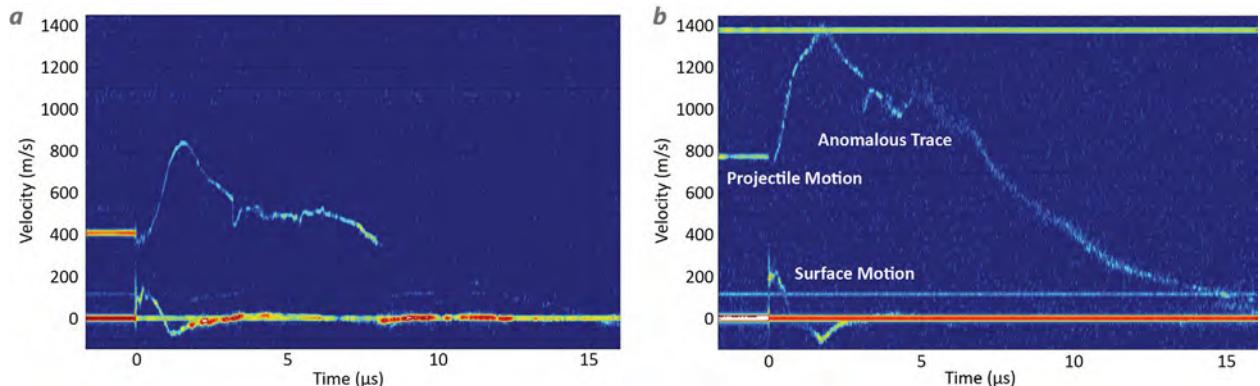
Figure 6. Spectrograms of the velocity traces recorded by a rear surface probe for (a) 400 m/s and (b) 800 m/s impacts. The bottom trace is believed to be associated with the motion of the surface inside the contact circle. The upper trace is of unknown origin.

11.5 mm from the center of impact for a shot with a nominal velocity of 400 and 800 m/s, respectively. As expected, higher impact velocities lead to surface waves with higher amplitudes. The times associated with the dilatational and Rayleigh waves are indicated in Figure 4b. It is clear that the measured velocity and displacement start to deviate significantly from the linear-elastic simulation results during the ramp up of the Rayleigh wave. This is believed to be due to the fact that the Rayleigh wave causes large tensile stresses to develop near the edge of the contact circle, which initiates the cone cracking. The behavior of the glass before this time of initial failure is approximately linear-elastic and then becomes inelastic for later times, as indicated in Figure 4a.

Single Rear Surface Probe

A single rear surface probe monitored projectile motion (to determine when impact occurred) and also recorded surface motion directly beneath impact. Figure 6 compares the recorded velocity profiles near the impact center for a (a) 400 m/s shot and an (b) 800 m/s shot.

A second velocity profile was noticed in the spectrograms recorded by the rear probe that initiates near time of impact. This second signal ramps up to a peak velocity of the order of twice the impact velocity. The origin of this signal is unknown at the present time; however, it does not seem to be related to a failure wave because there is no evidence of failure beneath
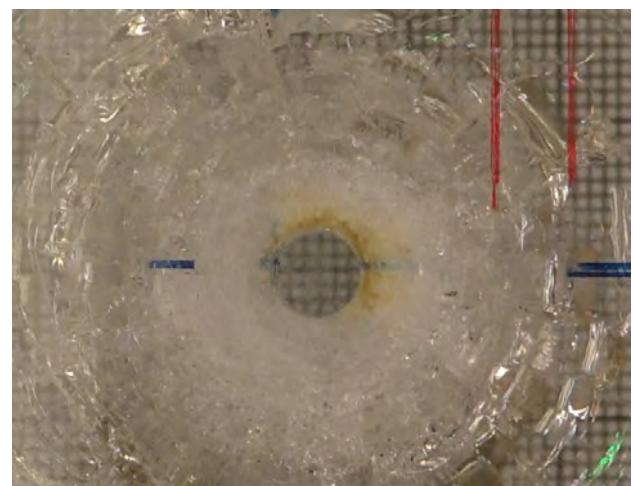
Figure 7. Image shows the absence of significant damage directly beneath the impact site. This would seem to eliminate failure waves as a source of the second velocity signal in the rear surface probes.

the impact, as demonstrated in Figure 7. We can observe these two distinct velocity traces using PDV, but it is not likely we would see them if we used a VISAR.

Multiple Rear Probes

The number of rear probes was increased to 24 in order to interrogate the surface motion at multiple locations directly beneath impact. A point map for the probe locations in a 400 m/s shot is shown in Figure 8.

Figures 9, 10, and 11 show comparisons between simulated and measured results for the displacement
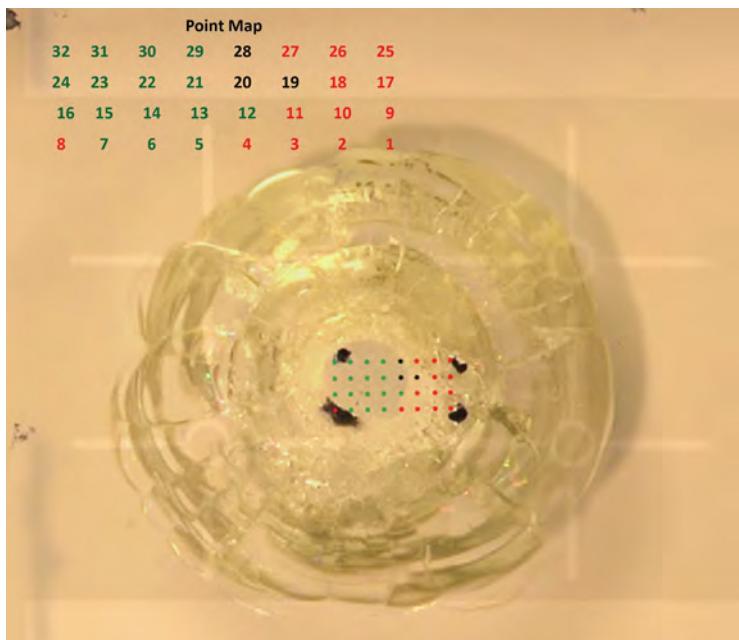
Figure 8. Rear surface probe map (inset, top) for a shot with a nominal impact velocity of 400 m/s. The points colored green yielded useable velocity traces. The points colored red did not yield useable data. The points colored black correspond to non-active sensors.
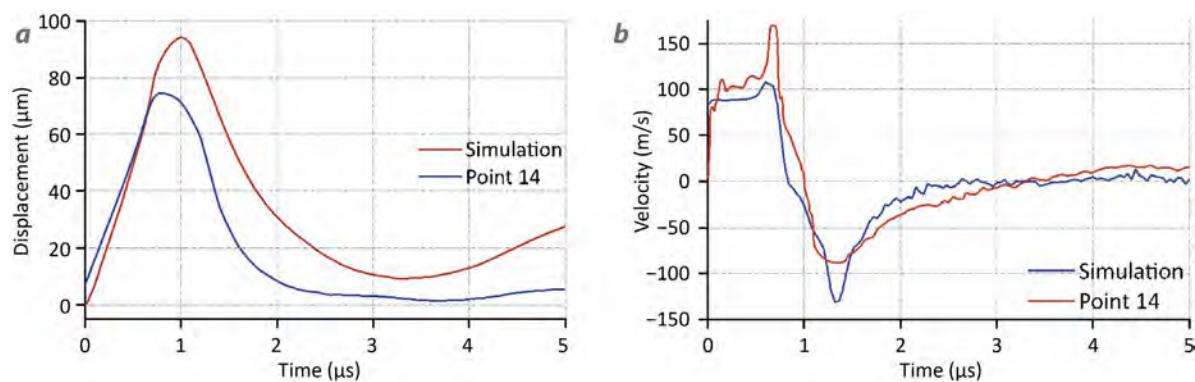
Figure 9. Comparison of simulated and measured results for the (a) displacement and (b) velocity approximately 0.75 mm from the center of the impact with a nominal impact velocity of 400 m/s
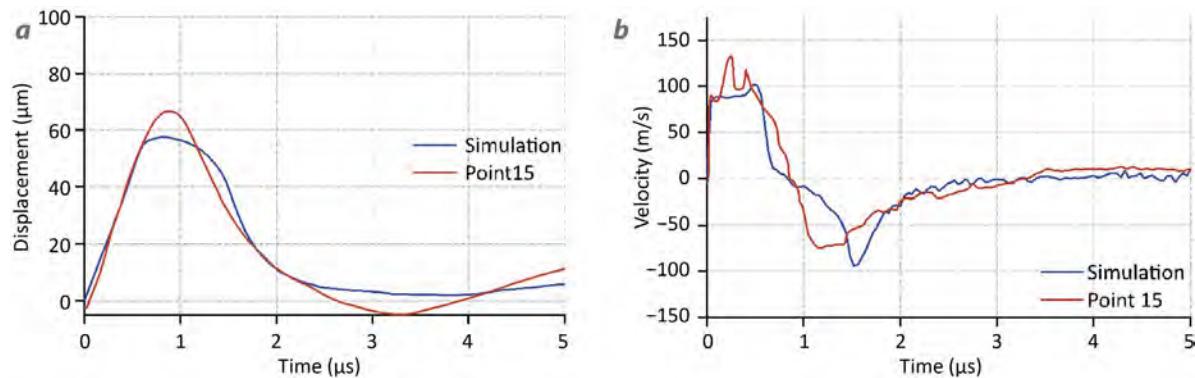
Figure 10. Comparison of simulated and measured results for the (a) displacement and (b) velocity approximately 1.25 mm from the center of impact with nominal impact velocity of 400 m/s
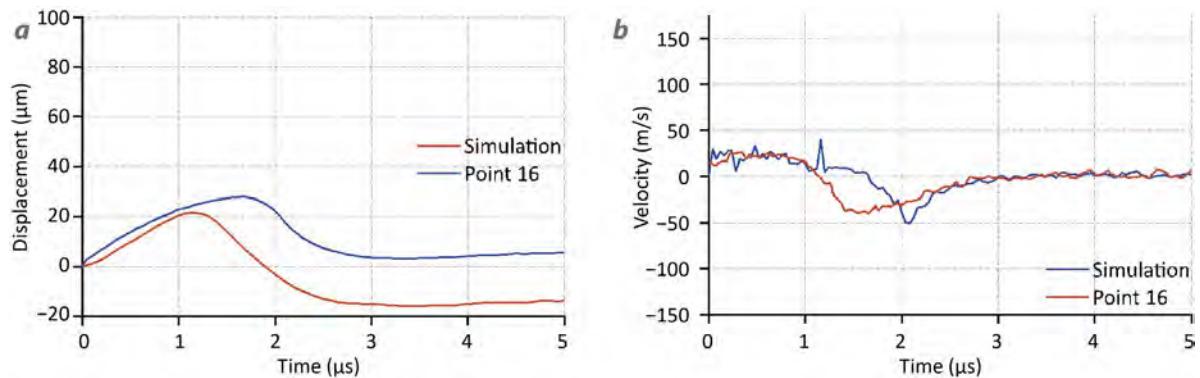
Figure 11. Comparison of simulated and measured results for the (a) displacement and (b) velocity approximately 2.7 mm from the center of impact with nominal impact velocity of 400 m/s
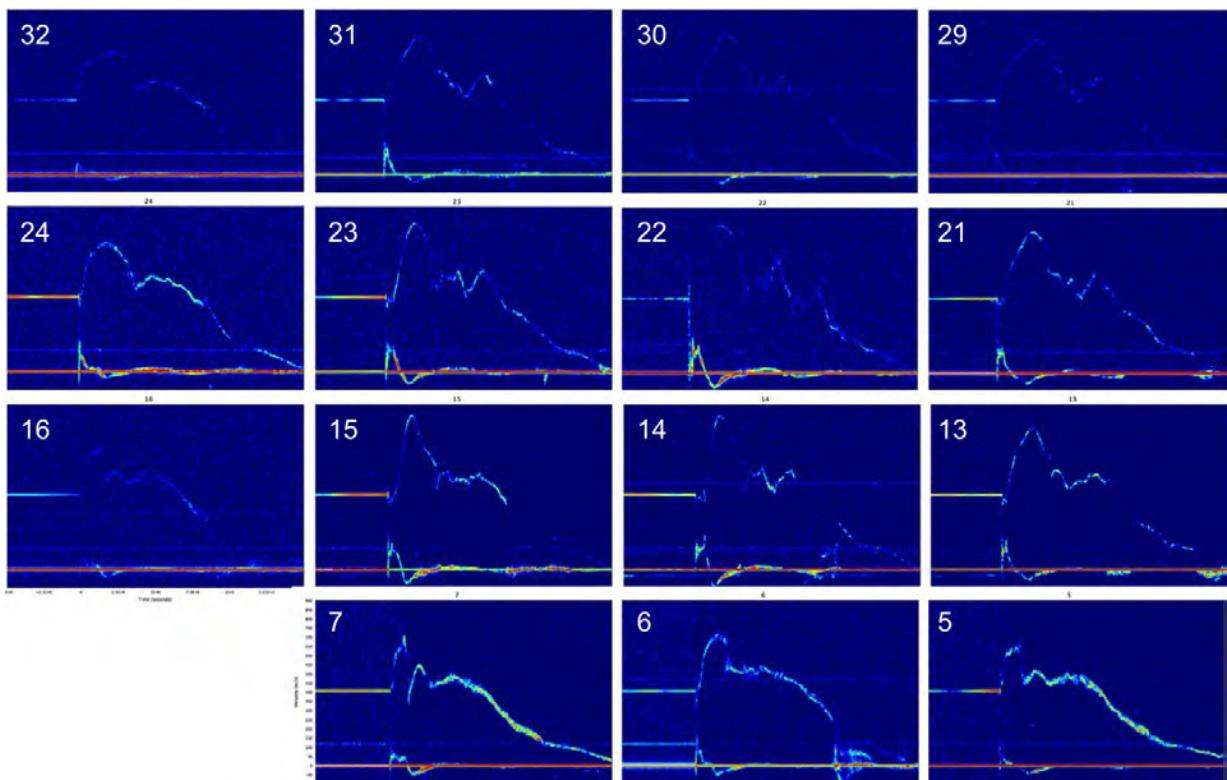
Figure 12. Spectrograms of the velocity profiles for points 7–32 interrogated from the rear arranged according to their respective location on the point map

and velocity profiles, corresponding to the lower velocity traces appearing in the spectrogram, for surface points located approximately 0.75 mm (point 14), 1.25 mm (point 15), and 2.7 mm (point 16), respectively, from the center of impact for a 400 m/s shot. Spectrograms for points 7–32 are shown in Figure 12.

Conclusion

Experiments, utilizing the MPDV method, and simulations were combined in the present study to detect impact-surface motion for a polycarbonate cylinder impacting a borosilicate glass block at 400 m/s and 800 m/s. It was found that the measured motion both beneath the site of impact and at more distant points can be adequately captured by the MPDV technique.

The initial failure can be detected, which should be useful in specifying criteria for onset of failure in these materials. The technique also provides information on the surface motion once the material has started to respond inelastically. This information will be useful in evaluating models of inelastic response and failure evolution in brittle materials.

It was discovered that a second velocity signal could be detected beneath the impact. This signal starts near the impact velocity and then increases to a peak value in the neighborhood of twice the impact velocity. The origin of this second signal remains a mystery at the present time. The possibility of a failure wave is inconsistent with the observation of the absence of damage beneath the impact. It may be due to the known anomalous behavior of silicate glasses in the low-stress regime or to densification of the borate component of the glass. Further study is needed to examine the various possibilities.

Acknowledgment

References

Alexander, C. S., L. C. Chhabildas, W. D. Reinhart, D. W. Templeton, "Changes to the shock response of fused quartz due to glass modification," *Int. J. Impact Eng.* **35** (2008) 1376–1385.

Anderson, C. E., T. J. Holmquist, "Application of a computational glass model to compute propagation of failure from ballistic impact of borosilicate glass targets," *Int. J. Impact Eng.* **56** (2013) 2–11.

Anderson, C. E., R. P. Bigger, C. E. Weiss, "Crack and damage velocities in ballistic experiments," *Int. J. Appl. Glass Sci.* **5** (2014) 374–383.

Bolt, B. A., J. C. Butcher, "Rayleigh wave dispersion for a single layer of an elastic half space," *Aus. J. Phys.* **13** (1960) 498–504.

Bourne, N., J. Millett, Z. Rosenberg, N. Murray, "On the shock-induced failure of brittle solids," *J. Mech. Phys. Solids* **46** (1998) 1887–1908.

Lamb, H., "On the propagation of tremors over the surface of an elastic solid," *Phil. Trans. R. Soc.* **A203** (1904) 1–42.

Love, A. E. H., *Some Problems of Geodynamics*, Cambridge University Press, Cambridge, 1911, 154-178.

McDonald, J., S. Satapathy, "Surface waves and their influence on cone cracking in brittle materials," *Int. J. Impact Eng.* **93** (2016) 144–152.

McDonald, J., S. Satapathy, private communication, 2016.

Rayleigh, J. W. S., "On waves propagated along the plane surface on an elastic solid," *Proc. London Math. Soc.* **17** (1885) 4–11.

Reddy, P. R. S., V. Madhu, K. Ramanjaneyulu, T. Balakrishna Bhat, K. Jayaraman, N. K. Gupta, "Influence of polymer restraint on ballistic performance of alumina ceramic tiles," *Def. Sci. J.* **58** (2008) 264–274.

Samiee, A., J. Issacs, S. Nemat-Nasser, "Ballistic performance of polyuria-coated armor grade ceramic tiles," *Proc. SPIE* **7644** (2010) 76441Y.

Sarva, S., S. Nemat-Nasser, J. McGee, J. Issacs, "The effect of thin membrane restraint on the ballistic performance of armor grade ceramic tiles," *Int. J. Impact Eng.* **34**, 2 (2007) 277–302.

Scholte, J. G., "The range of existence of Rayleigh and Stoneley waves," *Month. Notices Roy. Astr. Soc. Geophys. Suppl.* **5**, 5 (1947) 120–126.

Sezawa, K., K. Kanai, "Decay constants of seismic vibrations of a surface layer," *Bull. Earthquake Res. Inst.* **12**, Part 2 (1935) 251–257.

Sezawa, K., K. Kanai, "Relation between the thickness of a surface layer and the amplitudes of dispersive Rayleigh waves," *Bull. Earthquake Res. Inst.* **15**, Part 4 (1937) 845–849.

Sezawa, K., K. Kanai, "The range of possible existence of Stoneley waves and some related problems," *Bull. Earthquake Res. Inst.* **17** (1939) 1–8.

Stoneley, R., "Elastic waves at the surface of separation of two solids," *Month. Notices Proc. Roy. Soc. Geophys. Suppl. Ser. A* **106** (1924) 416–428.

Tsai, Y. M., H. Kolsky, "A study of fractures produced in glass blocks by impact," *J. Mech. Phys. Solids* **15** (1967) 263–278.

Woods, R. D., "Screening of surface waves in solids," *J. Soil Mech. Founds. Div. Am. Soc. Civ. Engrs.* **94** (1968) 951–979.

This page left blank intentionally

SYSTEMATIC STUDIES IN DYNAMIC MATERIAL RESPONSE – EARLY-CAREER POSTDOCTORAL RESEARCH

LAO-065-16 | Continuing in FY 2017 | Year 1 of 2

Sarah Thomas [1,a] and Robert S. Hixson [a]

Many areas of dynamic material properties are limited in scientific understanding. More work is warranted to improve fundamental input physics models for large-scale hydrodynamic codes, and thus improve prediction capabilities for integrated experiments. In the scope of this work, we chose to examine copper spall, strength of aluminum, and wave speeds in copper. While the data quality achieved in our strength of aluminum experiments was poor, we are refining the experiments for FY 2017; these improvements may allow us to see the dislocation dynamics unfold. Our polycrystalline copper spall data were matched well with single-crystal results, with the exception of two outlying points; these outliers will be more closely examined in FY 2017. The copper wave speed results matched relatively well with shock Hugoniot data from Los Alamos National Laboratory (LANL) (Marsh 1980) at this point in our analysis; however, error bars have yet to be assigned to the LANL data.

[1] thomassa@nv.doe.gov, 505-663-2068
[a] New Mexico Operations–Los Alamos

Background

The research we conducted this year directly addresses dynamic material properties issues that are called out in the *Nevada National Security Site Technology Needs Assessment*. Our work seeks to further understand fundamental dynamic material properties relevant to the NNSA mission in order to enhance development of robust physics models. Improving our ability to do high-fidelity simulations of dynamic events is a long-term goal of the national laboratories and the NNSA, and this work directly contributes to that goal. Data obtained on how materials yield in both compression and tension, shock wave velocities, and on the dislocation dynamics of materials as they yield will allow more robust equation-of-state (EOS) predictions to be developed.

Project

Over the course of this year, we conducted three different experiments: spall in polycrystalline copper, strength of aluminum, and wave speed in polycrystalline copper. This research complements similar work being done in a Strategic Opportunity SDRD project, "Enhanced Dynamic Materials Research" (Hixson 2016, La Lone 2017). Each experiment and its results are discussed in the following sections.

Copper Spall

The first set of experiments, copper spall, were conducted at the small-bore propellant launcher at the NSTec Special Technologies Laboratory (STL). Spall can be affected by a number of factors—dwell time, peak pressure, strain rate, etc. In this work, we attempted to isolate and examine dwell time, which is the time the material spends at peak pressure. Because the factors leading to spall are interdependent, it is not easy to isolate any one factor from the others. In

Table 1. Shot parameters for polycrystalline copper spall experiment

Shot	Flyer Velocity (km/s)	Target Thickness (mm)	Flyer Thickness (mm)	Description
1	0.299	2.963	0.946	Short dwell
2	0.305	3.954	1.988	Long dwell
3	0.301	2.969	0.939	Repeat short dwell
4	0.303	3.951	2.004	Repeat long dwell
5	0.604	3.958	2.006	Long dwell/high velocity [100] match
6	0.300	1.962	0.953	Short dwell [100] match
7	0.605	3.957	1.988	Repeat long dwell/ high velocity [100] match
8	0.304	1.979	0.947	Repeat short dwell [100] match

order to investigate dwell time, we designed a series of experiments that kept the velocity constant while varying flyer and target thicknesses to change the time spent at peak velocity. The variations in thickness also cause the tensile strain rate to vary. Table 1 presents the parameters for the shots performed for this experiment. The first two shots, whose peak velocities are the same, were designed so that Shot 1 had a shorter dwell time than Shot 2. Shots 3 and 4 replicated Shots 1 and 2 to assure reproducibility. Shots 5 and 6 reproduced shots carried out at STL on single-crystal copper, with Shots 7 and 8 repeating these. These shots had different dwell times than those we designed.

The geometry for these experiments is given in Figure 1. A single dual-fiber photonic Doppler velocimetry (PDV) probe looked at the center of the target in order to measure free surface velocity on the back face. An optical beam interrupt in the barrel of the launcher signaled the diagnostics to trigger.

The impactor and target have the same diameter, but the target is thicker than the impactor in order to keep the spall plane within the target. Figure 2 shows a diagram of the wave interactions in the material. You can see that when the flyer is half the thickness of the target, the spall plane is in the center of the target. Keeping near this ratio of flyer-to-target thickness keeps the spall plane within the target.

We completed all eight shots. Figure 3 shows an example wave profile from a short dwell time shot. The elastic and plastic waves are labeled E1 and P1, respectively. Δt labels the time spent at peak pressure, and the spall signature and ringing in the spall scab are labeled as such.
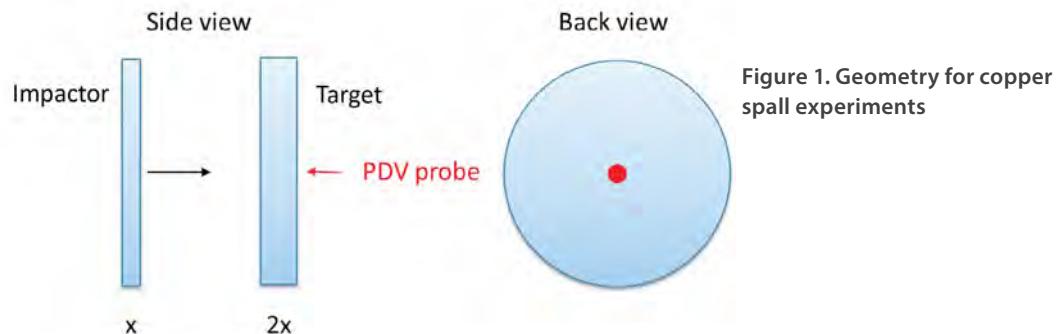
Figure 1. Geometry for copper spall experiments
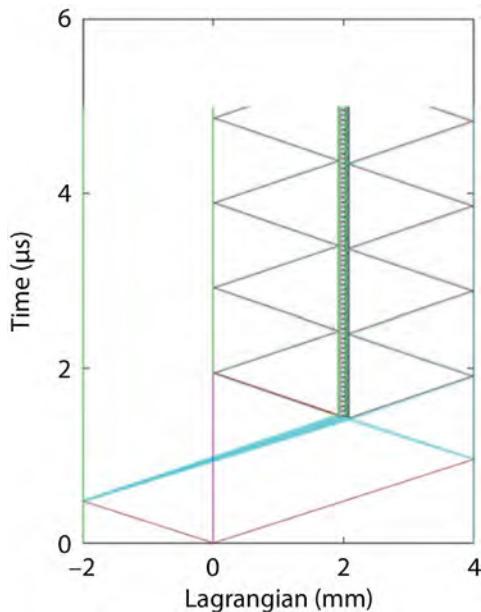
Figure 2. A wave interaction diagram of the long dwell shot
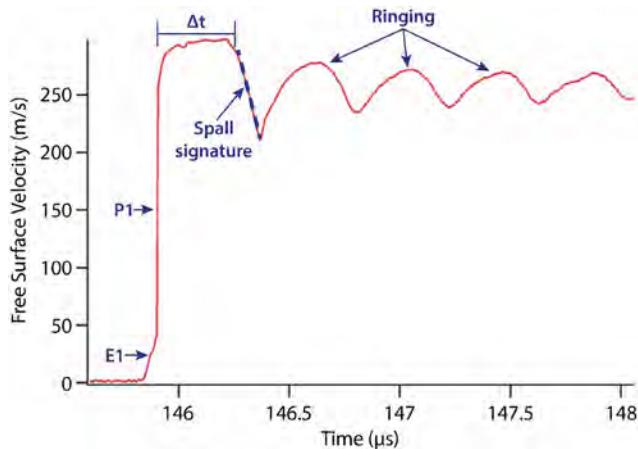
Figure 3. Wave profile of short dwell time polycrystalline copper spall shot. Dwell time had little effect on spall.

Figure 4. Comparison of spall signatures. Note that the depth of the release corresponds to the slope, or release rate.
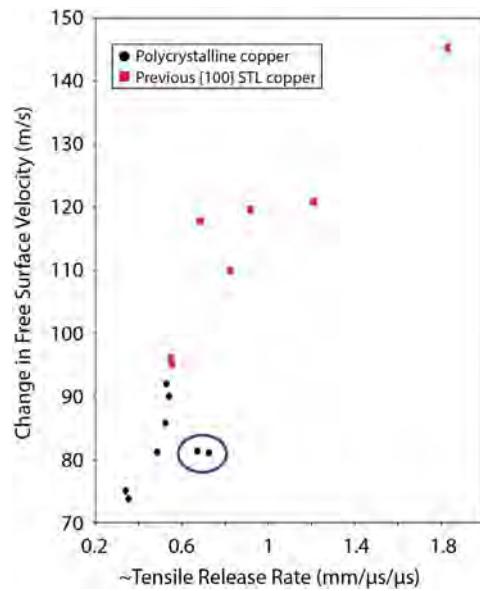
Figure 5. Change in free surface velocity vs. tensile release rate (slope of spall signature). Points off the trend are circled in blue.

After analyzing the data, we found that the dwell time did not seem to have much effect on the spall signature. However, we did find a correlation between the change in free surface velocity of the spall signature and the tensile release rate, as shown in Figure 4. Furthermore, this correlation matched well with data taken on [100] single-crystal copper at STL on other occasions, as shown in Figure 5. These data reveal a clear trend between the polycrystalline and single-crystal points. However, there are two outlying points in the polycrystalline data, circled in blue, that have a lower spall strength than would be expected from the release strain rate. We plan to duplicate these shots in order to confirm the off-trend points are indeed real. If they are, which we suspect, we will look further into the underlying cause.

Strength of Aluminum

Previous work by Winey (2009) has shown that elastic wave evolution in Al alloys is different for 1050 Al than 6061-T6 Al, with the Hugoniot elastic limit wave becoming steady much faster in 6061. Because the evolution of plasticity in ductile metals like Al is controlled by dislocation processes, this might imply that 6061 has much faster dislocation dynamic processes than does 1050 Al. We chose to do front surface impact shots to look at the precursor decay directly. Because of the difficulty in acquiring 1050 Al, we instead examined 1100 Al, which is still very pure.

Figure 6 shows the geometry of the aluminum shot, which was done in the so-called "front surface impact" geometry. An aluminum flyer strikes the front surface

of a lithium fluoride (LiF) window, which has an aluminized face. We used a PZT pin to trigger the diagnostics. One collimating PDV probe looked down the barrel of the launcher to measure projectile velocity. Another dual-fiber probe looked through the ~19 mm thick LiF window at the back of the very thin aluminized layer on the impact surface. We expected data from these shots to show a sharp increase in velocity as the impactor hit the target, with the initial velocity overshooting the steady state and then relaxing into the steady state. This precursor decay would give information on the dislocation dynamic process times.

Because the window was very thick (19 mm), the dual-fiber probe was unable to collect as much light as we would have hoped, resulting in a weak signal.
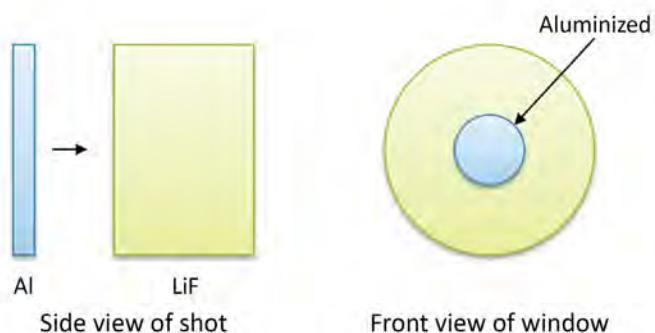
Figure 6. Geometry of aluminum front surface impact experiments explored precursor decay directly
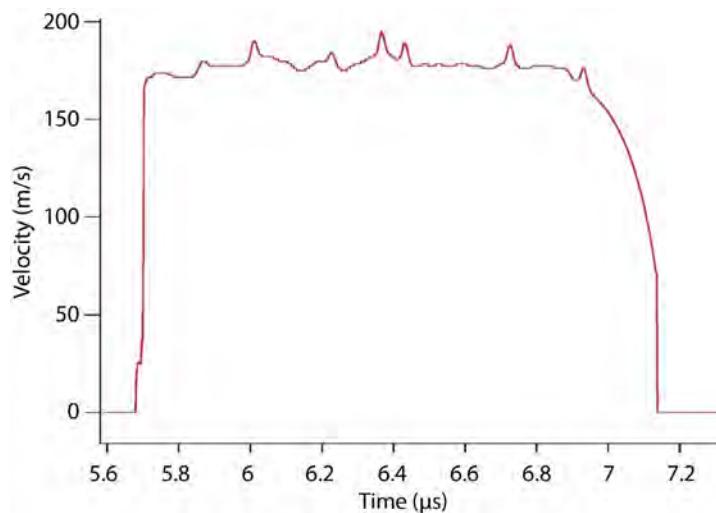
Figure 7. Wave profile of front surface impact aluminum shot. Noise indicates points at which the signal dropped.

In order to improve the signal, we used a focusing probe on the second shot. The focusing probe had the problem of dropping the signal periodically throughout the shot record as the aluminized surface of the target tilted with respect to the probe, causing the light to veer off. Because of the problems with the probes, we were unable to collect quality data for these shots. Figure 7 shows the resulting data from the focusing probe. The noise is due to the drops in signal.

Because of the noise, this experiment does not allow us to tell if the expected signature is there. In FY 2017, we plan to redo these experiments with a thinner (10 mm) window, so that the dual-fiber probe will be able to collect more light and improve the signal-to-noise ratio of the experiment.

Copper Wave Speeds

While the EOS for copper has been fairly well studied, wave speeds at low stress are not as well known. Systematic errors may be present in the data presented in the Marsh compendium (Marsh 1980), the standard manuscript in the community, due to the use of the flash gap method when collecting the data. We undertook experiments to measure wave speeds in polycrystalline copper at low pressures, with a view to examine single-crystal copper in the future. Single-crystal work will be done in FY 2017 to determine if shock speeds depend upon crystalline orientation.

As shown in Figure 8, a copper flyer impacted the base of a copper "top hat." Five channels of PDV, four around the brim and one in the center of the top, were used to measure the free surface velocity at these points.
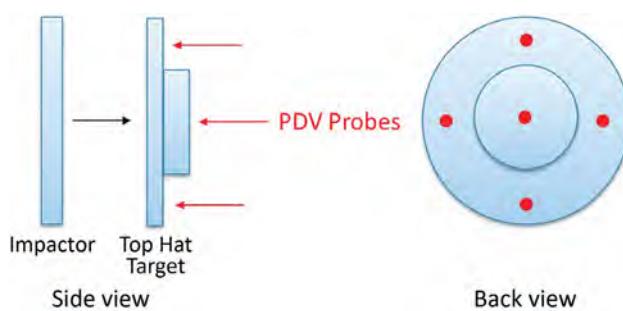
Figure 8. Geometry of copper wave speed experiments

From the four channels around the brim, we were able to determine the time that the elastic and plastic waves entered the base of the top part of the top hat. Measurements at the center probe gave us the time the elastic and plastic waves exited the back of the top. The five channels of PDV allowed cross timing to be well determined. Using these times and the thickness of the top part of the top hat, we were able to determine the speeds of the elastic and plastic waves. Figure 9 gives an example wave profile indicating the elastic (E1) and plastic (P1) waves.
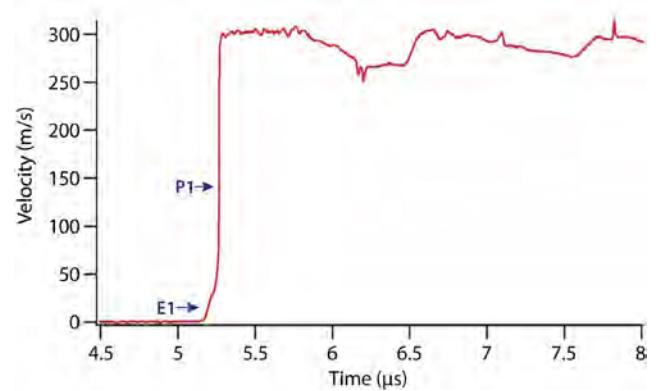
Figure 9. Wave profile extracted from PDV data taken at the brim of the target helped determine a wave speed of 4.75 km/s

After finding our measured elastic wave speed, we compared it to the measured longitudinal sound speed of the material, and found it to be in very good agreement, lending credence to our subsequent shock speed measurements. We determined the elastic wave speed, C_L, by taking the time the elastic wave entered the top section of the part, t_i, (the same as the time the wave exited the back of the brim) and subtracted from the time it exited the top, t_f, then divided into the thickness of the top, x:

$$C_L = \frac{x}{t_f - t_i}. \tag{1}$$

We got values of 4.75 and 4.76 km/s for Shots 1 and 2, which were no more than 0.2% different from our measured longitudinal sound speed of 4.75 km/s. Our values for shock speed vs. particle speed are plotted

$$U_S = 3.91 + 1.51u_p$$
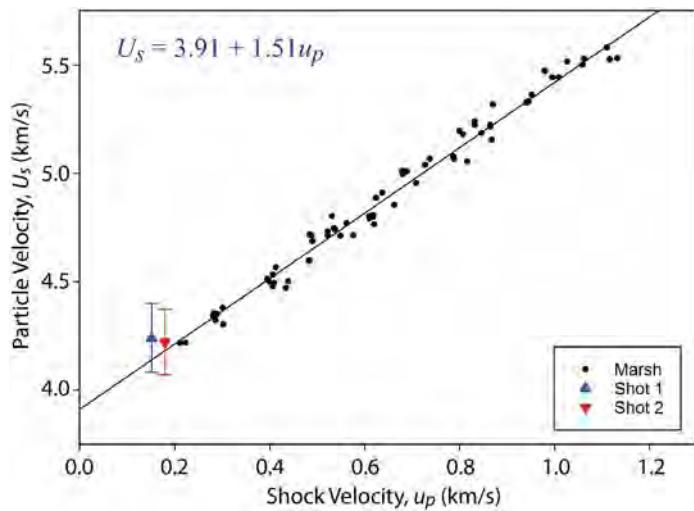
Figure 10. Copper equation of state shows agreement with our error bars to the Marsh data (Marsh 1980), but further analysis will be done

in Figure 10 along with data taken from Marsh (1980). We used the same technique as described for the elastic wave speed, and applied it to the plastic wave, giving values of 4.20 and 4.19 km/s.

Our measurements agree within our error bars to the Marsh data. We will continue to analyze these data, and work is ongoing to refine both data analysis and collection. We plan to compare our data with other literature values in the future, in order to better understand how well this technique works to determine EOS data.

Conclusion

In the first year of this project, we have studied copper spall, strength in aluminum, and copper wave speed. We have obtained new data on polycrystalline copper spall unlike any done before. This contributes to a fundamental understanding of spall damage in metals. This work, which will continue in FY 2017, is coordinated with research being done in a Strategic Opportunity SDRD project (Hixson 2016, La Lone 2017). We have initiated a research program to look at dislocation dynamic mediated yielding in polycrystalline metals. This effort will continue next year to improve data quality. Our new method (developed under the Strategic Opportunity SDRD project) for making low-pressure shock Hugoniot measurements looks promising, and next year we will

work to further refine it. This holds great promise for making better low-pressure Hugoniot measurements and contributing to the shock physics community.

Acknowledgments

We would like to thank Ed Daykin, Tom Graves, Cameron Hawkins, Melissa Matthes, Jeff Cates, Russ Howe, Dale Turley, Jerry Stevens, and Lynn Veeser for their contributions to this work.

References

Hixson, R. S., B. La Lone, G. D. Stevens, D. Turley, L. R. Veeser, "Enhanced dynamic materials research," in *Site-Directed Research and Development*, FY 2015, National Security Technologies, LLC, Las Vegas, Nevada, 2016, 15–29.

La Lone, B., G. D. Stevens, D. Turley, L. Veeser, R. S. Hixson, "Enhanced dynamic materials research," in *Site-Directed Research and Development*, FY 2016, National Security Technologies, LLC, Las Vegas, Nevada, 2017, 1–9.

Marsh, S. P., ed., *LASL Shock Hugoniot Data*. University of California Press, Berkeley, California, 1980, http://large.stanford.edu/publications/coal/references/docs/shd.pdf, accessed July 28, 2016.

Winey, J. M., B. M. La Lone, P. B. Trivedi, Y. M. Gupta, "Elastic wave amplitudes in shock-compressed thin polycrystalline aluminum samples," *J. Appl. Phys.* **106** (2009) 073508.

Next-Generation Photomultiplier Detectors Using Transmissive III-Nitride Semiconductor Electrodes

NLV-049-16 | Continuing in FY 2017 | Year 1 of 2

Robert Buckles,[1,a] Kristen Crawford,[a] Dr. Ke-Xun Sun,[b] and Patrick O'Gara[a]

We are developing a state-of-the-art, ultra-fast solid-state photomultiplier replacement for aging photomultiplier vacuum tubes (PMTs). Made from Group III-nitride semiconductor materials, the quaternary set composed of aluminum, indium, and gallium, these materials are both high speed and UV sensitive and will produce a device with enhanced quantum efficiency, better linearity, lower noise, and faster response time. This technology would ideally replace legacy glass-envelope bialkali photocathodes and metal-oxide dynodes that are increasingly expensive, unreliable, and unobtainable. PMTs are imperative for relatively low light levels where current solid-state devices fail to achieve the necessary high signal-to-noise ratio, a common requirement for dynamic experiments. With its wide band gap, gallium nitride is an excellent UV photonic material approaching nearly 100% quantum efficiency; our work extends into the near-UV, blue-VIS range of high-energy scintillators, as we are using a 12% fractional alloy of indium gallium nitride as the photonic sensitive absorber, which should still exhibit enhanced quantum efficiency (~400–425 nm). We replace the metal (oxide) dynodes, typically beryllium copper or aluminum, with a thin crystalline aluminum gallium nitride semiconductor as the transmissive electron multiplier in typical mesh PMT. Greater secondary electron yield is expected, as well as very high gain with very short transit distance, while avoiding concentrated space-charge density. These features should produce better linearity, lower noise, and faster response time, which are important characteristics for a variety of nuclear defense applications. With much reduced size and weight, next-generation PMTs will also serve in global security applications, especially where high count rate and ultra-low dark current are also important. In FY 2016, the focus was on the development of the photocathode. In FY 2017, both the characterization of the photocathode devices and the development of the mesh multiplier will be completed.

[1] bucklera@nv.doe.gov, 702-295-0323

[a] North Las Vegas; [b] University of Nevada, Las Vegas, Department of Electrical and Computer Engineering

Background

The photomultiplier tube (PMT) industry is rapidly becoming a market of the past, and there is little research on how to improve the technology, as industries look to silicon photomultipliers (SiPMs) or avalanche photodiodes (APDs). Although PMTs that meet our high performance standards can still be purchased, their quality has steadily declined. Tubes are gassier, have poorer linearity and impulse response, and simply do not perform as robustly as they once did. The trending decline of quality is directly related to the sparse number of markets seeking these devices, principally high-energy physics users such as ourselves and our nuclear defense customers. We are challenged two-fold as we (1) accurately measure

radiation yields on a nanosecond timescale with very high gain (10^5–10^8) and very low dark current (<1 fA), and (2) limit our interest to nonrepetetive or impulsive applications, while still requiring single-photon sensitivity and negligible spurious counts.

Many applications that once used PMTs have secured adequate alternatives, such as SiPM, APD, and microchannel plate (MCP) detectors. But each of these devices falls short of the high performance we expect for our detector applications. High flux, linear response, ultra-low noise figure, high bandwidth, and reliability were the biggest drivers for studying a potential solid-state device that cannot only meet but exceed the specifications of some of our best PMT devices. Furthermore, we desire the next-generation PMT marvel to meet the needs of our future interests, which are taking us into the picosecond regime.

Technical Motivation—"Why not Silicon?"

The inspiration for our new PMT was based on some recent advancements in both the study and manufacture of III-nitride devices. Many of these advancements have been the direct result of LED development for the lighting industry. Following the advancements

of metal-organic vapor phase growth processing of GaN and the development of the first blue laser diode and LED (Nakamura, Akasaki, Amano, 2014 Nobel prize winners in Physics), scientists mapped out the band gaps of these quaternary III-N alloys (Figure 1). Group III-nitride semiconductors are intriguing because of their wide band gaps, thermal insensitivity, high-voltage breakdown, and high-power handling. These are highly desirable characteristics for ideal PMT; using these materials should yield a more discrete primary electron energy for precise photosensitivity as well as discrete secondary electron emissions for avalanche gain, and should not allow the spontaneous thermal emissions that lead to dark current and noise. Similar techniques were pursued in the halcyon days of PMT development (Engstrom 1980); the use of gallium phosphide (GaP)–coated reflective metal dynodes in the first dynode stages produced nearly ideal Poisson statistics (as opposed to exponential), resulting in practically noise-free gain and very narrow energy resolution in single-electron pulse-height counting tritium sampling detectors (Figure 2). However, Electron Tubes Limited and Hamamatsu dropped these efforts.
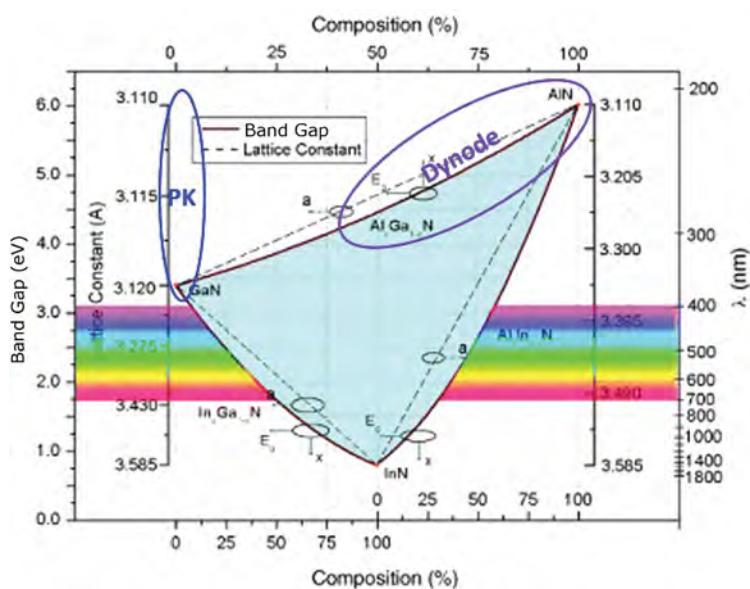
Figure 1. Energy band gap diagram for III-N materials (Morkoç 2013). Highlighted are the energy ranges relevant to photocathode (PK), which indicates using an indium gallium nitride (InGaN) alloy, and Dynode, which indicates an AlGaN alloy.
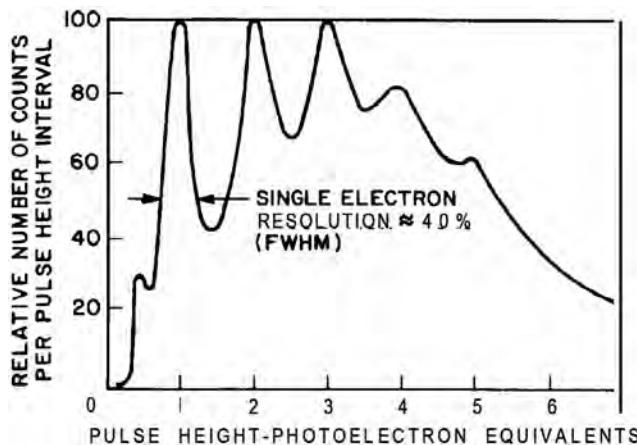
Figure 2. Discrete photoelectron pulse-height spectrum for a PMT having a GaP first dynode (Engstrom 1980). We expect GaN to have equal behavior, perhaps better, for all-GaN dynodes.

Besides silicon, there exists no possibility for electrons to be thermally promoted. (In fact, silicon is an indirect band gap semiconductor and actually depends on thermal excitation to bridge the band gap.) III-N materials have great mobility, many times that of silicon and, due to the nature of abrupt heterojunction interfaces, can achieve transport speeds fast enough for terahertz switching. The thermal dependence of III-N devices lies not in spurious carrier generation, but rather in freezing out the disruptive transport effects of crystal lattice defects, limiting mobility. Ultimately, we expect that III-N processing defects will be virtually eliminated in time, just as was done for the silicon industry, so future III-N devices can only improve. Other desirable attributes of III-N semiconductors are the radiation hardness and the perceived ability to use them as a direct radiation detector or imager, even in high background environments such as nuclear fission or fusion reactors. Consequently, direct applications beyond our present focus on PMT replacements exist.

Project

Development efforts were divided into two areas: (1) the design and fabrication of the InGaN photocathode and (2) the design and fabrication of the AlGaN dynode "mesh." Conceptually (Figure 3), the photocathode and mesh are made separately and the wafers bonded together, which may seem incongruous to all-solid-state techniques; however, this method preserves the necessary free-electron feature of high-quality PMTs. The free electron alleviates many difficulties with APD performance such as high dark current, high noise, and limited gain by completely separating the photoelectron conversion from the multiplication region in **all** physical respects. Fundamentally, the gain is provided simply by kinetic impact energy of the free-space primary and secondary electrons, rather than by a quasi-continuous acceleration/scatter/drift mechanism in a typical semiconductor. Furthermore, stacking multipliers can tailor the desired maximum gain in roughly 2^5 increments. In the proposed PMT, the applied field is modest with limited spurious noise, while for APDs it is very high, resulting in high spurious dark emission and noise. Even in APDs that attempt to separate the high-field gain region from the low(er)-field absorption region (McClintock 2010), the improvement in signal-to-noise
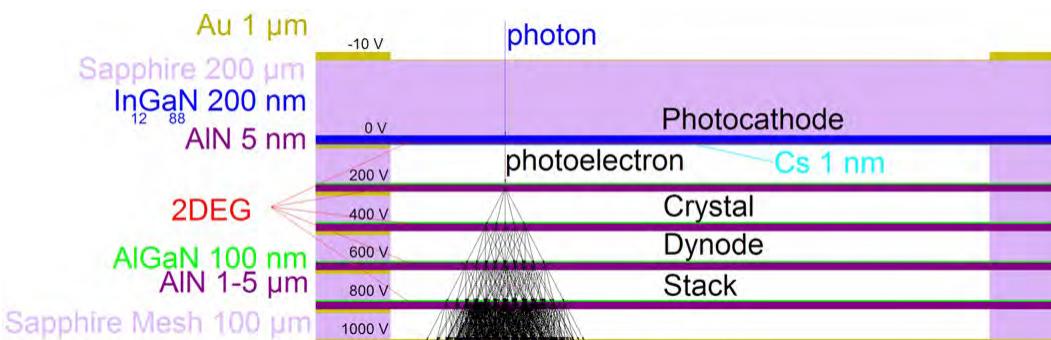
Figure 3. A conceptual model of one cell of a final device shows how a single photon will interact with the photocathode to create a photoelectron, which will interact with each dynode layer for gain and collection at a final anode

ratio is just marginal from a PMT perspective due to the too-soft barrier between the two regions. We do, however, encounter the vacuum energy barrier, or electron affinity, and surface energy modification techniques must still be considered in our conceptual design for cesium oxide as well as nitride treatments that produce negative electron affinity (NEA). Due to the band gap nature of III-N materials, however, nearly every incoming photon will promote a carrier, a small fraction lost in transport due to crystal defects, compounded by losses due to finite quantum tunneling through the surface energy barrier. Nevertheless, we believe quantum efficiency (QE) can be improved beyond the typical 20% of bialkali semitransparent cathodes to 50% with proper surface treatment. The first year of this project sought to understand the solid-state physics of III-N semiconductors in NEA application, and design and produce photocathode prototypes.

High-Field Transport and Models Using QuantumESPRESSO and nextnano

We performed an in-depth investigation of III-V electronics structure (Pearton 2000, Li 2006, Piprek 2007, Morkoç 2013) and high-field transport (Goano 2000; Ghillino 2001; Nilsson 2001a, 2001b; Martinez 2003; Bertazzi 2009; Moresco 2009; Bellotti 2010) and how we could use such advanced theory and calculations to simulate and design the photocathode and dynode devices. Accurate transport calculations depend, first, on knowing the precise electronic structure in terms of energy levels (eigenstates) as a function of carrier velocity and direction (vector momentum) within the crystal lattice. These conditions are not static, but depend especially on the high applied fields and inherent piezo strain fields in a wurtzite crystal structure. In fact, it is the piezo strain that allows for much of the intriguing behavior in III-N heterojunction devices, such as 2-D electron gas and hole gas formation (2DEG and 2DHG) and high conductivity. Therefore, material properties are essentially part of the (nonlinear) simulation solution requiring iterative processing beyond calculation of fields and transport.

To make fast processing possible, the electronic structure of atoms are modeled with parametric central potentials (pseudopotentials) that account for short- and long-range effects, such as tight binding to deep-core S-orbitals in nitrogen atoms and long-range D-orbitals of gallium atoms. Hence, the directional alignments of atoms in the crystal are an integral part of the crystal symmetry properties. Parameters of the pseudopotentials are adjusted to reproduce the experimentally measured material properties such as band gaps and effective masses along principal directions of the Brillouin (momentum) crystal cell (Figure 4), and strikingly reproduce in great detail the electronic structure of all the valence and conduction bands in III-N materials within a couple percent (Figure 5). Fortunately, these parameters and methods are already applied in electronic structure code libraries such as QuantumESPRESSO (Giannozzi 2009) and nextnano (Birner 2007), although more professional developers will generally customize these psuedopotentials to match their observed materials. High-Field III-Nitride semiconductor research focuses on the pseudopotentials for a given semiconductor. There are several variables that affect the pseudopotential for any one layer of the photocathode. The variables
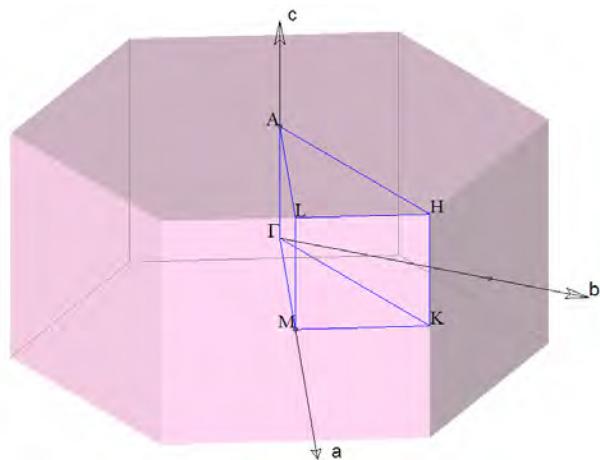
Figure 4. Irreducible wedge (blue) of the wurtzite crystal first Brillouin zone (BZ, pink), exhibiting P6$_3$mc space-group crystal symmetry (#186, aka C6v in Schönflies point-group notation). Axes a, b, and c are the principal momentum axes, and significant symmetry points in momentum space are indicated with letters Γ, A, M, K, L, H, etc., following standard notation.
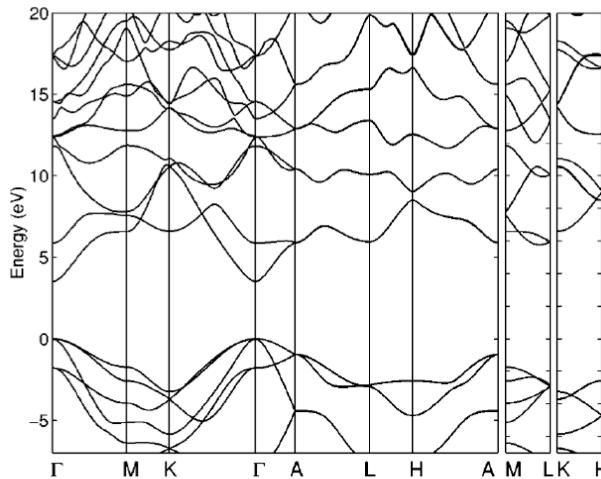
Figure 5. Resulting electronic structure of the wurtzite crystal in Figure 4 using an empirical pseudopotential method shows valence bands (below 0 eV) and conduction bands (above 3.4 eV) as eigenvalue solutions along the principal momentum directions from the irreducible BZ wedge. Goano's pseudopotentials reproduce all experimentally measured band gaps and effective masses (curvatures) within 1%–2% (Goano 2000).

include valence and conduction band energies, state populations, charge, current, applied field, and piezo strain. These pseudopotentials describe the electronic structures of the device. Each time a single variable changes, a new pseudopotential must be calculated in order to accurately model the device.

QuantumESPRESSO and nextnano were used in the modeling. QuantumESPRESSO, an open source computer code, provides electronic-structure calculations and materials modeling at the nanoscale. It has a large selection of material pseudopotentials to use

for modeling, including those used by Goano (2000), and can efficiently calculate the eigenvectors and scattering probabilities. Unfortunately, the program lacks a high-level interface that ties together all of the materials, interfaces, and applied fields in an iterative solver. Significant effort was expended to understand the interaction between the various pieces and setting up iterative solving given changing input conditions, which was especially taxing for simple visualizations.

But nextnano proved a useful tool for iteratively solving Schrödinger's equation in the presence of applied external fields, charge distributions following Boltzmann's equation, piezo-strain, and their resulting fields. nextnano produces a device electronic structure map as a visual diagram, and it became our go-to design tool for quickly adjusting parameters. We noted the lack of the surface vacuum emission physics of a single monolayer of cesium atoms that contribute a large dipole moment (more than any other known element), having a work function of just 0.45 eV (Spicer 1958). In this case we resorted to estimates of tunneling probability through the surface barrier (Mönch 1995, Wang 2012, Kibria 2014, Nishitani 2014). Consequently, though, the simulations are unfinished, and we are exploring vacuum state simulations. Our use of nextnano or QuantumESPRESSO will expand once we understand how to simulate the vacuum interface. Figure 6 (Nishitani 2014) illustrates the energetics of NEA surfaces. Siegmund (2003, 2006, 2008) explored NEA GaN photocathodes with cesium and showed promising results, although only for single photons (Figure 7). We believe this revealed
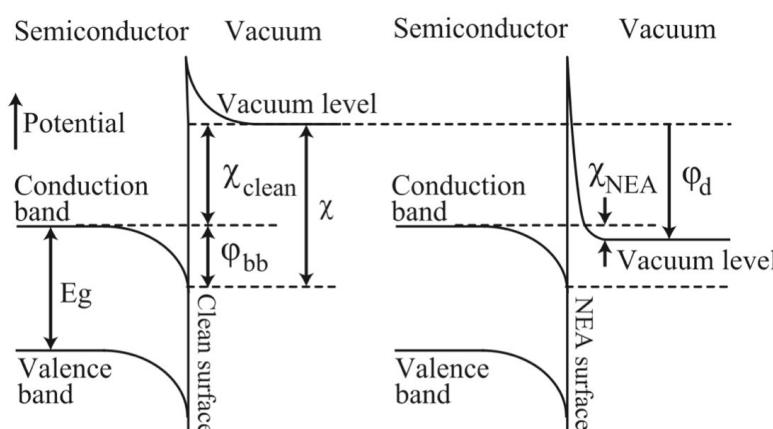
Figure 6. Energy diagram of uncesiated clean surface (left) and cesiated NEA surface (right). The clean surface may indeed emit electrons with sufficiently high field. The deposition of cesium provides a 0.45 eV work function that can actually lie below the conduction band energy level, and hence "negative" affinity, which freely emits into vacuum (Nishitani 2014).
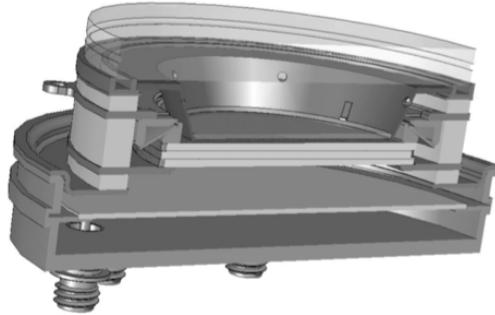
Figure 7. Actual MCP-type PMT with GaN cathode (Siegmund 2008)

the importance of transport saturation. Siegmund's photocathodes exhibited limited lifetime due to oxygen absorption and resulting collapse of the NEA chemistry. This is a fact with bialkali photocathodes as well, reiterating the need for high vacuum. We have much experience in this regard, and we are resolving these difficulties in our semiconductor-based design.

Photocathode Design

A photocathode with $In_{0.12}Ga_{0.88}N$ composition was selected for the prototype photocathode (Figure 8). This composition was selected for its UV/VIS sensitivity. The greater composition of indium lowers the band gap slightly and will make the device more sensitive to the near-UV spectrum, which is ideal for many of the high-energy scintillator applications we study. Good

bialkali (K,Cs) photocathodes have a 10%–20% QE, and we anticipate that this photocathode will perform at least as well and hopefully better than those.

The photocathode III-N crystal was grown on a 2″ sapphire wafer, for transparency wherein the photons illuminate the sensor. First, a thin AlN buffer layer is deposited on top of the sapphire that provides some lattice strain relaxation and establishes the energy level at the bottom ohmic contact. AlN has a much higher band gap than we require and will be transparent to our light. The photosensitive InGaN layer will promote valence electrons to the conduction band and, at the heterojunction interface, will form a 2DHG layer in the valence band. This will readily transport holes to the bottom contact and provide electron refreshment. The high conductivity of the 2DHG should also prevent
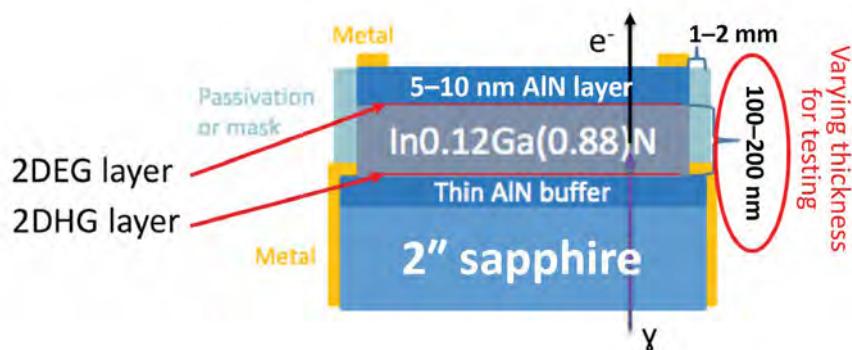
Figure 8. Photocathode design (inverted). Photons are absorbed within the InGaN layer, and resulting conduction photoelectrons are transported to the surface. The bottom metal contact provides the electrical current, while the top contact is isolated from the semiconductor and used to modulate the internal electric field to enhance transport. An applied external high-voltage anode (not shown) completes the circuit and should provide enhanced surface emission.

Figure 9. Nine unique wafers grown using the two parameters of InGaN absorption thicknesses (100, 150, 200 nm) and AlN surface caps (0, 5, 10 nm)

charge saturation without the use of a semitransparent metal contact across the optical face, as in bialkali PMTs. This feature should immediately double the net QE, pin the internal applied electric field, and improve transport. At the surface, a 5–10 nm AlN layer grown on top of the InGaN provides a 2DEG layer. This layer performs the same transport saturation and field control for conduction-band electrons. This is a very important performance aspect of photocathode devices that must provide continuous high current emission, and not just from a single photon "count." The thin top AlN layer will also protect the InGaN from oxidation that can interfere with the applied cesium monolayer coating. Not shown in Figure 8 is the photocathode being cesiated to produce NEA.

After the crystal structures were grown on the substrate (Figure 9), we partitioned them into several small device structures. The manufacturer, Kyma Technologies, expects that the inevitable crystal defects may limit the usefulness of larger area devices; therefore, we have divided the relatively large wafer into many smaller mesa devices with contacts (Figures 10 and 11). Metalizing the top (Figure 11) with a honeycomb-like pattern allows for ideal conductivity over a wide area and makes the metallic bond to the following mesh dynode structures.
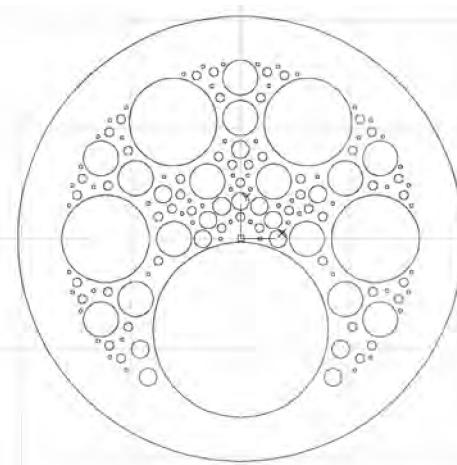
Figure 10. Distribution of large and small devices on the growth wafer. One 20 mm device and four 10 mm devices are hopeful candidates for detector development. Several smaller devices may be useful for experimental development and judging the yield statistics.

Dynode Design

While the design for the photocathode was being finalized, we worked with Dr. Jacob Leach from Kyma for the growth design for the dynode meshes we plan to make in FY 2017. The dynode mesh structure of this PMT is the innovative design that we extrapolated from the Hamamatsu wire mesh dynode concept. In our case, the dynodes will be made of transmissive AlGaN/AlN crystal intercepting all incoming electrons, but transporting to vacuum much in the way of the photocathode (Figure 12). These crystals have a band gap of
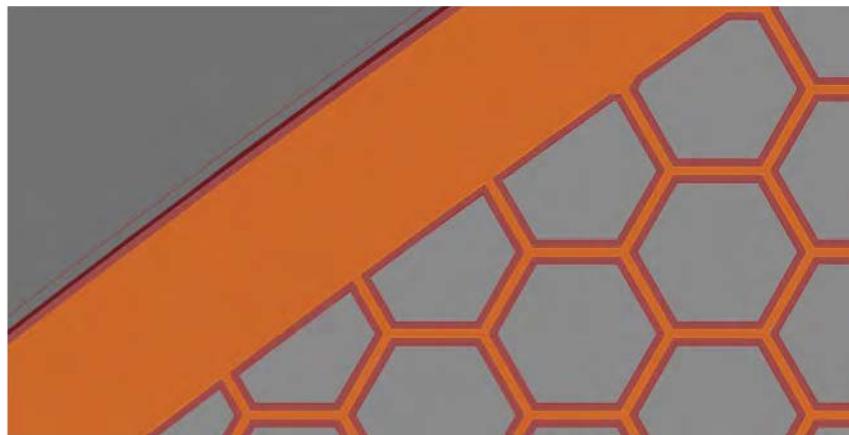
Figure 11. Magnified view of one device, illustrating the bottom and top edge metallization, passivation, and honeycomb "mesh" pattern over the active emission region
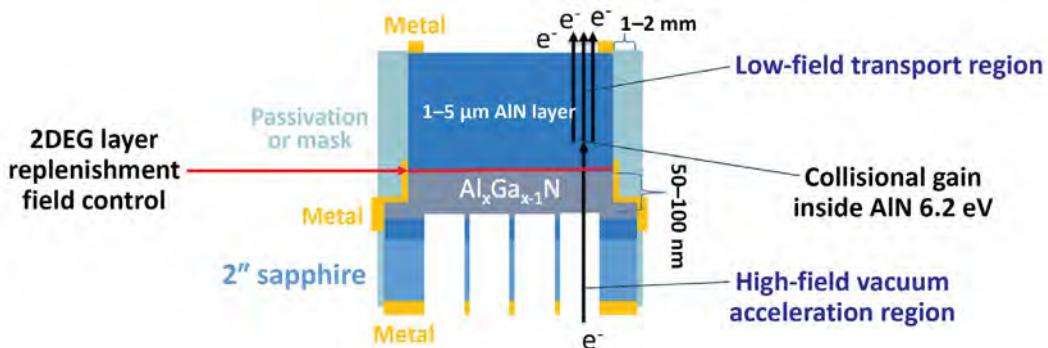
Figure 12. Proposed single mesh dynode (inverted). The dynode mesh structure of the device will have three distinct steps—acceleration, impact gain, and transport. A high-field region will exist in the free-space vacuum to create acceleration and allow for collisional gain. A low-field region within the AlGaN/AlN will transport generated carriers free of defects.

6.25 eV, which makes the material ideal for providing highly discrete secondary electron emissions. A 2-D electron gas layer will exist between the junction of the AlGaN and AlN to ensure the electrons in the AlN layer are quickly replaced as the collisions promote secondaries. The design will apply high-field acceleration to the free electron, providing the energy necessary for collisional secondary gain. Within the AlN the electrons are thermalized and transported in a relatively low-field region that should not promote any defect-generated carriers. To provide the free-space region, the substrate is etched in the same manner as the honeycomb pattern illustrated for the cathode, with an open-area ratio or fill factor of at least 90%. The thickness of the AlN structure mechanically allows

a free-standing thin crystal with an aspect ratio of about 1000:1 for a 1 μm thickness. The mesh substrate remains a stiff macroscopic support structure and voltage spacer. Each dynode can provide on the order of 40–50 gain and can be stacked as desired, with five dynodes equating to one 19-dynode Hamamatsu mesh PMT (Figure 3).

Conclusion

During Year 1 of this project we investigated high-field transport and negative electron affinity. After a thorough study of literature referencing gallium nitride photocathode development, preliminary prototype thicknesses were both hypothesized and modeled using the nextnano program. Once models confirmed

thicknesses were reasonable, we completed a photo-cathode design with a range of parameters to allow for experimental validation. Three prototypes with different InGaN thicknesses (100, 150, and 200 nm) were ordered to be fabricated during this year. The growth phase was completed in FY 2016, and the metallization of the wafers will be finished during the first quarter of FY 2017. Dr. Jacob Leach from Kyma was instrumental in finalizing the growth and device processing that met our design requirements. Continuing work in FY 2017 will include the metallization of the photocathode and testing of the devices. In parallel, the preliminary dynode design developed in FY 2016 will be modeled, finalized, and fabricated. Once the design for the dynode mesh structure is finalized, a technical abstract will be filed in preparation for a preliminary patent.

Acknowledgments

References

Bellotti, E., M. Moresco, F. Bertazzi, "Theory of high field transport and impact ionization in III-Nitride semiconductors," *Computational Electronics (IWCE)* 2010 (2010).

Bertazzi, F., M. Moresco, E. Bellotti, "Theory of high field carrier transport and impact ionization in wurtzite GaN. Part I: A full band Monte Carlo model," *J. Appl. Phys.* **106** (2009) 063718.

Birner, S., T. Zibold, T. Andlauer, T. Kubis, M. Sabathil, A. Trellakis, R. Vogl, "nextnano: General purpose 3-D simulations," *IEEE Trans. Elec. Dev.* **54**, 9 (2007) 2137–2142.

Engstrom, R. W., *Photomultiplier Handbook–Theory, Design, Application*, RCA Corporation, Lancaster, Pennsylvania, 1980, 160–176.

Ghillino, E., C. Garetto, M. Goano, G. Ghione, E. Bellotti, K. F. Brennan, "Simplex algorithm for band structure calculation of noncubic symmetry semiconductors: Application to III-nitride binaries and alloys," *Computational Electronics (IWCE)* 2000 (2000).

Giannozzi, P., et al., "Quantum ESPRESSO: A modular and open-source software project for quantum simulations of materials," *J. Phys. Condens. Matter* **21** (2009) 395502.

Goano, M., E. Bellotti, E. Ghillino, G. Ghione, K. F. Brennan, "Band structure nonlocal pseudopotential calculation of the III-nitride wurtzite phase materials system. Part I. Binary compounds GaN, AlN, and InN," *J. Appl. Phys.* **88**, 11 (2000) 6467–6475.

Kibria, M. G., S. Zhao, F. A. Chowdhury, Q. Wang, H. P. T. Nguyen, M. L. Trudeau, H. Guo, Z. Mi, "Tuning the surface Fermi level on p-type gallium nitride nanowires for efficient overall water splitting," *Nature Communications* **5** (April 30, 2014).

Li, S., *Semiconductor Physical Electronics*, 2nd edition, Springer, New York, 2006, 61–100.

Machuca, F., Z. Liu, Y. Sun, P. Pianetta, W. E. Spicer, R. F. W. Pease, "Oxygen species in Cs/O activated gallium nitride (GaN) negative electron affinity photocathodes," *J. Vac. Sci. Technol. B* **21**,4 (2003) 1863.

Magnuson, M., M. Mattesini, C. Höglund, J. Birch, L. Hultman, "The electronic structure of GaN and Ga investigated by soft x-ray spectroscopy and first-principles methods," *Phys. Rev. B* **81** (2010) 085125.

Martinez, A., U. Lindefelt, H.-E. Nilsson, "Investigation of quantum effects on the Bloch electron velocity around closely spaced bands at high electric fields," *J. Appl. Phys.* **93**, 12 (2003).

McClintock, R., E. Cicek, Z. Vashaei, C. Bayram, M. Razeghi, M. P. Ulmer, "III-Nitride based avalanche photo detectors," *Proc. SPIE* **7780** (2010) 77801B-1–77801B-13.

Mönch, W., *Semiconductor Surfaces and Interfaces*, Springer-Verlag, Berlin Heidelberg, 1995, 52–60.

Moresco, M., F. Bertazzi, E. Bellotti, "Theory of high field carrier transport and impact ionization in wurtzite GaN. Part II: Application to avalanche photodetectors," *J. Appl. Phys.* **106**, 6 (2009) 063719.

Morkoç, H., *Nitride Semiconductor Devices, Fundamentals and Applications*, Wiley-VCH Verlag Gmbh & Co., Weinheim 2013, 52.

Nemanich, R. J., M. C. Benjamin, S. P. Bozeman, M. D. Bremser, S. W. King, B. L. Ward, R. F. Davis, B. Chen, Z. Zhang, J. Bernholc, "(Negative) electron affinity of AlN and AlGaN alloys," *Proc. Materials Research Society Symposium* **395** (1996) 777–788.

Nilsson, H.-E., A. Martinez, E. Ghillino, U. Sannemo, E. Bellotti, M. Goano, "Numerical modeling of hole interband tunneling in wurtzite GaN and SiC," *J. Appl. Phys.* **90**, 6 (2001a) 2847.

Nilsson, H.-E., A. Martinez, U. Sannemo, "Numerical study of Bloch electron dynamics in wide band-gap semiconductors," *Appl. Surf. Sci.* **184** (2001b) 199.

Nishitani, T., M. Tabuchi, H. Amano, T. Maekawa, M. Kuwahara, T. Meguro, "Photoemission lifetime of a negative electron affinity gallium nitride photocathode," *J. Vac. Sci. Tech. B* **32**, 6 (2014) 06F901.

Pearton, S. J., M. O. Manasreh, eds., *Optoelectronic Properties of Semiconductors and Superlattices, Vol. 7, GaN and Related Materials II*, Gordon and Breach Science Publishers, Amsterdam, 2000.

Piprek, J., *Nitride Semiconductor Devices: Principles and Simulations*, Wiley-VCH Verlag GmbH & Co, Weinheim, 2007.

Siegmund, O. H. W., A. S. Tremsin, A. Martin, J. Malloy, M. Ulmer, B. Wessels, "GaN photocathodes for UV detection and imaging," *Proc. SPIE* **5164** (2003).

Siegmund, O., J. Vallerga, J. McPhate, J. Malloy, A. Tremsin, A. Martin, M. Ulmer, B. Wessels, "Development of GaN photocathodes for UV detectors," *Nucl. Instrum. Methods Phys. Res. A* **567** (2006) 110–113.

Siegmund, O. H. W., A. S. Tremsin, J. V. Vallerga, J. B. McPhate, J. S. Hull, J. Malloy, A. M. Dabiran, "Gallium nitride photocathode development for imaging detectors," *Proc. SPIE* **7021** (2008).

Spicer, W. E., "Photoemissive, photoconductive, and optical absorption studies of alkali-antimony compounds," *Phys. Rev.* **112**, 1 (October 1958) 114.

Wang, X.-H., "The optimal thickness of a transmission-mode GaN photocathode," *Chin. Phys. B* **21**, 8 (2012).

Ultra-Spectral Remote Imaging by Scanning Fabry–Pérot Etalons

STL-036-16 | Continuing in FY 2017 | Year 1 of 2

John Di Benedetto[1,a] and David P. Baldwin[a]

The first-year scope of work for this project was to develop a compact, rugged, sub-nanometer spectral-resolution spectrometer using Fabry–Pérot interferometers compatible with passive mobile, handheld, or airborne gas and solid chemical detection. Although several equipment obstacles were encountered during the first year, upgrades have been made to modernize the electronics of an existing interferometer-based spectrometer to allow its use in this project. The reassembly of this spectrometer and construction of a fixed-optic Fourier transform spectrometer in year two of this project will allow us to define and test critical design characteristics for portable, high-resolution spectrometers in a number of mission-relevant applications.

[1] dibeneja@nv.doe.gov, 805-681-2240
[a] Special Technologies Laboratory

Background

High-resolution spectroscopy is the key technique for passively detecting chemical species in several scenarios of importance to NSTec missions (e.g., gas-phase molecules in chemical releases, gas-phase chemicals emitted in thermal events, and solid materials exhibiting passive solar-induced fluorescence). In the presence of complex backgrounds and overwhelming background emission or scattering, these species require detection systems with sub-nanometer resolution to match the linewidths of the species of interest. Grating-based line scanners either lack the resolution or (if high resolution) lack the sensitivity at practical integration times to exploit high-resolution spectra of these target chemicals. Typically, the size of these grating-based systems increases with improved resolution. Thus, very high–resolution grating-based systems tend to be incompatible with portable, handheld, or unmanned aerial system (UAS) implementations.

To address this lack of technologies for portable, handheld, and UAS-based passive chemical detection methods, we are exploring the capabilities of interferometric spectrometers for high-resolution spectroscopy. The first year of this project focused on the assembly and testing of a Fabry–Pérot (FP) interferometer-based system for passive chemical detection. Three immediate applications are envisioned: small molecule gas detection (methane, SO_2, and others) by reflectance spectroscopy, imaging of gas and atomic emission spectra in high explosives testing programs, and detection of solids by fluorescence using Fraunhofer-line discriminators.

Project

Initial quoted prices for high-resolution, imaging FP devices exceeded the budget of this project. In order to test the FP concept without investing in an expensive device in the initial experimental phases, we examined available options for non-imaging FP etalons. Available options that can obtain the resolution required for the target applications envisioned for this project include bulk optics FPs (BOFPs) with limiting entrance aperture or fiber FP (FFP) tunable filters (TFs) where the cavity
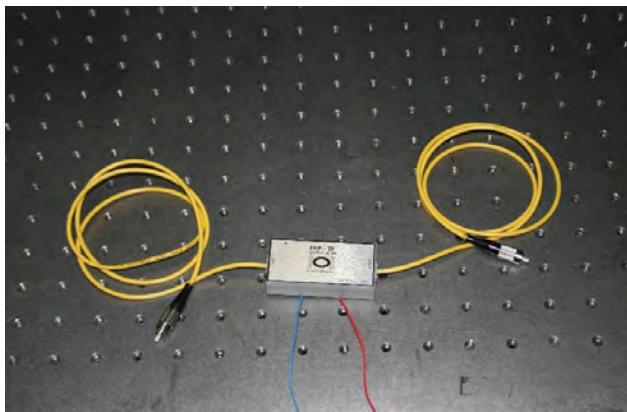
Figure 1. Custom wavelength Micron Optics, Inc., FFP-TF. This device was created for spectroscopic application with custom fiber and reflective coatings for the design wavelength range ~424 nm.

is limited to a single transmission mode by the use of single-mode fibers in the construction of the device. The BOFPs were once widely available, but one of the primary sources (Burleigh) has since gone out of business. Compared to FFP etalons, the BOFP devices are typically less expensive. However, due to dispersion of imperfectly collimated light within the cavity as well as difficulty in single-cavity mode introduction for non-laser sources, BOFP devices typically have lower finesse (poorer resolution) than FFPs.

Two projects were conducted at the Ames Laboratory in the mid-90s, funded by the DOE Office of Environmental Management. These projects resulted in the development of high-resolution compact spectrometers for (1) resolving isotopic emission lines of uranium isotopes in laser ablation-inductively

coupled plasma-atomic emission spectroscopy and (2) elemental emission lines of heavy metals in combustion stack analyses using reduced-pressure inductively coupled plasma-atomic emission spectroscopy (Baldwin 1996, 1997). Those projects used bulk optics–visible and UV FP etalons with order selection using acousto-optic tunable filters (AOTFs). They also used custom-assembled, visible-wavelength, FFP interferometers from Micron Optics, Inc. The FFP-TF that was custom built for the uranium isotope project is shown in Figure 1. It consists of two lengths of single-mode optical fiber, high reflectivity coatings on the faces of those optical fibers, a small piece of single-mode fiber bonded to one of those coated faces inside the cavity (to reduce loss in the cavity due to dispersion), and a concentric piezo attached to one of the fibers to scan the spacing of the cavity with an applied voltage ramp.

The free spectral range (FSR) of the FFP-TF cavity is approximately 1500 GHz, and the single-mode operating range of the device is from 395 to 430 nm. At higher wavelengths, the finesse is reduced by decreasing reflectivity of the coatings. At shorter wavelengths, the fiber is no longer single mode and additional mode structure adds extraneous features to the transmission spectrum.

In the middle of the first year of this project, we began to explore the use of existing FFP and BOFP devices to test the FP etalon spectrometer concept for the target applications at Ames Laboratory. The original spectrometer parts from 15 to 20 years ago were
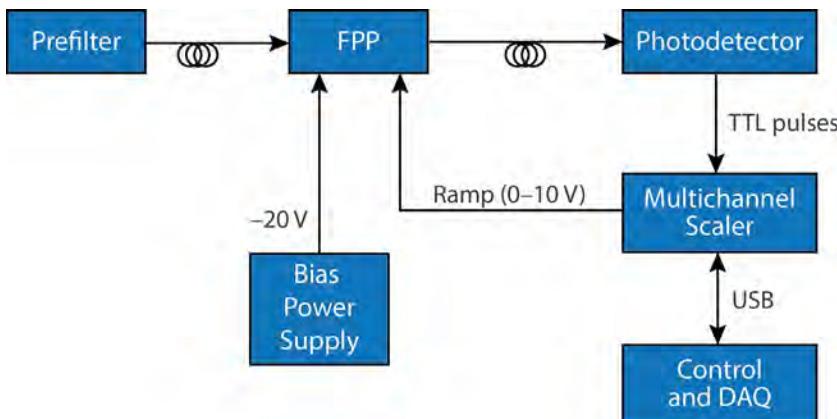
Figure 2. Block diagram of an FFP-based ultra-spectral spectrometer
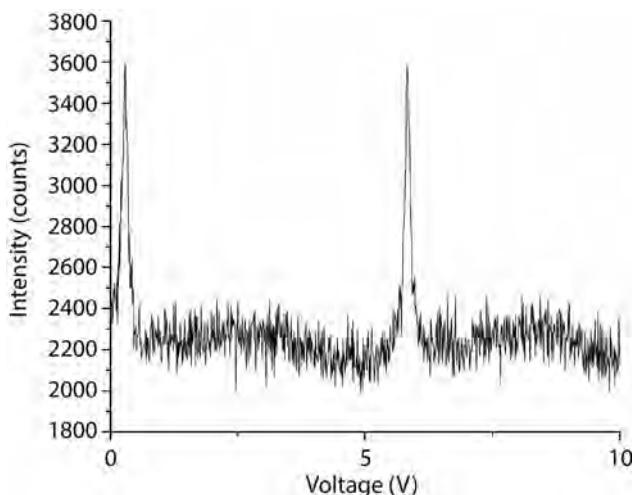
Figure 3. FFP spectrum of a mercury electrodeless discharge lamp collected with only a 490 nm low-pass filter as a prefilter. The strong features at <1 and ~6 V are multiple orders of the Hg 435.8 nm emission feature.

located at Ames, then later transferred to the NSTec Special Technologies Laboratory where reassembly of this spectrometer system continued.

The conceptual design of this spectrometer is shown in block diagram form in Figure 2. The original FFP and photodetector from the earlier work were reused. The multichannel scaler, used to scan the FFP with a voltage ramp and to synchronize the cavity spacing with event counting from the photodetector, had to

be replaced because the old system used a proprietary interface card that used an obsolete computer architecture. It was replaced with a USB interface ORTEC Easy-MCS multichannel scaler.

A spectrum of a mercury electrodeless discharge lamp accumulated using these components is shown in Figure 3. The peaks at around 1 and 6 volts are two consecutive orders of the same spectral feature at 435.8 nm of the mercury spectrum. For this experiment, the prefilter was simply a 490 nm short-pass colored-glass optical filter. Therefore, the "noisy" background includes weaker and poor-resolution argon and mercury emission features not rejected by this prefilter.

The original device assembled at Ames used an AOTF as a prefilter to allow selection of a range of wavelengths narrower than the FSR of the FFP. Experiments were attempted using an optical interference filter centered at 410 nm to select the Balmer delta line of hydrogen. The solar Fraunhofer region near this line is shown in Figure 4. While this prefilter was successful in selecting this very broad feature (compared to the FSR of the FFP) in emission from a hydrogen discharge tube, it became apparent that the interference filter's resolution of only 1.5 nm was a problem when we attempted to use this same configuration to replicate the reference solar spectrum in Figure 4.
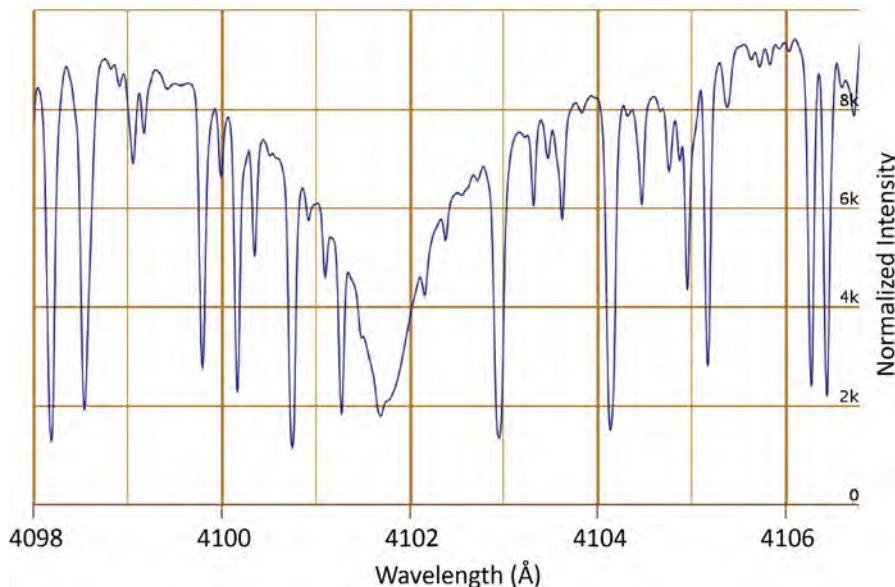
Figure 4. High-resolution solar reference spectrum around 410.1 nm showing both broad (hydrogen Balmer delta line) and narrow Fraunhofer spectral-absorption features

The prefilter bandwidth was so broad that it allowed several overlapping orders of solar radiation through to the FFP, preventing detection of the solar dark lines.

Interference filters with adequate resolution in this spectral region were not available. Thus, we have returned to service the AOTFs from the previous project. The 20-year-old RF drivers were built for use with Windows NT software that would not operate with modern laboratory computers. Thus, at the end of year one of the project, a new RF driver and software were obtained from Brimrose Corporation, the original AOTF vendor.

Conclusion

During the first year of this project, we obtained the FFP interferometer from Ames Laboratory, along with a blue-sensitive photon-counting photomultiplier tube. We have tested the scanning capability of the AOTF and the detector functionality. The electronics used in the AOTF-FFP spectrometer previously assembled at Ames have been replaced with a new USB-based multichannel scaler for voltage ramp control and event counting. A next step is to obtain and incorporate an appropriate prefilter; the previously used AOTF from Ames Laboratory is a likely candidate, which we will have to update with modern electronics for RF scanning and wavelength tuning. A new RF driver was purchased for this purpose near the end of year one.

Given the prior published performance and experience of the authors with the AOTF-FFP spectrometer that is being assembled, the spectrometer will likely meet or exceed the resolution requirements for the proposed applications. The reassembly of the spectrometer has entailed updating of several key electronic components and now seems likely to require the repair of the AOTF device. This project will permit the comparison of sensitivity and stability performance of the three major contending technologies for this set of high spectral resolution applications. The investigators already have an echelle-grating spectrometer with wavelength resolution of ~1:50,000. This AOTF-FFP system will provide an FP etalon-based system with wavelength resolution of ~1:75,000. The other candidate technology being addressed in year two of this project is spatial heterodyne spectroscopy, based on fixed-optic variations of a Michelson type interferometer. The design being considered (Cai 2016) has demonstrated spectral resolution exceeding 1:6,000, with potentially significant sensitivity advantages due to large entrance aperture, imaging capabilities, and the Fellgett or multiplex advantage. With these three systems available, relative performance measures for these technologies will be compared for the target applications.

Acknowledgments

References

Baldwin, D. P., D. S. Zamzow, A. P. D'Silva, "High-resolution spectroscopy using an acousto-optic tunable filter and a fiber-optic Fabry–Perot interferometer," *Appl. Spectrosc*. **50**, 4 (1996) 498–503.

Baldwin, D. P., D. S. Zamzow, "Limits of detection for an AOTF-FFP spectrometer in ICP atomic emission spectroscopy," *Talanta* **45**, 2 (1997) 229–235.

Cai, Q., B. Xiangli, Y. Fang, "Optical simulation of large aperture spatial heterodyne imaging spectrometer," *Opt. Commun.* **366** (2016) 136–141.

SILICON STRIP COSMIC MUON DETECTORS FOR HOMELAND SECURITY

RSLN-018-16 | Continuing in FY 2017 | Year 1 of 3

J. Andrew Green,[1,a] David D. Schwellenbach,[b] Ron Lipton,[c] Paul M. Rubinov,[c] Christinel V. Gingu,[c] Michael J. Utes,[c] William E. Cooper,[c] and Johnny B. Green[c]

Muon tomography and radiography are important detection technologies used to locate special nuclear materials in shielded containers for homeland security applications (Morris 2008). The current technology uses gas-filled drift tubes for position-sensitive particle detection and tracking. Drift-tube systems are prohibitively large in size and mass as well as having high development and maintenance costs. Due to the ambiguity of hit location and hit time, the tracking and calibration software needed for industrial-scale drift-tube systems is complex, labor-intensive, and costly. The purpose of this project is to build, test, and evaluate a muon tracking system based on silicon microstrip detectors similar to those used in the particle and nuclear physics communities for high-resolution tracking. For FY 2016 we have built a prototype detector string, and we have successfully read data from the first front-end chips. Next year we will build out the prototype toward completion of a 1 ft² demonstration tracker capable of collecting cosmic-ray data; we will also work toward development of additional applications.

[1] greenja@nv.doe.gov, 702-295-9803
[a] Remote Sensing Laboratory–Nellis; [b] New Mexico Operations–Los Alamos; [c] Fermilab

Background

High-energy protons and nuclei constantly bombard Earth's atmosphere from many different sources. Much of the sun's low-energy flux is captured by Earth's magnetic field, but higher-energy flux enters from outside the solar system. This flux of high-energy particles interacts with the upper atmosphere to create short-lived mesons that then decay into many different particles, but principally muons/antimuons, photons, and electrons/positrons. At sea level the muon flux, which dominates, is approximately 10,000/min/m² (Figure 1). The spectrum falls exponentially with energy (Grieder 2001).

Muons are similar to electrons but have about 200 times the mass (m_μ = 106 MeV). Unlike protons and neutrons, muons are subject only to weak and electromagnetic forces. The decay of a muon is described as

$\mu^+ \rightarrow e^+ + \upsilon_e + \bar{\upsilon}_\mu$, with a lifetime of τ = 2.2 μs at rest. The mean cosmic ray muon energy is about 4 GeV (Patrignani 2016), which means they have an effective lifetime of $\gamma\tau$ = (38) × (2.2 μs) = 83 μs. The properties of the muon make it a great candidate for passive imaging. At GeV and higher energies, the muon is highly penetrating through matter because of its high mass and low relative energy loss. A 4 GeV (relativistic) muon has a range of about 3 meters of iron or 18 meters of water (Groom 2001). Muon multiple scattering through matter depends on density and atomic number. Hence, tracking the muons above and below a scene allows us to see locations in space where most scattering occurs. The zenith-angle distribution of these particles is roughly $\cos^2(\theta)$, where θ is from the zenith (Grieder 2001, Patrignani 2016). This angular variation allows muons to more completely
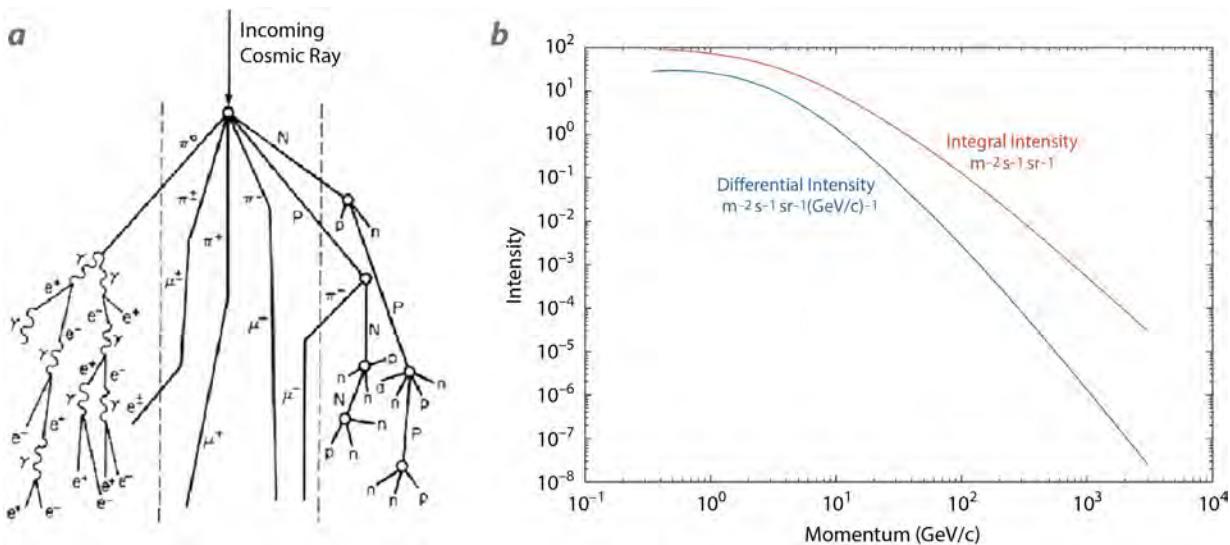
Figure 1. (a) A diagram illustrates how a high-energy cosmic hadron from outer space impacts Earth's atmosphere to create a flux of muons at sea level; (b) fitted differential and integral spectra of vertical muon data at sea level (data from Grieder 2001)

illuminate an object or scene, rather than from just one side. Furthermore, about 55% of the muons are positively charged (μ^+), and 45% are negatively charged (μ^-). The negatively charged muons can interact with atomic electron shells and nuclei, and they can create secondary coincident x-rays, gammas, and neutrons that may also be used for special nuclear material (SNM) detection (Nagamine 2007).

Multiple modes of tracking and detecting secondaries may be employed, and these were discussed in numerous prior works (Morris 2008, Schwellenbach 2013, Erlandson 2016). Regardless of the method to reconstruct via secondaries and/or multiple-scattering methods, an excellent tracking capability is required. The focus of this work is to develop a much more compact and efficient tracking technology for detecting charged-particle positions and trajectories when entering or exiting a scene of interest.

Though significant resources have been spent on drift-tube systems for cargo scanning, drift-tube detectors continue to present significant hardware, software, and physical stability/quality issues. While silicon detectors of the same scale will have a higher initial production cost, we expect that over time the long-term costs should decrease in some cases. High

channel density (factor of ~400 compared to drift tubes) allows silicon detectors to be used compactly for high solid–angle applications, such as muon or other high particle count production experiments for homeland security applications.

Additionally, silicon-based tracking opens up the field for the use of smaller, human-portable trackers. For demonstration purposes, one of our goals is also to construct a tabletop (or small rack-mount) system that may be used to demonstrate the capability.

Silicon sensors (Figure 2) are typically created from 0.5 mm thick silicon wafers that are several inches on a side (depending on crystal growth and fabrication technology), using lithography methods. They are fabricated so that the many separate aluminum microstrips on top are used to locate a charged particle passing through the silicon below. The detection medium for the charged particle is actually in the depletion layer (about 0.3 mm of bulk silicon), which is created by reverse-biasing the sensor (as one would reverse-bias a diode) with a nominal voltage of 200 V. This being a solid makes it an advantageous medium over gas-filled drift tubes due to the larger particle energy deposition (an order-of-magnitude higher than 2 inches of argon at one atmosphere) (Groom 2001). The hit location of
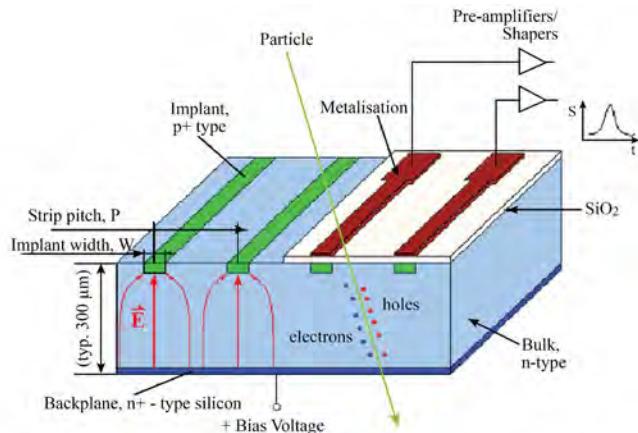
Figure 2. Cross section of a silicon strip detector (image from High Energy Physics Department of Firenze). The bias voltage is delivered at the bottom, and the electrodes are at the strip locations on top. Each silicon strip channel has a metallic pickup, giving an image-charge response to a minimum-ionizing particle in the bulk silicon. This yields position in one dimension via center-of-charge of channel numbers hit. Another sensor layer with orthogonal strips will yield the other needed hit coordinate. Multiple X–Y layers allow measurement of position and direction.

the particle is determined by taking a weighted-mean position of the hit, where the weights come from the pedestal-subtracted analog-to-digital converter (ADC) readout of each microstrip by a front-end chip called an ASIC (application-specific integrated circuit). ASICs are critical components in the design of high-density detection systems, because their properties must be tuned to the problem at hand. For instance, the detector capacitance that the ASIC "expects" must be part of the design. Also, the expected event rate and whether self-triggering and other logic will be required both affect how the chip is designed.

Project

Conceptual Design

We are designing a small-scale system of nominal tracking area, ~1 ft², with an emphasis on developing lower-cost scaling and maintaining the desirable aspects of silicon-strip detectors: high spatial resolution, ease of use, and compactness. We are investigating performance, feasibility, tracking capabilities, applications, cost-scaling, and reliability. To do this, we have teamed

with detector experts in the Particle Physics Division at Fermilab. This project seeks to develop variations that will reduce cost/area for cosmic muon tracking as opposed to the expense related to high-rate/radiation beam experiments on which they are typically used.

In FY 2016 we have begun building a new type of muon tomography detector based on silicon micro-strip technology. Our sensors, which are 122 µm pitch (Figure 2), work by immediate charge response (<1 ns); therefore, they do not depend on timing resolution or drift calibration to obtain good position-resolution tracking (as is the case for drift tubes). The small pitch is needed to ensure that sufficient spatial resolution for the muon track is available, to allow the silicon layers to be a few cm apart vertically to achieve the same or higher solid-angle acceptance as drift-tube detectors. Hence, detector thickness goes from about 2 feet (for the case of drift tubes) to about 4 inches (for the case of silicon microstrips). The 1 ft² detector will be composed of multiple 3 × 3 arrays of 10 cm square silicon microstrip sensors arranged for 3-D tracking. The sensors we are using were originally fabricated for the Compact Muon Solenoid (CMS, Figure 3) detector at the Large Hadron Collider (LHC) at CERN. There are sufficient quantities of these sensors in dry storage to complete this project. The tracking detector conceptual design will be composed of multiple X–Y layers of silicon strips to compute the cosmic-ray trajectories. To reduce risk, smaller sub-units are being prototyped to better understand how multiple detectors are wire-bonded to each other and to the ASICs, to produce the data acquisition readout, and to check performance and noise pedestals.

The Fermilab team has selected a path forward to complete the first detector string, which is based on an ASIC called the SKIROC (Silikon pin Kalorimeter Integrated ReadOut Chip) and shown in Callier (2011). This component was originally developed for current and future high-energy physics experiments. The SKIROC is a 64-channel front-end interface that amplifies and digitizes the microstrip signals. A given chip has 64 such channels, each reading out one microstrip. To provide greater dynamic range, high-gain and

CMS
A Compact Solenoidal Detector for LHC

Total Weight : 12,000 t
Overall diameter : 14.00 m
Overall length : 20.00 m
Magnetic field : 4 Tesla
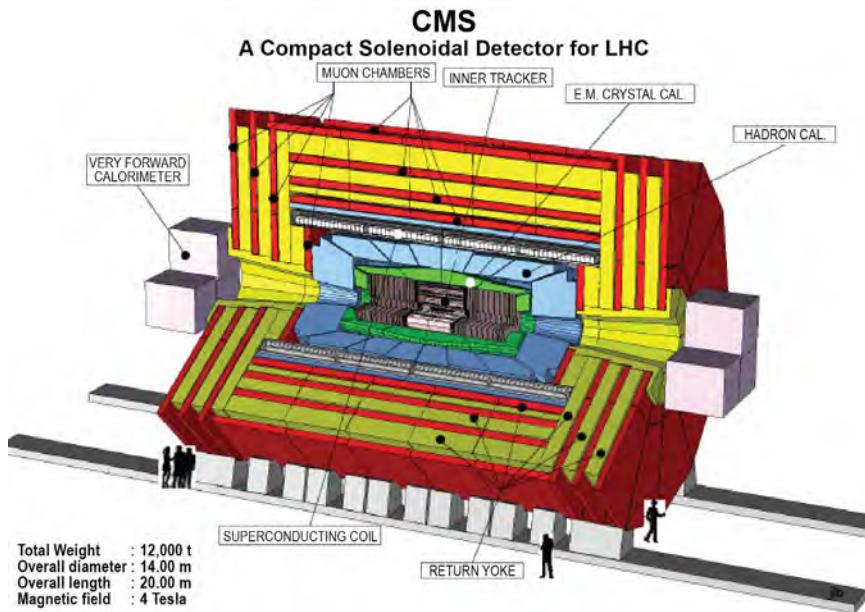
Figure 3. The sensors for this project were originally developed for the Compact Muon Solenoid (CMS) collider-detector at CERN (Krammer 2011), partly funded by the DOE Office of Science. Many tens of square meters of silicon sensors have been built to instrument the CMS central tracking system. This SDRD project leverages the same expertise and test equipment.

low-gain analog-to-digital conversion is provided. Internal or external triggering (triggers cause an event to be digitized and stored) is possible. Each chip is about 1 cm in size. We use the terms ASIC and SKIROC interchangeably. ASIC is the generic term for a dense integrated circuit used to process many channels of input to then produce digital output to a downstream interface. An ASIC's design is typically customized to a given need, footprint, and channel density. The SKIROC was designed for the CMS and International Linear Collider (ILC) programs to read out a fine-grained silicon-based calorimeter (Omega 2016).

The sensors for this project were designed, mounted, assembled, and tested at Fermilab. Sensor data are read by a hybrid of custom and off-the-shelf data acquisition architecture called Zedboard, a Xilinx-based field-programmable gate array (FPGA) board running Linux.

The minimum unit of this tracking system is called a detector string. Each string will consist of one to five daisy-chained microstrip sensors (10 to 50 cm in length) with sufficient ASICs on the end to read out the microstrips (Figure 4). Data will be taken for each of the configurations to study optimum daisy-chain length. Three in a daisy-chain and three strings side-by-side populate the 1 ft^2 tracker. Two such orthogonal
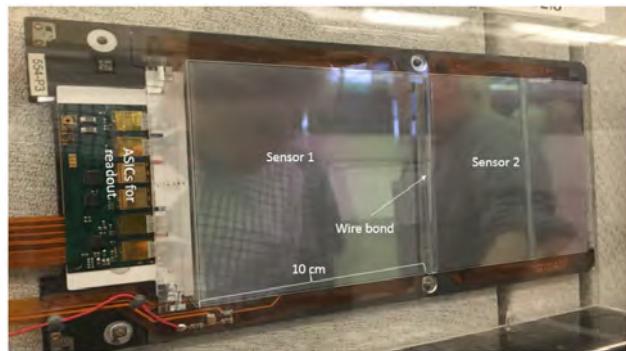
Figure 4. A display example with readout chips on the left with two sensors wire-bonded in series. Current experience suggests that up to five sensors may be put in series, depending on capacitance and noise characteristics.

detectors, a tile, fix one cosmic muon track point. With an external trigger, two track points are the minimum needed (three or more are needed for robust tracking to mitigate the effects of possible noise). In the future, many such tiles might compose a large area tracking panel. A muon tomography detector will consist of at least two top and two bottom panels, with sufficient space between the major sections for an object to be scanned.

The current silicon-strip sensors in use in high-energy physics (HEP) and associated ASICs were designed to function in high particle occupancy, event rate, and radiation damage environments. Being exposed to

high radiation, typical sensors need to be cooled to low ambient temperatures, such as −10°C. While our type of sensor does need a relatively high channel density and robustness, it will not operate in such a challenging environment. To reduce cost/area, we will pursue efficiencies that optimize our detectors for operation with cosmic-ray rates/occupancies and for room-temperature operation.

Electronics and Readout

Basic Architecture

The overall architecture to build the 1 ft² detector is as follows: A scintillator "paddle" will be used to trigger the tracker externally, at least for now. Self-triggering is certainly possible, but scintillator triggering is very simple and good for prototyping. A 3 × 3 array of 10 cm square sensors will measure one of the X or Y components of the particle tracks. Two orthogonal arrays will give one X–Y hit coordinate. The X–Y sensors will be mounted on carbon-fiber boards, which have a favorable coefficient of expansion and low mass. Each of the 3 × 3 arrays is composed of three columns of three sensors wire-bonded in series. Each column is read out by six SKIROC chips mounted on a carrier board (Figure 7 and the description below). A similar pair of X–Y sensor planes will be placed about 2 cm below the first plane-pair. If we did not have the trigger paddle, a third X–Y plane would be needed to filter out tracks

that do not fit to a line. These will create a tracking module. Another tracking module for the region below the object being scanned will be assembled. Each module will be housed in off-the-shelf electronics cases. All equipment will likely be mounted on a 19-inch rack.

Adaption of Previously Designed Electronics

This project will adapt previously developed technology to build our tracker. The silicon microstrip sensors, "CMS ST" sensors, have been in dry storage for over 10 years. Recent testing (Figure 5) has shown them to be in good condition for this project. The SKIROC ASIC chip for front-end readout of the microstrips was originally designed not for tracking, but for silicon-based calorimetry for the ILC program. However, the properties of the SKIROC are expected to be sufficient for readout of our microstrips. A Xilinx FMCIO (FPGA Mezzanine Card IO) board, interfaced to a University of Minnesota readout board, will be used initially to read out and collate the data, then push the data to an off-the-shelf Zedboard. This readout architecture was largely developed for test-beam setups that are used to develop detectors for the CMS upgrade program.

Because the SKIROC was not originally developed for reading out our microstrips, the pitch between the two is such that we will only read out every other microstrip. This will end up giving us effectively a
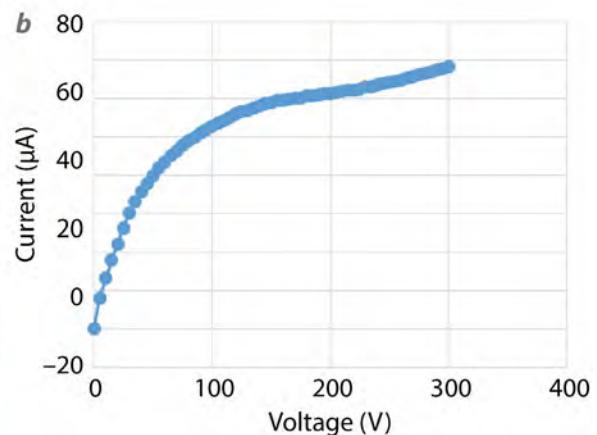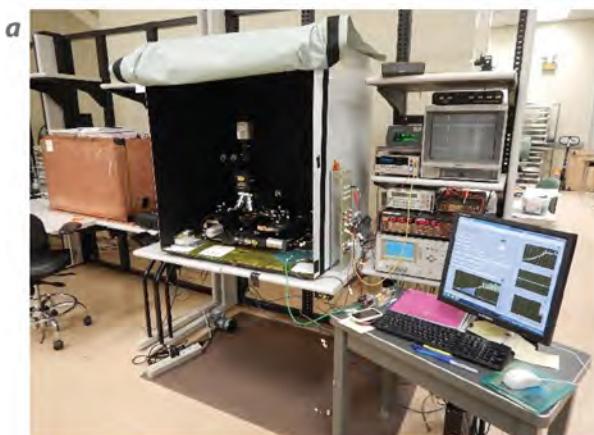
Figure 5. (a) Test-stand at Fermilab SiDet facility used to evaluate our sensors for current and capacitance vs. applied bias voltage. Each sensor has its own current-voltage curve plotted so that the operating bias voltage and sensor health may be determined. The typical value for bias voltage is 180–220 V. Sensors that do not have a normal plateau curve are rejected. (b) An example of a normal plateau curve.
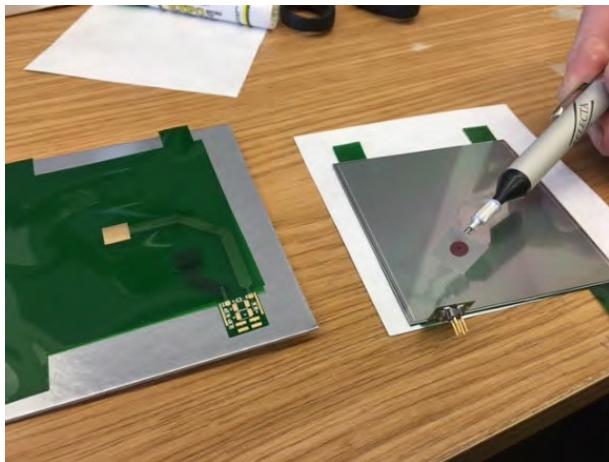
Figure 6. On the left is a flex/filter board (unpopulated), one of the boards designed for this SDRD. At right is a flex/filter board mounted to a sensor.

244 µm pitch instead of the more ideal 122 µm. The resulting tracking angular resolution is conservatively 5 milliradians, which is sufficient for proof-of-concept, as typical high-Z material scattering is in tens of milliradians. This is just one of the number of adaptations required to make forward progress. However, typical hit resolution with charge sharing is likely to be below 100 µm (competitive with the best drift tubes). While several ASICs were considered for our project, the SKIROC was the best combination of price and capability. The alternative would have been to purchase chips that are ~10 times the cost of the SKIROC, or worse, to design and fabricate our own ASIC, which is outside the scope of this SDRD.

Components and Software Development

Several components need to be adapted and modified to meet the requirements of this project. Our re-engineering of the components carefully considered proper electrical and mechanical interfaces needed for high-resolution tracking.

Flex Board

This board, pictured in Figure 6, provides filtered ground and high voltage (HV) to the sensor. It is a flexible Kapton-based board that has an HV pad on the sensor side and a ground pad on the support side. The grounding will be of the "star-pattern" ground always needed for low-noise electronics.

Figure 7. Sensor mounted to readout board for further testing. On the left is the silicon sensor. The microstrips run from left to right, and the sensor is nominally 10 cm on a side. The strips are wire-bonded to the readout board using an automated wire-bonding machine. The photo also shows only one SKIROC chip (the ASIC) mounted for this test. Six will be used on a fully populated board.

Carrier Board

Pictured in Figure 7 (right side), this board is where the ASICs are mounted, and to which the sensors are wire-bonded. Six ASICs are required to read out the microstrips for one 10 cm sensor (or series-string of sensors).

Firmware

FPGA firmware code has been developed to allow a set of SKIROC chips to be read out. We have produced our first data files and analyzed them for pedestal behavior. The full prototype readout string is shown in Figure 8. Analysis codes have been written in ROOT and Matlab to process the data. This effort will continue to fully collate data from the detectors and to fit tracks and to show event displays.

Conclusion

We are building a tabletop silicon microstrip muon-tracking system. We are adapting high-energy physics detectors previously developed at Fermilab. This experience will lead to larger-scale cosmic muon tracking and associated applications. We have built a prototype detector string, and we have successfully read data from the first SKIROC chips. Progress toward performance tests of the prototype system to include laser and diode tests has been made. In FY 2017 we
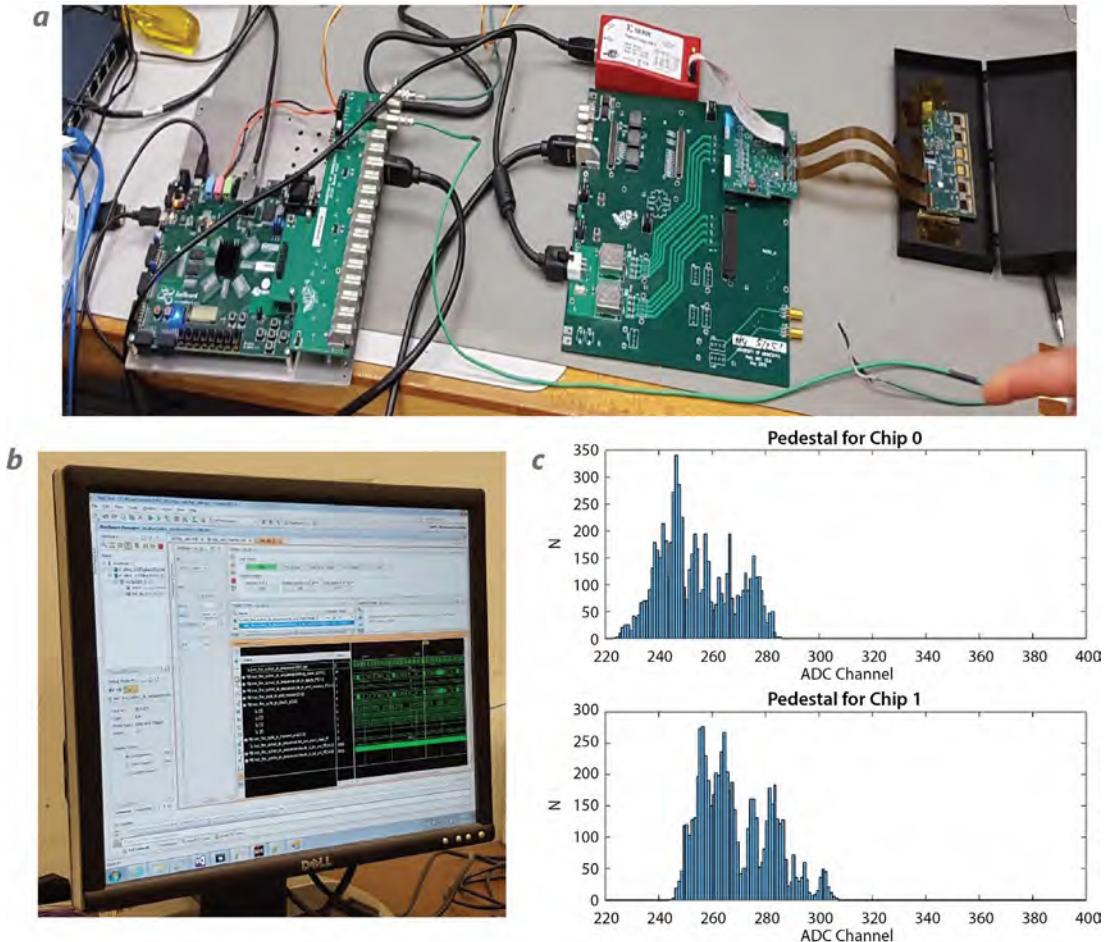
Figure 8. (a) Prototype readout setup used to do firmware and data-acquisition development. The board to the far left is the Zedboard (off-the-shelf); the board in the middle is an interface board developed at the University of Minnesota for test-beam experiments for CMS. The mezzanine board on top of it is the FMCIO board. Our sensor interface board, with four SKIROC chips (of six possible) mounted, is on the far right. (b) VIVADO firmware interface used to program the Xilinx FPGAs for readout. We have completed the initial firmware needed to read out a fully populated carrier board of ASIC chips. (c) Our first plots of uncorrected pedestals from two of the chips.

plan to complete a 1 ft^2 demonstration tracker and attempt to collect cosmic-ray data; we will also work toward development of additional applications.

Acknowledgments

We would like to thank Wendi Dreesen and Derek Aberle for their initial contributions to this work and for their contributions to the muon team over the years.

References

Callier, S., F. Dulucq, C. de La Taille, G. Martin-Chassard, N. Seguin-Moreau, "SKIROC2, front end chip designed to readout the Electromagnetic CALorimeter at the ILC," Topical Workshop on Electronics for Particle Physics, 2011, Vienna, Austria, http://iopscience.iop.org/article/10.1088/1748-0221/6/12/C12040/meta, accessed November 10, 2016.

Erlandson, A., S. Livingstone, V. Anghel, C. Jewett, O. Kamaev, M. Thompson, "Cosmic ray inspection and passive tomography: Recent results from Canada's unique Muon Scattering Tomography system," Poster 2B-7, SORMA West, University of California, Berkeley, May 22–26, 2016.

Grieder, P. K. F., *Cosmic Rays at Earth: Researcher's Reference Manual and Databook*, Elsevier Science Press, Amsterdam, The Netherlands, 2001, 363–364.

Groom, D. E., N. V. Mokhov, S. I. Striganov, "Muon stopping power and range tables 10 MeV–100 TeV," *Atomic Data and Nuclear Data Tables* **78**, 2 (2001) 183–356.

High Energy Physics Department of Firenze, "Silicon Detector.gif," http://hep.fi.infn.it/CMS/sensors/Silicon_Detector.gif, accessed December 5, 2016.

Krammer, M., "Silicon detectors," Institute of High Energy Physics, Vienna, Austria, 2011, http://www.hephy.at/fileadmin/user_upload/Lehre/Unterlagen/Praktikum/Halbleiterdetektoren.pdf, accessed November 10, 2016.

Morris, C. L., et al., "Tomographic imaging with cosmic ray muons," *Science and Global Security* **16** (2008) 37–53.

Nagamine, K., *Introductory Muon Science*, Cambridge University Press, New York, 2007, 40–68.

Omega Corporation, "SKIROC front-end chip," 2016, http://omega.in2p3.fr/index.php/products/skiroc.html, accessed November 10, 2016.

Patrignani, C., et al. (Particle Data Group), "Review of particle physics," *Chin. Phys. C*, **40** (2016) 100001.

Schwellenbach, D., et al., "Passive imaging of warhead-like configurations with cosmic-ray muon tracking scanners," in *Site-Directed Research and Development*, FY 2012, National Security Technologies, LLC, Las Vegas, Nevada, 2013, 129–134.

Pedestrian Mapping with Spectral Backpacks for GPS-Denied Areas

RSLA-010-16 | Year 1 of 1

Michael Hornish[1,a] and Ron Wolff [a]

This project investigated methods to modernize radiological/nuclear search operations in GPS-denied environments. Having a reliable way to track a searcher's position relative to the GPS-denied frame of reference (building, vessel, tunnel) is critical for characterizing the radiation fields. It would also enable more effective, higher-sensitivity searches when weak or heavily shielded source configurations are involved. In addition to position tracking, we have also explored technologies for producing interpolation maps of gamma spectral data originating from radiological search (pedestrian) backpacks, which is a capability gap for building, maritime, and other GPS-denied venues.

[1] hornismj@nv.doe.gov, 301-817-3347
[a] Remote Sensing Laboratory–Andrews

Background

Pedestrian mapping in GPS-denied areas is an important radiological search technique for DOE/NNSA emergency response teams such as the Nuclear Radiological Advisory Team (NRAT) and the Radiological Assistance Program (RAP) that include Remote Sensing Laboratory (RSL) personnel. Pedestrian mapping can be used for performing venue sweep operations, facility background surveys, and for conducting challenging search operations involving weak or shielded sources or complex radiation fields where source localization is difficult. While incorporating legacy systems that have proven very effective over the years, this project's primary goal was to develop an enhanced and up-to-date capability that exploits gamma spectral data and is safer and more efficient due to advanced tracking technologies. If successful, this project may not only result in increased use for existing NRAT and RAP search missions, but also may enable expansion into other DOE applications or missions.

When the original pedestrian mapper capability (Mattson 2005) was developed more than a decade ago, dead-reckoning and other position tracking technologies were too unreliable, too expensive, too bulky, or otherwise too impractical to be widely used to accurately track a searcher's location in GPS-denied environments such as buildings, parking garages, or GPS-irrelevant environments such as moving platforms and maritime vessels. The "no-tech" capability RSL pursued at the time relied on a trained user's input—individuals used a touch screen laptop and a stylus to denote their location on an electronic blueprint or floor plan of the area being searched. Lines were walked, thereby creating a grid pattern in the search area, and an interpolation method took advantage of nearest-neighbor data points to create maps of gross count backpack data (gamma rays and neutrons) that could be analyzed for weak or strong radiation fields that may warrant follow-on assessment with low- or high-resolution spectral detection equipment. Figures 1 and 2 show example pedestrian maps created with the legacy pedestrian mapper application.
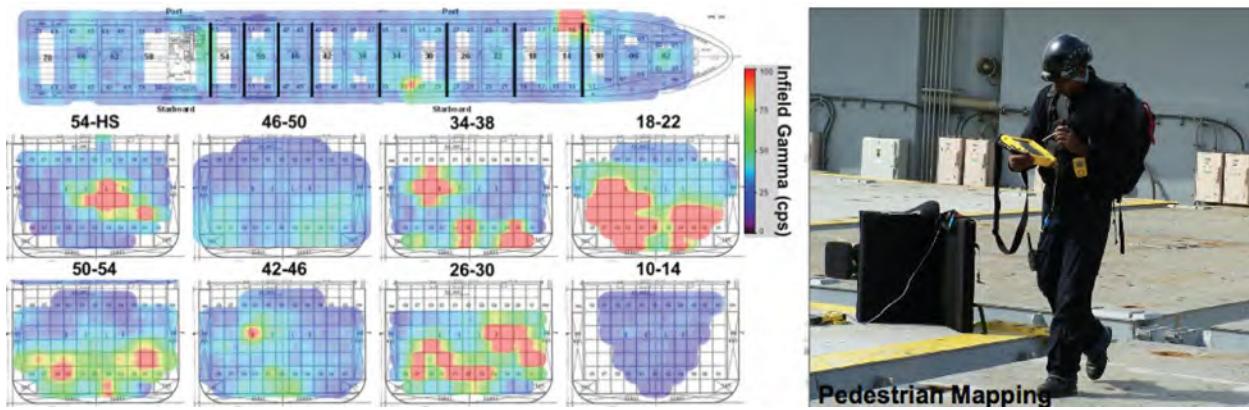
Figure 1. Sample pedestrian mapper results for maritime search using the RSL legacy system
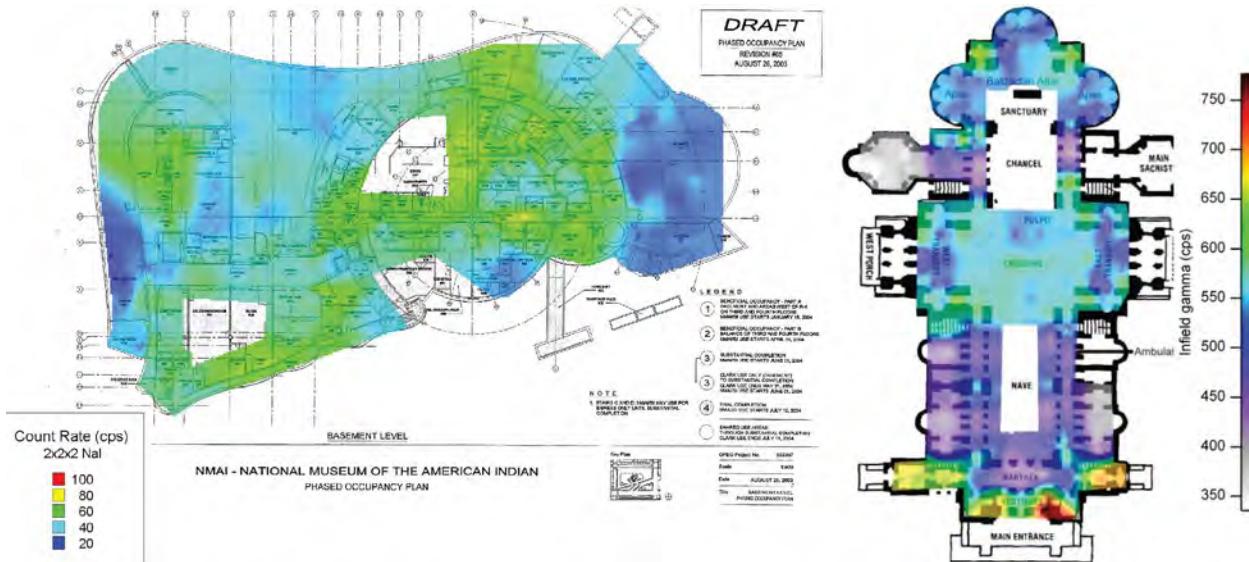
Figure 2. Sample pedestrian mapper results for building searches using the RSL legacy system

While this approach remains useful and is being effectively used by RAP and NRAT, it does have limitations: (1) it relies heavily on user input, (2) the users must be well trained or inherently effective at reading maps or floor plans to accurately denote their location, (3) it works best if electronic copies of floor plans or blueprints are available—and that is not always a given, and (4) it requires the user to frequently look down at his/her tablet interface to interact with the touch screen, which can both increase the time required to conduct a pedestrian mapping operation and can potentially lead to some safety risks involving slip, trip, or fall hazards. Moreover, this legacy system was based solely on gross count gamma ray and neutron information originating from the RSL-designed Infield backpack system, which is in the final stages of being phased out in favor of the new Spectral Infield Search System, commonly referred to as the Gemini. The Gemini uses the same detector systems, namely thallium-doped sodium iodide logs for gamma ray detection and pressurized ^{3}He arrays for neutron detection, as well as modern electronics that capture 1 Hz 1024-channel gamma ray spectra. The legacy pedestrian mapper application is not currently configured to accept the more complex data stream from the Gemini, thereby necessitating an upgrade to the capability.
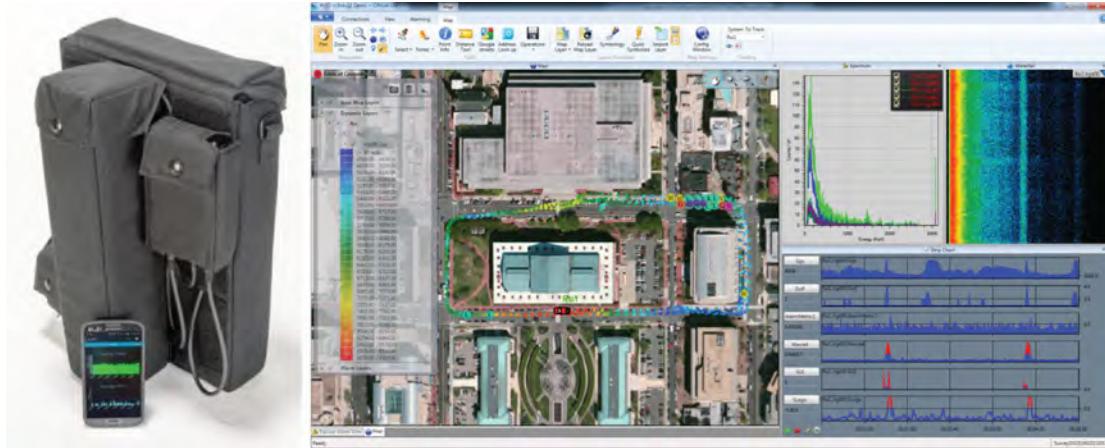
Figure 3. The Gemini backpack system and an AVID system screenshot

Project

This project seeks to enhance an updated pedestrian mapper software application that is compatible with the Gemini backpack system (Figure 3) while also allowing additional options for location tracking beyond the "no-tech" manual location marking approach on a touch screen interface. The two main project activities, updating the mapping application and investigating position tracking technologies that may replace or augment traditional pedestrian mapping techniques, are summarized below.

Pedestrian Mapper Development in AVID

The upgrade of the pedestrian mapper application is most readily accomplished by leveraging the RSL-designed Advanced Visualization and Integration of Data (AVID) user interface (Figure 3). AVID is an operational platform used by DOE emergency response assets for data acquisition and data analysis and has been in use for the last four or five years. In AVID, data can be acquired from multiple detector system types, including the Gemini backpack systems. Acquired data can be analyzed in real time or post-processing fashion with the use of sophisticated spectral anomaly detection algorithms, such as nuisance-rejection spectral comparison ratio anomaly detection (NSCRAD) (Pfund 2007), and isotope identification routines, such as Gamma Detector Response Analysis Software (GADRAS) (Mitchell 2014).

Complementary to this project, and with additional support from the NA-84 Office of Nuclear Incident Response Technology Integration (TI) program that sponsors AVID development overall, modifications to the AVID software platform were conducted to enable the collection of pedestrian mapper data in the traditional, or legacy, fashion from the Gemini data stream. This work involved adding a non-GPS–type tracking system based on image pixels taken from electronic copies of floor plans, blueprints, building/vessel arrangement plans or photographs, and recording of location in that virtual environment. Interpolation schemes inherent to the AVID framework could then be modified to account for non-GPS coordinates and scaled accordingly. Because the data collected in AVID from a Gemini system contain second-by-second gamma ray spectra, it now becomes possible to use interpolation schemes that are much more sophisticated than basic gross count–based methodologies. We pursued this capability not only because spectral triggers like NSCRAD are much more sensitive and are either already or will be soon implemented in most search equipment (in addition to AVID), but also because it will allow search teams to conduct advanced search operations with increased sensitivity at a significantly lower threshold for detection. An example of an interpolation "heat" map collected aboard a maritime vessel with this AVID pedestrian mapper application is shown in Figure 4.
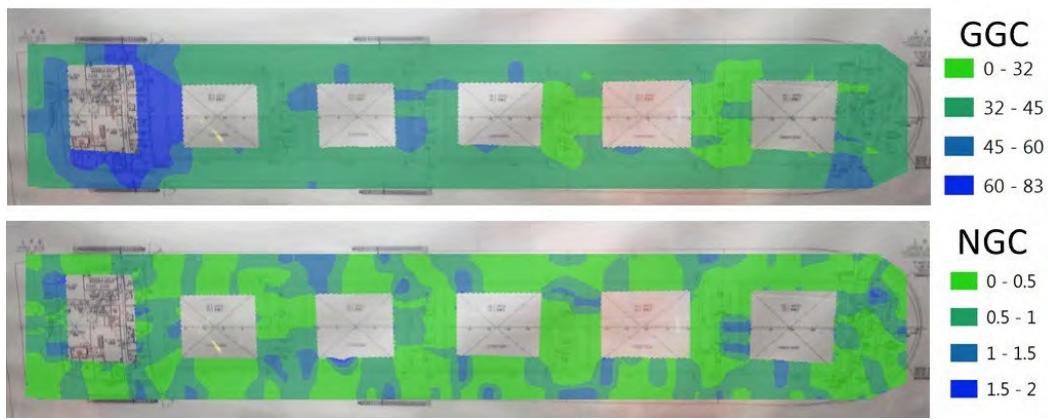
Figure 4. Sample pedestrian mapper result from AVID used with a Gemini backpack system. GGC/NGC = Gamma/neutron gross count rate in counts per second.

Technological Solutions for Position Tracking

This project takes advantage of advances in position tracking technologies that require significantly less user interaction and increased pedestrian mapping search efficiency. In this project, one class of devices that relies on non-image–based methods was studied for position tracking as an alternative to the "no-tech" touch screen interface now used. These solutions typically rely on inertial measurement units (IMUs) to augment an intermittent GPS position (outdoors but in a cluttered environment like a city with large buildings). For this project we acquired two systems to investigate, Robotic Research's MOLE boot tracker and the NEON Personnel Tracker by TRX Systems.

Both systems offer a lower profile or concealable form factors, which can be very important for some search missions. It is also true that given both of these systems' reliance on intermittent GPS coordinates as a signal to exploit, additional work would be required to make them compatible with the more complex searches that occur on moving platforms such as ships.

With a battery life in excess of 16 hours and a weight of 12.5 ounces, the MOLE sensor (Figure 5) contains an IMU that provides 6 degrees-of-freedom positioning while walking forwards, backwards, sidestepping, and during vertical movement. Its internal GPS unit provides updates if GPS is available. An internal ranging
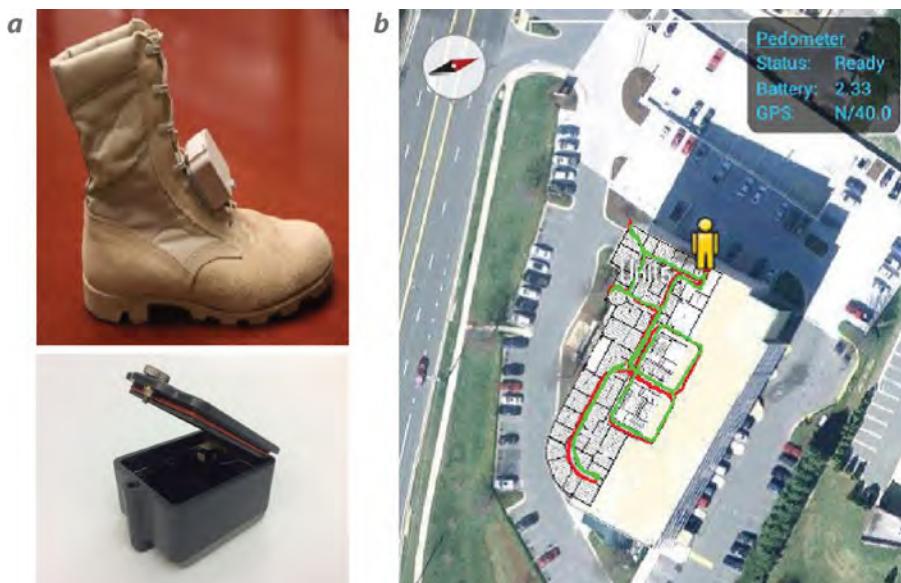
Figure 5. (a) Robotic Research MOLE sensor and the (b) ATAK interface showing position track reconstruction from two devices used jointly on two searchers
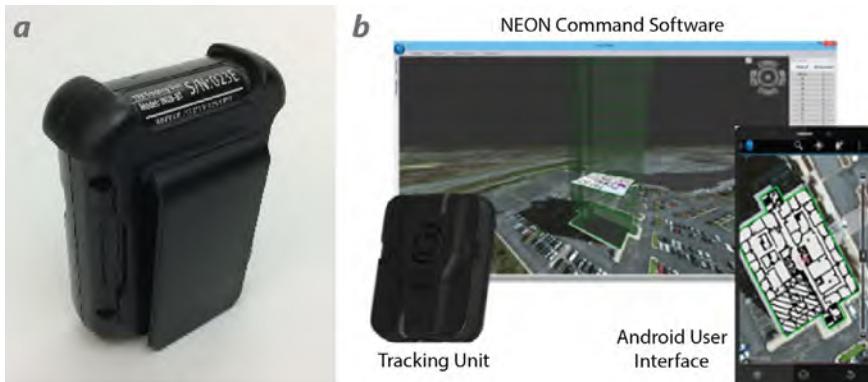
Figure 6. (a) The belt-worn TRX NEON Personnel Tracker system and (b) a depiction of the (PC) command software and Android User Interface

sensor provides automatic corrections between multiple MOLE devices (as well as anchor nodes, if deployed). Distributed algorithms provide very good accuracy for a team of users (position errors of <1% distance traveled in the x–y plane). There is an open interface that allows integration with outside systems and displays, which has already been demonstrated through integration into the Android Tactical Assault Kit (ATAK) system being employed by several partner organizations.

The NEON Personnel Tracker (Figure 6) exploits a number of technologies—sensor fusion, WiFi, Bluetooth, and GPS—to provide personnel location and tracking information. The currently available system has an API for third-party application integration, including with Android user interfaces whose data can be shared with other applications. The system is capable of detecting and mapping building features to enable tracking of assets in GPS-denied areas. The tracking units can be worn by individuals (e.g., on their belts), and their position accuracy can be augmented by fixed nodes as well.

Because both systems are Android-ready, they can be easily integrated into DOE search applications where ATAK is the primary means of tracking locations of mission partner team members in the field.

Several units of the MOLE and NEON sensors were acquired for evaluation. In order to perform direct comparisons of these two sensors and also compare them to data collected in the legacy "no-tech" pedestrian mapper technique, we had to develop additional software. We developed a logging software we named "Pedroid" that could operate in the Android platform, allow for connection via Bluetooth to both MOLE and NEON systems, and independently log each system's GPS-corrected position tracking data for post-processing comparison. At the same time, legacy pedestrian mapper data for position tracking had to be converted to GPS coordinates for side-by-side comparison and analysis, and this was accomplished by using a Python-based tool to create KML files from pedestrian mapper datasets. These software tools are shown in Figure 7.

The MOLE and NEON systems were run simultaneously along with the legacy pedestrian mapper for a series of paths traversed in and around the RSL–Andrews Building 1783 located on Joint Base Andrews, Maryland. The preliminary testing involved MOLE and NEON systems used as individual units, which means they were not leveraging the enhanced capability of cross-calibration provided by the internal ranging sensors between multiple systems of the same type. Consequently, the performance observed with these units is worse than can be expected when multiple units are used together, which is the more likely mode of operation for real-world applications. Sample 2-D and 3-D results are captured in Figures 8 and 9, respectively.

While we were able to successfully log data and conduct some analysis in GoogleEarth, we were not able to find a way to successfully integrate the MOLE and NEON data streams into the AVID framework. This limitation was in part due to restrictions on modification to the
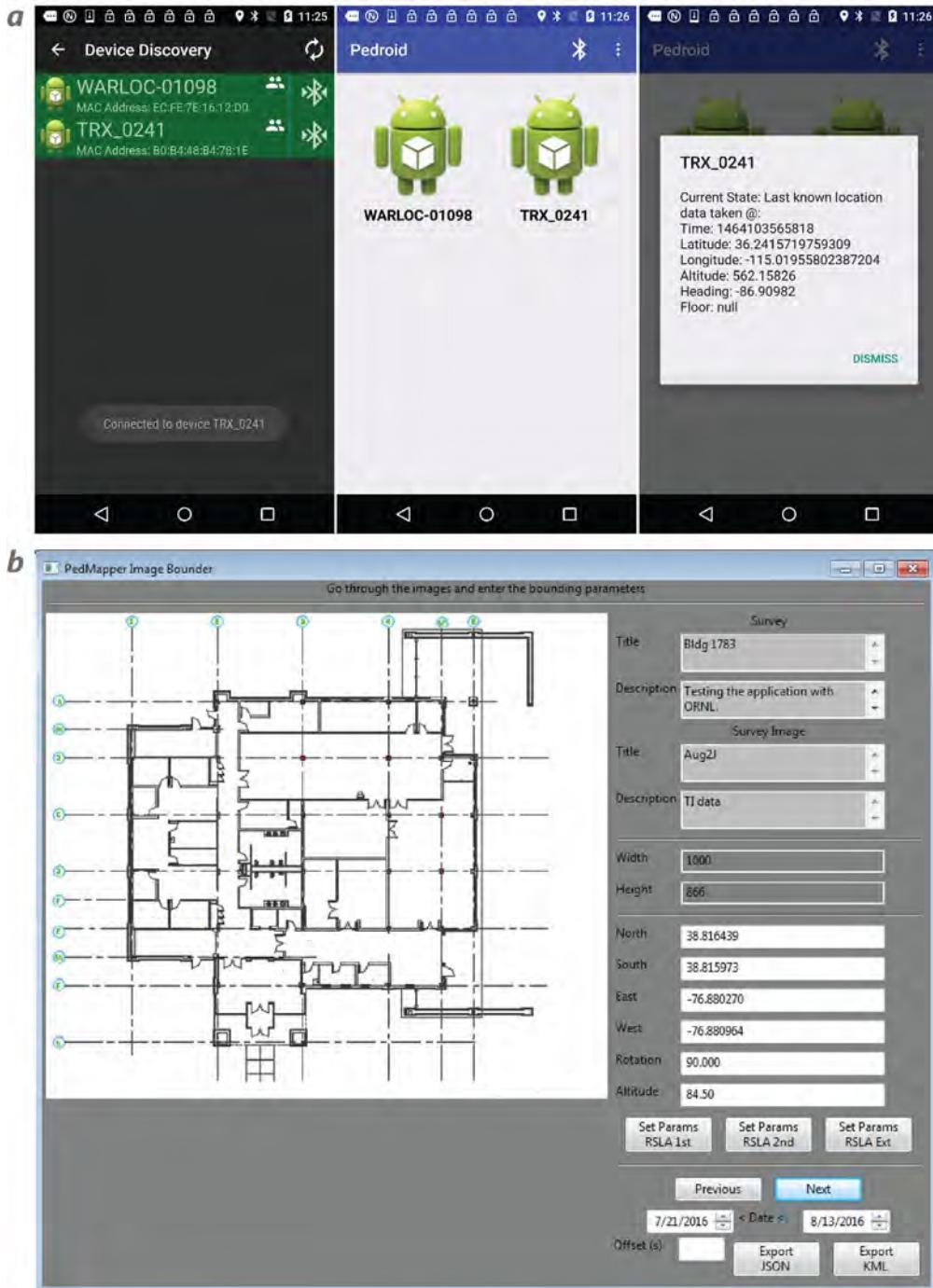
Figure 7. Screenshots from (a) Pedroid and (b) Ped-Mapper KML file generator

underlying data structures in the database upon which AVID relies when accessing historical data. Because both the MOLE and NEON systems are intended to provide dynamic updates to historical data tracks, they must be able to retroactively apply updates or corrections to historical data points. The AVID system does not currently allow for that type of modification, and the amount of work required to make AVID function in that mode was beyond the scope of this project.

There are some key observations that can be made from the limited testing that was conducted. While the
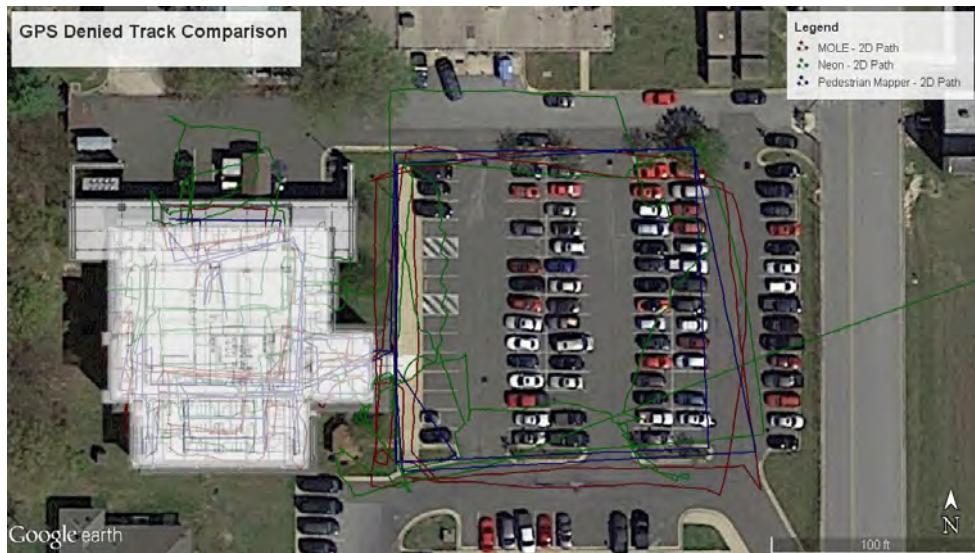
Figure 8. Sample 2-D results from a traversed path within and around the RSL–Andrews facility. Data were simultaneously logged with MOLE, NEON, and Pedestrian Mapper systems.
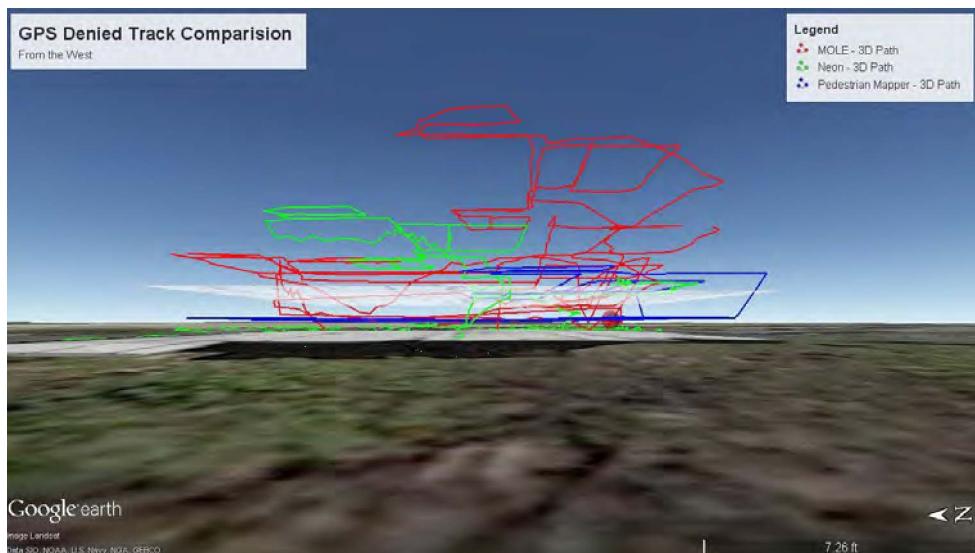
Figure 9. Sample 3-D results from a traversed path within and around the RSL–Andrews facility. Data were simultaneously logged with MOLE, NEON, and Pedestrian Mapper systems.

pedestrian mapping technique continues to provide the most accurate position tracking of the three approaches investigated, it remains constrained by specific modes of use, such as walking only at constant pace in straight lines (no curved or alternate trajectories can be accommodated) and user involvement in a way that continues to demonstrate the limited applicability for position tracking in a lower-profile fashion. In addition, both the MOLE and NEON systems allow for vertical tracking in a way that is not easily achieved

with the pedestrian mapping technique. The vertical tracking of the individual NEON systems appears to outperform the MOLE systems.

Conclusion

The AVID development team successfully generated a prototype pedestrian mapping capability that provides a solid foundation upon which to develop more sophisticated analysis techniques for high-sensitivity

spectral mapping and interpolation. This basic capability was successfully demonstrated in the lab and on a shipboard environment. Although our testing of the MOLE and NEON systems was limited, the performance observed with individual units was as expected, and the overall results do not incite concerns (i.e., when used in sync with multiple systems running concurrently as the manufacturers recommend, the performance will be inconsistent with design specifications). The inability to integrate the tracking systems into the AVID platform limited the development of a more advanced capability by project end. Overall, based on this preliminary evaluation, the capability appears to be solid. Provided that other programs will in the near future support full integration of this capability in AVID, thereby establishing the capability as a fielded, operational one, it would represent an important diversification of GPS-denied search tactics available to DOE emergency response assets, including those supported by RSL.

Acknowledgments

References

Mattson, J. E., "Automatic logging of position," in *Nevada Test Site–Directed Research, Development, and Demonstration*, FY 2004 Report, Bechtel Nevada, Las Vegas, Nevada, 2005, 177–182.

Mitchell, D. J., L. T. Harding, "GADRAS Isotope ID User's Manual for Analysis of Gamma-Ray Measurements and API for Linux and Android," SAND2014-3933, 2014, Sandia National Laboratories, Albuquerque, New Mexico, 2014, http://prod.sandia.gov/techlib/access-control.cgi/2014/143933.pdf, accessed August 31, 2015.

Pfund, D. M., R. C. Runkle, K. K. Anderson, K. D. Jarman, "Examination of count-starved gamma spectra using the method of spectral comparison ratios," *IEEE Trans. Nucl. Sci.* **54**, 4 (2007) 1232–1238.

Ultra-Low-Power Sensor Initiator

STL-072-16 | Year 1 of 1

Steven Koppenjan,[1,a] Duane Gardner,[a] and Kelly Painter[a]

In this project we researched zero-power and nano-power detection methods to initiate ultra-low-power sensors or tags associated with long-term (weeks, months, years) unattended persistent monitoring. We sought to address an ongoing need to activate a quiescent device from up to a 1 km standoff using RF energy because these remote devices rely on energy harvesting for power and cannot be in a receive mode 24/7. A primary focus area was to determine the noise limit boundaries in the frequency areas of interest. Nano-power detectors can be implemented with various filtering techniques accompanied with a low-power self-quenching receiver.

[1] koppensk@nv.doe.gov, 805-681-2453
[a] Special Technologies Laboratory

Background

This project explored implementing a scientific methodology similar to the "wristwatch" signal transmitted from Colorado radio station WWVB (Hanson 2013). This broadcast of a high-power 60 kHz signal is used to synchronize clocks throughout the United States (Hansen 1995). Our approach for this project was to mimic the wristwatch signal technique but use a higher frequency at a much lower transmit power and a receiver circuit with a high Q receiver circuit. The Q, or quality factor, of a resonant circuit is a measure of the "goodness" or quality. A higher value for this figure of merit corresponds to a narrower bandwidth, which is desirable in this application. The receiver or detector typically used in watches is a tiny loop around some ferrite, which may not be optimized for our frequency ranges. This project researched various detectors for this application and reviewed increased performance using modulation techniques (Burrus 2013).

Project

The project studied two approaches: (1) the zero- or near-zero-power method, and (2) the ultra-low-power method. Using the first approach we investigated converting RF waves to baseband DC through the use of semiconductor detectors. The second approach was based on the super regenerative receiver concept discussed below. Additionally, to better understand sensor limitations for an ultra-low-power initiator, the noise limits and parameters needed to be determined. This noise analysis allowed the most effective detector methodology to be pursued.

Two types of semiconductor detectors were investigated, the log detector and the biased diode. The log detector is a powered device with a large dynamic range that enables weak and large signal detection. The log detector typically has a power-down feature that allows for duty cycling. This can result in low average power consumption for low duty factors. Although its weak signal detection is very attractive, the power consumption of the log detector can only be reduced to about 10 µA with a duty factor of 1000. The biased diode converts the incident RF waveform into a DC voltage. A small but significant bias current is used to adjust the optimum RF sensitivity of the diode.

Piezo crystals and RF resonators were also investigated as a means of filtering out undesired RF frequencies and potentially interfering signals.

Baseline Experiment

A baseline experiment using the C-max receiver to receive a wristwatch-type signal was planned. Unfortunately, these parts are no longer produced and not available on the secondary market. Traditionally, filtering is accomplished using tuned loops, which provides a dual function as an antenna. The filtering properties are not typically consistent, and compensation is needed for temperature, humidity, vibration, etc. To reduce the dependence on the loop as a filter, piezo crystals were researched as they are key to the tuned high Q factor receiver concept (Lueg 2016).

Piezo Crystal Study

Several crystals were tested from various manufacturers, with the majority being Citizen, ECS, and Epson. The test consisted of variable impedance matching networks optimized for each crystal. The network provided minimal energy losses by matching to 50 Ω, which also normalized our measurements. Resonant frequencies were limited to those less than 1 MHz. These crystals tended to have similar characteristics (i.e., equivalent series resistance [ESR] and all ranged from 5 to 50 kΩ). The high ESR value is shown later to be a limit to the potential sensitivity of the biased diode detector. This ESR value is used in the noise calculations and is represented by the variable R_S in Equations 1 and 2.

Noise Relationship Simulation

Simulations were performed to analyze the noise relationship of both the log detector and biased diode. Figure 1 illustrates the basic circuit diagram we followed to simulate and evaluate components and key parameters, namely received signal level, bias current, impedance, and detected signal level. The biased diode was found to operate at a much lower current than the log detector without duty cycling. The measure of diode sensitivity, called tangential signal sensitivity (TSS) (Avago Technologies 2006, 2010), is measured in dBm and is the threshold value that yields a probability of false alarm of roughly three sigma. TSS is calculated as

$$TSS_{(dBm)} = -107 + 5 \log B_V + 10 \log I_d + 5 \log$$

$$\left\{ R_A + \frac{28}{I_d}\left[1 + \frac{f_N}{B_V}\ln\frac{B_V}{f_L}\right]\right\} + 10 \log\left\{1 + \frac{R_S C_{j(i)}^2 f^2}{I_d}\right\}. \tag{1}$$

Taking the derivative with respect to the current, the optimal current for any diode is calculated as

$$I_{d(OPT)\,(\mu A)} \cong R_{S(\Omega)}\left\{C_{j(i)\,(pF)}\right\}^2\left\{f_{(GHz)}\right\}^2. \tag{2}$$

Equation 2 indicates that the lowest bias currents can be obtained by using low frequencies and low source impedance.

Weak signal detection inherently drives the requirement for amplification in order to bring the signal amplitude up to a value compatible with trigger circuitry.
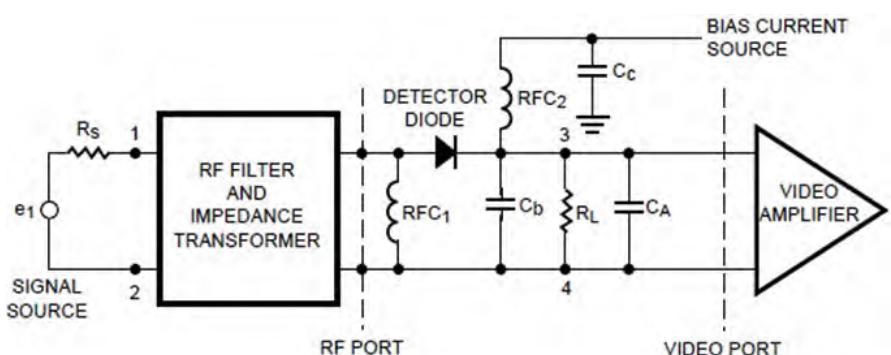
Figure 1. Basic circuit diagram used for simulations
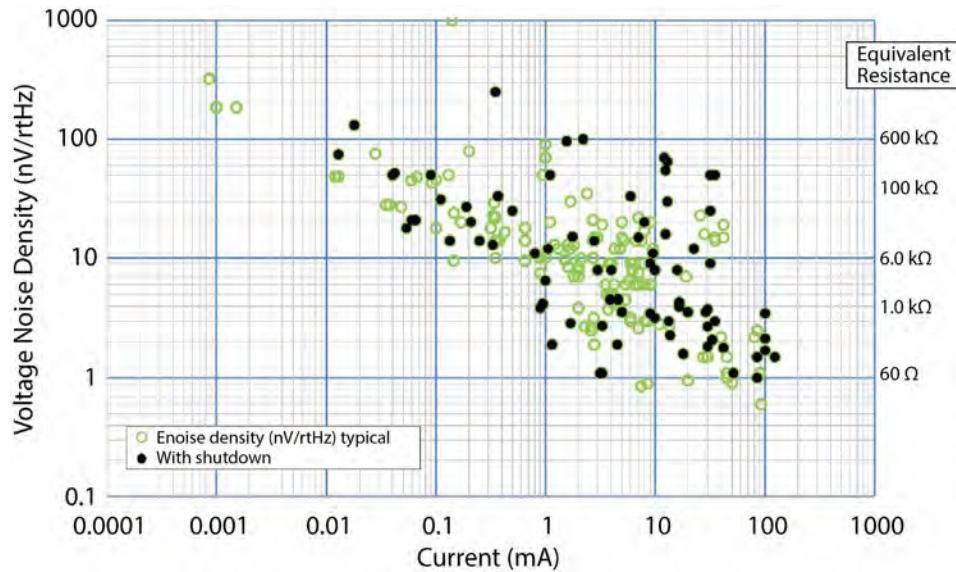
Figure 2. Noise current versus bias current. To achieve a low noise voltage, the operating current must be high. Voltage noise density is inversely proportional to the operating current.
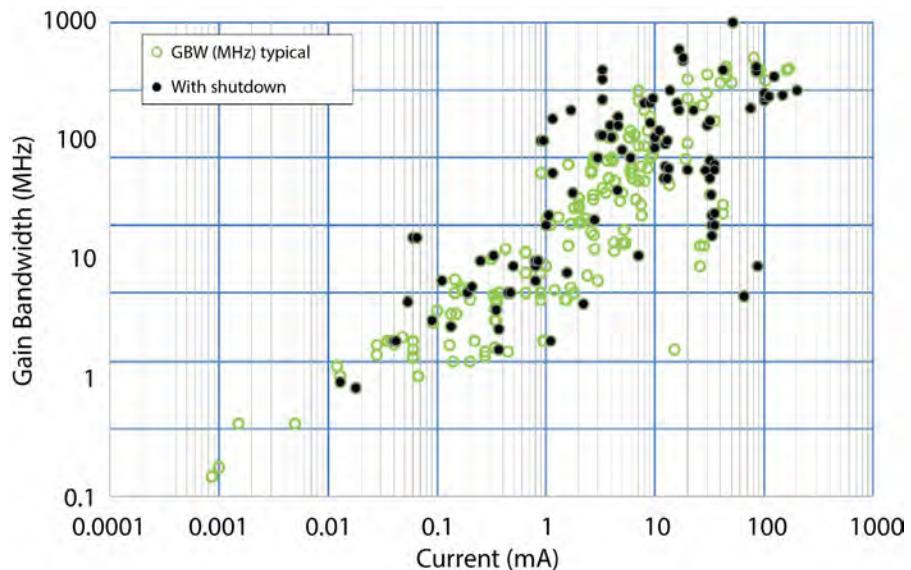
Figure 3. Gain bandwidth (GBW) versus bias current. To achieve a large GBW, the operating current must be high. The GBW is directly proportional to the operating current.

To find a suitable signal amplifier, we performed a survey of about 100 Linear Technologies, Inc., operational amplifier (op amp) components; the results are given in Figures 2–4. An appropriate op amp can be chosen, after selecting an operating frequency, based on the relationship of desired bias current and acceptable noise density.
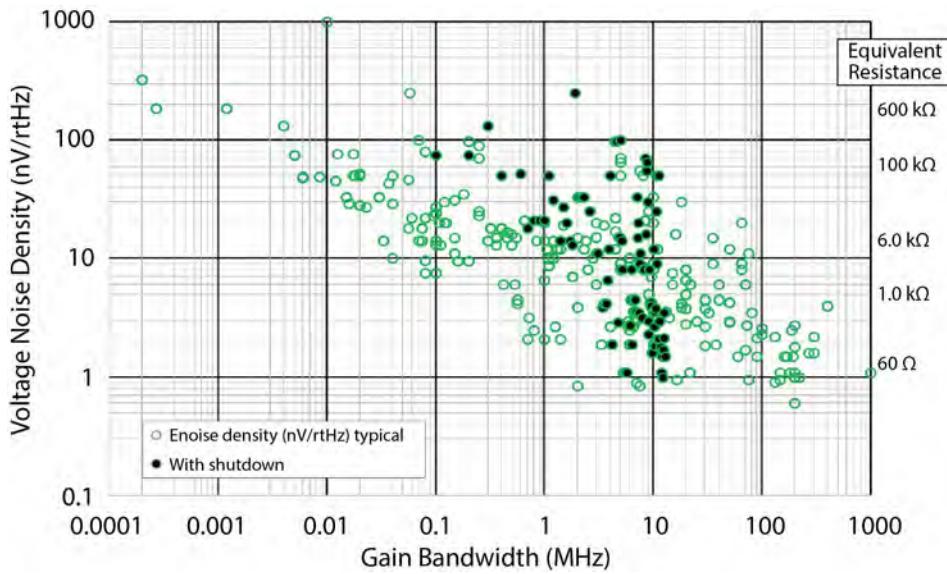
Figure 4. Voltage noise versus GBW. To achieve low noise, the GBW of the device must be high. No noise improvement is achieved for GBW <20 MHz. Voltage noise density is inversely proportional to GBW.

Simulation Experiment

Super Regenerative Receiver Concept

Based on the super regenerative receiver concept, we began with a transistor oscillator circuit tuned to the frequency at which the transmission would occur (Armstrong 1922, Moncunill-Geniz 2005). The oscillator has the Q factor of the resonator reduced in such a way that oscillations either will not occur without an external influence or will take a long time to start. The bias of the active element is made to be exceedingly small. Figure 5 shows the circuit diagram of a prospective super regenerative receiver.
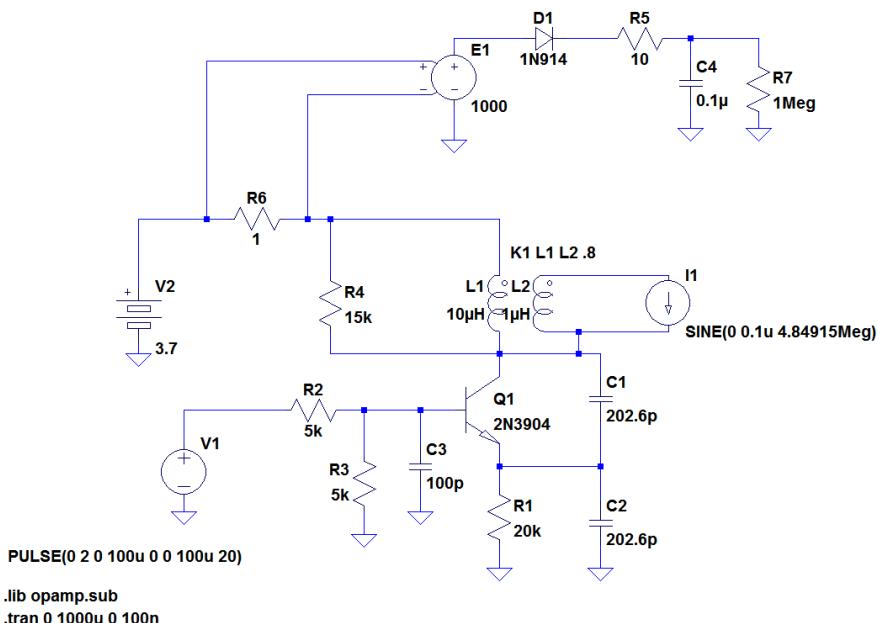
Figure 5. Super regenerative receiver
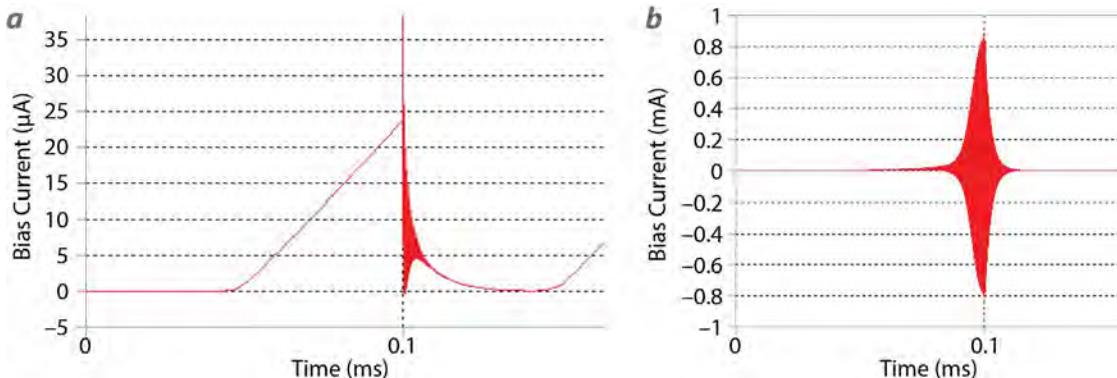
Figure 6. (a) Bias current without external signal present and (b) bias current with an external signal present

In this simulation, the resonator inductor L1 has the external signal injected with mutual inductance via L2. A current source is used to not load the resonator. Loading is accomplished via resistor R4. The quench signal is a linear ramp provided by voltage source V1. This signal is used to ramp the bias of the active element transistor Q1.

An oscillator is not generally started by the amplification of thermal noise as commonly believed. It is the transient from the power supply turning on that causes a ringing in the resonator. If this transient can be suppressed, it is possible to power up an oscillator and not have oscillations. In this state, the oscillator will draw very little current. The quench signal is tuned such that no oscillations will occur and the oscillator does not ever reach full bias condition (Figure 6). The current draw can be monitored; if it is below the threshold at the point at which the bias is quenched, it can be assumed that oscillations did not occur.

As Figure 6 shows, the average current over 0.1 ms is 6 nA. If the quench duty cycle is once per second rather than 0.1 ms, the average current would be 0.6 pA. This neglects the current of support circuitry but illustrates that the power required can be made to be extremely low. This simulation also shows that when the bias is quenched, a transient is created that starts the oscillator. Because power is not removed, oscillations continue until the bias voltage is completely bled out of capacitor C3.

If a weak signal is injected at the frequency of oscillation into the resonator, this energy will be enough to start the oscillator despite not having the "power on" transient. Due to the positive feedback nature of an oscillator, the amplitude of the oscillations will grow until a physical limit is reached. That is, the amplitude of the oscillation will grow as fast as the bias will allow. The oscillator will draw much more current at the point at which the bias is quenched. If this current is above the threshold, we can assume oscillation did occur and therefore a signal has been received (Figure 6b).

This arrangement can be used as a data transceiver using on-off amplitude shift keying (OOASK). In transmit mode, the oscillator output can be amplified and radiated from an antenna. To transmit data, the quench bias signal is altered to come up instantly, rather than ramp up slowly. The transient will ensure oscillations occur. In receive mode, the quench signal is used and the current monitor output passes through a low-pass filter. The output of the filter can then be sampled and demodulated in a microcontroller.

The super regenerative receiver can be set to occasionally power on to look for a pilot tone. If one is detected, the quench signal duty cycle would be increased to the receive rate, and the receiver would look for a sequence containing a command indicating the unit should respond. The simulation circuit in Figure 5 demonstrates the principle, but it is far from anything that can be implemented. For example, getting the circuit to bias up without any transients is
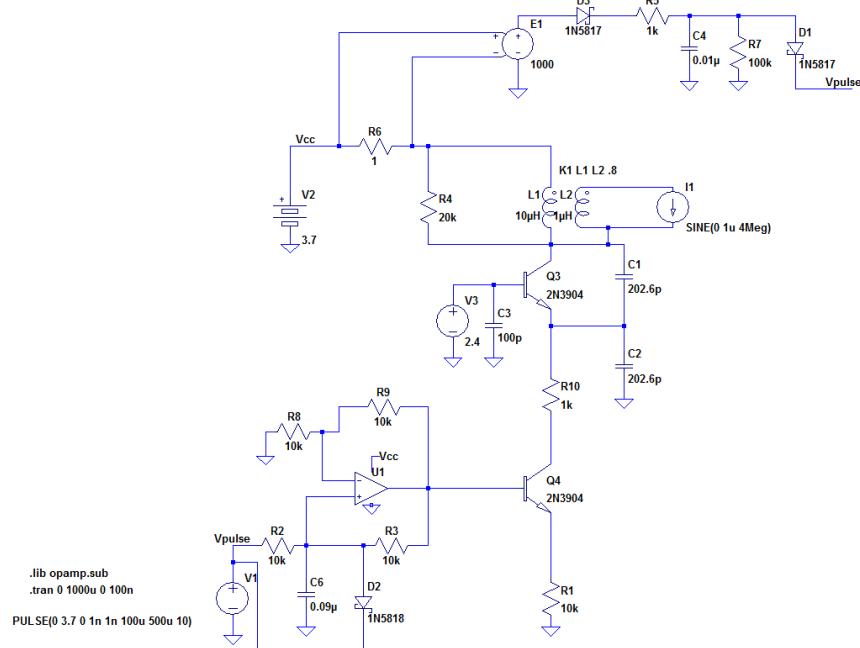
Figure 7. Circuit with quench of bias
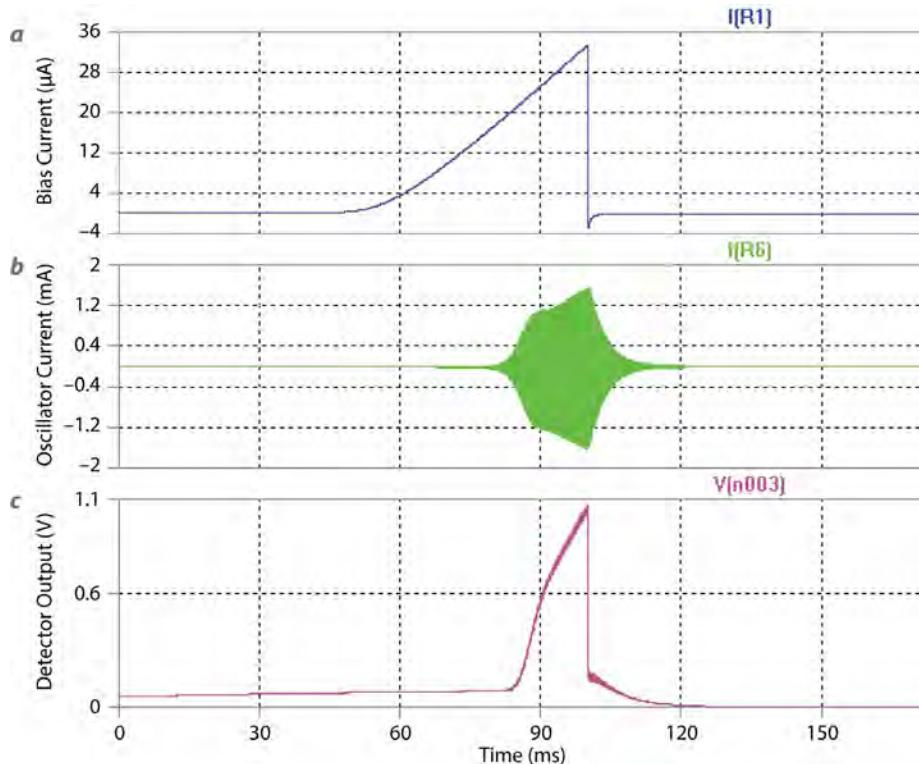
Figure 8. (a) Bias current, (b) oscillator current, and (c) detector output with signal present
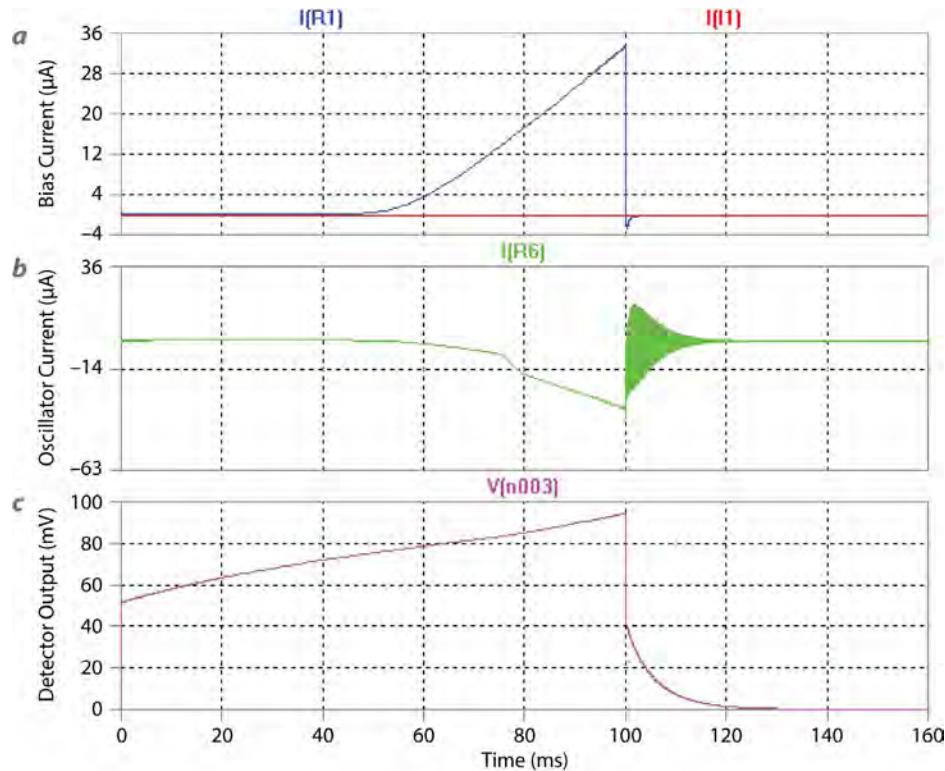
Figure 9. (a) Bias current, (b) oscillator current, and (c) detector output with no signal

very challenging, as a transient will start the oscillation even when there is no received signal. This condition is quite difficult to achieve in a nano-power environment. To test the "bias up without any oscillation" concept, the low power requirement was waived in favor of simulating a working super regeneration receiver.

Figure 7 shows a linear ramp bias quench circuit. A non-inverting integrator integrates the pulse from a microcontroller. The circuit can be further optimized to self-quench when the   current detector output exceeds a particular threshold (i.e., 0.6 V). Once a signal has been detected, causing the threshold to be crossed, the microcontroller becomes fully active and allows the receiver to sample and process the incoming signal. Figures 8 and 9 show the bias current, oscillator current, and detector output with signal present and without the signal present, respectively. The received signal strength cannot be determined, but to some degree, the relative strength will affect the rate at which oscillations start.

Conclusion

During this project a nano-power initiator was researched, and we modeled and evaluated its potential components: collector, conditioner, and discriminator. It was determined that the 100 kHz to 1 MHz frequency range offers the best low-current options. The tuned loop antennas provide good capture area as a collector as well as front-end filtering. The collector must also provide impedance matching to the conditioner. The conditioner should use piezo components to provide additional out-of-band rejection to optimize frequency conversion. A low-noise discriminator is needed to convert to baseband in order to make a decision to initiate a "trigger."

However, low-noise (high-sensitivity) circuits are not necessarily low power. Some amplification (active circuitry) will always be needed to raise the voltage levels up to usable levels. This could be problematic, but a hybrid concept based on the super regenerative receiver method may be a solution. We recommend

implementing a super regenerative receiver as a non-nano power device, then adapting it to nano-power applications tailored to specific scenario, purpose, and size requirements. Such requirements could be those being developed by the DARPA Near Zero Power RF and Sensor Operations (N-ZERO) program, which seeks to reduce or eliminate the need for standby power on unattended sensors.

References

Armstrong, E. H., "Some recent developments of regenerative circuits," *Proc. IRE* **10** (August 1922) 244–260, http://aireradio.org/Superet_arms/Armstrong%203.pdf, accessed January 16, 2016.

Avago Technologies Application Note 923, "Schottky barrier diode video detectors," 2006, https://docs.broadcom.com/docs/5954-2079?eula=true, accessed July 10, 2016.

Avago Technologies Application Note 969, "An optimum zero bias Schottky diode," 2010, https://docs.broadcom.com/docs/5963-0951E?eula=true, accessed July 10, 2016.

Burrus, J., "New NIST time code to boost reception for radio-controlled clocks," March 5, 2013, https://www.nist.gov/news-events/news/2013/03/new-nist-time-code-boost-reception-radio-controlled-clocks, accessed January 16, 2016.

Hansen, P. M., D. Gish, "WWVB antenna and antenna tuning system, Baseline measurements," Technical Report 1693, Naval Command, Control and Ocean Surveillance Center, San Diego, California, February 1995, http://www.google.m/b&cd=1&ved=0ahUKEwjc5ePbhOXPAhVH5iYKHW5bAUwQFggeMAA&url=http%3A%2F%2Fwww.dtic.mil%2Fcgi-bin%2FGetTRDoc%3FAD%3DADA299080&usg=AFQjCNFAsw8VlXTXPwR8xQPiYI3XCFQyOw, accessed January 16, 2016.

Hanson, J., "The most important radio station you've never heard of marks 50 years on the air," *Wired*, July 2, 2013, http://www.wired.com/2013/07/wwvb-time-radio/, accessed January 16, 2016.

Lueg, J., Rugby MSF Atomic Clock, http://www.roevalley.com/newsbrowser/v-projects/MSF_clock/v-rugby.htm, accessed January 16, 2016.

Moncunill-Geniz, F. X., P. Pala-Schonwalder, O. Mas-Casals, "A generic approach to the theory of super regenerative reception," *IEEE Trans. Circuits Sys. I, Reg. Papers* **52**, 1 (January 2005).

CANARY: LOW-POWER, SELF-ORGANIZING REPORTING DEVICES: SITUATIONAL AWARENESS USING DISTRIBUTED SENSOR ARRAYS

STL-102-16 | Continuing in FY 2017 | Year 1 of 2

Jim Kornell,[1,a] Pamela Rangel,[b] and Sashi Ono[c]

Canary is a low-cost sensing and communications platform meant for persistent monitoring in a wide range of circumstances. Using high-quality, low-power components, it can provide once-a-second samples for a decade. Groups at (a) Lawrence Berkeley, Lawrence Livermore, Oak Ridge, Pacific Northwest, Sandia, and Los Alamos National Laboratories; (b) UC Berkeley, UC Davis, Arizona State, and Rensselaer Polytechnic; and (c) in the intelligence community have expressed interest in or already taken delivery of Canaries. Applications at the NNSS are planned. In Year 2 we will implement virtual events, implement domain semantics, and connect semantics to network health self-awareness for flexible mission fit.

[1] korneljm@nv.doe.gov, 805-681-2309
[a] Special Technologies Laboratory; [b] Red Six Solutions; [c] Pure Engineering, LLC

Background

Canary is a Hershey bar–sized sensing and communications platform. It reports GPS coordinates, temperature, air pressure, humidity, and the presence of volatile organic compounds. Canary is equipped with a microphone, infrasound (planned), visible and infrared light sources, a magnetometer, an accelerometer, and both serial and parallel ports for daughtercards. It has mesh and Bluetooth low-energy (BLE) radios and a low-bandwidth long-distance (15+ km) long-range (LoRa) radio. Normal sensing mode runs at ~70 uW, which yields roughly 11 years of unattended use without the photovoltaic and supercapacitor that complement the two AAA rechargeable batteries. It costs about $100 USD to build. Canaries are designed to work in arrays.

Canary is needed for circumstances in which signals will be transitory, acyclic, trace, and unpredictable. Continuous on-site monitoring over long periods of time is the only way to detect such signals. For example a canary is appropriate in monitoring-denied areas to detect chemical effluents associated with reprocessing. A great deal of intelligent effort goes into making sure such effluents are not released. Another practical application is monitoring ambient radioactivity when fires at the NNSS burn over areas that may have residual fallout. Shallowly buried radioactive particulates can become aerosolized, and monitoring is necessary for the safety of the firefighters.

Project

Design Goals

Our goal is to build a detection platform on which a to-be-discovered number and type of applications can be placed. Our approach is to talk with sponsors in the morning and show them a working prototype in the afternoon. Design affordances and constraints flowed from this central goal.

A key feature is modular hardware architecture. A design where boards can be populated or depopulated according to specific need is extremely advantageous (e.g., Don't need GPS for your application? OK, it's gone. Smaller footprint? OK, we'll fold it. And

so on.) Likewise for modular software architecture; standard interfaces and predictable operation, with as many existing applications made portable as is feasible, leads to a completely customizable platform. Both hardware and software should make integration of new sensors, communications capabilities, or new software functionality as easy as possible.

Another goal was to have Canaries autonomously self-organize into a network in a way that makes the network the sensor. Also important is having a virtual event system, so that "localization" of physical signal is elastic across multiple devices. For example, four closely placed Canaries may vary in quality of audio, light sensing, magnetic field sensing, and vibration detection. Regardless of which physical devices collected the data, the most accurate readings can be automatically combined into a single event detection.

Further, we aimed to have the sensor field be a participant in the mission, specifically by monitoring node health and the nonlinear algorithms for data relay that balance the importance of the information with the continued functionality of the sensor field, as is contingent on the battery/power state of the devices on the distribution path.

Finally, we designed Canary to have emergent distributed semantics for whatever specific mission domain is the target. Mission semantics refers to a list or hierarchy of what information is most important for a specific mission. For instance, for one mission, command may only want notification on the first occurrence of Event A. Notification on every occurrence might fit a different mission. Emergent means it is the cumulative decision of the sensor network as a whole whether a mission's semantic requirement is met. This makes the sensor field tremendously more robust to degradation than a normal approach, and far less vulnerable to hacking or reverse engineering from a single node.

Design Approach

Canary is designed to work in teams with other Canaries and with other sensors. Four aspects of teamwork were emphasized in design:

1. Know you're on a team

The self-organizing mesh includes unique identification of each node and the capacity to dynamically reconfigure if new nodes are added or existing nodes drop out. Individual devices recognize the network and know the relative proximity of the other connected devices.

2. Mutual monitoring

Data flow through the mesh includes status. We have not yet created the state-model for "other" nodes (e.g., so that the nodes know each other's health); that will be a primary task for the second year of this project. Also in Year 2, we hope to allow nodes to have a history together (e.g., so that environmental degradation or anomalous detections can be checked against an evolving norm). Further, upcoming algorithm development will take advantage of Canaries' ability to be connected over distance: if a vehicle leaves a facility, Canaries on opposite sides of a T-junction can, via mutual monitoring, know when to expect the vehicle, and can confirm which side of the T it took.

3. Reciprocal backup

Mutual event construction is intrinsic in the concept of virtual events (i.e., physical events whose virtual representation melds data from multiple Canaries). Not discussed above is disconfirmation, an element of virtual events in which a reading from a single device has no corresponding readings from other sensors and other devices. This is mission-sensitive false-positive/false-negative dynamism, emergent from the networked devices. Consider three Canary devices near a road. If a truck were to drive by, we would expect all three Canaries' magnetometers and accelerometers to register the vehicle, with those closer or on harder surfaces showing stronger readings than those further away or on sand or grass. But if one strong magnetometer reading is reported and two "silences" occur, and lacking vibration (accelerometer), the Canaries as a group could reject the reading as an error. "As a group" is key: reciprocal backup will keep reporting accurate, which of course is the point.
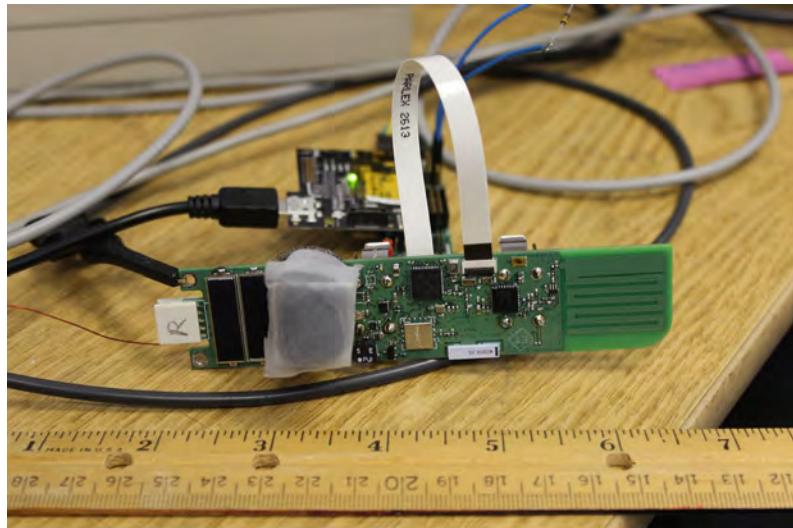
Figure 1. Canary circuit board

4. Anticipatory compensation

In FY 2017 we plan to implement system and individual node health as part of the semantics of mission spaces. This means that the value of any particular item of information needs to be balanced against (a) the momentary, low but real increased RF visibility of the system when broadcasting, and (b) the energy cost of the transmission and the corresponding effect on network connectivity. Because Canaries are designed to support a "sowing" deployment model (e.g., tossing or dropping them randomly on the ground), mesh connectivity will potentially include configurations where a single Canary connects two sensor fields. (Picture an hourglass or a figure eight.) Allowing the batteries to be overstressed by flowing communications through a single device can cause the device to die, and as a result half of the sensor field may be lost to exfiltration. This kind of potential failure drives the need for anticipatory compensation, in which load bearing is distributed and minimum energy paths (if they all lead through a single node) are abjured for a *seemingly* less efficient routing pattern, anticipating potential failure and compensating in advance.

Key Design Choices

Four specific design choices deserve discussion: reconfigurability, our decision to use the Contiki operating system, our selection of the MQTT-SN protocol, and the ultimate creation of an event-triggered sensor.

The modular hardware and software architectures make reconfiguring Canary for specific missions straightforward. We made Canary "big" to make soldering components and inserting logic analyzer probes easier (Figure 1). We can keep the same sensing and make it one-quarter its current size, and we can pull sensors, or add a daughtercard, with minimum difficulty.

A common open-source Internet of Things (IoT) operating system (i.e., a system that allows everyday objects to be networked, thereby enabling them to send and receive data), Contiki is small, fast, and reliable. It is widely used, easy to learn, and has a large library of applications available. We believe using a standard OS makes it easier to rapidly develop applications. Even better, our partners can develop applications without our knowledge, as is appropriate when we have no need to know.

MQTT-SN is a lightweight publish-subscribe messaging protocol that sits above TCP/IP (that is, at Layer 3 of the ISO stack). SN stands for sensor network, reflecting specialization of the protocol expressly for sensor networks where "always listening" for published messages is impractical. MQTT-SN includes a secure socket layer (SSL) for encrypted communications when needed. The value of MQTT-SN parallels that of Contiki: wide existing user base, high reliability, speed,

and small computational demand. With both Contiki and MQTT-SN, developers can start from established standards with good training materials and reams of existing, tested code.

An event-triggered sensor stays in low-power sleep mode until an event of adequate magnitude or intensity occurs, causing it to awaken and report. For example, if an accelerometer is reporting vibration when cars enter or exit a parking lot, then an empty lot between 9:00 at night and 6:00 in the morning means the sensor can stay in sleep mode. The alternative is to awaken twice a second to check for activity, a far more energy-costly approach. In addition, a 100-Canary sensor field would generate over 100 million data points daily if sampling only once a second; therefore, the vast majority of those data points would be pointless.[1]

Open Source

The Canary platform, but not mission-specific applications developed for it, is open source in both hardware and firmware. Platform entails the full basic functionality. Meshing, all of the sensors, short- and long-range communications, and so on are all part of the platform. By contrast, a team might implement an algorithm for a highly specific detection task and augment Canary with task-specific sensing. The algorithm would comprise an application. We chose the Contiki open source license for the firmware because it absolutely stipulates that authors own their applications and are not required to publish them.

Open source, a method of authoring source code that is then shared at no cost and distributed widely through the Internet, is the default method used when growth of a platform is desired. In the specific case of Canary, we describe below a number of cooperative activities in which other organizations are relying on Canary for support. Making Canary open source reduces their risk while having no adverse impact for NSTec.

---

[1] There are times when nothing happening—the dog that did nothing in the nighttime—is significant. This can and will be handled by the distributed semantics.

Concerns have been raised about operational security (e.g., should a Canary or a derivative be discovered by a country we suspect of covert proliferation, a trail could lead back to a national laboratory). We believe this represents a fundamental misunderstanding of what Canary is—a collection of COTS parts that we have cleverly arranged to operate at low power. Discovery of a Canary in the field by an adversary would amount to the discovery that someone was using electronic means for data gathering. It is difficult to imagine surprise.

Acceptance

Canary is the result of several converging streams. Stephan Weeks advocated for a decade for such a device, and before his retirement directed a prior SDRD to develop the extreme low–power Urchin device (Weeks 2014, 2015). Canary is Urchin's direct descendant. The second stream grew from Pamela Rangel's experience with Army and Special Operations Forces (SOF) "red-team" field exercises, in which mid- to high-TRL (technology readiness level) equipment is tested in realistic conditions. It became obvious that ubiquitous and persistent sensing and communications was necessary to manage situational awareness in the field exercises, and that such capabilities could be used directly by soldiers as well. Third, the Talking Drums project developed a detailed concept of operations for distributed, hard-to-hack nuclear materials security. This scope, too, needed a device like Canary.

In parallel with this SDRD work, the DOE Defense Nuclear Nonproliferation Research and Development organization (NA-22) funded the SEBATT project, where Canary capabilities were mapped to a specific set of proliferation detection scenarios. This work is expected to continue in FY 2017 under the NA-22 LUNAR CAT and MINOS programs.

As a result of the various swirls and eddies of these streams described, current commitments to Canary include:

- NNSS: fire station monitoring, exploration of other possible operational applications

- University of California, Berkeley: network science applied to nonproliferation (in conjunction with MINOS)

- Rensselaer Polytechnic Institute: real-time continuous water-quality monitoring

- Los Alamos National Laboratory: advanced data analytics, and (separate project) tipping and cueing of advanced detection technologies

- Lawrence Livermore National Laboratory: tipping and cueing of advanced detection technologies (two projects)

- Lawrence Berkeley National Laboratory: advanced nuclear field data repository

- Sandia National Laboratories: tipping and cueing of advanced detection technologies, cross-level heterogeneous data plus context mixed-initiative analysis

- Idaho National Laboratory: data collection and analytics

- Oak Ridge National Laboratory: data collection and analytics, and (separate project) applications and analytics for subgroups

- An intelligence community client who understands, embraces, and wants to further the Canary "platform + modular apps" model

In support of the above, we have begun discussions with IT at the Special Technologies Laboratory and other cyber personnel regarding structuring a Canary app store in FY 2017.

Conclusion

Year 1 of Canary work has succeeded beyond expectation, and Canary has some seriously fun technical developments we plan to implement in FY 2017. Virtual events are (we believe) a matter of discipline, diligence, and a mountain of testing. Emergent semantics, whether mediated by dynamical traveling (opportunistic, non-local) agents or distributed

non-deterministic finite state automata, will be worthy of publication if we succeed (which is not at all guaranteed).

An additional opportunity we hope to pursue will be to find routes to making Canaries effective tools for NNSS operational needs. Analogous to RaptorX, one or more pilot projects are needed, with the idea that a broad range of potential applications might be addressed once we have shaken it out in the field. We are mindful that, "in theory, there is no difference between theory and practice; in practice there is."[2]

References

Weeks, S., S. Sawyer Armand, H. McHugh, "Chemically activated quiescent persistent sensors," in *Site-Directed Research and Development*, FY 2013, National Security Technologies, LLC, Las Vegas, Nevada, 2014, 149–159.

Weeks, S., S. Sawyer Armand, Y. Ono, J. Kornell, "Chemically activated quiescent persistent sensors for semantic networks," in *Site-Directed Research and Development*, FY 2014, National Security Technologies, LLC, Las Vegas, Nevada, 2015, 175–182.

---

[2] Quote generally attributed to Jan van de Snepscheut, as overheard at a computer science conference. It is believed to have first appeared in print in *Pascal: An Introduction to the Art and Science of Programming*, by Walter J. Savitch (1986).

This page left blank intentionally

Ionospheric Detection of Decoupled Underground Nuclear Detonations
LAO-012-16 | Year 1 of 1

Alfred Meidinger,[1,a] Jessica Clayton,[a] David D. Schwellenbach,[a] and Kelsey Kramer[a]

Experiments were conducted in an attempt to verify (or refute) the hypothesis that a fully seismically decoupled nuclear detonation in the 1-kiloton and lower-yield range will magnetically couple to the ionosphere, creating localized perturbations in the ionosphere electron density. Experiments were conducted at the very end of the fiscal year based on magnetic field source tests. Initial results have proven that further exploration is required and will be the subject of future investigations.

[1] meidina@nv.doe.gov, 505-663-2018
[a] New Mexico Operations–Los Alamos

Background

During FY 2014–FY 2015, the two-year SDRD project "Ionospheric Detection of Decoupled Underground Nuclear Detonations" investigated prior research and modeling efforts addressing geomagnetic coupling to the earth's ionosphere (Meidinger 2015, 2016). The results of the 2014 investigation not only indicated high-frequency signatures related to lightning strokes appear to couple with the ionosphere plasma (Pilipenko 2012), but also the signals can travel several thousand kilometers from their source. Also noted in the FY 2014 SDRD report is the fact that magnetic signatures anticipated for fully seismically decoupled underground nuclear proliferation experiments (UNPEs) are of the same magnitude as average lightning strokes (Jhavar 2005), although magnetic field geometries are different; UNPEs generate dipole magnetic fields while lightning strokes generate azimuthal fields. Another important difference is that lightning strokes typically generate signatures with higher frequency components than those associated with UNPEs.

FY 2015 results show low-frequency geomagnetic earthquake precursors appear to couple to the ionosphere plasma, generating large-scale variations in the ionospheric total electron content (TEC). Analysis of Global Navigation Satellite System (GNSS) data for the May 12, 2008, Wenchuan earthquake that took place in southwest China shows an apparent increase in TEC correlated with increases in surface geomagnetic field measurements. The source of geomagnetic field fluctuations is not known at this time. In the case of earthquake precursors, frequency components are several orders of magnitude lower than those expected for UNPEs.

Project

As a follow-on to the previous SDRD work, the goal of this project was to conduct experiments to verify (or refute) the hypothesis that a fully seismically decoupled nuclear detonation in the 1-kiloton and lower-yield range will magnetically couple to the ionosphere, thereby creating localized perturbations in the ionosphere electron density. The experiment plan was designed to monitor electron density fluctuations using the existing GNSS system combined with specialized scientific-grade high sampling–rate GNSS receivers to capture electron density fluctuations

in an expected range of 0.1 to 10 Hz, a frequency region between those of lightning strokes and earthquake precursors. In addition, Air Force Research Laboratory (AFRL) scientists at Kirtland Air Force Base (AFB) monitored the experiments using bottom-side ionosonde techniques.

Conducting an underground detonation as a source for ionospheric electron density fluctuations is not feasible for this set of experiments. Instead, a pulsed solenoid that mimics the magnetic signature of the explosion-induced magnetic bubble was employed. The solenoid is a system that was designed and built by researchers at Los Alamos National Laboratory (LANL) Intelligence and Space Research Space and Remote Sensing (ISR-2). The solenoid system was used in prior experiments to verify that magnetic signals mimicking those of an underground nuclear detonation do propagate through soil and can be measured at the earth's surface. Based on this verification the pulsed solenoid is representative of the type of source required for generating ionospheric electron density perturbations.

The solenoid is made using heavy-gauge welding cable wound around a 1-meter-radius wooden frame. The solenoid is composed of 50 turns and is driven by a 48-volt pulser (four automotive batteries). Figure 1 provides a solid body rendering of the wooden frame. The frame is designed to roll into a tilted orientation to match the 63° geomagnetic field inclination at Los Alamos, New Mexico; the 9° declination is accommodated by rotating the frame on its base. This allows the solenoid to be aligned antiparallel to the Los Alamos local geomagnetic field in a fashion identical to that of an explosion-induced magnetic bubble.

The pulser is designed to operate at pulse widths of approximately 100 ms and maximum currents of approximately 250 A. Figure 2 represents a single measured current profile for a 70 ms pulse, showing an exponential rise and abrupt fall.

The magnetic moment of the solenoid accurately tracks the input current profile and scales linearly with the current. The magnetic moment of the solenoid is calculated using the linear relationship

$$M(t) = N \cdot I(t) \cdot \pi \cdot r^2 (A \cdot m^2). \tag{1}$$

For this solenoid N = 50 turns, using a peak current of I = 250 A, the peak magnetic moment of the solenoid is approximately 39 $kA \cdot m^2$. This magnetic dipole moment corresponds with the peak magnetic bubble–induced magnetic moment of a fully seismically decoupled detonation, where the yield (Y, in kilotons) given by the equation (Karlykhanov 2004)

$$M = 2.5 \cdot 10^5 \cdot Y (A \cdot m^2), \tag{2}$$

is ~0.16 kilotons.
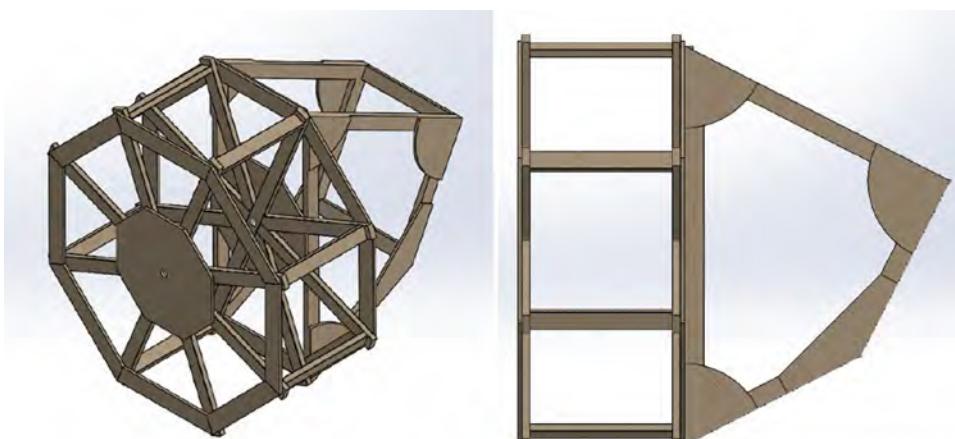
Figure 1. Solid body rendering of the wooden frame used for solenoid windings. The frame is built to roll into the correct pitch to align with the geomagnetic field inclination at Los Alamos, New Mexico. Image courtesy of LANL.
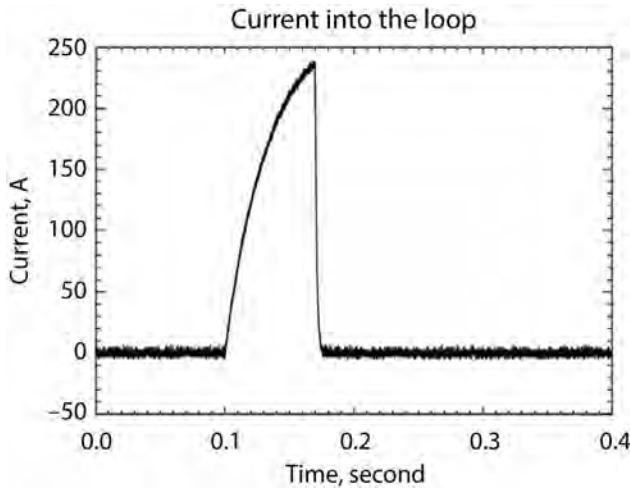
Figure 2. Current profile of the pulsed solenoid used for experiments. The profile is for a 70 ms pulse width, 30 ms shorter than the 100 ms pulses used in our experiments. Image courtesy of LANL.

A magnetic perturbation at or near the surface of the earth is expected to propagate outward from the source in a spherical pattern, that is, as a spherical wave front.

Because the perturbation occurs within the earth's magnetic field, when the wave front reaches the ionosphere, plasma effects should manifest. Although not well understood, expected effects include development of Alfvén waves along the geomagnetic field lines and magnetosonic waves perpendicular to the geomagnetic field lines with possible excitation of the ionospheric Alfvén resonator.

For Los Alamos, New Mexico, the geomagnetic meridian follows a geometry that is favorable for monitoring using existing AFRL ionosonde stations. The 9° declination allows monitoring of several preexisting ionosonde locations at Kirtland AFB; the Very Large Array and Long Wavelength Array located near Socorro, New Mexico; and the White Sands Missile Range in Southern New Mexico. Figure 3 illustrates the geomagnetic meridian geometry for our experiments, showing the favorable alignment of existing ionosonde locations.
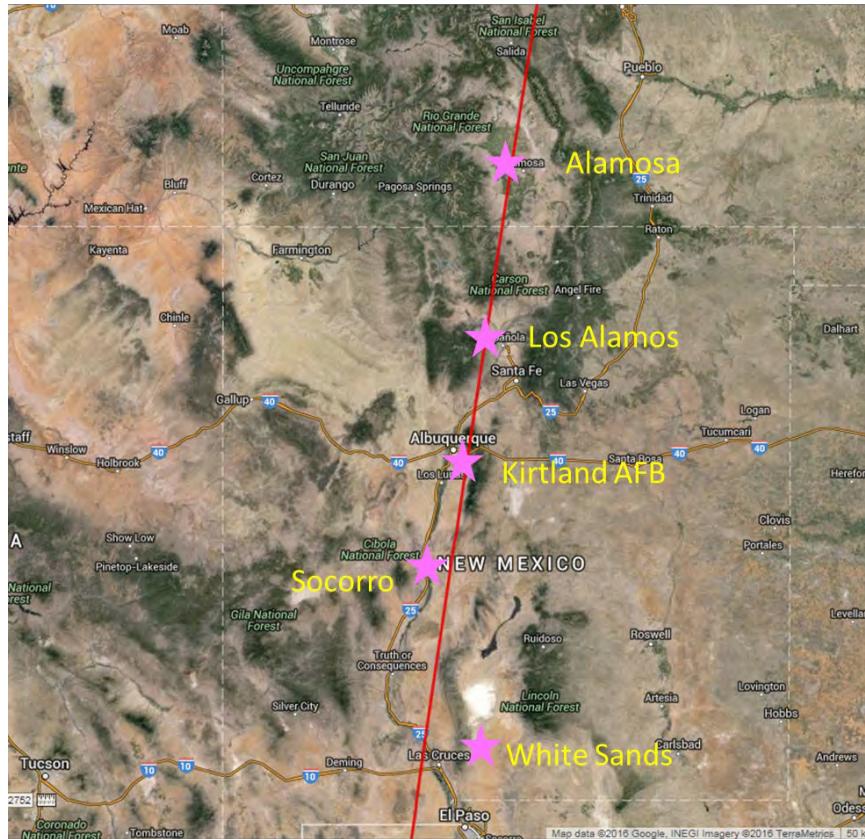
Figure 3. Geomagnetic meridian geometry of the Los Alamos, New Mexico experiments. AFRL ionosonde stations at Kirtland AFB, the Very Large Array, the Long Wavelength Array, and White Sands Missile Range fall on or near the Los Alamos geomagnetic meridian. Also shown is a possible site for portable monitoring systems near Alamosa, Colorado. Image courtesy of AFRL.
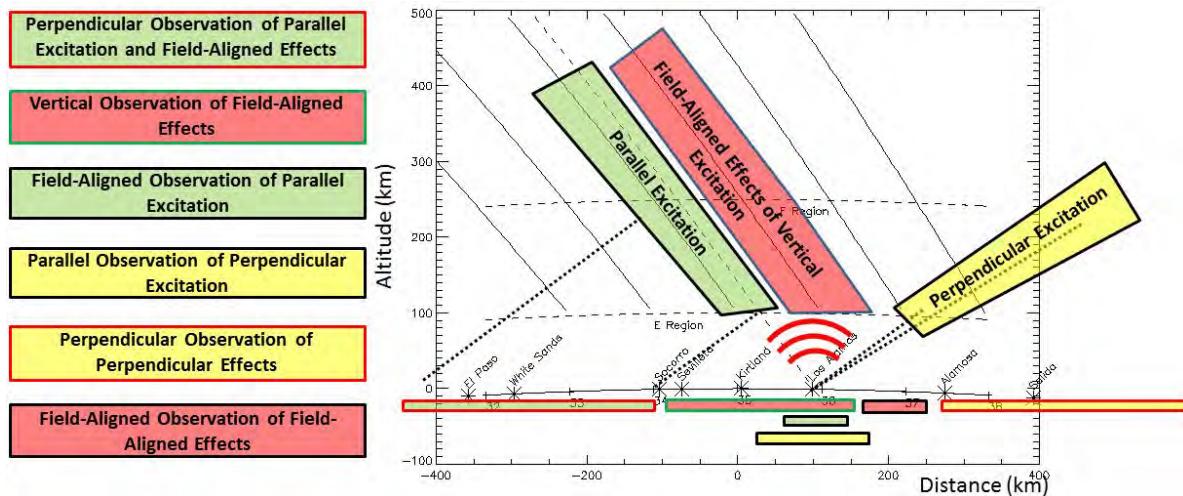
Figure 4. Observation orientations for the pulsed solenoid experiment. Instruments were placed at the Los Alamos site, Kirtland AFB, and White Sands Missile Range.

As noted, some combination of Alfvén waves and magnetosonic waves are expected. Locating GNSS and ionosonde stations at select locations along the geomagnetic meridian will allow monitoring for both modes of wave propagation. In principle, we wish to observe possible wave structure by observing magnetic field lines parallel to the principal geomagnetic field lines passing through the source and magnetic field lines perpendicular to the source geomagnetic field lines. By viewing in these orientations, we maximize our ability to detect wavelike structure in the ionosphere plasma. Figure 4 illustrates the observation schemes considered for this experiment, although not all schemes were realized. Locating detection equipment near the Los Alamos magnetic source permits observation of excitations parallel to the local geomagnetic field lines, observation of perpendicular excitation, and vertical observation. GNSS observation was employed in this location, but ionosonde equipment was not installed in time for the experiment. Observation at Kirtland AFB permitted vertical observation of parallel field excitation and observation of possible field-aligned currents using both ionosonde and GNSS receivers. Instruments at the White Sands Missile Range provided perpendicular observations of parallel geomagnetic field and field-aligned excitation using both ionosonde and GNSS

receivers. No instruments were placed for recording field-aligned observations of field-aligned effects and perpendicular observation of perpendicular effects.

Although we conducted a preliminary experiment late in FY 2016, we encountered unforeseen circumstances with data analysis. Results were inconclusive, and the data suggest that additional experiments beyond the scope of this project would be required. We are investigating alternate approaches that are aligned with future planned SDRD activities.

Conclusion

This project achieved significant progress in developing methods to understand ionospheric signatures for the detection of underground nuclear detonations. Prior research was leveraged in order to determine prudent experimental techniques. We instrumented an initial test utilizing pulsed magnetic sources and obtained preliminary results. Analysis of the data proved to be inconclusive and indicates that more experiments would be necessary. We also concluded that the scope of the tests would be more substantial than previously conceived. Therefore, we are investigating new approaches to provide further ground truth and are looking to propose such concepts in the future.

Acknowledgments

References

Jhavar, A. B., "Triggered-lightning properties inferred from measured currents and very close magnetic fields," Master's Thesis, University of Florida, 2005, http://etd.fcla.edu/UF/UFE0013160/jhavar_a.pdf, accessed October 1, 2014, 36–37.

Karlykhanov, N. G., A. A. Kondrat'ev, V. I. Matvienko, V. N. Nogin, "Magnetic dipole moment from a one-kiloton underground nuclear explosion in a cavity," *J. Appl. Mech. Tech. Phys.* **45**, 3 (2004) 311–315.

Meidinger, A., D. Clayton, D. Aberle, K. Kramer, W. Zimmerman, "Ionospheric plasma coupling to low-frequency electromagnetic radiation," in *Site-Directed Research and Development*, FY 2014, National Security Technologies, LLC, Las Vegas, Nevada, 2015, 147–155.

Meidinger, A., K. Kramer, J. Green, D. Aberle, "Ionospheric plasma coupling to low-frequency electromagnetic radiation," in *Site-Directed Research and Development*, FY 2015, National Security Technologies, LLC, Las Vegas, Nevada, 2016, 81–87.

Pilipenko, V. A., "Impulsive coupling between the atmosphere and ionosphere/magnetosphere," *Space Sci. Rev.* **168** (2012) 533–550.

This page left blank intentionally

RGB Wavefront Sensor for Turbulence Mitigation

STL-078-16 | Continuing in FY 2017 | Year 1 of 2

Mary D. O'Neill [1,a] and David Terry [b]

Atmospheric effects reduce the ability to detect or identify objects of interest due to spatial and spectral scintillation. Algorithms alone cannot correct for turbulence over long-range horizontal paths. While adaptive optics (AO) work well for astronomical viewing, the same methods do not adapt directly for complex imagery over long-range horizontal paths. In this two-year research project, we combine an off-the-shelf high-frame-rate USB3 color camera with a compact 90 mm Maksutov-Cassegrain telescope to create a portable red/green/blue wavefront sensor. The 90 mm aperture is covered with an aluminum plate holding three separate narrowband color filters. These filters, specifically matched to the relative spectral response of the sensor's Bayer mask, provide nearly complete separation of the three color planes.

This device enables portable imaging through atmospheric turbulence and analysis thereof, where relative motion of the three-color Bayer-pixel video provides real-time wavefront information on the second-order statistics of Kolmogorov turbulence. We not only extract dwell-averaged wavefront tip and tilt as a function of time, but also, using our spectral filtering algorithm, are able to fit higher-order modes to the imaged wavefront statistics. In our second year, we will combine this sensor with a deformable mirror to complete the AO system for long-range horizontal paths.

[1] oneillmd@nv.doe.gov, 805-681-2477
[a] Special Technologies Laboratory; [b] Fifth Gait Technologies, Santa Barbara

Background

The atmosphere has three major effects on a propagating wave: absorption, scattering, and refractive-index fluctuations (optical turbulence). Atmospheric turbulence–induced image degradation presents a significant problem in extended range surveillance and signal processing because, in many applications, these effects are more restrictive to viewing resolution than the diffraction limit.

Turbulence is strongest when there is a large temperature differential between the earth (ground) and the surrounding air. When the earth is warmed by the sun, energy is injected back into the air as wind mixes the buoyant warm bubble of air with the surrounding cooler air. The energy dissipates into the next layer; thus, cell size reduces from larger to smaller. The larger cells act as refractive elements, and the smaller cells act as diffractive elements. In general, the smallest and largest cells determine the inner (l_0) and outer (L_0) scales of turbulence (Max 2010). The inner scale defines the size of the smallest inhomogeneities in the turbulence, below which we use fluid viscosity to describe flow. The outer scale defines the point beyond which the turbulence becomes anisotropic, resulting in structural and refractive index effects (Tofsted 2000).

Fried's atmospheric coherence length, r_0 (Fried 1967), is the standard parameter used to characterize the point spread function (PSF) for imaging through the

atmosphere (*seeing* conditions, Martinez 2010). This can be computed from the path-length integrated c_n^2 as

$$r_0^{-5/3} \equiv \frac{2.91}{6.88}\left|\frac{2\pi}{\lambda}\right|^2 \int_0^L \left[1-\frac{z}{L}\right]^{5/3} c_n^2 dz$$

$$\equiv \frac{2.91}{6.88}\left|\frac{2\pi}{\lambda}\right|^2 \left|\frac{3}{8}\right|\langle c_n^2 L\rangle.$$

(1)

Here, λ is the monochromatic wavelength, L is the integrated line-of-sight (LOS) path length, and we have defined the "constant-equivalent" average index of refraction structure constant $\langle c_n^2 L\rangle$ as if c_n^2 were constant along the entire path. Note that r_0 is inversely proportional to c_n^2 and thus to the strength of turbulence. Algorithms used to mitigate image degradation and analyze signals are increasingly dependent upon the character and strength of the turbulence.

Figure 1 contains images of a standard target (USAF 1951 resolution test chart) taken during a warm day in California as the sun heated the atmosphere and LOS turbulence increased such that the aperture diameter to the coherence radius D/r_0 increased.

Even though the image is not monochromatic, it is obvious that *perceived image quality correlates with* D/r_0. Consequently, D/r_0 can be used as a dimension-less, macroscopic turbulence strength parameter. In practice, we find a D/r_0 of ~20 produces images that have insufficient high spatial frequency detail and cannot be reliably improved by image processing.

Fried (1978) postulated that there is some probability of getting a lucky or clear image through turbulence. Many algorithms rely on this probability to get high spatial frequency content. Hufnagel (1989) deter-mined that if wavefront distortion could be corrected, the probability would increase. Zernike polynomials are used for describing aberrations in optical systems and are often used to describe the wavefront distor-tion associated with atmospheric turbulence (Born 1965, Noll 1976). The first twelve Zernike degrees of freedom (DOFs) are shown in Figure 2a. Figure 2b shows the improvement in the probability of getting a lucky image with different DOFs of Zernike corrections.

Adaptive optics (AO) systems have been used for years in astronomy to correct for the wavefront distortion
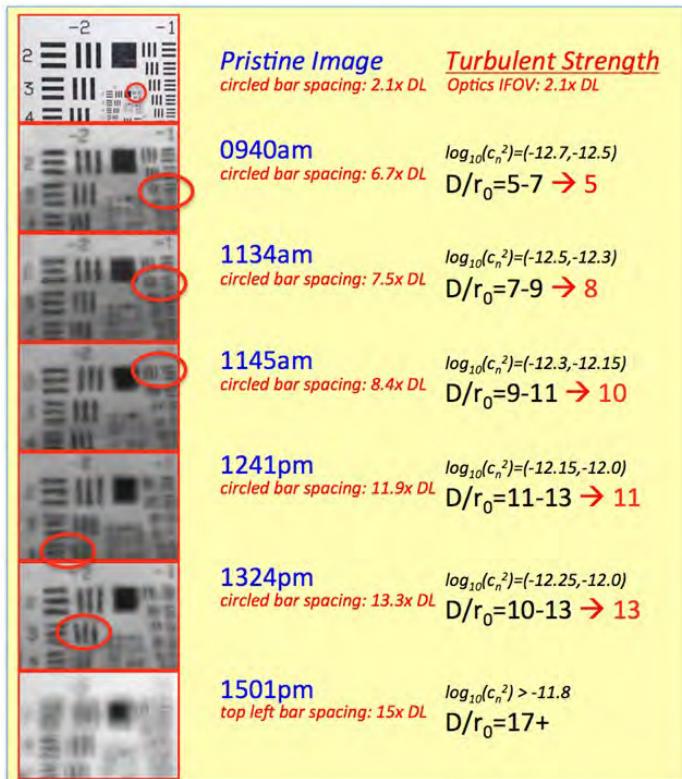

Figure 1. Turbulence strength chart. The target is taken through increasing levels of turbulence characterized by D/r_0 shown on the right. The USAF 1951 resolution test chart aids in extracting an "apparent turbulent resolution" that can be directly compared to a scintillometer measurement.
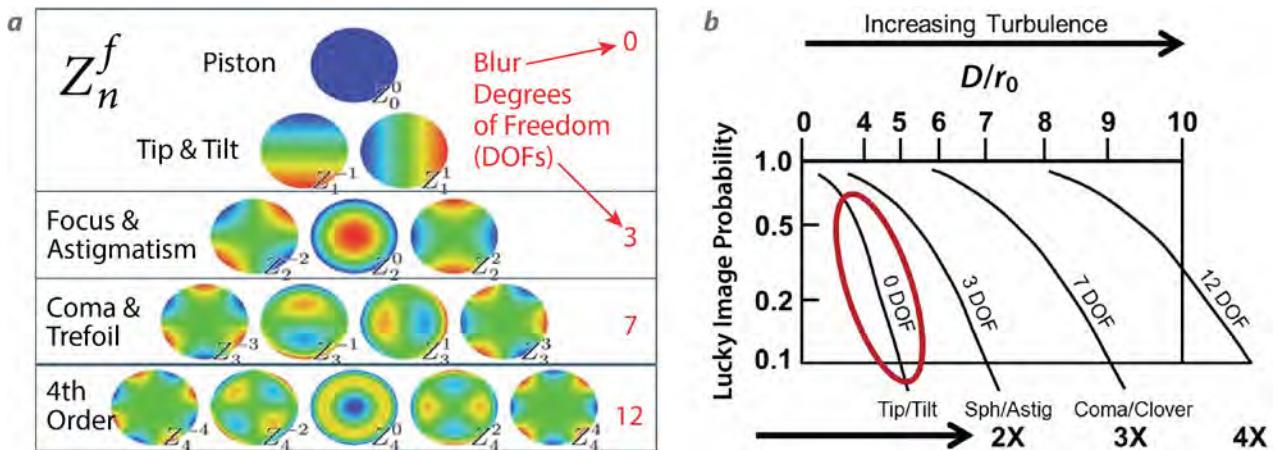
Figure 2. (a) The first twelve Zernike DOFs, and (b) the probability of getting a lucky image with different DOFs of Zernike corrections

associated with atmospheric turbulence (Beckers 1993). For scene-based Shack-Hartmann AO systems, the source is not completely coherent, so interferometers are not used. Instead, an image of the pupil is projected onto a lenslet array, such that each lenslet represents a different portion of the entrance aperture. Each lenslet images the scene onto a different portion of an image plane. In the absence of turbulence, the images of the point source are uniformly distributed based on the lenslet configuration. With wavefront distortions, the images of the point source will shift from their nominal positions. The corresponding pixel shifts are related to the slopes of the phase of the wavefront for each aperture location. Algorithms for extracting the wavefront distortion exist, but these all rely on high spatial frequency content and typically require a point source in the scene. The phase map derived from these algorithms generates the commands to a deformable mirror that corrects for the wavefront distortion associated with turbulence. The algorithms for detecting the shifts must be fast enough to change the mirror as the turbulence changes.

While AO works well for astronomical viewing, the same methods do not work well for complex imagery from long-range horizontal paths. Some Shack-Hartmann analysis has been done for astronomical extended sources with this sensor type (Sidick 2007, 2013; Lukin 2010, Rais 2016), but this work has not

been extended to horizontal paths. The Army Research Laboratory passive adaptive imaging is specifically designed to mitigate horizontal path turbulence (Tofsted 2016), but its implementation includes moving parts not suitable for a compact AO system. Each of these methods for extended sources uses the received imagery to compute pixel shifts associated with wavefront distortion, and all suffer from the same lack of high spatial frequency content that is characteristic of high turbulence. Currently, no adequate compact solution exists for significant long-range horizontal path–induced degradation.

Project

The goal of this project is to develop a compact AO system for long-range horizontal paths that improves severely degraded images. To do this, we are leveraging the statistical tools developed as part of a prior SDRD project (O'Neill 2014, Terry 2014), AO work from literature, and bispectrum methods developed by Lawrence Livermore National Laboratory (Carrano 2013).

There are two key aspects to this research. First, instead of using a lenslet array, we are leveraging commercial off-the-shelf (COTS) cameras and filters to create a red/green/blue (RGB) wavefront sensor (WFS). This allows the same imagery used for obtaining the wavefront distortion to be provided seamlessly to the user. It also

allows us to access second- and third-order statistics via RGB color separation. We use the method to obtain temporal variance images developed in an FY 2013 SDRD project (O'Neill 2014, Terry 2014) to extract high spatial frequency content associated with the scintillation index; this helps determine wavefront distortion, even in strong turbulence. By updating this variance image at each frame, new pixel shifts can be obtained on a frame-by-frame basis. Using these techniques, in Year 2 we will integrate a deformable mirror into our telescope that will improve overall image quality and will enable existing algorithms to further the improvement.

Figure 3 shows the RGB WFS block diagram and the hardware developed in Year 1. Solar illumination reflects off the scene and enters the three sub-apertures. When the telescope is focused and there are no turbulent effects, the three images align perfectly. Because individual light rays go through different points of a plane before or behind focus, any defocus shows up as a pixel shift. When in focus, the pixels are oriented to the same point on the image plane, but when out of focus, the shifted pixels indicate degrees of tip or tilt.

We selected a Meade EXT-90 Maksutov-Cassegrain telescope and a Point Grey Grasshopper camera for our first breadboard. We verified the operation of this camera with an off-the-shelf mobile Samsung-based 8-CPU single-board computer (SBC) that drives the USB3 camera, runs Linux, operates on battery, and offers WiFi hot spot connectivity. Full integration with this type of SBC will take place in Year 2.

The filters for this system were carefully chosen. We measured the relative spectral response of the Point Grey Grasshopper camera using an Ocean Optics HL-2000 tungsten halogen light source, an Ocean Optics FlameT spectrometer, an Edmund Optics 37-597 mini-Chrom monochromator, and custom Matlab analysis code. We used these data along with the ASTM-G173 solar spectrum to select filters that maximized the ratio of band color to leakage from the other two bands while providing approximately equal photon flux in each of the three bands. A filter set from Edmund Optics was selected. It provided signals that were within 15% of the mean photon flux with worst-case leakage signals that were about 25% of the total received flux. More information on the measurements and analysis to select filters is available from the authors upon request.

Once the system was constructed, three different datasets were collected. Two collection tests were done in the Special Technologies Laboratory (STL)
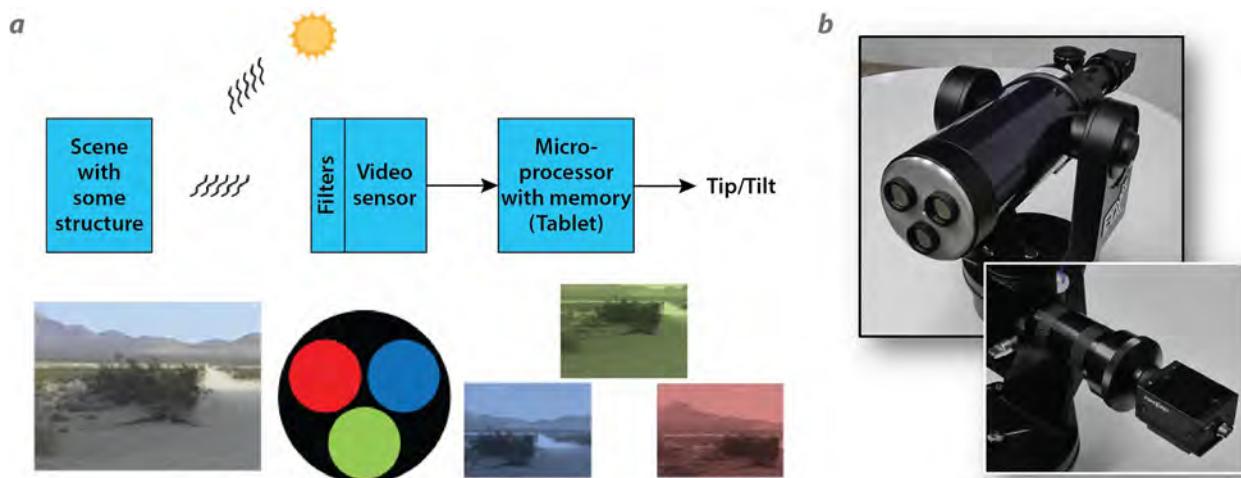


Figure 3. (a) RGB wavefront sensor (WFS) Year 1 block diagram and (b) hardware. The sun illuminates the scene with some structure. The reflected light enters the three filters at the entrance to the telescope. When in focus all three images align, but out of focus the pixel shifts correspond to the slope of the phase errors. These errors can be used to compute commands to a deformable mirror.

Figure 4. STL parking lot tests. The RGB WFS is approximately 175 meters from the target vehicles. These tests confirmed our ability to get pixel shifts and helped determine how to correlate these shifts to defocus.

parking lot at a distance to target of about 175 meters. Targets for these collection tests were the scientists' own vehicles and glint from an unidentifiable vehicle. A photo of this setup is shown in Figure 4. These tests were intended to verify the ability of our system to detect pixel shifts. Figures 5a–5c show a glint off the tail of a vehicle as we manually took the telescope through different modes of focus.

Figure 5d shows the relative pixel shift rows (horizontal) and columns (vertical) for red to green and green to blue. Note that the direction of focus error is evident by the locations of the red, green, and blue relative to each other.

For the third test, we piggybacked on a sponsor test at White Sands Missile Range (WSMR). This test provided us with scintillometer data and data at horizontal path ranges of 125, 300, 800, and 1800 meters using a 1951 USAF target in each scene.

This test occurred in mid-September 2016. Although data analysis is still in progress, the initial analysis is promising. The variance image developed in the earlier SDRD project enhances the turbulent flows even with minimal image contrast and thus will provide image shifts even in extremely high turbulence. It is the refractive index structure function that is paramount to creation of the variance image. While other AO

methods rely on the structure in the image, using the variance image relies on the movement of the turbulence itself. This not only enhances edges, but also enables visualization of any intensity changes associated with the turbulence. This visualization allows detection of pixel shifts even in strong turbulence. Because we have three co-aligned apertures, the pixel shifts in the variance image correspond to the phase shifts associated with the apertures.

Given an intensity measurement imaged onto a focal plane at pixel location x, y, at time t, and based on proportionality to Kolmogorov's ansatz (Kolmogorov 1941), we define the received flux variance as the normalized variance over all pixels on the focal plane over n samples in Δt increments as

$$\sigma_z^2\left(x,y,t\right)=\frac{\left\langle I\left(x,y,\tau\right)^2\right\rangle_{\tau=t_0\text{ to }t_0+n\Delta t}-\left\langle I\left(x,y,\tau\right)\right\rangle_{\text{all }x,y\,\&\,\tau}^2}{\left\langle I\left(x,y,\tau\right)\right\rangle_{\text{all }x,y\,\&\,\tau}^2}. \quad \textbf{(2)}$$

In this equation, the variables x, y, and t represent the x pixel location on the detector, the y pixel location on the detector, and the time of the frame. The variable I represents received intensity in counts.

To extract only the turbulence information, and not the scene or sensor noise, for each row, r, or column, c, in the image, the 1-D Fourier transform is computed to
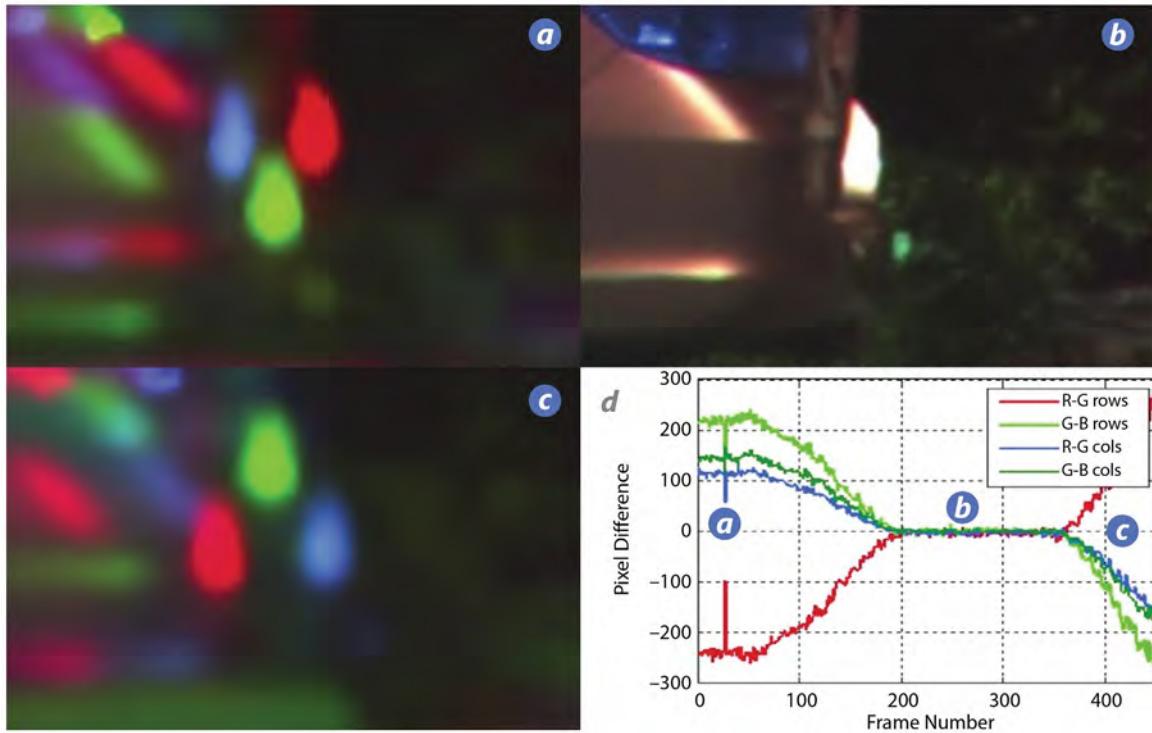
Figure 5. RGB WFS image as the telescope is manually run through (a) focus short, (b) in-focus, and (c) focus long, also evident in (d) the focus plot at lower right

obtain the 1-D power spectral density (PSD) of turbulence, $V(k)$. In practice, a fast Fourier transform may be used for horizontal calculations by defining k as the spatial frequency in radians/pixel and the estimated 1-D PSD for each row, r, for the Bayer red (R) channel, as

$$V_R\left(k_x, y = r, t\right) = \left| \sum_{x=0}^{N-1} \sigma_{z\_R}^2\left(x, y = r, t\right) e^{-ik_x x/N} \right|. \qquad (3)$$

This can be repeated for green (G) and blue (B). Using the variance image, tip and tilt are derived directly from image shift differences between colors. Furthermore, because we use the relative shifts between colors, any platform motion is cancelled out—which is a critical requirement for compact operation. We compute the relative phase shift in the image in radians for red to green as

$$\alpha_{R/G}\left(k, r, t\right) = imag\left[\frac{V_R\left(k_x, y = r, t\right)}{V_G\left(k_x, y = r, t\right)} \right]. \qquad (4)$$

This process is repeated for G/B and R/B to get all three cases. To get the horizontal pixel shifts related to tip, we then multiply by the frequency such that

$$\Delta x(r,t) = \left| \sum_{k_x} \alpha_{R/G}\left(k_x, r, t\right)/k_x \right|. \qquad (5)$$

This process can be repeated for all columns to get the vertical shifts related to tip.

Data from the September test at the WSMR at 800 m to target were analyzed. Figure 6 shows a histogram-stretched demosaicked image (Figure 6a) and the variance image (Figure 6b). Note that there is information in every pixel, even in the dark areas, as can be seen by the different color pixels in the inset.

Color cameras automatically demosaic imagery by converting Bayer pixel space to RGB color planes, so the user sees only a color picture, which typically has mixing of the original Bayer pixels. Our processing is done on the raw Bayer pixels; therefore, the color separation remains intact, thus producing images directly associated with the three apertures. A first-order calculation of the vertical pixel shifts that relate to tilt was done on the whole image. A histogram of the vertical shifts associated with all frequencies is shown in Figure 7.
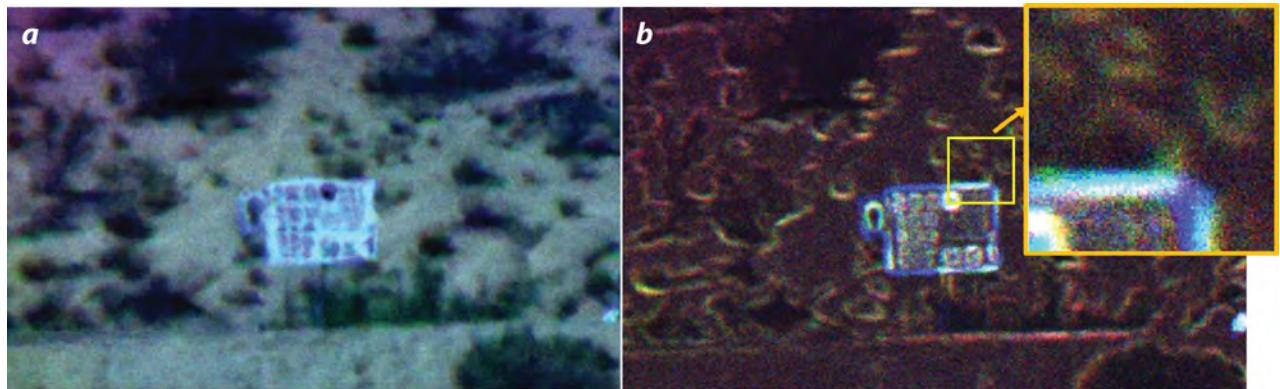
Figure 6. (a) A stretched demosaicked image from the sensor allowing a better visualization of the imagery. Note that the red in the sky is an anomaly of the stretching, which caused the blue and green channels to saturate and is not in the original, darker image. (b) The variance image with an inset showing that there is information even in the dark areas where the pixel color varies due to the shifts.

Note that the green and blue apertures were aligned in this dimension, so no information can be obtained. The red/green and blue/red show shifts at the peak of about 5 and 10 pixels. The width of the histogram indicates variations in the shifts throughout the image and confirms that by using various regions of the image we should be able to extrapolate to various regions of the aperture. We plan to use our phase correlation registration algorithms (that are already implemented on an SBC) on received variance images to extract pixel shifts. In addition, we will leverage the existing block shift methods developed by Fifth Gait (O'Neill 2014, Terry 2014) to extract pixel shifts for different separated regions of our variance images. Based upon statistical analysis, we then extrapolate tips and tilts associated with the separated regions of the aperture for anisoplanatic imaging conditions associated with higher turbulence levels.

We have already implemented the phase correlation registration and high confidence block shifts on regular images using Linux SBC (ODROID XU4 featuring a Samsung Exynos 5422, 8-core mobile chip). Because this chip is common to many Samsung Galaxy tablets, implementation of this work into a tablet with a real-time display should be straightforward.
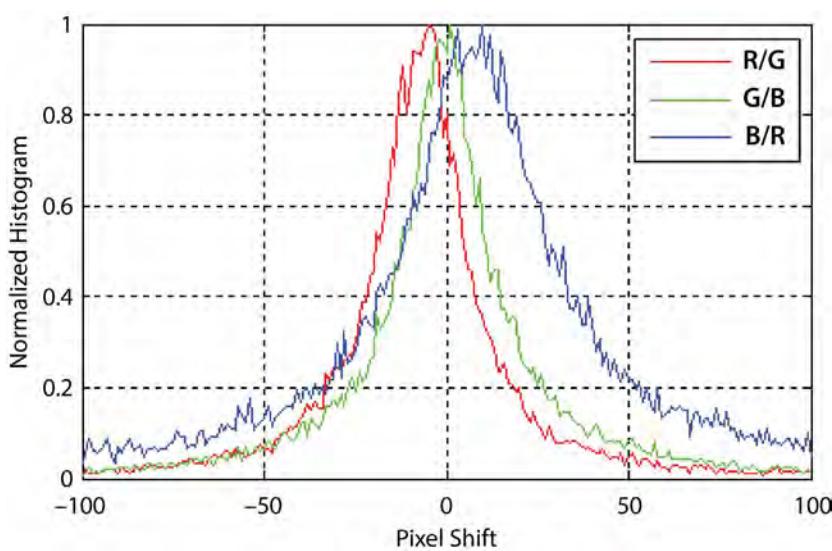
Figure 7. Histogram of vertical pixel shifts for red to green (red), green to blue (green) and blue to red (blue). Note that the green and blue apertures were aligned in this dimension; thus, there are no shifts. The other two show shifts on the order of 5 and 10 pixels at the peak. The width of these histograms indicates variations within the scene.

Conclusion

In our first year, we created a prototype RGB WFS using COTS components. We developed methods to extract tip/tilt degree using the Kolmogorov nature of turbulence. We proved that additional modes are available via variations in the pixel shifts throughout the image.

The key to this work is the three-color aperture configuration and the use of the temporal statistics associated with the variance image to improve the ability to get pixel shifts even in high turbulence.

In Year 2 we will select and integrate a deformable mirror and a suitable SBC or tablet. This deformable mirror will replace the standard mirror in the telescope at the exit pupil. We will analyze data to correlate deformable mirror piston position with our measured pixel shifts. Ideally we will integrate our algorithms and deformable mirror control into our tablet to create a fully compact system. At the end of Year 2, we hope to demonstrate this AO system for long-range horizontal paths as shown in Figure 8.

Acknowledgments

References

Beckers, J. M., "Adaptive optics for astronomy: Principles, performance, and applications," *Ann. Rev. Astron. Astrophys.* **31** (1993) 13–62.

Born, M., E. Wolf, *Principles of Optics*, Section 9.2, Pergamon, New York, 1965.

Carrano, C., "Bispectral speckle imaging algorithm performance on specific simulated scenarios," LLNL-TR-645877, Lawrence Livermore National Laboratory, Livermore, California, November 2013.

Fried, D. L., "Optical heterodyne detection of an atmospherically distorted signal wavefront," *Proc. IEEE* **55** (1967) 57–77.

Fried, D. L., "Probability of getting a lucky short-exposure image through turbulence," *J. Opt. Soc. Am.* **68** (1978) 1651–1658.

Hufnagel, R. E., "The probability of a lucky exposure," Tech. Memo, REH-0155, Perkin-Elmer, Norwalk, Connecticut, February 1989.

Kolmogorov, A. N., "The local structure of turbulence in incompressible viscous fluid for very large Reynolds numbers," *Dokl. Akad. Nauk SSSR* **30**, 4 (1941) 301–305.

Lukin, V. P., N. N. Botygina, O. N. Emaleev, P. A. Konyaev, "Wavefront sensors for adaptive optical systems," *Meas. Sci. Rev.* **10**, 3 (2010) 102–107.
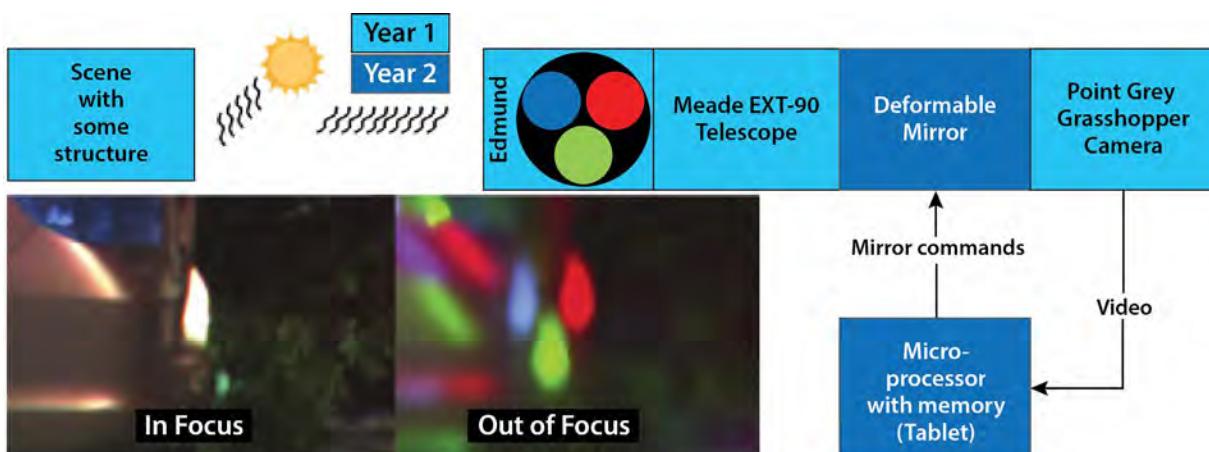
Figure 8. Completed system at the end of Year 2

Martinez, P., J. Kolb, M. Sarazin, A. Tokovinin, "On the difference between seeing and image quality: When the turbulence outer scale enters the game," *European Southern Observatory Messenger* **141** (2010) 5–8.

Max, C., Lecture 3 of Astronomy 289C: Adaptive Optics and its Applications, University of California, Santa Cruz, April 8, 2010.

Noll, R. J., "Zernike polynomials and atmospheric turbulence," *J. Opt. Soc. Am.* **66** (1976) 207–211.

O'Neill, M. D., D. Terry, A. Potter, I. McKenna, "Passive method to characterize atmospheric turbulence," in *Site-Directed Research and Development*, FY 2013, National Security Technologies, LLC, Las Vegas, Nevada, 2014, 125–135.

Rais, M., J.-M. Morel, C. Thiebaut, J.-M. Delvit, G. Facciolo, "Improving the accuracy of a Shack-Hartmann wavefront sensor on extended scenes," *6th International Workshop on New Computational Methods for Inverse Problems (NCMIP)*, May 2016, Cachan, France, https://hal-enpc.archives-ouvertes.fr/hal-01344949/document, accessed October 5, 2016.

Sidick E., J. J. Green, C. M. Ohara, D. C. Redding, "An adaptive cross-correlation algorithm for extended scene Shack-Hartmann wavefront sensing," in *Adaptive Optics: Analysis and Methods/Computational Optical Sensing and Imaging/Information Photonics/Signal Recovery and Synthesis Topical Meetings on CD-ROM*, OSA Technical Digest (CD) (Optical Society of America, 2007), paper JTuA7, http://www.meripet.com/Papers/JTuA7.pdf, accessed October 5, 2016.

Sidick, E., "Extended scene Shack–Hartmann wavefront sensor algorithm: Minimization of scene content dependent shift estimation errors," *Appl. Opt.* **52** (2013) 6487–6496.

Terry, D., M. D. O'Neill, "Passive method to characterize atmospheric turbulence," *MSS Passive Sensors*, Gaithersburg, Maryland, 2014.

Tofsted, D. H., "Turbulence simulation: Outer scale effects on the refractive index spectrum," ARL-TR-548, Army Research Laboratory Technical Report, November 2000, http://www.arl.army.mil/arlreports/2000/ARL-TR-548.pdf, accessed April 6, 2015.

Tofsted, D., "Passive adaptive imaging through turbulence," *Proc. SPIE* **9833** (2016) 98330B.

This page left blank intentionally

High-Yield X-Ray Photocathodes for Next-Generation Imaging Detectors
LO-03-15 | Continued from FY 2015 | Year 2 of 2

Kathy Opachich,[1,a] Andrew MacPhee,[b] Otto Landen,[b] Ning Chen,[c] Ashwini Gopal,[c] Salah Udin,[c] Terry Hilsabeck,[d] Eric Huffman,[d] Jeffrey A. Koch,[a] Jun Feng,[e] Patrick Ross,[a] Dave Bradley,[b] and Sabrina Nagel[b]

In this two-year project we are developing a next-generation, high-yield x-ray photocathode for use in the spectral energy range from 1 to 20 keV. In our first year (Opachich 2016a), we fabricated a silicon photocathode and developed a coating procedure for the gold metal emission layer. This anisotropic, high-aspect ratio structure was produced in silicon using inductively coupled plasma-etching technology. The process was specifically developed to generate the high pattern density of the photocathode chip to achieve the desired sidewall profile angle. The tapered sidewall profile angle precision has been demonstrated to be within ±2.5° for a ~12° wall angle, with feature sizes that range between 3 to 9 μm wide and 3 to 17 μm deep. The second year of this project involved photocathode characterization and testing of the photocathodes in an x-ray streak camera. The structured photocathodes showed an increase in secondary electron yield of up to 3x over the standard planar photocathode. Here we discuss the device design, the method used to produce a set of geometrically enhanced high-yield x-ray photocathodes in silicon, along with the characterization and testing results.

[1] opachiyp@nv.doe.gov, 925-960-2520

[a] Livermore Operations; [b] Lawrence Livermore National Laboratory; [c] NanoShift, LLC; [d] General Atomics; [e] Lawrence Berkeley National Laboratory

Background

Time-resolved x-ray diagnostics are widely used at the National Ignition Facility (NIF) (Miller 2004). Currently the facility uses streak camera detectors, such as the Diagnostic Insertion Manipulator Imaging Streak Camera (Opachich 2012), Streaked Polar Instrumentation for Diagnosing Energetic Radiation (SPIDER) (Khan 2012), and time dilation imaging tubes (Hilsabeck 2010, Nagel 2012) for imaging in the 5 to 10 keV range. The introduction of the Advanced Radiographic Capability on NIF will provide imaging sources that extend well above the 10 keV limit. However, current detectors rely on photocathode materials to convert photon signals to electrons, which are then dispersed temporally with the use of voltage ramps and magnetic fields. The imager

detector efficiency and operational range is somewhat limited to below 10 keV due to a sharp reduction in quantum efficiency (QE) of most photocathode materials (i.e., gold and cesium iodide) (Hara 2000, Khan 2013, Opachich 2014). Geometrically enhanced photocathodes provide a potential solution, and they can be easily integrated into existing detectors without compromising performance.

The electron yield can be improved by better matching the x-ray path length to the very thin top-most emission layer of the photocathode, defined as the electron escape depth. This is accomplished by changing the incidence angle of x-ray photons to a very shallow, near-grazing geometry, as shown in Figure 1. The secondary electron escape depth is typically very
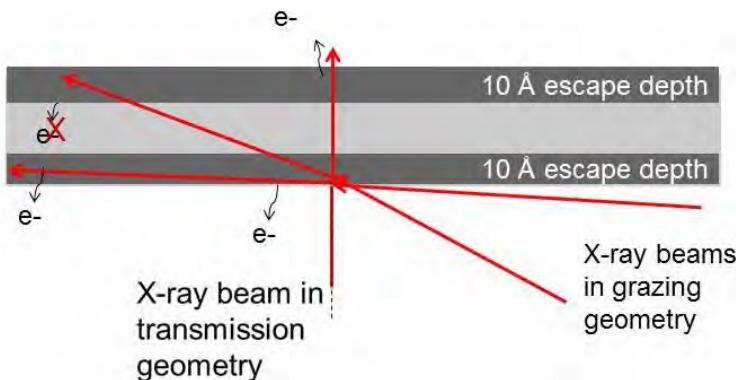
Figure 1. Example of the grazing incidence and transmission geometry. The electron escape depth (not to scale) is shown on both sides of the photocathode. Electrons that are generated within the bulk do not contribute to the measured yield.

thin; for example, in Au it is limited to the top 10 Å and to 250 Å of the photocathode surface (Henke 1981, Fraser 1992). Angles θ below ~20° are needed to provide significant enhancement. Grazing incidence detectors have utilized this geometry and demonstrated improvement in photocathode QE by a factor of 15–20 times in the soft x-ray range (Feng 2010). This effect can also be extended to the 10–20 keV range, as predicted by the semi-empirical model by Fraser (1983a, 1983b).

Changing the incidence angle of current NIF detectors is costly and may not be possible due to engineering design constraints; however, it is fairly simple to change the design of the photocathodes by introducing geometrically enhanced surfaces such as pillars, cones, or recessed cavities. A recent study used CST Studio Suite, an electromagnetic modeling software, to determine a set of structured photocathode designs

that would increase the observed yield by up to 3.5 times without changing the spatial and temporal performance of current x-ray detectors (Opachich 2014). Based on this work, we decided to use recessed cone and pyramid designs to develop a set of structured photocathode prototypes. The two designs are shown in Figure 2. It was later determined that the pyramid structures are more efficient and easier to fabricate, which drove the decision to make a full-scale recessed pyramid cathode for characterization and testing in a streak camera.

Project

Prototype Photocathode Design and Production

Based on CST Studio Suite modeling work previously done at NSTec Livermore Operations, two structures were chosen: the recessed cone and pyramid
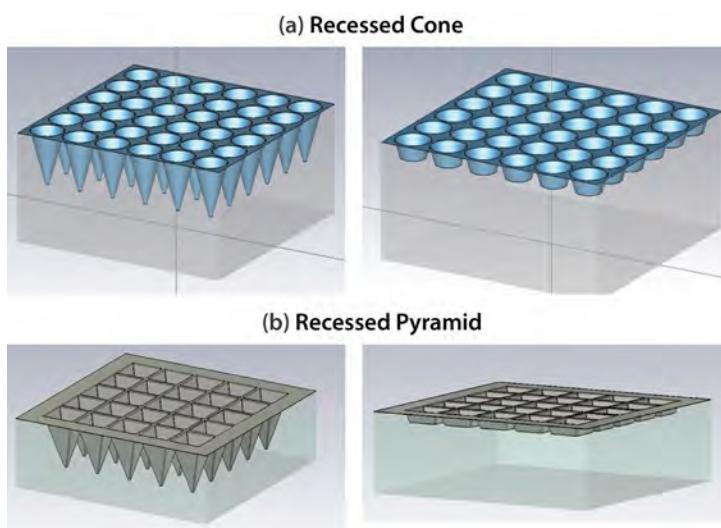
Figure 2. The recessed designs: (a) full-length and shallow cone structures and (b) the full-length and shallow pyramid structures. The substrate material is Si with a 700 Å Au coating at the top surface.

Table 1. Cone and pyramid prototype specifications

| Cathode Type	Incidence Angle (degrees)	Width (µm)	Depth (µm)	Predicted Yield Increase
Full-Scale	12 ±2.5	6 × 6	4	2.3
Full-Scale	12 ±2.5	6 × 6	8	3.2
Full-Scale	12 ±2.5	6 × 6	16	3.6
Test Sample	12 ±2.5	9 × 9	3	1.63
Test Sample	12 ±2.5	9 × 9	8.4	2.45
Test Sample	12 ±2.5	9 × 9	16.8	3.2

Table 2. Fabrication requirements

Requirement #	Description	Value	Tolerance
1	Wall Angle	12°	±2.5°
2	Depth	3, 8, and 16 µm	±2 µm
3	Pitch	2 µm	±0.2 µm
4	Diameter/Width	9 µm or 6 µm	±0.2 µm
5	Coating Thickness	20 Å Ti (wetting layer) and 700 Å Au	±200 Å
6	Coating Roughness	200 Å	--
7	Substrate Thickness	150 µm	±2 µm

(Opachich 2014). The model predicted a yield increase as a function of structure depth. To test this prediction, depths of 3, 8, and 16 µm were chosen for cathode characterization and testing. For this work, two types of test sample sets were fabricated: a set of 16 × 16 mm wide recessed pyramid cathodes, along with a set of full-scale photocathodes (8 × 30 mm) that were tested in a NIF streak camera. The full-scale design used a split photocathode, with the planar and structured surface located side-by-side for ease of comparison in a single image. Table 1 summarizes the requested structure types, the depth and width of the structures, and their relative expected yield. The photocathode fabrication specifications are listed in Table 2. The conceptual drawings of the test photocathode and full-scale cathode are shown in Figure 3.

After the simulation stage, we developed a plasma etch recipe with NanoShift, LLC. The final photocathode prototype was fabricated according to the requirements in Table 2. The coatings were electron beam sputter–deposited onto the Si substrate. The project was split into four phases and accomplished in several development steps in order to minimize risk. In the first
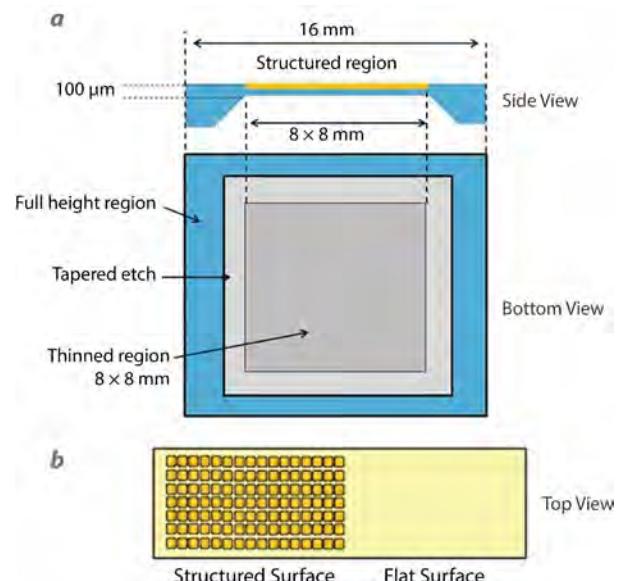

Figure 3. (a) Test photocathode design and (b) full-scale photocathode detail, showing the split planar and structured side-by-side cathode design. The full-scale photocathode dimensions are 30 × 8 mm.

- Silicon on insulator (SOI) wafers
- Substrates coated with Ti + Au using e-beam sputter deposition

Figure 4. Summary of the six-step process used to fabricate the structured photocathode prototypes

Photoresist   Device layer   Box layer   Handle layer   Metal layer
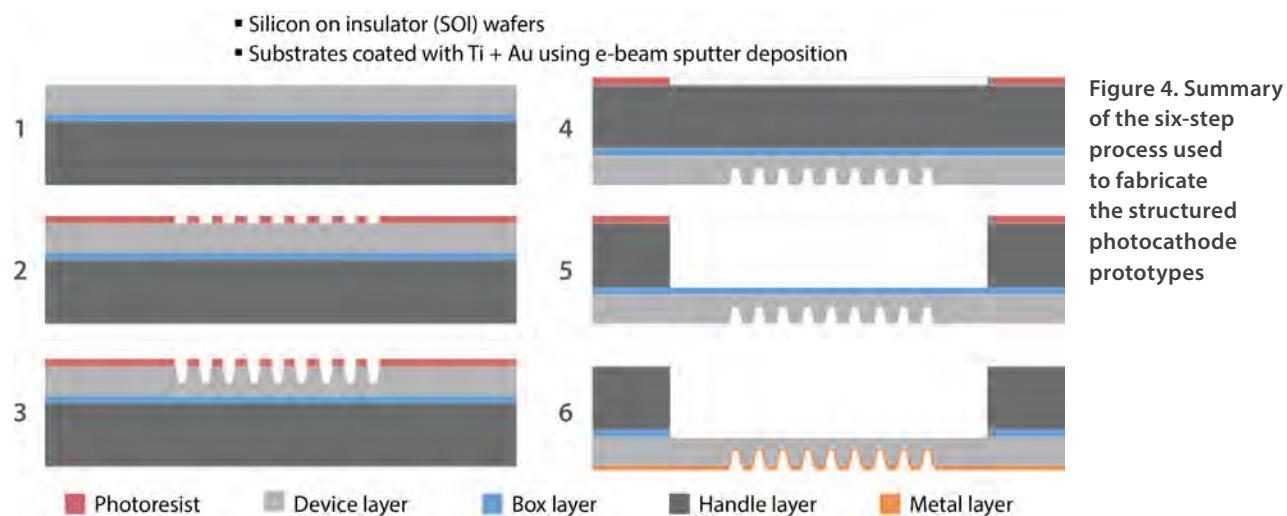
phase an initial resist mask was developed, and several methods were evaluated on test wafers. Because the pyramid structures had a better etch quality than the recessed cones, the pyramid design was chosen as the preferred structure for the remaining work. In phase two, the etching process was further tested and developed on prototype wafers. Phase three focused on coating methods and developing an etch recipe for back thinning the devices. During the final phase, the prototype structures were completed.

Figure 4 summarizes the final etching and coating process that was developed. The devices were built from Si on insulator (SOI) wafers that have an insulating layer that separates the device into two regions, the device layer and the handle. The device layer was masked with photoresist, and the structures were etched out by using a plasma-etching system. After etching, the mask was removed and a photoresist applied to the handle region for back thinning. After back thinning was completed, the total device thickness was 150 μm. The final step involved electron beam sputtering onto the substrate a thin wetting layer (20 Å) of titanium (Ti) followed by a 700 Å coating of Au.

Examples of the recessed-pyramid photocathode prototypes are shown in Figures 5 and 6. The recessed pyramid devices show a wall width of 9 μm, a depth of ~8 μm, and a sidewall angle of ~12°. The coating thickness is from 900 to 1100 Å with a roughness of ~200 Å.
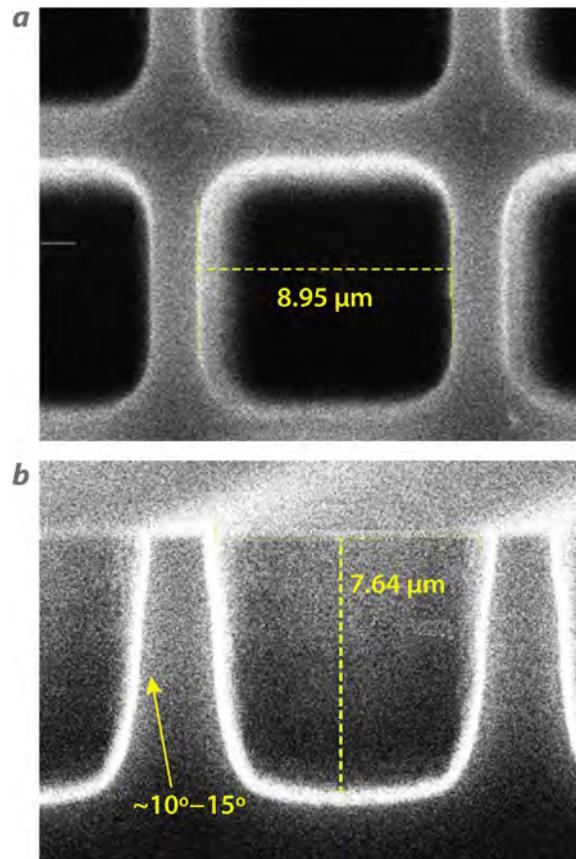
Figure 5. Scanning electron microscope images of a mid-length recessed pyramid structure showing (a) a top view of the structured photocathode and (b) a cross-sectional pan view of the quality of the coating at the edge
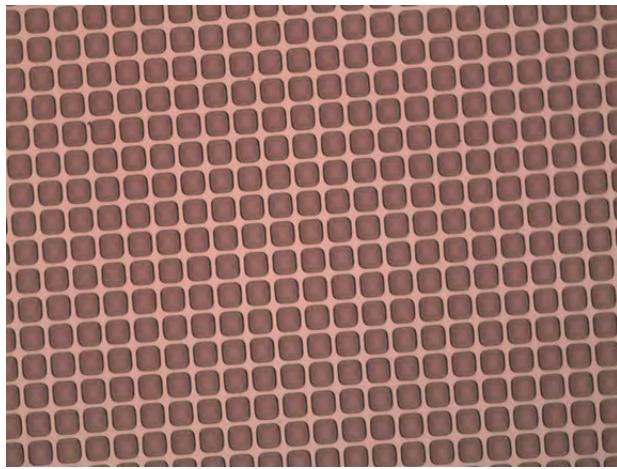
Figure 6. Optical image of the recessed pyramid structures. Some rounding is present at the corners due to the plasma-etching process. This will help alleviate field reduction in future detector testing. Because this is an image taken on an optical system, only the top surface is seen due to the depth of focus of the microscope objective.
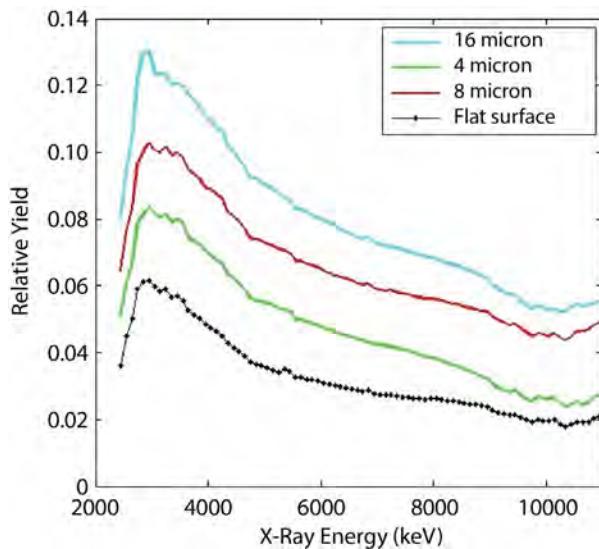
Figure 7. Relative electron yield measured for three test sample prototypes and a planar photocathode shows increases of ~1.3x, ~2.3x, and 2.7x for the shallow, mid-depth, and full-depth structure geometries, respectively

This thickness is adequate for higher x-ray energies and satisfies our requirement. An optical image of the recessed pyramid test structures is shown in Figure 6. Here we see that the structures are 9 µm in width, are very periodic, and show little deviation from the pitch and width requirements.
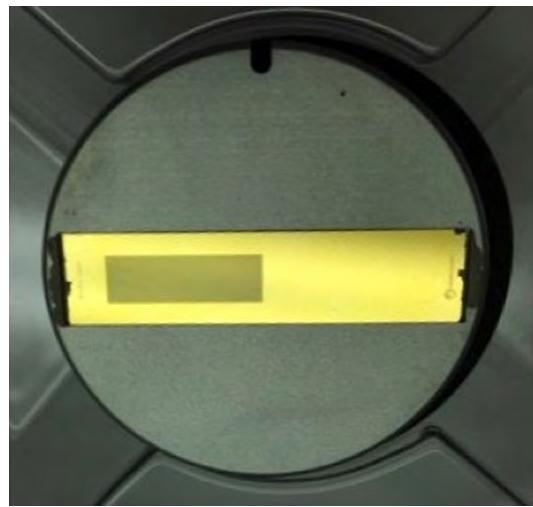
Figure 8. Image of the full-scale photocathode in a SPIDER mount

Prototype Photocathode Characterization

The photocathode prototypes were first characterized at the Advanced Light Source (ALS) and then tested in a NIF streak camera, SPIDER. The characterization results from the ALS are shown in Figure 7. From these data, we see that the relative yield increases by ~1.3x, ~2.3x, and 2.7x for the shallow, mid-depth, and full-depth structure geometries. The effect is also seen at higher energies, at 5–10 keV. These data will be remeasured with higher accuracy and published in a journal in the near future.

The photocathodes were further tested in a streak camera; these tests measured the overall yield improvement and characterized detector performance changes that might have been introduced by the structured surface (Opachich 2016b). An image of the large-format full-scale photocathode is shown in Figure 8. The study determined the overall detector efficiency increase as well as changes in spatial resolution of the detector. The work was performed using a Manson x-ray source tuned to emit the Ni K-α lines at ~7.5 keV by adjusting the anode to filament voltage and using a 3 µm thick nickel (Ni) filter (Figure 9).

To characterize improvement in signal level, x-ray images were collected using each full-scale prototype. The recorded side-by-side signal image of the
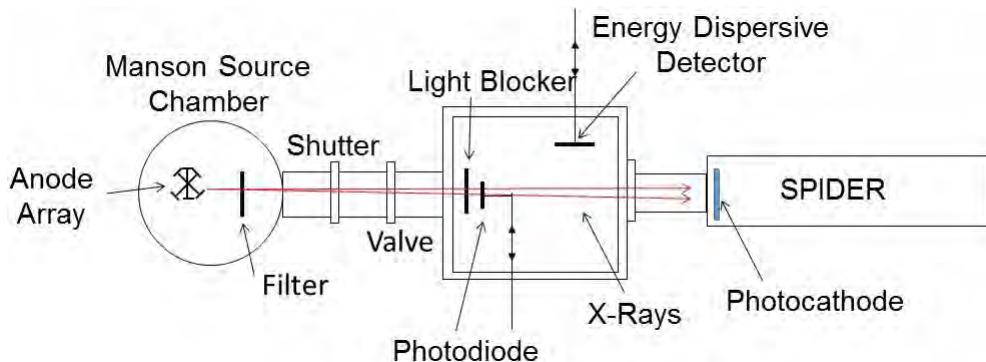
Figure 9. Experimental setup. The Manson source layout is shown, starting with the vacuum chamber that contains the anode array on the left. The streak camera and test photocathodes are 1 m away from the anode source.
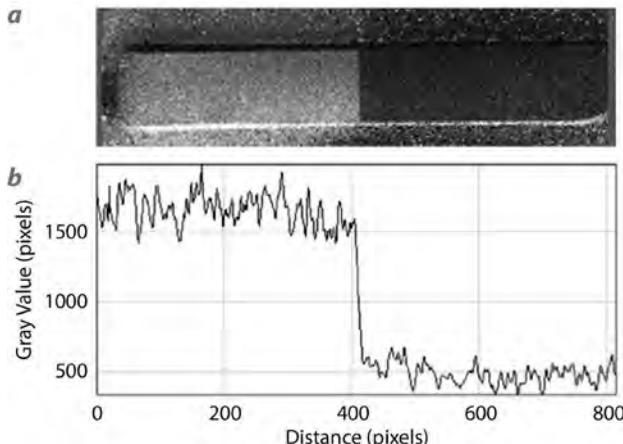
Figure 10. Structured photocathode test results: (a) The photocathode CCD image and (b) a lineout covering the central ¼ regions through both the structured and planar cathode areas

full-depth structure prototype is shown in Figure 10. The image was background subtracted and flat fielded to take out non-uniformities introduced by the SPIDER imaging system. Typically background levels were near ~510 counts, with the lowest signal of 500 counts above background recorded in the planar cathode region. The bright region seen in Figure 10 corresponds to that of the full-depth recessed pyramid structures. A lineout through the interface is presented in Figure 10b, showing an increase in signal of ~3.5x. An increase in signal between 2.7x and 4.5x was expected for this structure; details of the model and calculations are given in our previous publication (Opachich 2014). In terms of total QE, a planar Au photocathode at 7.5 keV emits an average of 0.015 (Henke 1981) electrons per

photon; we measured that the structured surfaces in our work increase this number to 0.05. The predicted and measured yields from all three structures are summarized in Tables 1 and 3, respectively. The measured fractional increase is defined as the ratio between the signal recorded in the structured region and flat surface region. The increase in yield from the mid-depth to the full-depth is smaller than predicted. We believe this discrepancy is potentially caused by differences in the etched wall angles and widths of the two prototypes, namely an etch that is not fully tapered to a full cone and a decrease in the electric field strength within the full depth cavity that may be trapping emitted electrons. In general, the measured data fall within the predicted yield increase, verifying our model and calculations.

The spatial resolution of SPIDER was measured using a standard planar photocathode and compared with the results from all three prototypes. A single spatial resolution mask was used for all measurements, and the resulting image and line spread functions (LSFs) are shown in Figure 11. Each LSF was normalized to unity and then fitted to a Gaussian function to determine the FWHM. The mid-depth structure appears to have the widest FWHM. This condition is typically caused by a slightly wider width of the etched recessed pyramid. For all three structures no correlation was seen between the LSF width and structure depth, showing that the chosen 6 × 6 μm width was appropriate and the spatial resolution of the detector is not compromised by the introduction of the structured

Table 3. Characterization results

Cathode Type	Incidence Angle (degrees)	Diameter / Width (μm)	Depth (μm)	Measured Yield Increase	Spatial Resolution
Full-Scale	12 ±2.5	6	4	2.6	87 ±8
Full-Scale	12 ±2.5	6	8	3.2	88 ±10
Full-Scale	12 ±2.5	6	16	3.5	85 ±14
Test Sample	12 ±2.5	9	3	1.3	N/A
Test Sample	12 ±2.5	9	8.4	2.3	N/A
Test Sample	12 ±2.5	9	16.8	2.7	N/A
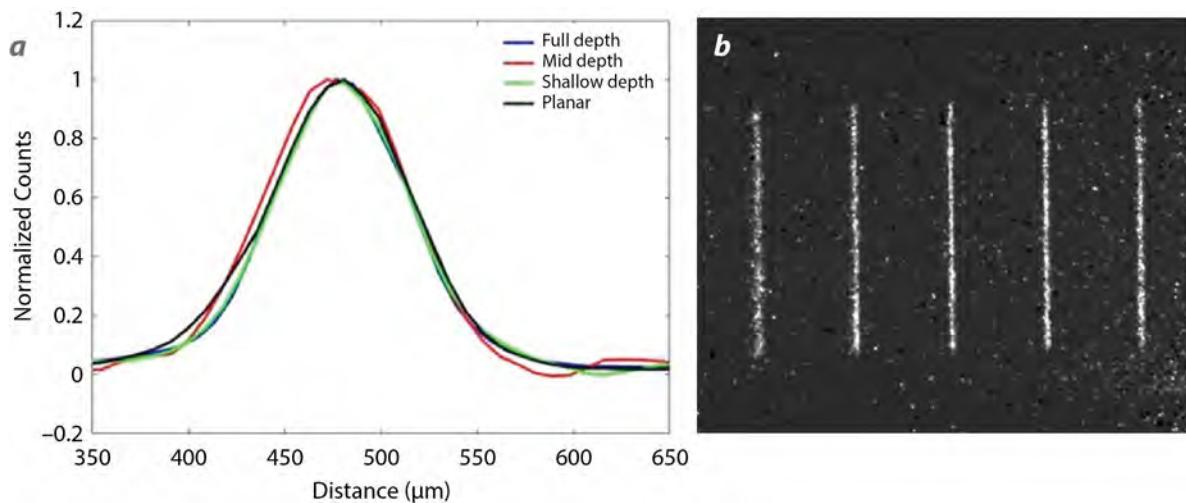
Figure 11. Measured spatial resolution: (a) The calculated LSF for each cathode type and (b) an example of the recorded spatial resolution pattern. Spatial resolution is not affected by the addition of the structured surface. Resolution matches that of the standard cathode for structures of all depths.

surfaces. The standard spatial resolution at the photocathode was measured to be 87 ±10 μm, while the spatial resolution obtained from the structured region ranged from 85 to 88 μm. The width varies mostly due to different signal-to-noise ratio levels. The spatial resolution results are summarized in the last column of Table 3.

Conclusion

In this two-year SDRD project, a geometrically enhanced photocathode has been developed, characterized, and tested in a NIF streak camera, SPIDER. The results show an increase in yield of up to 3.5x at 7.5 keV. The measured increase in yield is within the predictions made for this structure. It was also shown that the structured photocathode surface does not affect the spatial resolution of the detector. Temporal

resolution measurements should be performed in the future to ensure that the detector performance remains unchanged. This demonstration with Au motivates exploration of comparable enhancements with cesium iodide (CsI) and may revolutionize x-ray streak camera photocathode design.

This work resulted in a full patent application (Opachich 2016b), several presentations at the High Temperature Plasma Diagnostics Conference (Opachich 2014, 2016c), a talk at the SPIE Optics and Photonics Conference (Opachich 2015), and two talks at the National Inertial Confinement Fusion Diagnostics Meeting (Opachich 2014). Further work will be transferred to programmatic funding, where a full-scale CsI photocathode will be developed for the NIF streak camera and time dilation tube detectors.

References

Feng, J., K. Engelhorn, B. I. Cho, H. J. Lee, M. Greaves, C. P. Weber, R. W. Falcone, H. A. Padmore, P. A. Heimann, "A grazing incidence x-ray streak camera for ultrafast, single-shot measurements," *Appl. Phys. Lett.* **96**, 13 (2010) 134102.

Fraser, G. W., "The characterisation of soft x-ray photocathodes in the wavelength band 1–300 Å: I. Lead glass, lithium fluoride and magnesium fluoride," *Nucl. Instrum. Methods Phys. Res.* **206**, 1–2 (1983a) 251–263.

Fraser, G. W., "The characterisation of soft x-ray photocathodes in the wavelength band 1–300 Å: II. Caesium iodide and other insulators of high photoelectric yield," *Nucl. Instrum. Methods Phys. Res.* **206**, 1–2 (1983b) 265–279.

Fraser, G. W., M. T. Pain, J. E. Lees, C. R. Binns, J. F. Pearson, P. R. Houghton, "The characterisation of gold x-ray photocathodes," *Nucl. Instrum. Methods Phys. Res. A* **321**, 1–2 (1992) 385–391.

Hara, T., Y. Tanaka, H. Kitamura, T. Ishikawa, "Performance of a CsI photocathode in a hard x-ray streak camera," *Rev. Sci. Instrum.* **71**, 10 (2000) 3624–3626.

Henke, B. L., J. P. Knauer, K. Premaratne, "The characterization of x-ray photocathodes in the 0.1–10-keV photon energy region," *J. Appl. Phys.* **52**, 3 (1981) 1509–1520.

Hilsabeck, T. J., et al., "Pulse-dilation enhanced gated optical imager with 5 ps resolution," *Rev. Sci. Instrum.* **81** (2010) 10E317.

Khan, S. F., et al., "Measuring x-ray burn history with the Streaked Polar Instrumentation for Diagnosing Energetic Radiation (SPIDER) at the National Ignition Facility (NIF)," *Proc. SPIE* **8505** (2012) 850505.

Khan, S. F., et al., "Characterization of the x-ray sensitivity of a streak camera used at the National Ignition Facility (NIF)," *Proc. SPIE* **8850** (2013) 88500D.

Miller, G. H., E. I. Moses, C. R. Wuest, "The National Ignition Facility: Enabling fusion ignition for the 21st century," *Nuclear Fusion* **44**, 12 (2004) S228.

Nagel, S. R., et al., "Dilation x-ray imager a new/faster gated x-ray imager for the NIF," *Rev. Sci. Instrum.* **83**, 10 (2012) 10E116.

Opachich, Y. P., et al., "High performance imaging streak camera for the National Ignition Facility," *Rev. Sci. Instrum.* **83**, 12 (2012) 125105.

Opachich, Y. P., P. W. Ross, A. G. MacPhee, T. J. Hilsabeck, S. R. Nagel, E. Huffman, P. M. Bell, D. K. Bradley, J. A. Koch, O. L. Landen, "High quantum efficiency photocathode simulation for the investigation of novel structured designs," *Rev. Sci. Instrum.* **85**, 11 (2014) 11D625.

Opachich, Y. P., et al., "Precision fabrication of large area silicon-based geometrically enhanced x-ray photocathodes using plasma etching," *Proc. SPIE* **9591** (2015) 95910O.

Opachich, Y. P., et al., "High-yield x-ray photocathodes for next-generation imaging detectors," in *Site-Directed Research and Development*, FY 2015, National Security Technologies, LLC, Las Vegas, Nevada, 2016a, 147–152.

Opachich, Y. P., A. MacPhee, "Photocathode," U.S. Patent Application 15,24,9197, filed August 26, 2016 (2016b).

Opachich, Y. P., P. W. Ross, A. G. MacPhee, T. J. Hilsabeck, S. R. Nagel, E. Huffman, P. M. Bell, D. K. Bradley, J. A. Koch, O. L. Landen, "Structured photocathodes for improved high-energy x-ray efficiency in streak cameras," *Rev. Sci. Instrum.* **87**, 11 (2016c) 11E331.

Thermal Microwave Kinetic Inductance Device
RSLN-023-16 | Continued from FY 2015 (RSLN-21-15) | Year 2 of 2

David D. Schwellenbach,[1,a] Craig Kruschwitz,[a] Paul Guss,[b] Mark Croce,[c] Michael Rabin,[c] and Veronika Mocko[c]

Decay-energy spectroscopy is a transformative method for nondestructive isotopic assay of trace-level nuclear materials with potential applications in areas including nuclear forensics. In this project we concentrated on optimizing this technology for low-energy electron spectroscopy. Measurement of the decay by electron capture of holmium-163 (^{163}Ho) was explored because its low energy decay allowed us to accurately study energy-resolution capabilities of decay-energy spectroscopy. Experiments indicated that contaminants from chemical processing of the ^{163}Ho were the limiting factor in improving energy resolution. Simulations and experiments were used to extend our understanding of the energy absorption process with the goal of improved energy resolution.

[1] schweldd@nv.doe.gov, 505-663-2017
[a] New Mexico Operations–Los Alamos; [b] Remote Sensing Laboratory–Nellis; [c] Los Alamos National Laboratory

Background

A transition edge sensor (TES) is a thermal sensor that measures an energy deposition by the increase of resistance of a superconducting film biased within the superconducting-to-normal transition (Irwin 2005). A TES is essentially a calorimeter made up of two components: (1) a bulk absorber that stops the *incident* gamma rays and (2) a thermometer made from a thin film electrically biased in the superconducting-to-normal phase transition (Horansky 2007).

In approaching this work, we sought to leverage several key science ideas related to low-temperature detectors. To begin, very low temperatures translate into low noise; this is now much more easily achieved (10 mK < T < 10 K with no liquid helium and no liquid nitrogen). We also sought to exploit the low noise aspect for unparalleled measurement performance of signal-to-noise ratio (for magnetic or electric field response, absorbed power or energy, and response time). Superconductors allow us to do things impossible with conventional materials, one example being their very low band gap (meV) compared to that of

semiconductors or scintillators (eV). Ultimately, our successful development of this technology would benefit quantitative nuclear materials characterization, including x-ray, gamma ray, alpha particle, and nuclear reaction energy spectroscopy. The technology could be useful in the areas of actinide chemistry, nuclear forensics, treaty verification, and safeguards.

TESs, superconducting single-photon detectors, have been useful thermal detectors since the 1990s (Figure 1). When an x-ray is absorbed in a detector, its energy is converted into heat; the TES measures the temperature change in the following manner. A very small current is run through a thin superconducting film whose temperature is kept just inside the transition region between its normal and superconducting states (Figure 2). The transition is not a step function, and it occurs over a narrow range in temperature. In that narrow temperature range, the TES acts as a very sensitive thermometer. We exploit this effect to make a very precise measurement of the energy of incoming x-rays. TESs not only have high resolution, but also are
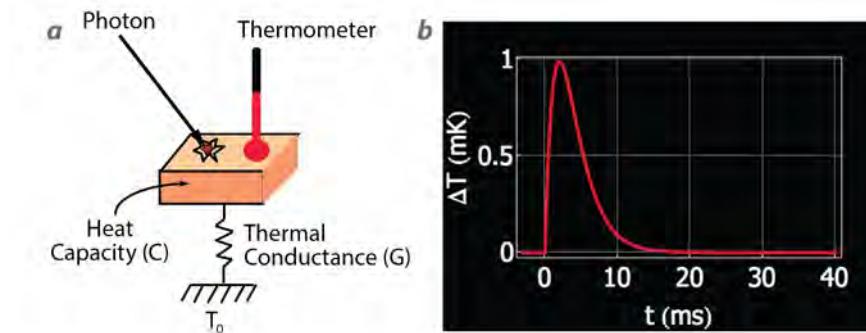
Figure 1. (a) A superconducting TES works on the principle that photon absorption in a membrane is converted to heat, which in turn creates a change in electrical resistance; (b) thermal relaxation times may be long (i.e., milliseconds) (Rabin 2013)
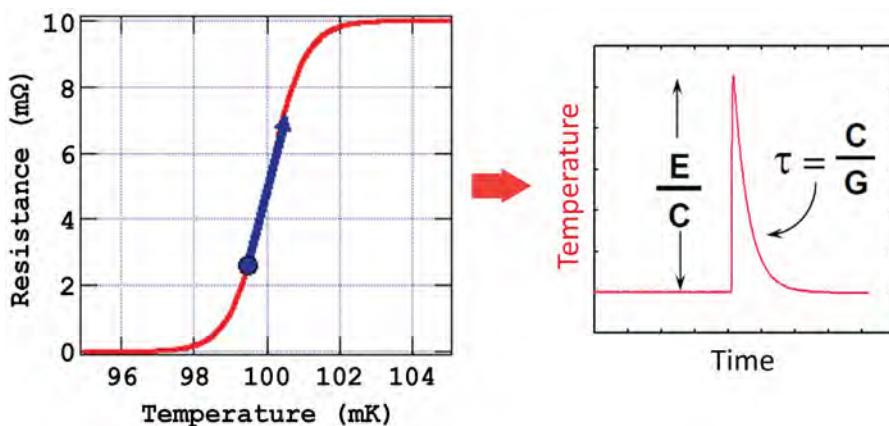
Figure 2. A TES is a thermometer made from a superconducting film operated near its transition temperature Tc, during which, in its transition from superconductor to normal metal, a small change in temperature causes a large change in resistance (figure based on Figueroa 2014)

high-efficiency detectors. Their characteristics make them superb x-ray spectrometers. Being able to do high-resolution spectroscopy allows us to analyze a large number of measurements relevant to DOE core missions (Morgan 2015).

A TES is a thermometer made from a superconducting film operated near its transition temperature Tc. The low temperature is needed because the energy resolution of these devices scales with temperature, so cryogenic temperatures are needed for high energy resolution. While in its transition from a superconductor to normal metal, a very small change in temperature causes a large change in resistance. Transition widths are typically on the order of a millikelvin. The figure of merit for microcalorimeter resistive thermometers is a parameter called α, defined as

$$\alpha = (d \ln R/d \ln T)V = \text{constant}, \qquad (1)$$

where T is the temperature and R is the resistance of the TES. The energy resolution of a TES can be approximated by (Figueroa 2014)

$$\Delta E_{FWHM} = 2.355 \, [4 \, k_B \, T^2 \, C \, [n/2]^{0.5}/(\alpha)]^{0.5}, \qquad (2)$$

where k_B is Boltzmann's constant, T is the TES temperature, C is the microcalorimeter's heat capacity, n is a number whose value depends on the dominant thermal impedance between the substrate and the electrons in the superconducting film, α is as defined in Equation 1, and the factor of 2.355 converts the standard deviation into FWHM. For good energy resolution, one wants to have a low heat capacity C, have a high α, and operate the devices as cold as achievable. An important limitation is that the TES operates well as a thermometer only in its transition. When it goes normal, resistance becomes a weak function of temperature, and $\alpha \to 0$. This implies a maximum temperature change in the TES, which in turn implies a maximum energy of the incoming photons (Figueroa 2014),

$$E_{MAX} = C \, T_{MAX} \sim C \, T/\alpha. \qquad (3)$$

The parameters C and α are tied by the desired energy bandpass of the microcalorimeter. The theoretical energy resolution of a microcalorimeter is displayed in

a simple formula that only depends on the temperature of operation and the bandpass of the device (Irwin 1995a, 1995b; Figueroa 2014):

$$\Delta E_{FWHM} = 2.355$$
$$\times [4\, k_B\, T\, E_{MAX}\, [n/2]^{0.5}]^{0.5}/(\alpha)]^{0.5}. \tag{4}$$

Groups both at the National Aeronautics and Space Administration (NASA) and NIST have demonstrated TESs with resolving powers of over 1000, or from 1 to 2 eV resolution at 1 keV, and TESs have been successfully used at the longer wavelengths, such as the submillimeter wavelength on ground-based telescopes and balloons. In this context they are no longer single-photon detectors, as they are measuring the average power of the incoming light. In this case, the TES acts as a bolometer, which is a microcalorimeter, as opposed to a single-photon detector. Bolometers have been successfully deployed in a number of scientific instruments; for example, they have a long history of use on x-ray sounding rockets. As single-photon detectors, TESs are at a low technical readiness level and not far along in the laboratory (Morgan 2015).

Project

Decay-energy spectroscopy is a transformative method for nondestructive isotopic assay of trace-level nuclear materials, especially particulate samples. We foresee three major applications in this field and have preliminary evidence indicating their feasibility. The first application is direct analysis of as-received micron-scale particles, the nuclear industrial dust of extraordinary value for International Atomic Energy Agency safeguards and treaty verification. Second is determination of plutonium chemical age of trace-level samples in a single measurement via the ^{241}Am/^{241}Pu chronometer that is especially effective for young plutonium (e.g., that from a new proliferator). The third use is simultaneous analysis of multiple isotopes of several elements without standards, tracers, or time-consuming chemical separation. These applications become practical by achieving ultra-high energy resolution, which requires a nanostructured composite material for the absorbing element of the microcalorimeter sensor.

Los Alamos National Laboratory (LANL) collaborators recently published results (Hoover 2015) indicating that engineered nanostructure of the radioactive material within a radiation-absorbing matrix is the key enabling technology for decay-energy spectroscopy. Figure 3 illustrates this breakthrough result. Figure 3a shows the measured decay-energy spectrum resulting from 10 µm scale plutonium nitrate crystals within a gold foil absorber, shown in an optical microscope image. Instead of a single peak corresponding to the total nuclear decay energy (Q) for each isotope, as would be expected for alpha decay, the left spectrum consists of a complex distribution of energies. By taking the same sample and performing a simple mechanical alloying process to fracture the plutonium nitrate crystals and homogenize their distribution within the gold matrix, LANL obtains the spectrum on the right (Figure 3b), which resolves the ^{239}Pu and ^{240}Pu Q-value peaks with excellent fidelity. A transmission electron microscope (TEM) image of a non-radioactive surrogate that was mechanically alloyed in the same way, lanthanum nitrate within a gold matrix, is seen in Figure 3b. The lanthanum nitrate occurs in sub-50 nm domains. By making a nanocomposite material that is homogeneous on the scale of the absorbed decay radiation, spectral artifacts and low-energy tailing are nearly eliminated.

Developing an optimized absorber structure for low-energy beta and electron capture decaying isotopes, such as ^{241}Pu (endpoint energy 20.9 keV) requires further development. Compared to alpha decaying isotopes, these isotopes have much more stringent requirements for absorber structure and sample purity due to their comparably shorter radiation interaction lengths. Our work focused on exploring what is required to enable high-resolution decay-energy spectroscopy for beta and electron capture decaying isotopes. A particularly useful test case is that of holmium-163 (^{163}Ho) (endpoint energy 2.8 keV). As an electron capture decaying isotope with a low Q-value, it has been the subject of intense theoretical and experimental study in recent years as a potential tool to measure the mass of the neutrino. The decay-
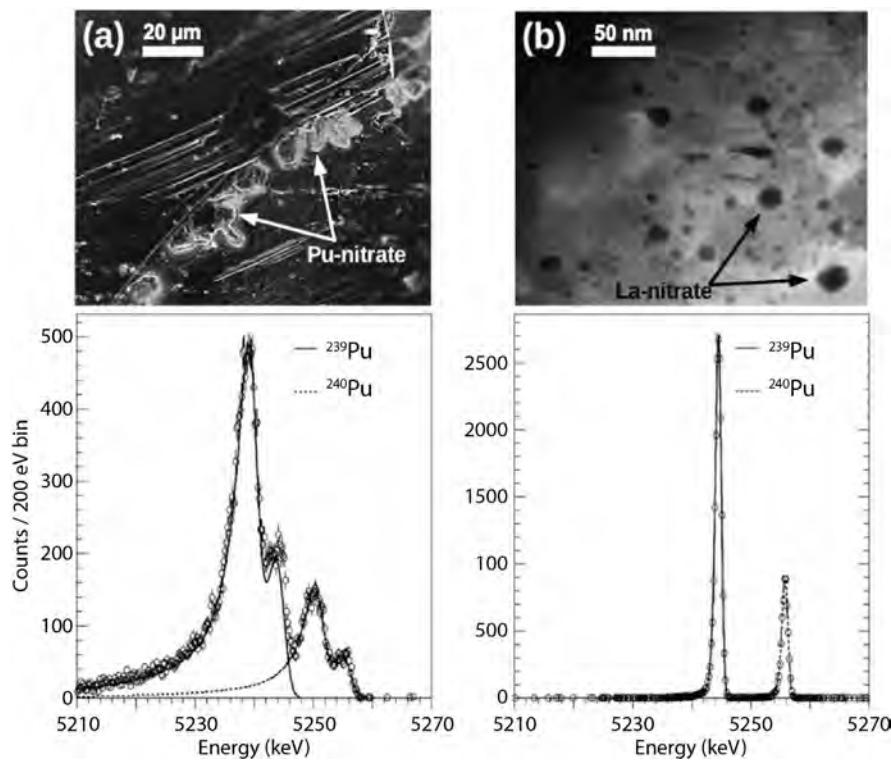
Figure 3. (a) Rather than (a) microscale composites (optical image and spectrum), development of (b) nanoscale composites (TEM image and spectrum) with radioactive materials is the key enabling technology for high-resolution decay-energy spectroscopy
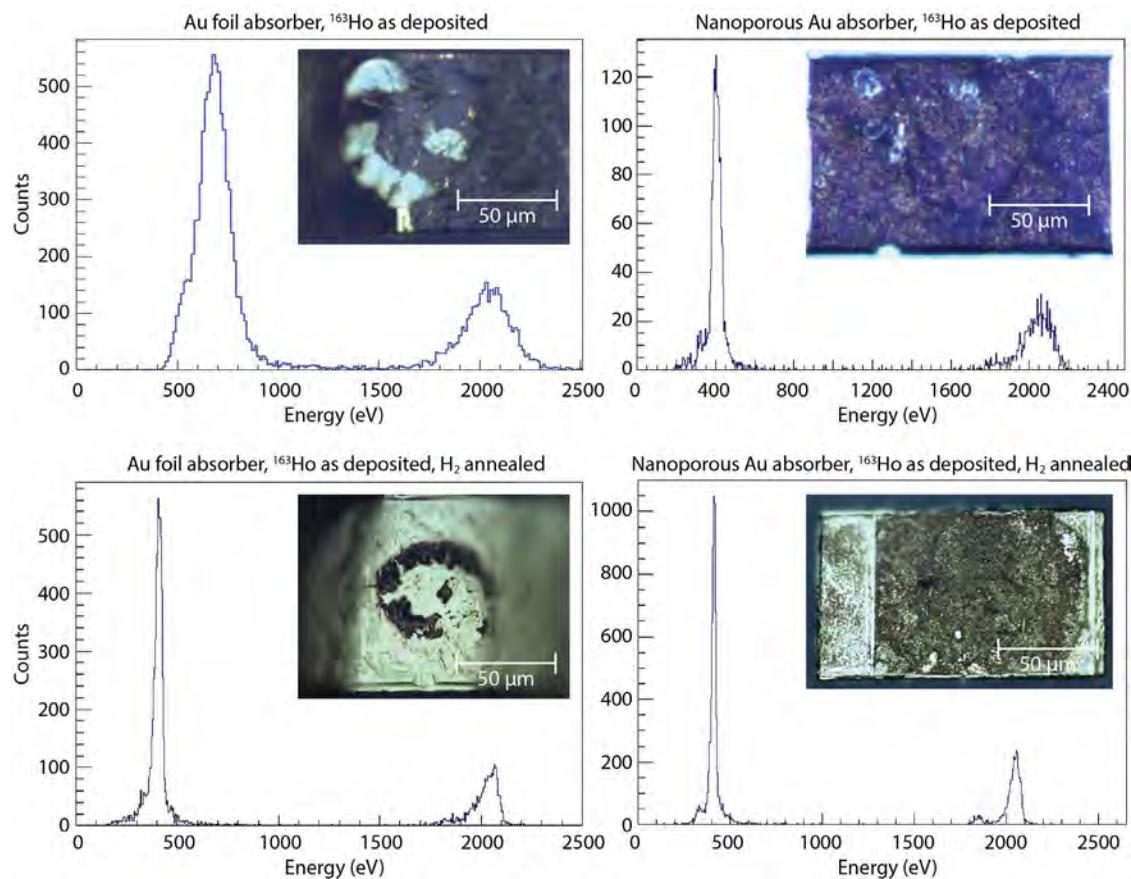

Figure 4. Improving the structure and composition of ^{163}Ho deposits (insets) within the absorber led to significant improvements in measured energy resolution

energy spectrum of [163]Ho is therefore relatively well described by theoretical models, and there is a body of experimental data with which to compare our results.

Early [163]Ho spectra measured at LANL showed that the energy resolution depended strongly on sample purity and absorber structure (Figure 4). We therefore focused on understanding the effects of sample purity and absorber structure. We determined that the two main categories of impurities in [163]Ho samples are inorganic salts (primarily sodium chloride [NaCl]) and organic residues (Figure 5). These impurities are present at concentrations far greater than the [163]Ho itself. In fact, in an energy-dispersive x-ray spectrum of the sample measured in a scanning electron microscope, the Ho is below detection limits. The elimination of these impurities is expected to enable much higher-resolution decay-energy spectra.

As shown in Figure 5, high-temperature annealing (800°C) in an atmosphere of 5% H_2-forming gas was found to be an effective way to eliminate the NaCl. The remaining residue appears to be primarily made of carbon. This is interpreted to be the result of organic residues in the original sample material. To eliminate the organic residues, we investigated perchloric acid digestion. Perchloric acid is very strong, capable of breaking bonds in organic molecules, and is used to eliminate organic residues in other applications. This appears to be a very promising method to use in future work.

To understand and optimize the physical structure of the absorber, we performed simulations using Geant4 (Agostinelli 2003). Geant4 has two physics models able to describe transport and energy deposition by low-energy (<10 keV) electrons. We used the
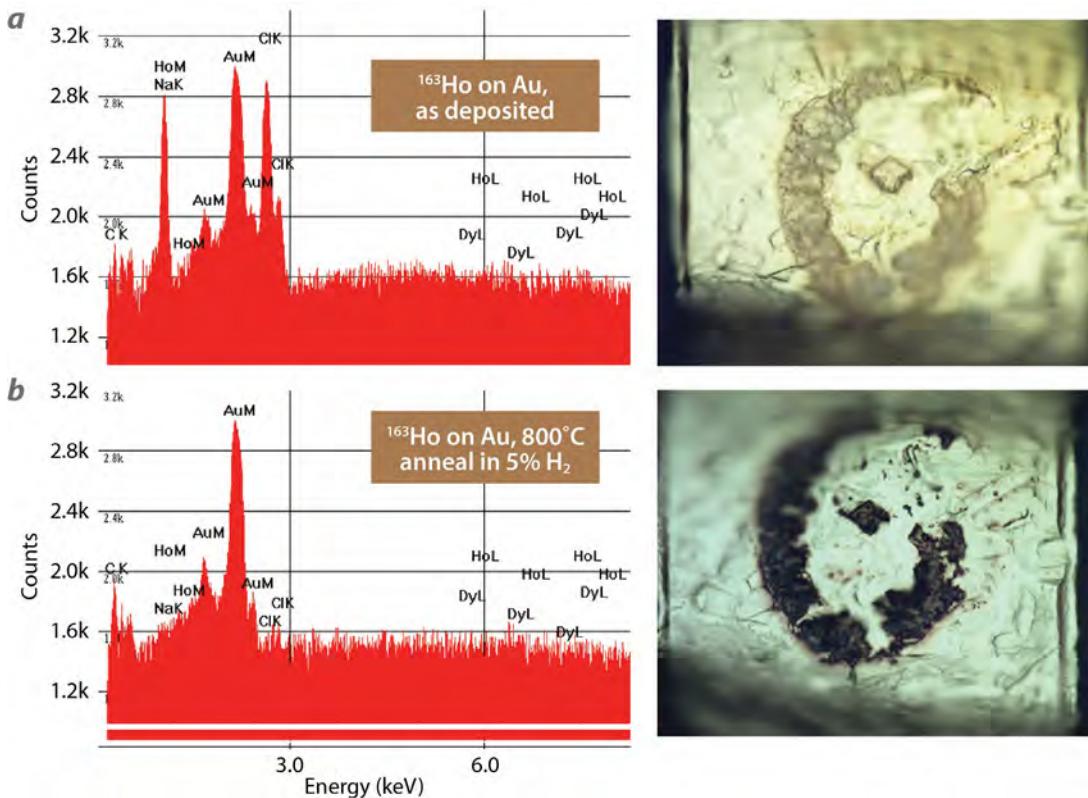
Figure 5. The two main categories of impurities in [163]Ho samples are inorganic salts (primarily NaCl) and organic residues. (a) NaCl crystals are visible in the optical micrograph in the sample as deposited as well as an energy-dispersive x-ray spectrum. (b) Annealing in 5% H_2 effectively eliminates the NaCl, but carbon-rich impurities remain. These carbon-rich impurities are likely the result of organic residues in the original sample.
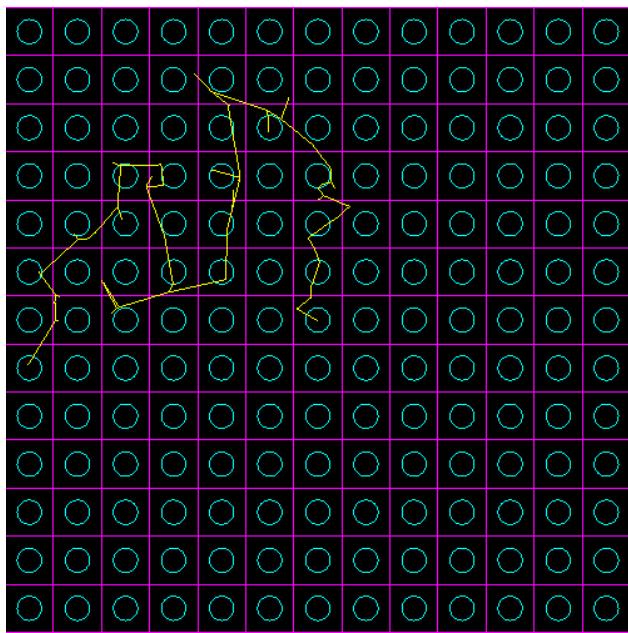
Figure 6. Geometry used in the Geant4 simulation. The green circles represent the NaCl deposit containing trace amounts of holmium. The areas outside of the green circles are pure Au. The yellow lines indicate trajectories for the source electron (emitted from the central NaCl-containing cell) and secondary electrons generated from collisions.

G4EmLivermorePhysics package, which in principle is valid down to electron and photon energies of 10 eV. We believed this to be sufficient for our purposes. A simple geometry was set up to approximate the energy deposition in the Au nanofoam and absorber versus the holmium-containing deposits. The deposits are assumed to consist of NaCl, with holmium and other components assumed to be trace elements and thus negligible from an energy deposition standpoint. A schematic of the geometry is shown in Figure 6.

Electrons of different energies and with random directions were generated at random locations in the deposit material, and the energy deposited in the NaCl and in the Au was tallied; the yellow lines in Figure 6 show some typical tracks for a source electron and secondary electrons. Electron energies were chosen to cover the range of energies expected as a result of Ho electron capture decay. We used the simulations to investigate a range of porosities of the Au nanofoam, with the ultimate goal of maximizing the energy deposition in the Au versus the ^{163}Ho deposit and thus
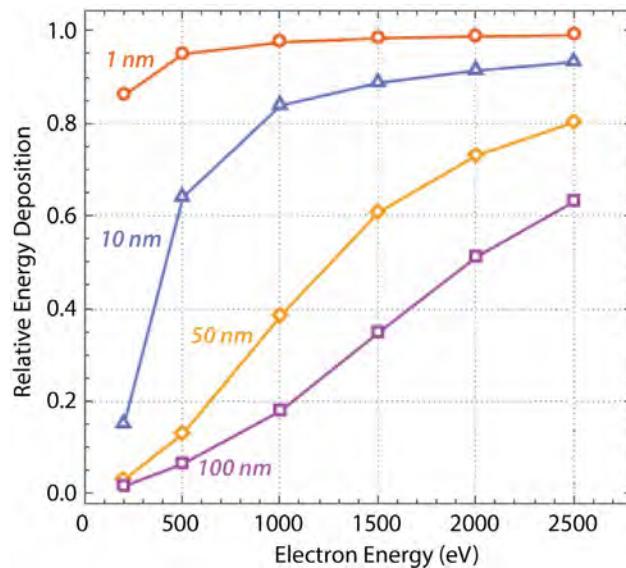
Figure 7. Mean relative energy deposition in Au versus total source electron energy. Foam relative density is 0.6; cell sizes shown in nanometers. As indicated, the energy deposited in Au is greater for smaller cell sizes/Au nanofoam porosities.

maximizing performance of the TES. Figure 7 shows the mean relative source electron energy deposited in Au as a function of source electron energy and for different pore size. It is clear that smaller pore sizes lead to a greater fraction of the source electron energy being deposited in the Au, which is what we desire. We assume that energy deposited in the NaCl/Ho deposit is more likely to be lost to non-thermal processes and thus lead to a loss of resolution for the TES. Typical pore sizes for the nanofoams are 10–100 nm. Figure 7 shows that for such pore sizes, a significant fraction of source electron energy is deposited in the NaCl rather than Au, which is not optimal.

Conclusion

Early in this project we determined that regardless of the type of sensor array that is considered, a complete characterization and development of the individual TES sensors was required to move this technology forward. The focus was placed on improving sensors with an emphasis on optimizing the ability to determine the ^{163}Ho electron capture spectrum. This study used ^{163}Ho because understanding its spectrum has promise for determining the mass of the neutrino

(Faessler 2015). In addition to the basic science question, the recent interest in [163]Ho means its decay energy has been extensively studied, so we have a well-documented decay spectrum for sensor development. Ultimately, this work will enable quantitative decay-energy spectroscopy on low-energy beta and electron-capture decaying isotopes for nuclear forensics applications, such as [241]Pu and fission products.

References

Agostinelli, S., et al., "GEANT4—A simulation toolkit," *Nucl. Instrum. Methods Phys. Res. A* **506**, 3 (2003) 250–303.

Faessler, A., C. Enss, L. Gastaldo, F. Šimkovic, "Determination of the neutrino mass by electron capture in [163]Ho and the role of three-hole states in [163]Dy," *Phys. Rev. C* **91**, 6 (2015) 064302.

Figueroa Group, Massachusetts Institute of Technology, "Transition edge sensors (TES)," 2014, http://web.mit.edu/figueroagroup/ucal/ucal_tes/, accessed September 30, 2015.

Hoover, A. S., et al., "Measurement of the [240]Pu/[239]Pu mass ratio using a transition-edge-sensor microcalorimeter for total decay energy spectroscopy," *Anal. Chem.* **87**, 7 (2015) 3996–4000.

Horansky, R. D., et al., "Superconducting absorbers for use in ultra-high resolution gamma-ray spectrometers based on low temperature microcalorimeter arrays," *Nucl. Instrum. Methods Phys. Res. A* **579**, 1 (2007) 169–172.

Irwin, K. D., "An application of electrothermal feedback for high resolution cryogenic particle detection," *Appl. Phys. Lett.* **66** (1995a) 1998.

Irwin, K. D., "Phonon-mediated particle detection using superconducting tungsten transition-edge sensors," Ph.D. Dissertation, Stanford University, Stanford, California (1995b), http://cdms.berkeley.edu/Dissertations/irwin.pdf, accessed September 30, 2015.

Irwin K. D., G. C. Hilton, "Transition-edge sensors," *Topics Appl. Phys.* **99** (2005) 63–150.

Morgan, K., "Developing transition-edge sensors for new space-based applications," NASA Early Stage Technology Workshop: Astrophysics & Heliophysics, Crystal City, Virginia, March 27, 2015, https://www.youtube.com/watch?v=vGHB80tqD5w, accessed September 30, 2015.

Rabin, M. W., et al., "Cryogenic detectors and neutrino mass measurement," Los Alamos National Laboratory (July 26, 2013), http://public.lanl.gov/friedland/info13/info13talks/Rabin-INFO13.pdf, accessed January 11, 2016.

This page left blank intentionally

Development of Fluorescent Technetium Compounds as a Radioactive Distributed Source

RSLN-25-14 | Continued from FY 2015 | Year 3 of 3

Eugene Sheely,[1,a] Gary Cerefice,[a] Wendy Chernesky,[b] Ken Czerwinski,[c] Fred Scudiery,[d] and Bill Martinez[e]

The focus of this three-year project was to incorporate radioisotopes into robust, fluorescent material for operational radiation detection training. The project began by investigating metastable technetium-99m (^{99m}Tc). Its low-energy, short half-life gamma decay (142 keV, $t\frac{1}{2}$ = 6.01 hours) allowed for small amounts of the radionuclide to be added to a host phase and dispersed. Following its decay to ^{99}Tc, which is a pure β-emitter, detection by standard radiological techniques becomes challenging for field responders. By incorporating the technetium into a fluorescent material, training can be extended to longer periods because dispersed samples can be located using UV black light. Scheelite samples doped with ^{99m}Tc and molybdenum-99 (^{99}Mo) were prepared for use in two training exercises to be completed in December 2016.

[1] sheelyev@nv.doe.gov, 702-295-8668

[a] Remote Sensing Laboratory–Nellis; [b] Radiation Emergency Services; [c] University of Nevada, Las Vegas; [d] Defense Nuclear Weapon's School, Defense Threat Reduction Agency; [e] Technical Evaluation Assessment and Monitoring Site, Defense Threat Reduction Agency

Background

The initial scope of work for this project was to develop florescent radioactive sources for use in training and evaluation. Desired characteristics of these sources include: (1) short half-life (quickly decay away if lost), (2) reusable, (3) easy to fabricate or obtain, (4) ability to vary the half-life (e.g., vary isotopes used in fabrication), (5) does not create contamination, and (6) has multiple methods of locating and tracking. Ideal characteristics of the fluorescing material include resistance to chemical and environmental degradation, resistance to UV damage from the sun, and ease of synthesis (i.e., one-pot synthesis, absence of atmospheric oxygen in reaction system, short reaction time, fabrication temperatures below 1000°C, low cost and availability of starting products).

Due to its relatively short half-life, gamma emission, and availability from commercial generators, metastable technetium-99m (^{99m}Tc) was the first radioisotope studied during this project. Incorporating ^{99m}Tc into a chemical form that fluoresces provides a means to track the Tc. Natural fluorescent materials, based on silicate species, can provide a robust host matrix that is stable and benign in the environment. During the first year of the project, fluorescent compounds were prepared. These included fresnoite ($Ba_2TiSi_3O_8$), calcium tungstate (e.g., scheelite) ($CaWO_4$), and calcium molybdate (e.g., powellite) ($CaMoO_4$). Powellite and scheelite were chosen as the fluorescent compounds of greatest interest (Chernesky 2015). During the second year of the project, Tc was incorporated into $CaWO_4$ and $CaMoO_4$ matrices. The fluorescence and stability of powellite and scheelite containing Tc were examined through optical spectroscopy and examination of Tc released in aqueous environments. The fluorescence behavior provided quantitative data for selecting and establishing practices that

can be employed in the field. The aqueous solubility studies demonstrated the desired characteristic of very low Tc solubility. Modeling studies supported the selection of both $CaWO_4$ and $CaMoO_4$, with expected enhanced stability due to interstitial coordination of Tc (Chernesky 2016).

While the ceramics containing ^{99m}Tc exhibit many desirable characteristics, they also have some significant limitations. The short half-life of ^{99m}Tc limits when and where the sources can be used, and the ceramics must be fabricated in a licensed radio-laboratory. In order to expand the value of this project, the possibility of embedding isotopes other than ^{99m}Tc in fluorescing ceramic matrices was pursued. Isotopes that are not radioactive, but transform into radioactive isotopes upon irradiation where chosen. The viability of this concept was demonstrated using an isotope of molybdenum, [98]Mo, which, when subjected to neutron irradiation transforms into [99]Mo. Through the use of this process, it is possible to fabricate sources in laboratories that are not licensed by the Nuclear Regulatory Commission, that have a longer half-life than [99m]Tc (yet still short), and that can be re-irradiated and therefore reused.

Project

Scheelite and Powellite Synthesis and Characterization

Scheelite and powellite can both be synthesized from the solid-state reaction of MO_3 (M = Mo, W) and calcium oxide (CaO) at elevated temperatures (Abdel-Rehim 2001). Scheelite emits a blue phosphor, whereas the powellite is yellow. In FY 2015 the scheelite and powellite samples were prepared from powders of MO_3 and CaO (M = Mo, W) at a 1:1.25 mol stoichiometry. This ratio was based on FY 2014 results. These samples were fabricated under argon atmospheric conditions in a furnace at 860°C for 2 hours. It was later determined that scheelite could be synthesized at temperatures as low as 400°C.

Samples with Tc were prepared from 2 grams of precursor. A stock solution in water of $KTcO_4$ at 14.7 mg

Tc/mL was added to the precursor at a 1:1.25 mol ratio of MO_3 and CaO. The Tc concentration was varied from 0.1 mol % to 10.0 mol %, which corresponds to 8 µL to 800 µL of TcO_4^- stock solution. After the addition and mixing of the Tc stock, the resulting mixture was treated with methanol in a ratio of 1 gram of oxides to 100 µL of methanol. When heated to 860°C for 2 hours, the powder produced fluorescent particles approximately 2 mm in diameter (Figure 1). Later ceramic particles of scheelite approximately 5 cm in diameter were prepared.
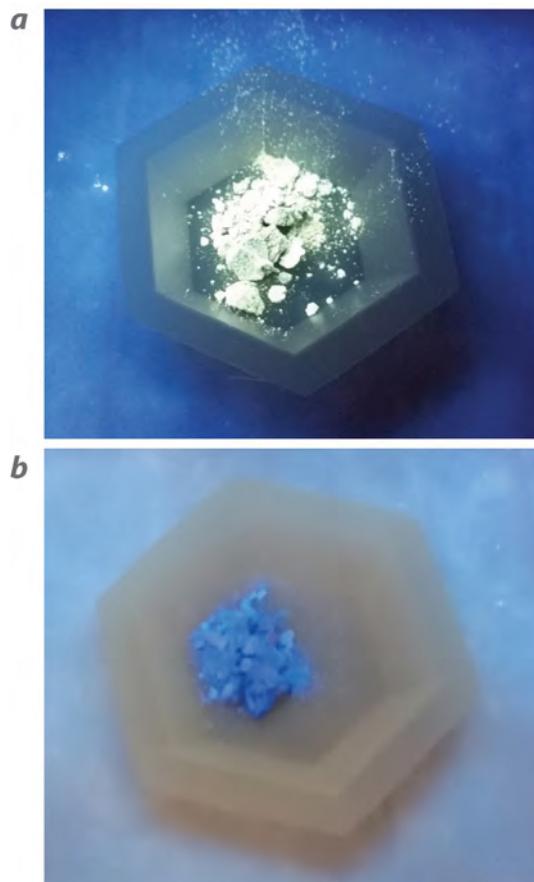
Figure 1. (a) Powellite ($CaMoO_4$) and (b) scheelite ($CaWO_4$) with 1 mol % Tc

The samples in Figure 1 fluoresce under a standard, handheld UV lamp. To provide the optimal conditions for observing fluorescence, the optimal excitation and emission properties of the materials were quantified. The samples were examined with a Fluorolog-3
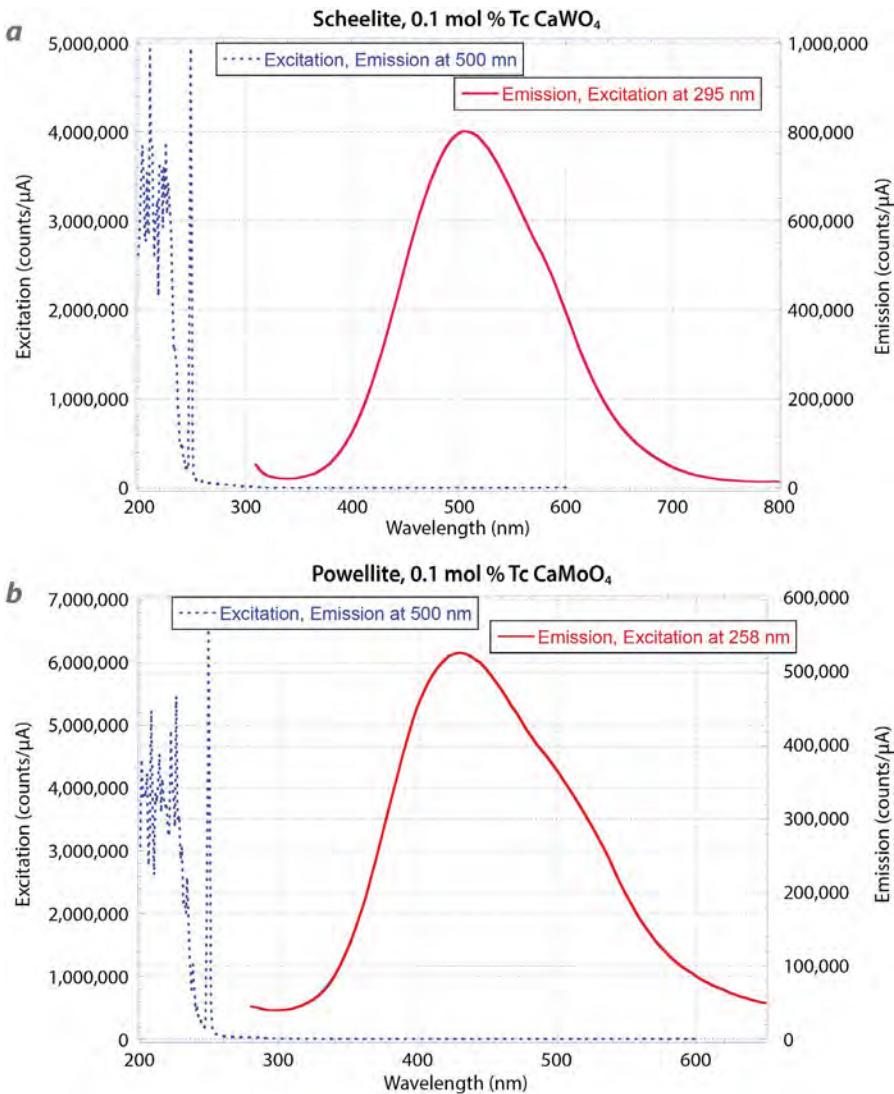
Figure 2. Excitation and emission spectra for (a) scheelite (CaWO$_4$) and (b) powellite (CaMoO$_4$) with 0.1 mol % Tc; changes in the bonds of the silicate from the incorporation of Tc into the matrix may be causing changes in the emission peak for powellite

Spectrofluorometer for both emission and excitation from 200 to 800 nm. Samples of CaMoO$_4$ and CaWO$_4$ with 0 mol % to 1 mol % Tc were placed in reduced-volume fluorescence cuvettes and sealed. The optimal excitation condition was evaluated by measuring emission at 500 nm for each sample. These results determined the excitation wavelength, which was, in turn, used to evaluate the sample emission spectra (Figure 2). The data were fairly consistent for the examined samples (Table 1). Variations were observed between the excitation and emission peaks for the materials, indicating a route for discrimination between these matrices. Some change in the emission peak for powellite was observed with increased Tc

concentration, which may be due to changes in the bonds of the silicate from the incorporation of Tc into the matrix (Tc coordination).

Leaching of Tc from the prepared samples under aqueous conditions was investigated. The samples had Tc concentrations from 0.1 mol % to 10 mol % Tc. The leaching was examined using 100 mg of material, similar to that shown in Figure 1, in 10 mL of water. The solution was mixed; 100 µL was periodically removed for scintillation counting to determine Tc solution concentration. Both materials exhibited a small rapid initial release followed by a constant Tc concentration. Higher Tc release was observed for powellite, with a

Table 1. Emission and excitation data for scheelite and powellite with varied Tc concentration. FWHM is the full-width, half-maximum of the emission peak.

Sample	mol % Tc	Excitation Wavelength (nm)	Emission Peak (nm)	FWHM (nm)
Scheelite	0	295	505	149
Scheelite	0.1	295	505	160
Scheelite	1.0	295	508	211
Powellite	0	257	421	113
Powellite	0.1	258	430	161
Powellite	1.0	257	466	166

maximum Tc concentration of 1×10^{-7} M in solution. For all systems examined, the released Tc represented less than 0.01% of the total inventory. This release mechanism is consistent with rapid surface desorption for a minor fraction of surface sites.

Computational Studies

The Tc-doping mechanisms in scheelite based on an atomistic approach were investigated using density functional theory (DFT) and compared with experimentally reported results. Technetium incorporation into scheelite was also systematically investigated. The defect formation energies were calculated and used to determine the most energetically stable sites for Tc in scheelite. First-principle total energy calculations were performed using spin-polarized DFT, as implemented in the Vienna ab initio simulation package (VASP) (Kresse 1996). The exchange-correlation energy was calculated using a generalized gradient approximation with the parameterization of Perdew and Wang (1992). Convergence testing was performed by varying the plane-wave cutoff energy for the electronic wave functions from 300 to 500 eV. Structural optimization and physical property calculations were carried out using the Monkhorst-Pack special k-point scheme (Monkhorst 1976). A ($4 \times 4 \times 4$) k-point mesh was used for integrations in the Brillouin zone of bulk systems. Periodic boundary conditions were employed to mimic the bulk system. The total energy and cell volumes of scheelite and powellite were used to derive equations of state,

$$P = -\frac{\partial E}{\partial V}. \tag{1}$$

Calculations were also performed to determine the compression behavior, the bulk modulus (K), for $CaWO_4$.

$$K = V_0 \frac{\partial^2 E}{\partial V^2} \tag{2}$$

A single technetium atom was included at predicted sites among the powellite lattice, and the total energy was calculated. In the case of the Tc-doped species of powellite studied here, the inclusion energy, E_I, was calculated as

$$E_I = \left| \ E_{products} \ \dashv \ E_{reactants}. \right. \tag{3}$$

The calculated lattice constants, bulk modulus, and volume compression data of $CaWO_4$ are in excellent agreement with experimental data. Defect formation energies have been calculated for several possible sites of Tc in scheelite. The calculated vacancy formation energies of tungsten (W) and calcium (Ca) are between 11 and 18 eV. It was determined that both interstitial octahedron $I(O_h)$ and substitutional tungsten $S(W)$ are energetically compatible with Tc doping (Figure 3). The diffraction patterns of each Tc defect were predicted from the optimized structures calculated using DFT. This helped in the interpretation of experimentally determined complex x-ray diffraction patterns.

The first [98]Mo ceramic samples were prepared at the University of Nevada, Las Vegas, in August 2016. The
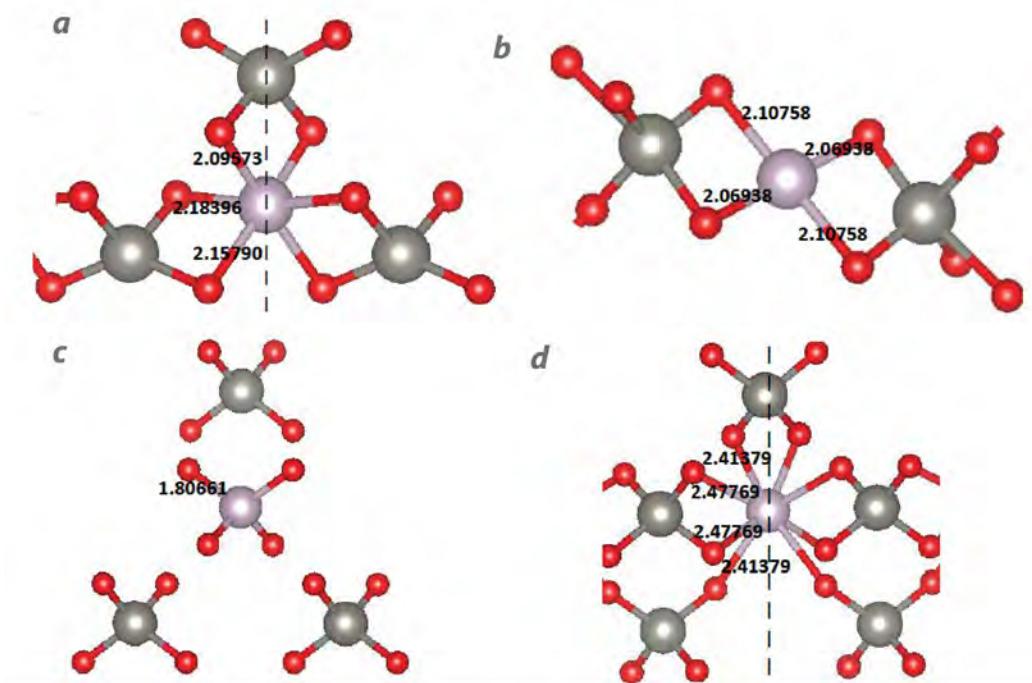
Figure 3. Tc-O bonds and bond distances for (a) CaWO$_4$:Tc; I(O$_h$), (b) CaWO$_4$:Tc; I(C), (c) CaWO$_4$:Tc; S(W), and (d) CaWO$_4$:Tc; S(Ca). Where appropriate, symmetry in the bond lengths has been indicated by dashed lines. The bond distances are in angstroms (Å).

samples were irradiated to produce ^{99}Mo at the Global Medical Isotope System's southern Nevada facility. The activity of the samples is controlled by adjusting the irradiation time and time between irradiation and use.

Response Exercises

In order to perform operational testing of the developed sources, two exercises were planned for September 2016; however, due to needed repairs on the irradiator, the exercises were postponed until December 2016. The exercises will use a variety of sources, including six of the ^{99}Mo-containing ceramic sources developed during this project. The molybdenum sources used in the exercises will vary in activity from 1 to 15 mCi.

The first exercise will simulate a nuclear weapons accident. Approximately 30 responders will search for radioactive material and characterize the contamination. The exercise will take place at simulated nuclear accident sites that have been seeded with thorium-232 and have a variety of sources scattered around the sites. All responders will be fully dressed out, set up air

samplers, go through a hot line, etc. The primary instrument used to locate sources is a survey monitor from Southern Scientific, the ADM-300 with an attached sodium iodide (NaI) x-ray probe. Spectroscopy will be performed using NaI and cadmium-zinc-telluride (CZT) spectrometers. This exercise will be done in cooperation with the University of Nevada, Las Vegas, and the Defense Nuclear Weapons School on U.S. Air Force Training Sites.

The second exercise will take place at the Defense Threat Reduction Agency's Technical Evaluation Assessment and Monitoring Site (TEAMS). Students and instructors from the Defense Nuclear Weapons School will search for sources of varying strength in rail cars, buildings, motor vehicles, and underground. The ability of responders to locate and characterize the sources using a variety of equipment will be tested. Sources will be located using Geiger-Müller, CZT, and NaI detectors. Gamma spectroscopy of the sources will be performed using NaI, CZT, high-purity germanium, and lanthanum bromine spectrometers.

Conclusion

The fluorescence and stability of matrices in scheelite and powellite were established. Technetium was successfully incorporated into both matrices as 1 to 5 cm monoliths and 2 mm particles. The fluorescence behavior provided quantitative data for selecting and establishing techniques for field observation. The aqueous solubility studies demonstrated the ability of powellite and scheelite to maintain incorporation of Tc. The modeling studies support the selection of both materials, with expected enhanced stability due to interstitial coordination of Tc. In FY 2016 scheelite samples doped with ^{99m}Tc and ^{99}Mo were prepared for use in training and exercises. Both the Counterterrorism Operations Support Center for Radiological Nuclear Training and the Defense Threat Reduction Agency's Defense Nuclear Weapons School have shown interest in using the sources developed during this project. How much they are incorporated into training will depend on the availability of the sources, access to irradiators, and cost.

Some of the results of this study have been published in *Dalton Transactions* (Ackerman 2016).

References

Abdel-Rehim, A. M., "Thermal analysis and x-ray diffraction of synthesis of scheelite," *Journal of Thermal Analysis and Calorimetry* **64** (2001) 1283–1296.

Ackerman, M., E. Kim, P. F. Weck, W. Chernesky, K. R. Czerwinski, "Technetium incorporation in scheelite: Insights from first-principles," *Dalton Trans.* **45** (2016) 18171–18176.

Chernesky, W., E. Johnstone, R. Borjas, W. Kerlin, M. Ackerman, K. Mayo, E. Kim, F. Poineau, K. Czerwinski, "Development of fluorescent technetium compounds as a radioactive distributed source," in *Site-Directed Research and Development*, FY 2014, National Security Technologies, LLC, Las Vegas, Nevada, 2015, 59–69.

Chernesky, W., M. Ackerman, K. Mayo, E. Kim, F. Poineau, T. Low, J. Bertoia, K. Czerwinski, "Development of fluorescent technetium compounds as a radioactive distributed source," in Site-Directed Research and Development, FY 2015, National Security Technologies, LLC, Las Vegas, Nevada, 2016, 75–80.

Kresse, G., J. Furthmüller, "Efficient iterative schemes for ab initio total-energy calculations using a plane-wave basis set," *Phys. Rev. B* **54** (1996) 11169–11186.

Monkhorst, H. J., J. D. Pack, "Special points for Brillouin-zone integrations," *Phys. Rev. B* **13** (1976) 5188–5192.

Perdew, J. P., Y. Wang, "Accurate and simple analytic representation of the electron-gas correlation energy," *Phys. Rev. B* **45** (1992) 13244–13249.

Time-Synchronized, Microsecond-Gated Digital Video to Enhance Optical Tracking and Surveillance for an Unmanned Aerial Vehicle Payload

STL-001-16 | Year 1 of 1

Dale Turley,[1,a] Eric Larson,[a] Roy Abbott,[a] E. Kirk Miller,[a] and Kevin Lee[a]

The goal of this project was to develop a new camera system for unmanned aerial vehicle implementation. This camera is an extension of an existing handheld electro-optic system developed by NSTec for vehicle identification applications. This new, synchronized camera features precision timing, and it will address an ongoing need for identifying objects of interest remotely and uniquely through video means.

[1] turleywd@nv.doe.gov, 805-681-2239
[a] Special Technologies Laboratory

Background

There is a continuing need for precise, positive, day and night (24/7) vehicle identification at moderate ranges (~1 km). In support of this need, NSTec has developed a proprietary system using a time-gated and synchronized electro-optic sensor, based on night-vision goggles (NVGs). Users of this handheld system have expressed a desire for an unmanned aerial vehicle (UAV) payload with the same capability. To enable this transition, two key technologies were developed: (1) a digital sensor comparable in performance to the customized NVGs and (2) a time-synchronization method that persists with high accuracy if GPS is unavailable. We used advances in digital camera technology and chip-scale atomic-clock timing devices to address these two gaps.

Project

This project consisted of three key activities: (1) selection, acquisition, and evaluation of digital camera and timing devices; (2) implementation into a brassboard system; and (3) development of specialized timing and interface electronics.

The essential elements of the brassboard system used for the laboratory evaluation are shown in Figure 1.
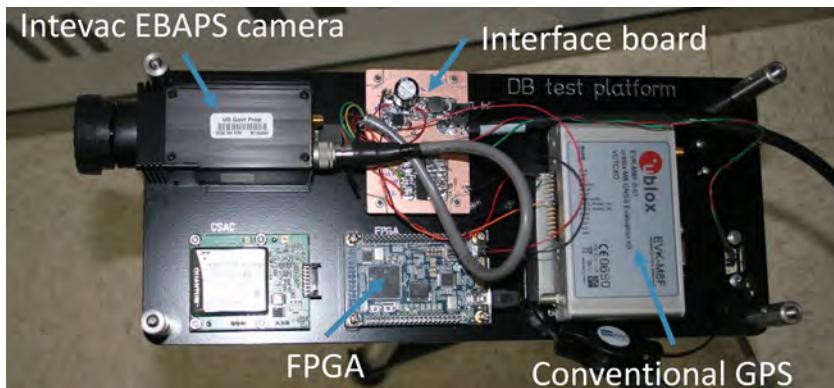

Figure 1. Brassboard hardware attached to tripod mount

Included are an Intevac ISIE11 Electron Bombarded Active Pixel Sensor (EBAPS) camera, an NSTec interface PCB for signal conditioning and power distribution, a chip-scale atomic clock, an Altera Cyclone IV field-programmable gate array (FPGA), and a u-blox GPS device.

Camera Selection

We conducted a comprehensive survey of available cameras for our application as well as a calculated comparison of the relative merit of different sensor types. The following key parameters considered in this comparison were:

- Signal-to-noise ratio (SNR) in the spectral range of interest (near infrared [NIR])

- Ability to block energy outside of desired gate time

- Ability to control gate integration time

- Size, weight, and power (SWaP)

The SNR is calculated with Equation 1, where Qe is quantum efficiency (the number of electrons created per photon), $\#\ of\ Photons$ is the number of photons striking a pixel element in a unit time of one frame, enf is the excess noise factor, dcn is the dark current noise, cln is the clock noise, rdn is the read noise, and $gain$ is the gain function of the pixel (PCO-TECH 2015). The results of the SNR calculations for each type of camera we evaluated are shown in Figure 2.

Following is a discussion of the other three parameters (gating, timing, and SWaP) we considered for each camera system.

Scientific CMOS (SCMOS) cameras (both the rolling-shutter [RS] and global-shutter [GS] types) combine low read noise, clock noise, and excess noise factor (ENF) for good high-light performance and very good low light performance. However, active cooling

is necessary to reduce dark current and clock noise, adding too much bulk to the profile of the camera. This cooling also reduces sensitivity at longer wavelengths. A small reduction in performance is necessary to implement a GS.

EBAPS cameras combine a GaAs photocathode with a silicon readout array (Williams 1995, Aebi 2005). Signal is generated when electrons are generated at the photocathode, accelerated by a high-voltage (HV) field, and impinged onto the silicon array. Gain is achieved by accelerating the photoelectrons produced by the cathode with a HV vacuum potential, thereby creating multiple electron hole pairs in the silicon upon impact. This results in current gains of about 200 for a kilovolt of acceleration ($gain$ in Equation 1). Controlling the HV potential performs a gating function. The cathode electron potential barrier reduces the dark current and allows room-temperature operation at low noise.

At higher light levels (1000 photons per frame [PPF]), the Interline CCD camera has very good performance, as the high quantum efficiency and low ENF overcome the read noise, clock noise, and dark current.

Electron-multiplied CCDs (EMCCDs), both back- and front-illuminated (BI and FI), perform well at low light levels (under 10 PPF) but are hampered by ENF at higher light levels. As with the SCMOS, active cooling is necessary to reduce dark current and clock noise, yet this cooling also reduces sensitivity at longer wavelengths and adds bulk. Of the two types of EMCCDs, the back-illuminated version has better quantum efficiency but at a higher cost.

Microchannel plate (MCP)–based intensified CCD (ICCD) cameras have good high-speed gating characteristics (out-of-gate energy rejection and in-gate gain). The high gain improves the very low light level performance (below 10 PPF). The cathode electron potential barrier reduces the dark current and

$$snr = \frac{Qe * \left(\#\ of\ Photons\right)}{\sqrt{\left\{enf^2 * \left(\left(Qe * \left(\#\ of\ Photons\right)\right) + dcn + cln^2\right)\right\} + \left\lceil \dfrac{rdn^2}{gain^2} \right\rceil}} \tag{1}$$
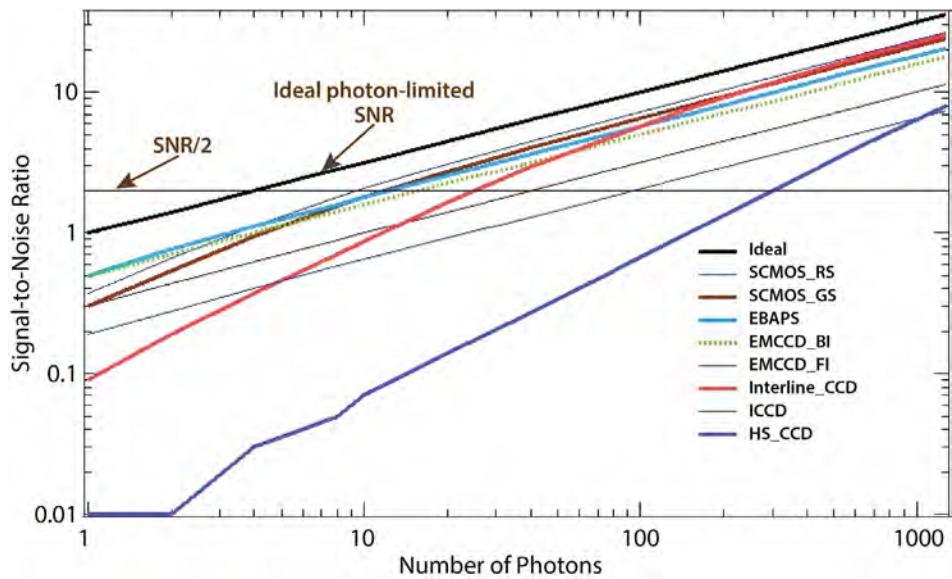
Figure 2. Results of SNR calculations comparing cameras of interest, showing the relative performance of the camera systems at high and low light levels. The SCMOS (both RS and GS), EBAPS, and the EMCCD (both BI and FI) performed well at both high and low light levels, while the Interline CCD, ICCD, and HS CCD performed well at only one or the other, making them unsuitable for our purposes.

allows room-temperature operation at low noise. But the lower quantum efficiency and high ENF hurt performance at higher light levels.

For the blocking and gating portion of the UAV application, the ICCD and EBAPS have electronic cathode shutters in addition to the charge integration time shutter on the focal plane. But the ICCD has better out-of-gate light blocking due to the internal MCP structures. The EMCCDs and the SCMOS RS do not perform global gating functions. The high-sensitivity (HS) CMOS camera does have a charge integration shutter with charge dumping to block out-of-gate-time light and a sufficiently short charge gate time.

In terms of SWaP, the EMCCDs, SCMOSs, and Interline CCDs are cooled and kept in a vacuum Dewar, so they are bulky and power hungry. The SCMOS requires less cooling power than the EMCCD but still needs a Dewar assembly to keep the window clear of condensation

Table 1. Comparison of camera technologies

Camera Type	SNR	Blocking	Gating	SWaP	Total
SCMOS RS	10	5	3	5	23
SCMOS GS	9	8	7	5	29
EBAPS	10	9	9	8	36
Front-Illuminated EMCCD	9	3	6	5	23
Back-Illuminated EMCCD	10	3	6	5	24
Interline CCD	4	5	6	6	21
ICCD	6	10	10	8	34
HS CMOS	1	8	9	10	28

and to save power. The EBAPS and ICCD do not require cooling but do need a HV power supply for the cathode potential. The HS CMOS does not require cooling or special power.

Table 1 shows a qualitative comparison of camera technologies. The table compares SNR, out-of-gate blocking, gate control, and SWaP. Each performance criterion is given a numerical ranking of 1 to 10, with 10 being the highest performance. The total score indicates the overall camera performance.

In summary, the EBAPS camera performs best for the desired UAV application. The SCMOS GS and EMCCD are equally strong contenders in terms of sensitivity for the day and night (24/7) requirement, but inferior gating performance and bulky cooling systems count heavily against them. The Interline CCD and HS CMOS both have good packaging and power requirements for SWaP but lack sensitivity for the day and night (24/7) requirement. The ICCD is the EBAPS's closest competitor for our application, but it is slightly larger and has less sensitivity.

Comparison of EBAPS Camera to Existing Handheld Electro-Optic System

A direct comparison of images taken from the EBAPS camera and a handheld MCP tube–based viewer operating at the gating and lighting conditions required for our expected application is shown in Figure 3. The images show the better image quality of the EBAPS camera. The primary reason for this higher

performance is because EBAPS has a lower ENF due to the low noise gain characteristic of the silicon sensor. The ENF is lower because the EBAPS gain is lower (200 versus 10,000 for the MCP) and the gain is single stage rather than cascaded. The resulting image appears "crisp" and higher in resolution than the noisier MCP tube.

For our desired application, we need a 1 μs gate "on" time, with absolute blocking of the image outside of this on time. This is achieved by setting the gate time remotely via computer control. The computer sends commands to the FPGA in the camera, which then sets the HV gate and the charge integration time. Initially, simply setting the HV gate time to 1 μs did not have the desired effect, as the camera did not create an image. Careful measurement with a synchronized short-pulse (200 ns wide) 600 nm light source revealed two issues: (1) the HV gate time setting in the manufacturer's software did not correspond to the actual gate on time, and (2) the CCD charge integration time was independent from the HV gate time setting. We performed a series of measurements to map the CCD charge integration time to the time setting in the manufacturer's software, followed by another series of measurements to map the HV gate time setting to the actual gate on time. Results are shown in Figures 4 and 5.

We determined that when the HV gate on time and the CCD charge integration time were set (using the manufacturer's software settings) to 15 μs and 50 μs,
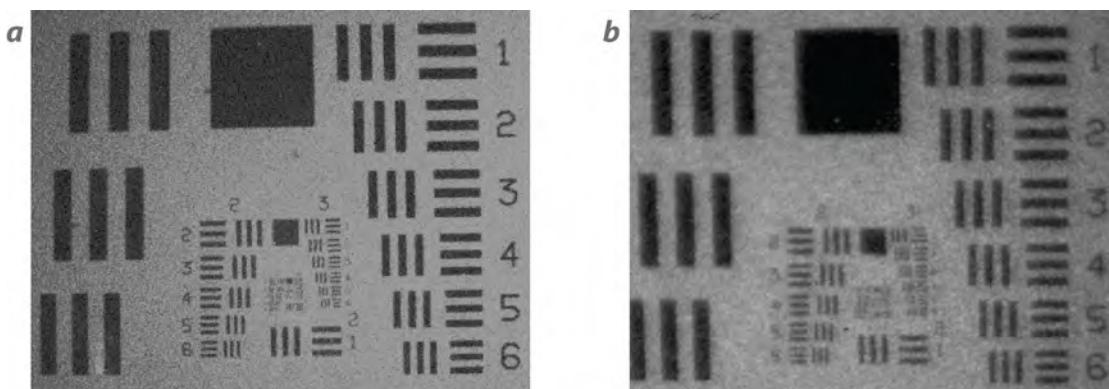
Figure 3. Images (a) from EBAPS camera and (b) from a handheld MCP tube–based imager captured by a lens-coupled CMOS camera. The EBAPS has better performance.
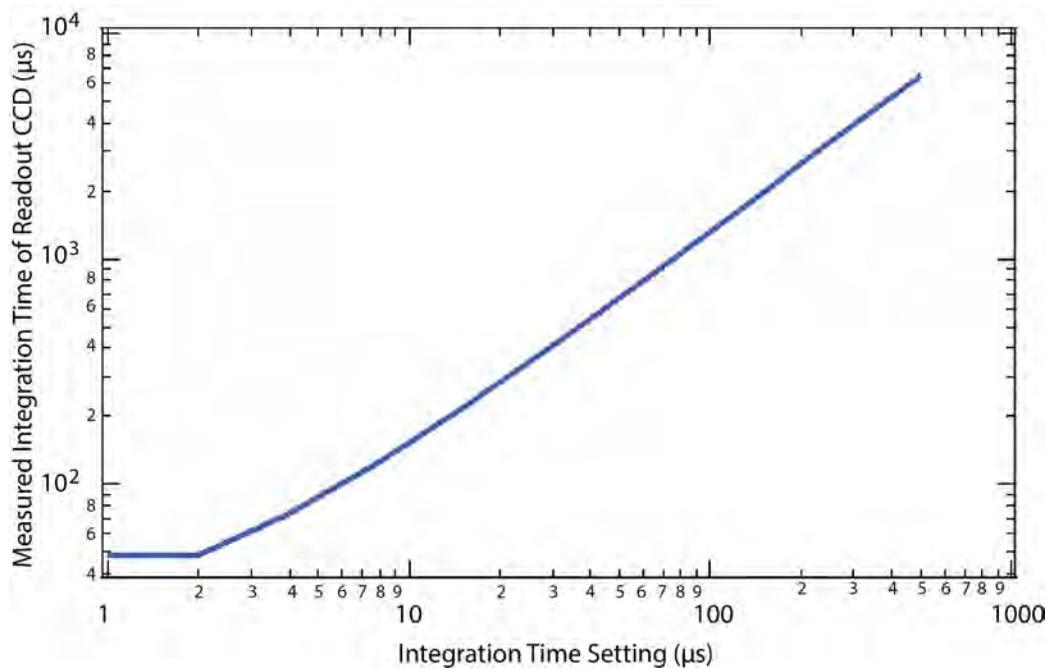
Figure 4. Measurements mapping the actual CCD charge integration time to the CCD integration time setting in the manufacturer's software
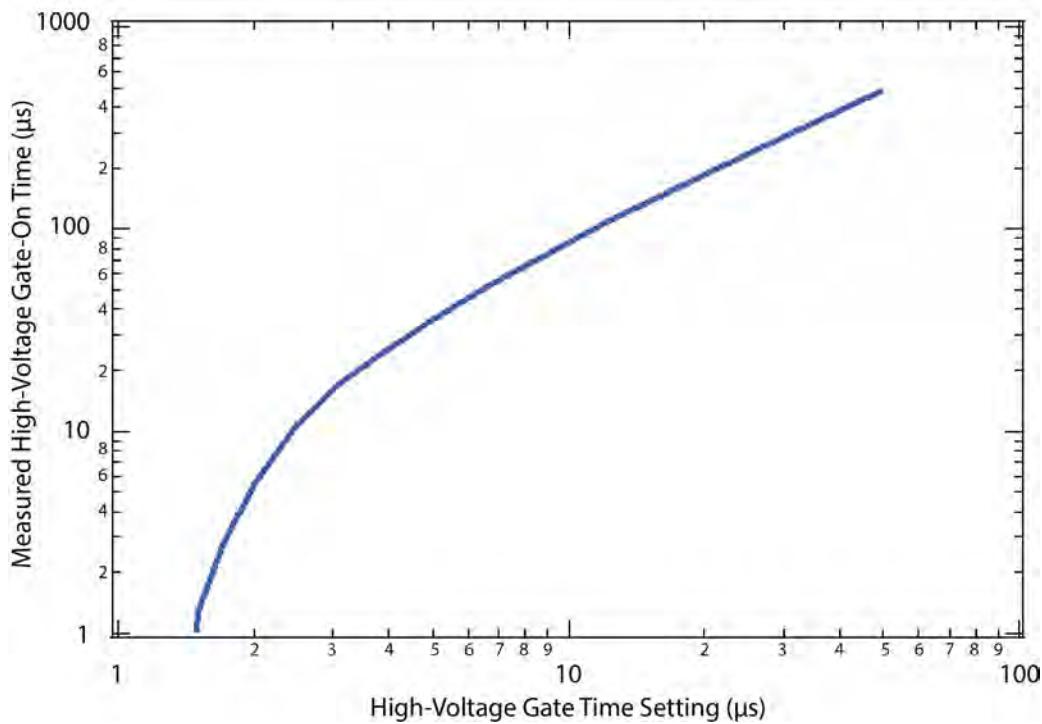

Figure 5. Measurements mapping the HV gate time to the HV gate time setting in the manufacturer's software
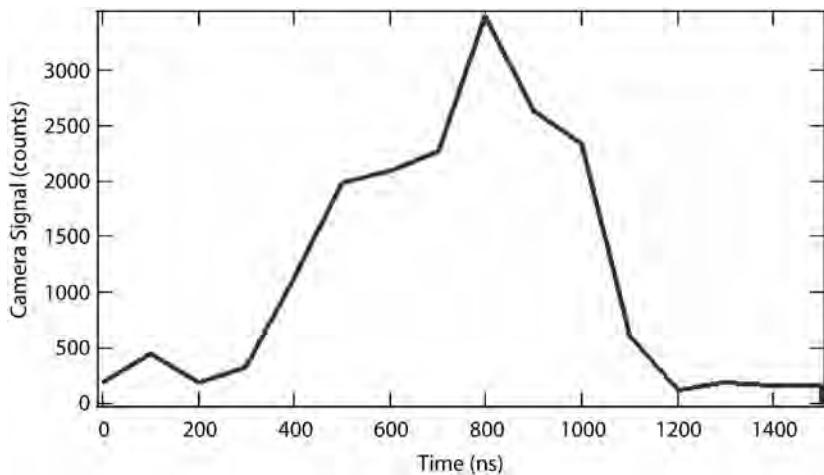
Figure 6. Measured camera minimum integration gate time

respectively, the camera operated at the minimum gate on time for both the HV and CCD gates. At these settings, the gate time was then mapped showing 1 μs performance capability (Figure 6). We mapped the actual gate timing by incrementally delaying the arrival of the pulsed light source while keeping the camera timing fixed and measuring the camera signal at each timing increment.

Brassboard Evaluation

A brassboard camera system (Figure 1) was developed for laboratory and field evaluation of the synchronized camera concept. The key components of the brassboard system are the Intevac ISIE11 EBAPS camera with NSTec internal gating modification, an NSTec interface PCB, a chip-scale atomic clock, a u-blox GPS module, and an Altera Cyclone IV FPGA for timing.

Gate timing for the camera was critical to the success of the system. We worked closely with Intevac to get the software and hardware working properly, particularly to refine CCD control and HV gate settings for the camera. The camera can be internally configured for a specific gate time setting in the software. However, the timing offset relative to the GPS must be externally controlled. We accomplished this task using an FPGA to produce a timing signal for the camera's external "GENLOCK" input. In addition to the GPS synchronization, the HV gate control is "double gated" in the CCD charge integration period of the frame time (one for the desired synchronized function and another

variable time gate for scene illumination to create a context image). To accomplish the double gate, we internally modified the camera to intercept the HV gate signal between the camera's internal control FPGA and rerouted that signal through our external FPGA to achieve the required function.

Chip-Scale Atomic Clock

GPS timing is very accurate for operation where there is a signal available. However, if the GPS signal is unavailable, then our required timing uncertainty of 500 ns or less is not possible, and the system is no longer "locked." The GPS module's onboard oscillator can operate without the GPS signal, but timing synchronization will typically drift beyond the 500 ns limit in a matter of minutes. Recent advances in device integration have made possible the "chip-scale" atomic clock. These devices use micro-optical and RF components to stabilize a clock to two orders of magnitude better than the crystal oscillator in the GPS. By modulating a 780 nm diode laser near a hyperfine (9.2 GHz) transition line in rubidium gas, the lock frequency can be determined from the optical transmission through a small gas cell. The package is about 1 cubic inch and can be soldered to a PCB. We selected the Microsemi Quantum SA.45s clock, implemented by Jackson Labs on an evaluation board. An illustration of an atomic clock physics package and a picture of an actual assembled device are both shown in Figure 7 (Fossi 2016).
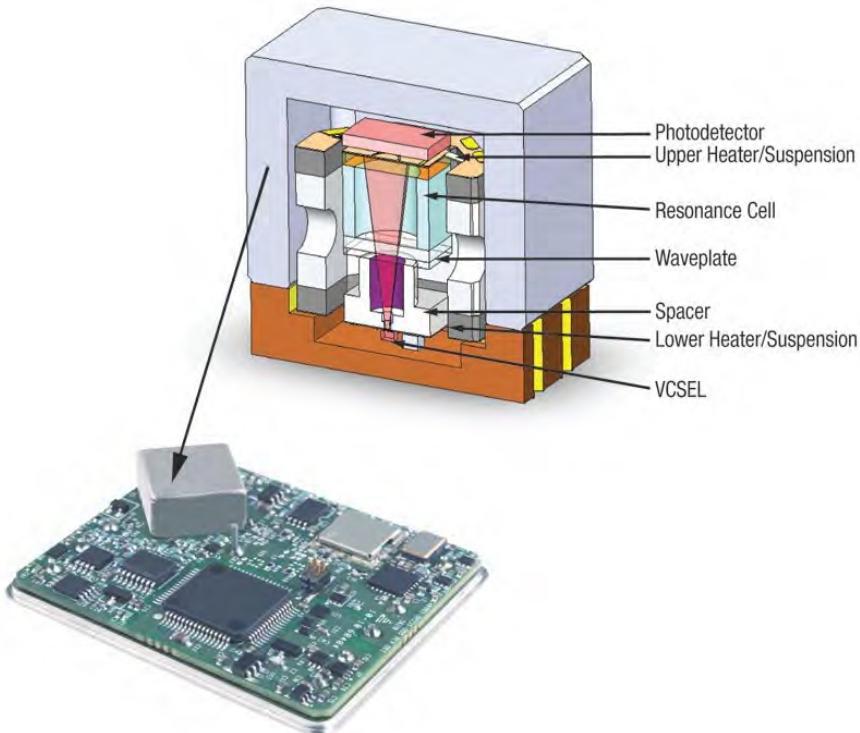
Figure 7. Illustration of an atomic clock physics package next to a picture of an actual assembled device (Fossi 2016)

Photodetector
Upper Heater/Suspension

Resonance Cell

Waveplate

Spacer
Lower Heater/Suspension

VCSEL
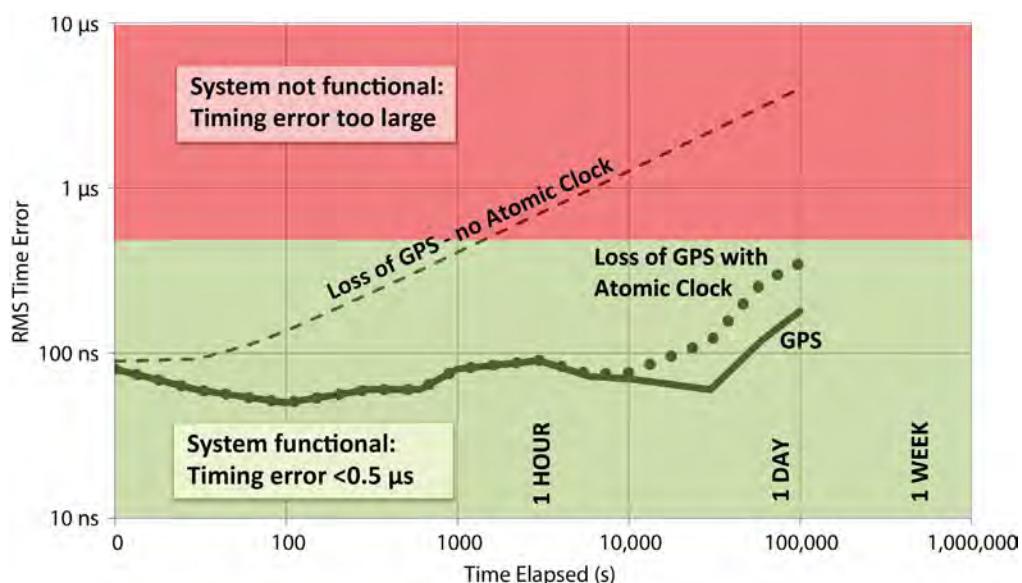
Figure 8. Notional diagram showing how time error in the various clock technologies drifts over time (Jackson 2014, Stanford 2015)

GPS and Chip-Scale Atomic Clock Evaluation

Evaluation of the u-blox GPS receiver showed that the receiver lost timing lock after a few minutes. The chip-scale atomic clock was able to maintain frequency lock for about 6 hours after GPS loss. Figure 8 is a notional diagram based on data from the vendor, showing how time error in the various clock technologies drifts over time. In the condition where a GPS signal is not denied, the system maintains lock in

excess of 1 day (solid line in Figure 8). If the GPS signal is lost (dashed line in Figure 8), then the timing error rapidly increases and exceeds the required accuracy after 1000 sec (indicated where the dashed line crosses from the green to red region in Figure 8). Alternatively, when the GPS signal is lost, a GPS-assisted atomic clock maintains the required accuracy up to 1 day of operation (solid dots in Figure 8).

Conclusion

After careful evaluation of a broad range of sensor and timing technologies, we selected components and assembled a functional brassboard. This effort required extensive coordination with the sensor vendor to develop a system design compatible with the SWaP constraints of operation in a UAV platform. We tested the digital camera and timing technology brassboard in a laboratory environment. The brassboard system was then tested in an operational field environment, and video was captured demonstrating the desired performance (day and night vehicle identification). As a result of these tests, we feel confident that this technology is ready to be integrated into a UAV payload.

Acknowledgments

References

Aebi, V. W., K. A. Costello, P. W. Arcuni, P. Genis, S. J. Gustafson, "EBAPS®: Next generation, low power, digital night vision," OPTRO 2005 International Symposium, Paris, France, May 10, 2005, http://www.intevac.com/wp-content/uploads/2012/01/EBAPS.pdf, accessed September 30, 2016.

Fossi, S., "Chip scale atomic clocks improve for UAV system designs," http://cotsjournalonline.com/articles/view/102375 (site discontinued), accessed September 30, 2016.

Jackson Labs Technologies, Inc., "HD CSAC GPSDO User Manual," Document 80200510, version 1.3, 18 March 2014, http://www.jackson-labs.com/assets/uploads/main/HD_CSAC_Manual_v1_3.pdf, accessed October 15, 2015.

PCO-TECH, Inc., "sCMOS: On the cutting edge: pco.edge family," product brochure v1.02, accessed January 1, 2016.

Stanford Research Systems, "PRS10 — Rubidium frequency standard with low phase noise," http://www.thinksrs.com/downloads/PDFs/Catalog/PRS10c.pdf, accessed October 15, 2015.

Williams, G. M. Jr., A. L. Rheinheimer, V. W. Aebi, K. A. Costello, "Electron-bombarded back-illuminated CCD sensors for low-light-level imaging applications," *Proc. SPIE* **2415** (1995) 211.

Tri-Mode Radiation Detector

RSLN-009-16 | Year 1 of 1

Eric Wagner,[1,a] Alexander Barzilov,[b] Paul Guss,[a] Amber Guckes,[c] and Molly Wolfson[d]

This project sought to develop a new sensor that can detect and distinguish between gamma rays, thermal neutrons, and high-energy neutrons. Moreover, the tri-mode detector would also have the added function to determine the gamma ray and neutron energy spectra "on-the-go." Neutron spectral signal processing would be utilized to determine if the radiation source is an alpha-Be reaction or a suspect spontaneous fission source. We validated that a ^{6}Li-depleted cerium-doped elpasolite (CLYC, Cs_2LiYCl_6:$Ce_{0.5\%}$) detector preserved photon sensitivity and resolution and found that we could measure fast neutron energy. We are confident that the crystal can discriminate against neutron sources and fission emitters. The detector was not tested in the field.

[1] wagnerec@nv.doe.gov, 702-295-8828
[a] Remote Sensing Laboratory–Nellis; [b] University of Nevada, Las Vegas; [c] North Las Vegas; [d] University of Chicago

Background

Present-day in situ radiation detectors use multiple sensors to detect neutrons and high-energy photons. In most cases the neutron sensors can only detect thermalized neutrons, relying on the person carrying the detector or an added hydrogenous material as a moderator. Once thermalized, nearly all the relevant information one can obtain from the source has been eliminated. Although some information from the timing of emissions is still available, the initial energy and trajectory data are not.

By reducing the number of sensors and electronics needed, costs should be minimized, creating a detector of simpler design with greater capability. A sensor's ability to identify the source neutron spectra enables it to distinguish between (alpha, Be) sources and even some spontaneous fission sources.

Project

The project leverages three primary nuclear reactions for detection of neutrons:

$$^6Li + n \rightarrow {}^4He + {}^3H + 4.78 \text{ MeV} \qquad (1)$$

$$^{35}Cl + n \rightarrow {}^1H + {}^{35}S + 0.62 \text{ MeV} \qquad (2)$$

$$^{35}Cl + n \rightarrow {}^4He + {}^{32}P + 0.94 \text{ MeV} \qquad (3)$$

Equation 1 is the dominant reaction for thermal neutrons and produces a peak just above 3 MeV$_{ee}$. The unit MeV$_{ee}$ represents the electron equivalent units of energy, as the varying linear energy transfer (LET) values do not produce the same amount of light output as that of the electrons produced from photon interactions. Therefore, the absolute energy calibration of each particle type varies.

Using pulse shape discrimination (PSD), the incoming radiation can be categorized based on the LET value, hence identifying the radiation as either alpha, proton, or photon. The lower LET events produce a faster pulse than those from higher LET particles such as alphas. Integrating the pulse over a short time period, referred to as the partial integration time, and a long time period, called the integration time, yields real-time
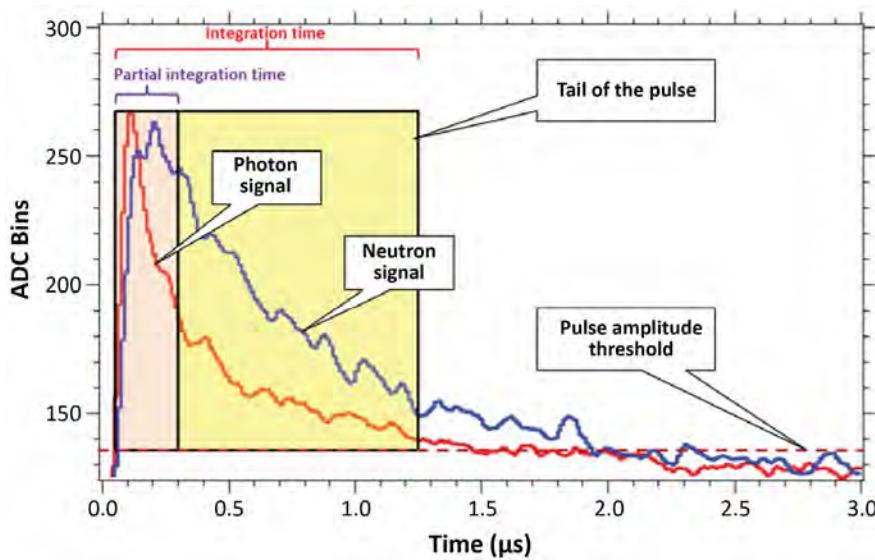
Figure 1. The pulse shape discrimination scheme shows an alpha and triton compared to a gamma detection event

discrimination. The long period integration is designed to collect the full integral of the pulse and to minimize the noise. Discrimination is performed by evaluating the ratio of the integration over the partial integration time to that of the integration time (Brubaker 2013). Figure 1 shows an example of a neutron capture event that produces an alpha and triton (as in Equation 1) compared to that of a gamma detection event.

The goal for this work was to discriminate between various neutron emitters based on the fast neutron energy spectrum generated by spontaneous fission (Herold 1965, Koçak 2014) and (alpha, Be) nuclear reactions (Vega-Carrillo 2002). Figure 2 shows the variation between several spontaneous neutron emitters of concern. Neutron production from alpha emitters such as americium (Am) and plutonium (Pu) combined with beryllium (AmBe, PuBe) produces neutrons from the reaction as shown in Equation 4. The Q value of this reaction is 5.7 MeV and does not share the same energy profile as spontaneous fission emitters. This provides for the possibility to categorize a spectra as characteristic of a fission vs. non-fission source.

$$\propto + {}^9\mathrm{Be} \rightarrow n + {}^{12}\mathrm{C} \tag{4}$$

Prior work (D'Olympia 2014, Guss 2014) used ^{6}Li-enriched and natural lithium detectors having a very strong signal for thermal neutrons due to the high thermal cross section for the reaction in Equation 1. In this work we explored the response to fast neutrons using a cerium-doped elpasolite (CLYC, $\mathrm{Cs_2LiYCl_6:Ce_{0.5\%}}$) crystal depleted in ^{6}Li in order to reduce interference in our measurements from the ^{6}Li reaction. We obtained a 2″ × 2″ CLYC detector depleted in ^{6}Li that upon exposure to cobalt-60 (^{60}Co) and an AmBe source provides clear discrimination between photon and neutron events, as shown in Figure 3.

Data were collected from an AmBe source, californium-252 (^{252}Cf) source (Figure 4), and an accelerator producing several mono-energetic beams. The accelerator data are shown in Figure 5. The accelerator generated neutrons according to the two nuclear reactions shown in Equations 5 and 6; the resulting neutron reactions are commonly referred to as deuterium-deuterium (D-D) and deuterium-tritium (D-T), respectively. Unfortunately, changing the accelerator's neutron generation method from Equation 5 to Equation 6 presented a significant jump in the response of the crystal, resulting in a discontinuity. We have not determined the reason for the jump, but possibilities include a much higher flux rate from the D-T reaction and misalignment of the target after switching from one to another.

$$^2\mathrm{H} + {}^2\mathrm{H} \rightarrow n + {}^3\mathrm{He} \tag{5}$$

$$^2\mathrm{H} + {}^3\mathrm{H} \rightarrow n + {}^4\mathrm{He} \tag{6}$$
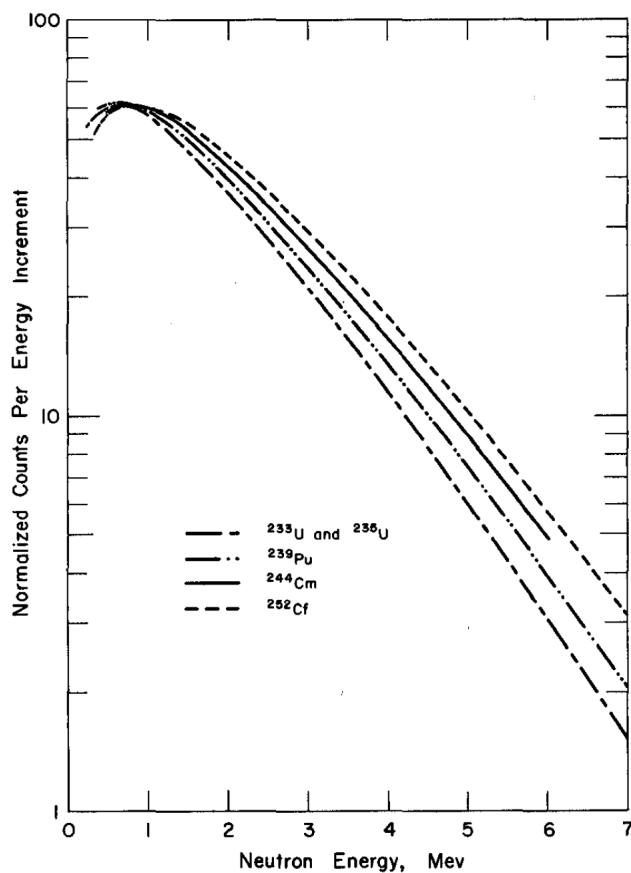
Figure 2. Spontaneous fission energy distribution of sources of interest. Energy spectra of neutrons and gamma rays from spontaneous fission of ^{241}Cm from Herold (1965).
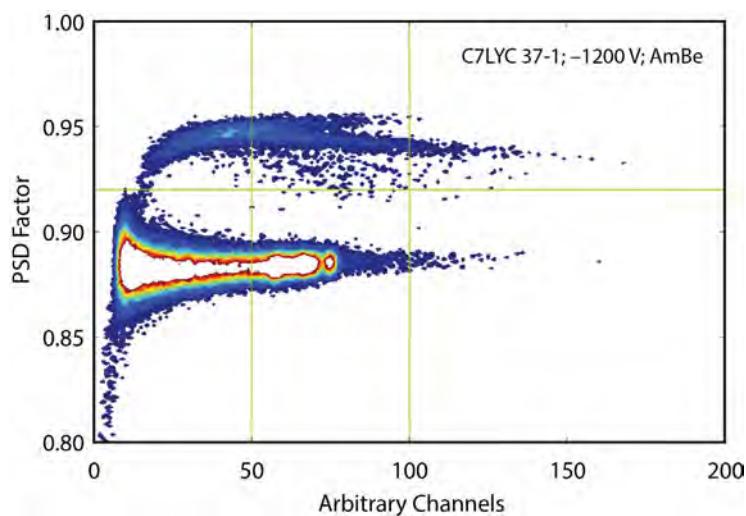
Figure 3. CLYC detector response to AmBe and ^{60}Co

It was also observed that as the incident neutron energy from the accelerator increased, competing nuclear reactions, such as in Equation 3, captured significant numbers of neutrons as their interaction cross sections increased. This resulted in a lower net count rate for incident neutron flux for the reaction in Equation 2, providing our highest energy peak. Eventually at energies beyond 8.5 MeV, the peak we were tracking (from Equation 2) was no longer able to be resolved. Fortunately, as shown in Figure 2, the bulk of the signal of interest is well below the 8.5 MeV threshold.
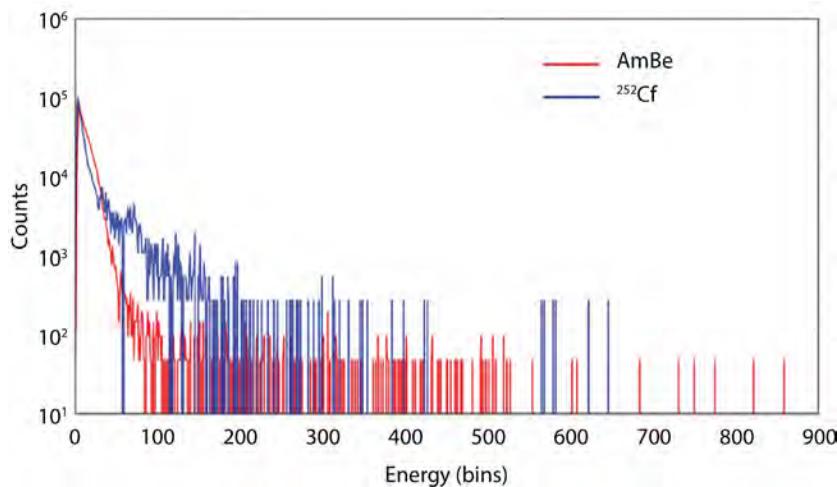
Figure 4. Spectrum collection of AmBe and ^{252}Cf normalized to equivalent count rates
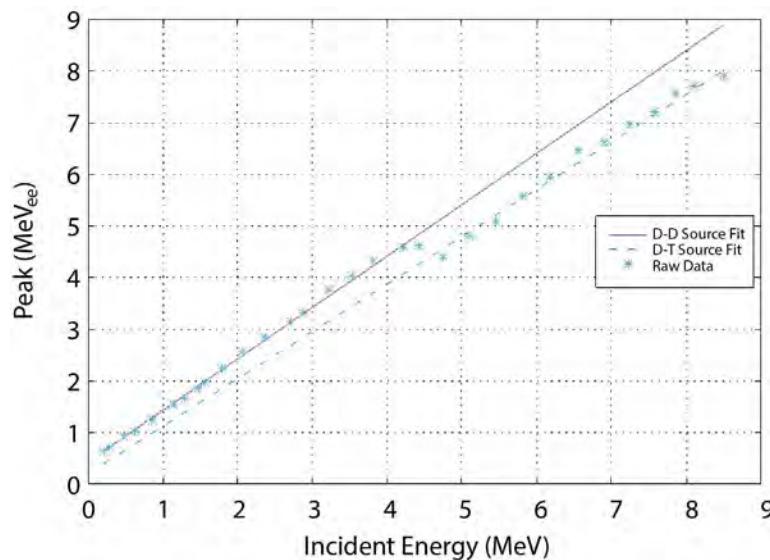
Figure 5. Energy response to mono-energetic neutrons shows itself to be highly linear, with the exception of the discussed discontinuity, allowing simple conversion from detected MeV$_{ee}$ to incident neutron energy
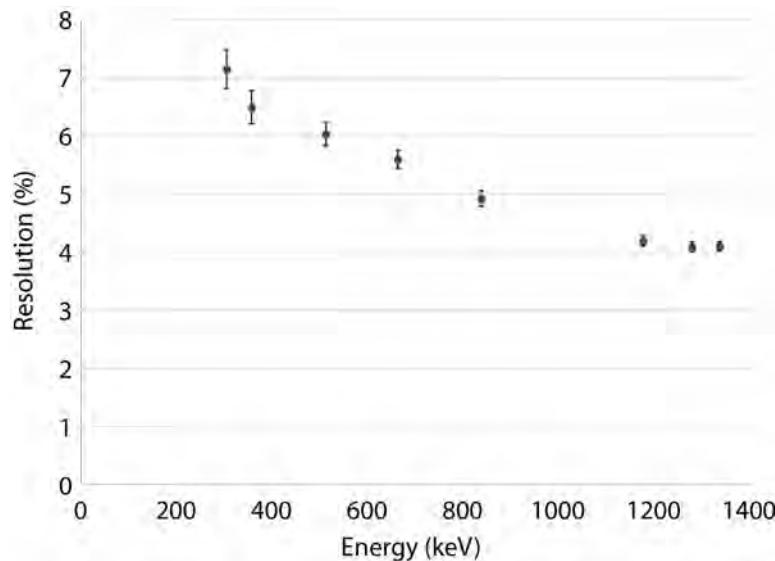
Figure 6. Measured CLYC energy resolution provides better results than NaI, the baseline standard (6.5% at 662 keV)

Although not a focus of this work, the response to gamma ray emitters was also characterized. Figure 6 shows the energy resolution as a function of gamma energy. The crystal is capable of producing better energy resolution for gamma radiation spectra than the commonly used sodium iodide crystals deployed in the majority of spectral field equipment.

Conclusion

This project continued prior work (Guss 2014) on ^{6}Li-enriched CLYC detectors that had demonstrated high thermal neutron discrimination and sensitivity while simultaneously collecting photon spectra. We obtained a ^{6}Li-depleted CLYC detector, validated that it still preserved the same photon sensitivity and resolution, and determined that it can measure fast neutron energy. Work still remains to validate the measurements, especially the discrepancy we observed in our experiment that offset the energy values when modifying the beam line, and to calculate the level of discrimination of varying spontaneous neutron emitters. We are confident the crystal can discriminate against (alpha, Be) neutron sources and fission emitters. Outfitting this into field units would provide a powerful tool to assist in assessing the potential threat level of an unknown shielded neutron source detected in the environment (i.e., an innocuous AmBe moisture density gauge versus a large quantity of plutonium). Additionally, optimization of the ^{6}Li level to preserve both fast and thermal neutron sensitivity and cost should be performed, although natural levels in larger crystals would likely keep costs at a minimum while providing acceptable sensitivity to all three radiation fields.

Acknowledgments

References

Brubaker, E., D. Dibble, M. Wondwosen, P. Yang, "Thermal neutron detection using alkali halide scintillators with Li-6 and pulse shape discrimination," SAND2013-8329, Sandia National Laboratories, Albuquerque, New Mexico, 2013.

D'Olympia, N., P. Chowdhury, E. G. Jackson, C. J. Lister, "Fast neutron response of ^{6}Li-depleted CLYC detectors up to 20 MeV," *Nucl. Instrum. Meth. Phys. Res. A* **763** (2014) 433–441.

Guss, P. P., T. G. Stampahar, S. Mukhopadhyay, A. Barzilov, A. Guckes, "Scintillation properties of a $Cs_2LiLa(Br_6)90\%(Cl_6)10\%$:Ce (CLLBC) crystal," *Proc. SPIE* **9215** (2014) 921505.

Herold, T. R., "Energy spectra of neutrons and gamma rays from spontaneous fission of ^{241}Cm," DP-949, AEC Research and Development Report, Savannah River Laboratory, Aiken, South Carolina, 1965.

Koçak, M., H. Ahmadov, G. Dere, "On prompt fission neutron spectrum in spontaneous fission of ^{252}Cf," *Ann. Nucl. Energy* **70** (2014) 82–86.

Vega-Carrillo, H. R., E. Manzanares-Acuña, A. M. Becerra-Ferreiro, A. Carrillo-Nuñez, "Neutron and gamma-ray spectra of ^{239}PuBe and ^{241}AmBe," *Appl. Radiat. Isot.* **57** (2002) 167–170.

Vega-Carrillo, H. R., V. M. Hernández-Dávila, T. Rivera-Montalvo, A. Sánchez, "Characterization of a ^{239}PuBe isotopic neutron source," in *Proceedings of the ISSSD 2012*, Applied Radiation Isotopes, Mexico City, Mexico, December 2012, **71** Supplemental, 64–69.

This page left blank intentionally

Quantifying Uncertainties through Advanced Theoretical Analysis for Image and Signal Reconstruction

NLV-02-15 | Continued from FY 2015 | Year 2 of 2

Aaron Luttman,[1,a] Marylesa Howard,[a] Jared Catenacci,[a] Kevin Joyce,[a,b] Johnathan Bardsley,[b] Jesse Adams,[a,c] Matti Morzfeld,[c] Brian Helenbrook,[d] and Indika Udagedara[d]

The primary diagnostic systems fielded on subcritical experiments at the NNSS's U1a Complex are producing data whose scale is quickly exceeding the pace at which standard analysis methods can manage. Moreover, rigorously quantifying the uncertainties in large-scale data requires algorithms that add significantly to the computational complexity of the analysis. This project provides methods for accelerating the estimation and analysis process in three different applications that reduce computation and increase the speed of algorithms to make estimation and uncertainty quantification feasible on large scales. The first application is modeling the point spread function (PSF) of the radiographic imaging system at U1a, and we have designed a novel theoretical formulation of radial symmetry in Gauss Markov random fields to reduce the dimension of the problem while maintaining a high-resolution non-parametric form. We also developed state-of-the-art Markov Chain Monte Carlo algorithms to compute the PSF from measured data. The second application we developed calculates the spatial extent of the x-ray source at the diode using x-ray radiographs. The model for this application results in a large-scale linear system, and we have adapted matrix-free methods to eliminate the large memory requirements of standard implementations and make extremely high-resolution estimation and analysis possible. The third application involved developing a novel, fully stochastic reduced-order model that incorporates uncertainty in training data as well as in estimation, hence providing the first method for projection onto reduced models incorporating a model for covariances in the training and tests data errors.

[1] luttmaab@nv.doe.gov, 702-295-0303

[a] North Las Vegas; [b] University of Montana; [c] University of Arizona; [d] Clarkson University

Background

In many cases, traditional data processing and analysis algorithms do not scale with the increasing volume of data. For example, the Cygnus radiographic diagnostic system produces high-resolution images on grids of the order of 4000 × 4000 pixels. A matrix-based optimization method for linearly modeling the image capture would require in excess of a petabyte (10^{15} bytes) of memory to store a dense representation of an operator on the image. The need for robustly quantifying uncertainties in data capture and analysis further exacerbates the computational complexity of estimation, because many algorithms require computation at timescales that are at least that of the estimation and often are longer by orders of magnitude. Clearly, alternatives to traditional approaches must be developed in order to utilize and keep pace with the sheer volume of "big data" coming from many new experimental diagnostic systems.

Bayesian methods provide a framework for handling large-scale data problems that have garnered significant attention in recent literature (Stuart 2010, Howard 2016). By imposing a prior model for the quantity of interest, one can recast the solution space to not only reduce the number of computations needed to find an optimal solution, but also regularize potential instability. In image analysis, the most common model is linear with additive noise,

$$b = Ax + \varepsilon, \tag{1}$$

where b is the measured data subject to measurement error ε and x is the quantity of interest, modeled as input to a linear operator A that maps to a noise-free representation of the auxiliary data. For example, in x-ray imaging, we often wish to measure an object's density from attenuated x-ray intensity measurements. In this case, b is an array of measurements from a radiograph, x is a representation of the object's density, and A is a model that links the two quantities. In many of the cases of interest to us, solving Equation 1 is ill-posed in that a solution may not exist, may not be uniquely determined, or is sensitive to perturbations in the data. Such problems require additional prior knowledge about x in order to formulate a well-posed problem. Prior knowledge about x can be modeled through a prior probability distribution as

$$\pi\left(x|\delta\right) \propto \exp\left[-\frac{\delta}{2}\|x\|_{reg}^2\right], \tag{2}$$

where $\|x\|_{reg}$ denotes a regularization norm of the solution. From this, we develop a posterior density based on the prior density (Equation 2) and the stochastic measurement error. For example, a Gaussian measurement-noise model gives

$$\pi\left(b|x,\lambda\right) \propto \exp\left[-\frac{\lambda}{2}\|b-Ax\|^2\right], \tag{3}$$

which implies, via Bayes' theorem, that

$$\pi\left(x|\delta,\lambda,b\right) \propto \pi\left(x|\delta\right)\pi\left(b|x,\lambda\right) \tag{4}$$

$$= \exp\left[-\frac{\lambda}{2}\|b-Ax\|^2 - \frac{\delta}{2}\|x\|_{reg}^2\right].$$

This model can be augmented so that the parameters λ and δ can also be estimated within a hierarchical framework.

This framework provides a fully quantitative and stochastic formulation of the data collection and estimation process, and is illustrated schematically in Figure 1. Typically, the mode of the posterior density defined by Equation 4, which is called the maximum a-posteriori (MAP) estimator, is used for estimation and is equivalent to the classical variational Tikhonov solution (Vogel 2002). Note that using the MAP estimator involves an optimization, which for large data can be computationally costly. Statistical sampling methods, such as Markov Chain Monte Carlo (MCMC), can also be used with Equation 4 to estimate uncertainties in the calculations. Our work aims to develop methods within this Bayesian framework that focus on accelerating applications to large data.

Project

This work continues our FY 2015 effort (Luttman 2016) in which we developed the individual components that were improved and integrated this year. We addressed three problems in the second year of this project. The first was to accelerate point spread function (PSF) estimation on two fronts—through advanced theory in modeling and through improved Monte Carlo algorithms for uncertainty quantification. In particular, a novel theoretical framework was developed in order to incorporate symmetry-based dimension reduction into the Bayesian statistical framework for uncertainty quantification, and state-of-the-art MCMC algorithms that accelerate convergence were implemented and shown to improve convergence. The second problem addressed developing new matrix-free implementations of optimization-based x-ray source shape (spot) reconstruction and deconvolution computer codes. The algorithmic development made analysis on high-resolution images from various x-ray diagnostics possible, whereas previous implementations were constrained by memory requirements and not capable of analysis on grids beyond 100 × 100 pixels. The final problem in this work was to develop a fully stochastic
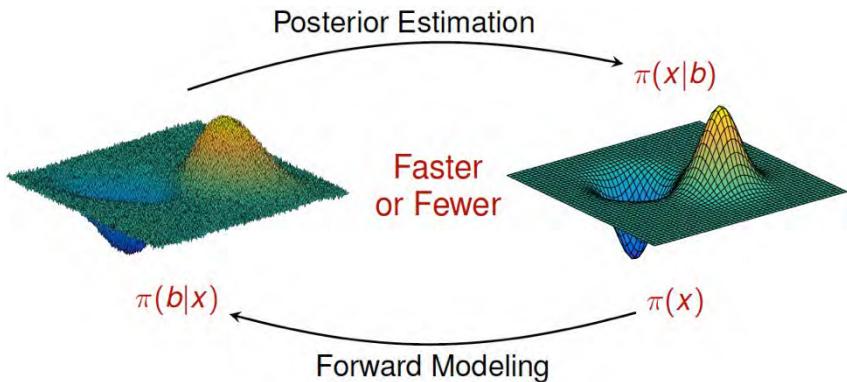
Figure 1. Schematic for Bayesian estimation. A prior density encapsulates what is known (or unknown) about the quantity of interest, then a posterior density is formed by incorporating data. Evaluation of the model can be made by comparing the forward model of the estimate with the data.
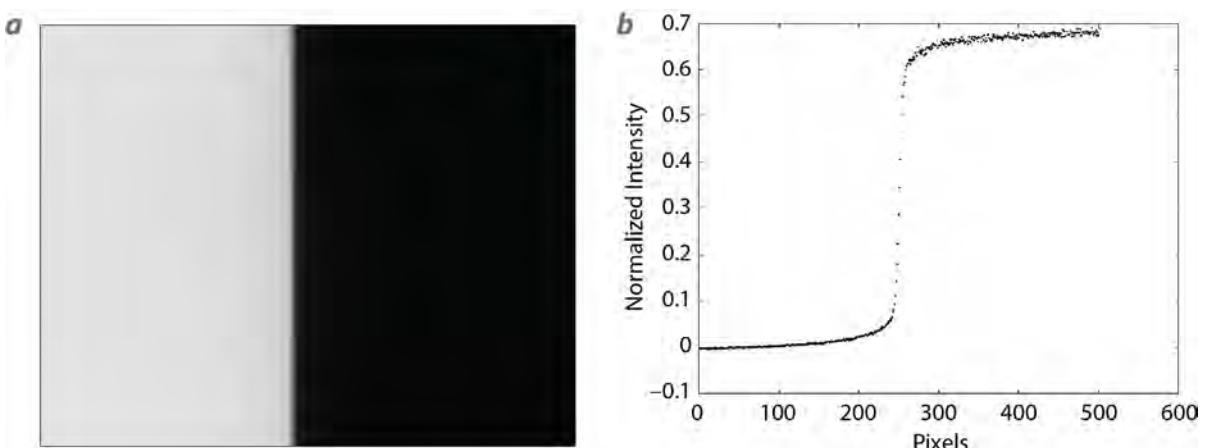

Figure 2. (a) Rolled edge radiographic processed image data and (b) a lineout of the radiograph used to reconstruct the PSF

reduced-order modeling scheme in a statistical framework that accounts for covariances between the errors in training and test data. In this report we lay out the model and demonstrate the results.

Point Spread Function (PSF) Estimation

In this section, we present the work we have done on the problem of estimating a PSF from the radiographic image of a rolled edge (Figure 2). While algorithms for estimating the PSF from edge data have existed for a long time, a rigorous mathematical model describing the nature of possible solutions to the PSF reconstruction model have not. In this project, we developed theory that lays the groundwork for a high-dimensional, non-parametric estimate of the PSF

that is completely novel, and we have adapted state-of-the-art algorithms for uncertainty quantification in the estimation process that accelerate the convergence of standard Gibbs-based MCMC sampling methods (Bardsley 2016a, 2016b).

Deblurring, systematic amelioration of an image corrupted by blur due to the imaging system, is an important problem in computational imaging. Typically, this is modeled as integral convolution of an ideal image with the impulse response, or PSF, of the imaging system (Epstein 2009). In these cases, algorithms for deblurring are referred to as *deconvolution* algorithms. Many methods require an estimate of the PSF, and there exist many imaging applications where an estimate is readily available as

the system impulse response. For example, a focused laser can be used to estimate the impulse response of an optical microscope (Shaw 1991). For many pulsed x-ray imaging diagnostics, measuring a point impulse is not feasible, and the PSF must be estimated indirectly. When blur is isotropic, the functional form of the PSF is radially symmetric and depends only on Euclidean distance $p(|s - t|_{\mathbb{R}^2})$, where we refer to p as the radial profile of the PSF. In this case, the PSF can be estimated by imaging an edge and solving an inverse problem. Specifically, we model the image of an opaque vertical rolled-edge with a known location as integral convolution with an indicator function on the half-plane

$$\int\int_{\mathbb{R}^2} p\left(\|s-t\|_{\mathbb{R}^2}\right)\chi_E(t)\,dt\,ds = \int_{-\infty}^{\infty} p(r)g(r,s)\,dr, \qquad (5)$$

where

$$g(r,s)=\begin{cases} 0 & s<-r \\ 2\left(\pi-\cos^{-1}(s/r)\right) & |s|\le r. \\ 2\pi & s>r \end{cases} \qquad (6)$$

The change of variables in Equation 5 can be interpreted functionally as an operator that takes the PSF as a function of two variables (r,s) to the radial profile that depends only on r. The operator is called the pullback operator of p, and we can use it to extend the space of possible PSFs to a subspace of distributions. In order to apply relevant optimization and stochastic analysis, this space of solutions must be shown to be a Hilbert space.

Specifically, the pullback by $T(s,t) = \|s - t\|_{\mathbb{R}^2}$ is a map $T^\#$ from the space of distributions on an open subset $\Omega_1 \subset \mathbb{R}$, to the space of distributions on an open subset $\Omega_2 \subset \mathbb{R}^2$, such that $\langle T^\#\rho,\phi\rangle = \langle \rho \circ T,\phi\rangle$ whenever ρ is given by integration against a smooth function. It can be expressed explicitly as its action on test functions by a map $T_\#$ that satisfies $\langle T^\#\rho,\phi\rangle = \langle \rho ,T_\#\phi\rangle$. The L^2 completion of the forward image of $T^\#$ on the test functions of Ω_1 is the space of radially symmetric distributions, which we denote $\mathcal{K}$. The pre-image under $T^\#$ of $\mathcal{K}$ is the distribution space of radial profiles $\mathcal{P}$. The following two results establish the necessary requirements of the space $\mathcal{P}$:

Theorem 1: The pullback map $T^\#$ is injective, continuous, and unique.

Theorem 2: The space $\mathcal{P}$ is a Hilbert space with respect to the inner product $\lim_n\langle T_\# T^\#\rho_n,\phi_n\rangle$. Moreover, the restriction of $T^\#$ to $\mathcal{P}$ provides an isometry with $\mathcal{K}$.

The details of this construction and proofs of the previous theorems can be found in Joyce (2016). The space $\mathcal{P}$ has a regularizing norm given by

$$\|p\|_{reg}^2 = \int_0^\infty p(r)\left[Lp\right](r)r\,dr, \qquad (7)$$

where L is the radial component of the Laplacian with a zero right boundary condition and a reflective left boundary condition. The integral inner product includes multiplication by r due to the change of variables.

This lays the necessary theory to apply the recently developed statistical framework for uncertainty quantification in Dashti (2016) that outlines the mathematical foundations for seamless integration of stochastic models with infinite-dimensional data. The theoretical work has practical significance in that high-dimensional data can be analyzed in the continuous limit. Moreover, our framework gives estimation in the space for radial representations $\mathcal{P}$, which dramatically reduces the computational dimension of the PSF.

In order to carry out the estimation on a computer, the problem must be discretized. Then, modeling with Gaussian measurement noise, a Gaussian prior on p, and gamma priors on λ and δ gives a posterior density

$$\pi\left(p,\lambda,\delta|b\right)\propto \lambda^{\frac{M}{2}+\alpha-1}\delta^{\frac{N}{2}+\alpha-1} \qquad (8)$$

$$\times \exp\left[-\frac{\lambda}{2}\|b-Ap\|^2 -\frac{\delta}{2}\|p\|_{reg}^2 -\beta\left(\lambda+\delta\right)\right].$$

The second novel contribution in the PSF estimation analysis was the development of an enhanced Gibbs sampling scheme for MCMC uncertainty analysis. The standard hierarchical Gibbs sampler for posterior analysis is susceptible to poor convergence when a fine discretization is used for deconvolution problems

(Agapiou 2014). The algorithm can be modified to address this deficiency through a process called partial collapse. The partially collapsed Gibbs sampler replaces a sample from $\pi(\delta|\lambda, p)$ with $\pi(\delta|\lambda)$ by integrating the partial joint density with respect to the solution vector, i.e.,

$$\int_{\mathbb{R}^N} \pi\left(\delta, p|\lambda\right) dp \propto \tag{9}$$

$$\exp\left(\left(n/2\right)\delta - \ln\left|\det J_{\lambda,\delta}\right| - \lambda/2\langle b, H_{\lambda,\delta}b\rangle - \alpha\delta\right),$$

where $J_{\lambda,\delta} = \lambda G^T G + \delta L$ and $H_{\lambda,\delta} = I - \lambda G J_{\lambda,\delta}^{-1} G^T$. This density is not a common form, and in order to sample it, a Metropolis-Hastings step is used within the sampler. Observe that a determinant and large matrix solve are required to evaluate this density, but the improvement in convergence that it provides objectively offsets the additional computational complexity.

A statistical analysis of the benefits of this new algorithm were conducted and implemented on radiographic data from Shot 2443 of the Cygnus x-ray imaging system at the NNSS. The 2-D PSF and 1-D radial profile, with statistical quantiles for uncertainty estimation, are shown in Figure 3. The enhanced algorithms we developed have significantly improved convergence properties, as shown in Figure 4. In particular, the number of effectively uncorrelated samples was improved by a factor of 13, with only a factor 4 increase (number of additional matrix factorizations) of additional computational effort.
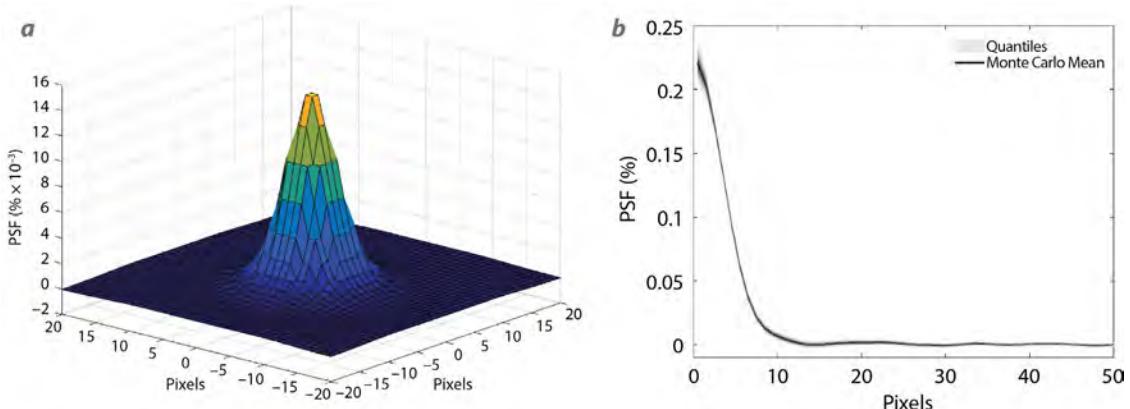
Figure 3. PSF reconstruction for Cygnus radiographic data in Shot 2443. (a) The estimated 2-D Monte Carlo mean PSF. (b) The central 10%, 25%, 50%, 70%, and 90% quantiles of the posterior reconstruction of the radial profile for *p* at each pixel.
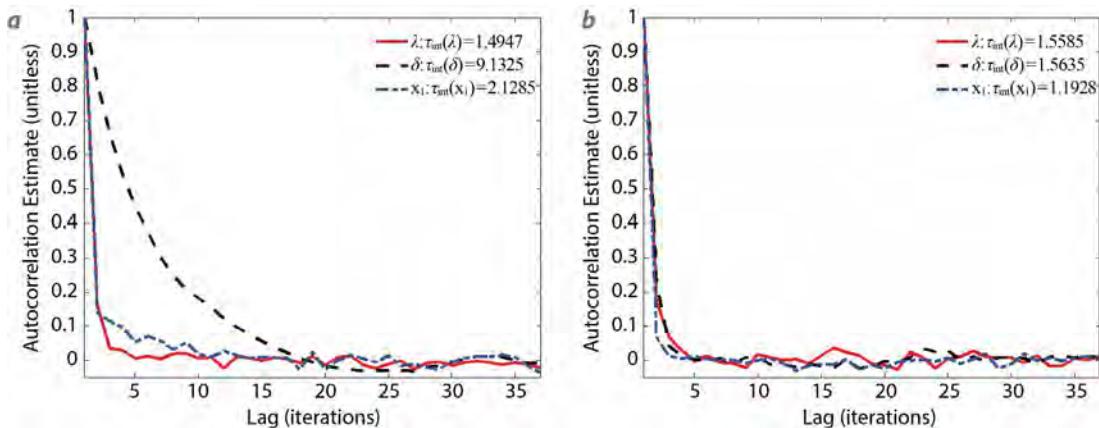
Figure 4. Autocorrelation estimates for the posterior MCMC samples of λ, δ, and the central pixel of the PSF with integrated autocorrelation times indicated in the key. (a) Results from the standard Gibbs sampler and (b) the partially collapsed Gibbs sampler with five Metropolis-Hastings substeps.

X-Ray Spot Estimation

Characterizing the source shape, or spot, of a pulsed power x-ray imaging system is essential in determining a lower bound for the overall resolution of the system. In this subsection, we present a spot estimation method we developed that builds upon previous methods by implementing matrix-free algorithms that decrease computational demands and large memory overhead that would be required in previous implementations on high-resolution images.

Our method for spot estimation involves imaging an L-rolled edge (LRE), which is a calibration object with a 90° aperture and beveled inner edges. Photons not attenuated by the LRE are absorbed by a scintillator, which then emits photons; see Figure 5. In Barnea (1994), the image intensity is modeled as a function of the spot profile via the integral operator equation

$$b(s,t) = \kappa \int\int_{\Omega(s,t)} u(x,y)\,dy\,dx, \tag{10}$$

where u is the spatial profile of the source shape, $\Omega(s,t)$ is the profile of LRE, and κ is a geometry-dependent constant. The intensity values are given on a discrete grid from which we use numerical quadrature to estimate the integral in Equation 10, which in the presence of Gaussian measurement error leads to the discrete matrix equation

$$b = Au + \epsilon. \tag{11}$$

When b and u are organized by stacking columns of the image into a column vector, the operator discretization for A is a structured lower triangular $n \times n$ matrix, where n is the number of pixels in the image; see Fowler (2016) for details.

In the cases of interest to us, n is on the order of 10^7 to 10^8, so explicit construction of A is not feasible. Moreover, estimation and Bayesian uncertainty quantification will require matrix-solves involving A and other matrices of similar order. Hence, solutions at
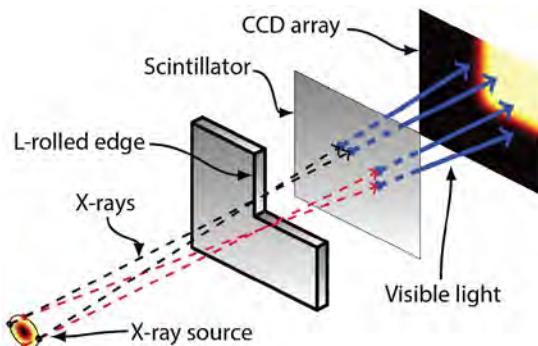

Figure 5. Schematic for modeling the x-ray source shape as a function of image intensity via the image of an LRE

the scale of the data will require that the action of the matrix operator be coded using the structure of A and also that backsolving algorithms for A use only forward evaluations. These techniques are referred to as iterative methods, and many have been studied for large-scale linear inverse problems. In particular, we make use of the projected Newton (PN) algorithm within a conjugate gradient framework. Part of the novelty of our work is in applying this approach to the Bayesian framework for x-ray spot reconstruction, which builds upon the work presented by Fowler (2016).

We assume that u has a non-negative Gaussian prior with precision δL, the intensity data are subject to Gaussian noise with precision λI, and both are subject to gamma hyper-priors similar to the model of PSF reconstruction. For MCMC estimation, we use Gibbs sampling to obtain Monte Carlo samples $(u_k, \lambda_k, \delta_k)$ of the posterior density. The addition of non-negativity is incorporated by solving Equation 12 (below), where w_k is white Gaussian noise. Due to the constraints, this optimization problem is nonlinear, and we utilize the PN algorithm, which uses pseudo-Newton iterations by using an estimate of the Hessian of $\lambda_k A^*A + \delta_k L$, and projecting onto non-negative solutions. See Vogel (2002) for details. The inversion of the Hessian is carried out using the conjugate gradient algorithm.

$$u_k = \arg\min_{u \geq 0}\left\{ \left\| \left(\lambda_k A^*A + \delta_k L\right)^{1/2} u_k \right\|^2 - \left\langle u_k, \lambda_k A^*b + w_k \right\rangle \right\}, \tag{12}$$
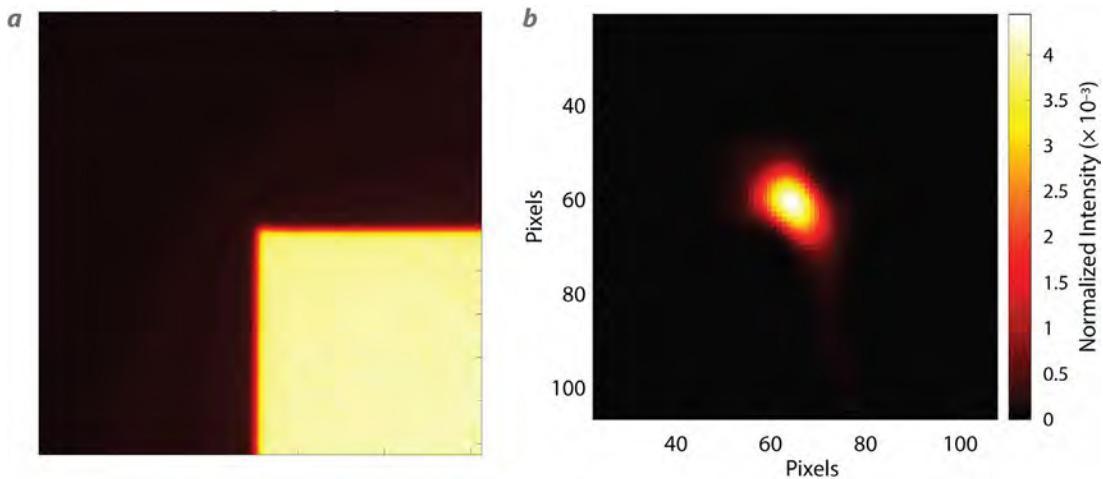
Figure 6. (a) A 500 × 500 pixel radiograph of an LRE and (b) the computed spot shape reconstruction

This method provides a fast and robust way to obtain x-ray spot shape estimates of arbitrarily large images of LREs. Results on a 500 × 500 pixel image are given in Figure 6.

The computational methods developed for this aspect of the project have direct programmatic implementations, and many of the techniques can be adapted for future work in developing algorithms for deconvolution.

Reduced-Order Modeling for Radiation Transport

Reduced-order modeling (ROM) is often used to develop compact representations for high fidelity, computationally intensive models; the most common approach to linear model reduction is principal component analysis (PCA). In PCA, training data are used to construct a reduced basis that serves as a surrogate model. As new data (test data) become available, the new data can be projected onto the reduced space, thus giving an approximation of the test data. However, it is often the case that both the training and test data are contaminated with noise. The noise in the training data causes errors in the basis functions. By projecting noisy data onto noisy basis functions, the resulting approximation has a nonlinear dependence upon both sources of errors, even in the case where the training and the test are both assumed to follow a simple additive error model. In order to formulate

a meaningful measure of the uncertainty present in the results of the PCA approximation, the nonlinear relationship between the noise in the training data and the test data must be accounted for. In this project we first explored this relationship, and then showed that under certain conditions the test data can be approximated by a normal random variable. This information is then used to construct an asymptotic prediction envelope for repeated measurements.

PCA-based methods build a ROM from previously acquired high-fidelity training data. The training data can be obtained from simulations of a high-fidelity model or accurate experimental measurements. More specifically, given a set of high-fidelity training data $D = \{\boldsymbol{\phi}_1, \boldsymbol{\phi}_2, \ldots, \boldsymbol{\phi}_N\}$, the covariance matrix is $C = DD^T$. Then, the eigenvalues r_j and the eigenvectors v_j are computed from C. The reduced basis is constructed by retaining the eigenvectors associated with the first M principal components. Then test data, which are often computed from low-fidelity simulations or coarse measurements, can be approximated in the reduced space by

$$\boldsymbol{y}^M = \bigg|_{m=1}^{M} \left(\boldsymbol{y}^T \boldsymbol{v}_m \right) \boldsymbol{v}_m, \tag{13}$$

where $\boldsymbol{y}$ is the test data and $\boldsymbol{y}^M$ is the projection onto the M principle components. As mentioned previously, both the test data and the training data have uncertainties. The uncertainty in the training data manifests

in the eigenvalue decomposition of the covariance matrix, so uncertainty in the training data directly affects the accuracy of the reduced model. The test data that we want to represent in the reduced basis also contain errors, and this inaccuracy is projected onto the reduced model. Due to this process, the uncertainty in the projection y^M will be affected by the uncertainty in both the training data and the test data; however, the coupling of the uncertainty occurs in a nonlinear way.

The challenge in this setting is to provide a measure of uncertainty for the projection result y^M. We show how the uncertainty can be quantified and used to construct a predictive interval in a simple scenario. We must first specify a statistical model for the test data, and for this we take a standard additive error model given by

$$y = y^M + \theta + \eta, \tag{14}$$

where η is the measurement error associated with the acquisition of the test data, and θ accounts for the so-called modeling error, which comes from errors in the training data. We make the standard assumption that the measurement errors η are independent and identically distributed (i.i.d.) random normal variables with mean 0 and variance σ_η^2. To simplify the scenario, we make the additional assumption that the modeling

error is an i.i.d. random normal variable with mean 0 and variance σ_θ^2. With these assumptions, the 95% predictive envelope can be formulated as

$$y^M \pm 2\left(\sigma_\theta^2 + \sigma_\eta^2\right), \tag{15}$$

which gives a region in which 95% of future observations of the test data should fall.

To test our analysis, we perform the ROM approach and envelope construction on a simple example. In this example we take the training data as

$$\phi_n = sin\,(n\pi x) + \varepsilon_n, \; n = 1, \ldots, N, \tag{16}$$

where $\varepsilon_n \sim N(0, \sigma_\varepsilon^2 I)$ is a random vector representing error in the training data. The test data are given by

$$y = 0.3sin\,(\pi x) + 0.4sin\,(3\pi x) \tag{17}$$
$$+ 0.3sin\,(5\pi x) + \eta,$$

where $\eta \sim N(0, \sigma_\eta^2 I)$ is a random vector representing the measurement error in the trial data. The projected data are shown in Figure 7, and we see that the projection provides a reasonable approximation to the signal without noise present (labeled as y_{true} in the legend). We also see that the 95% predictive envelope is effective at capturing roughly 95% of the data in an independently generated test data set.
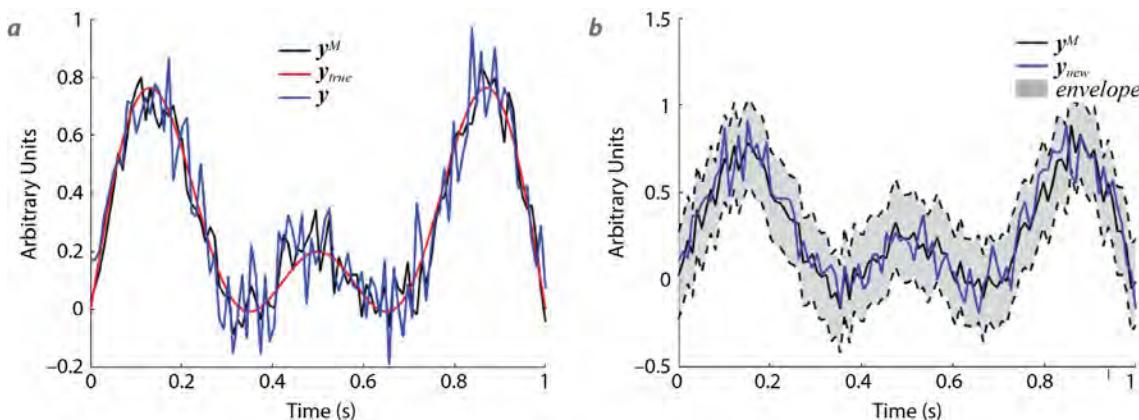

Figure 7. The results from a simple example for using PCA and constructing a predictive interval. (a) The true signal data (red) are compared with the simulated measured data (blue) and the projection obtained from the ROM (black). (b) The 95% predictive interval on an independently generated test signal.

Future work includes adapting this methodology to experimentally collected signals. There are two major difficulties in applying this work to experimental data. The first difficulty is that the errors may not be well approximated by a normally distributed random variable, and the second is that experimental data may not be densely sampled enough to use standard variance estimation techniques. Future efforts will involve understanding how to incorporate more general error structure into the statistical model and constructing an appropriate predictive envelope in these cases.

Conclusion

In each of the three applications we have presented, our work has shown how advanced analysis can be used to improve the computational efficiency of Bayesian statistical methods. Moreover, our efforts have provided several novel contributions to this literature in the form of publications and computer codes implementing the methods (Bardsley 2016a, 2016b; Howard 2016; Joyce 2016; Udagedara 2016). This work is aimed directly at furthering mission goals related to improving computation of quantifications of uncertainty—a central goal of the Stockpile Stewardship program.

Acknowledgments

References

Agapiou, S., J. M. Bardsley, O. Papaspiliopoulos, A. Stewart, "Analysis of the Gibbs sampler for hierarchical inverse problems," *SIAM/ASA J. Uncertainty Quantification* **2**, 1 (2014) 511–544.

Bardsley, J. M., A. Luttman, "A Metropolis-Hastings method for linear inverse problems with Poisson likelihood and Gaussian prior," *Int. J. Uncertainty Quantification* **6**, 1 (2016a) 35–55.

Bardsley, J. M., K. Joyce, A. Luttman, "Partially collapsed Gibbs sampler for linear inverse problems and applications to x-ray imaging," DOE/NV/25946--2713, National Security Technologies, LLC, Las Vegas, Nevada, 2016b.

Barnea, G., "Penumbral imaging made easy," *Rev. Sci. Instrum.* **65**, 6 (1994) 1949–1953.

Dashti, M., A. M. Stuart, "The Bayesian approach to inverse problems," in *The Handbook of Uncertainty Quantification*, R. Ghanem, D. Higdon, H. Owhadi, eds., Springer, 2016.

Epstein, C. L., *Introduction to the Mathematics of Medical Imaging*, SIAM Publishing, Philadelphia, 2008.

Fowler, M., M. Howard, A. Luttman, S. E. Mitchell, T. J. Webb, "A stochastic approach to quantifying the blur with uncertainty for high-energy x-ray imaging systems," *Inverse Probl. Sci. Eng.* **24**, 3 (2016) 353–371.

Howard, M., M. Fowler, A. Luttman, S. E. Mitchell, M. Hock, "Bayesian Abel inversion in quantitative x-ray radiography," *SIAM J. Sci. Comput.* **38**, 3 (2016) B396–B413.

Joyce, K., "Point spread function estimation and uncertainty quantification," PhD dissertation, University of Montana, 2016.

Luttman, A., M. Howard, K. Joyce, J. Adams, J. Bardsley, "Quantifying uncertainties through advanced theoretical analysis for image and signal reconstruction," in *Site-Directed Research and Development*, FY 2015, National Security Technologies, LLC, Las Vegas, Nevada, 2016, 179–188.

Shaw, P. J., D. J. Rawlins, "The point-spread function of a confocal microscope: Its measurement and use in deconvolution of 3-D data," *J. Microscopy* **163**, 2 (1991) 151–165.

Stuart, A. M., "Inverse problems: A Bayesian perspective," *Acta Numerica* **19** (2010) 451–559.

Udagedara, I., B. Helenbrook, A. Luttman, S. E. Mitchell, "Reduced order modeling for accelerated Monte Carlo simulations in radiation transport," *Applied Mathematics and Computation* **267** (2015) 237–251.

Vogel, C. R., *Computational Methods for Inverse Problems*, SIAM Publishing, Philadelphia, 2002.

Multichannel, Cross-Band UAS Radio Relay Using Polyphase Signal Processing

STL-089-16 | Year 1 of 1

James Peterson,[1,a] Kelly Painter,[a] Duane Gardner,[a] and Howard Wong[a]

This project developed polyphase channelizer signal processing techniques for efficient implementation on an aerial relay system with dynamic channel allocation and frequency translation capabilities. Stringent size, weight, and power constraints on unmanned aerial system platforms demand highly miniaturized and power-efficient circuitry. Polyphase channelizer signal processing techniques are very computationally efficient for processing communication bands with many narrowband channels, and may even be extended to wideband signals through the use of perfect reconstruction filter banks. Our primary focus was to investigate different polyphase channelizer attributes suitable for various aerial relay applications and implement these signal processing functions into a Xilinx Zynq 7000 series programmable system-on-chip (PSoC) platform.

[1] petersjc@nv.doe.gov, 805-681-2307
[a] Special Technologies Laboratory

Background

With the evolution of modern very-large-scale-integration (VLSI) technological capabilities, the "RF-to-bits" signal processing paradigm continues to move forward, utilizing the advantages of digital signal processing (DSP) (Harris 2003). In order to leverage such digital signal processing techniques onto size, weight, and power (SWaP)–constrained platforms such as an unmanned aerial system (UAS), careful consideration must be taken in order to maximize computational efficiency of these algorithms. A Work for Others sponsor previously inquired about using a UAS as a communications relay between disparate ground operators over occluded terrain, as illustrated in Figure 1. Besides accommodating different radio equipment between the operators, the sponsor also desired the ability to utilize existing communications infrastructure if possible to maximize signal coverage. While dedicated cross-band commercial repeaters
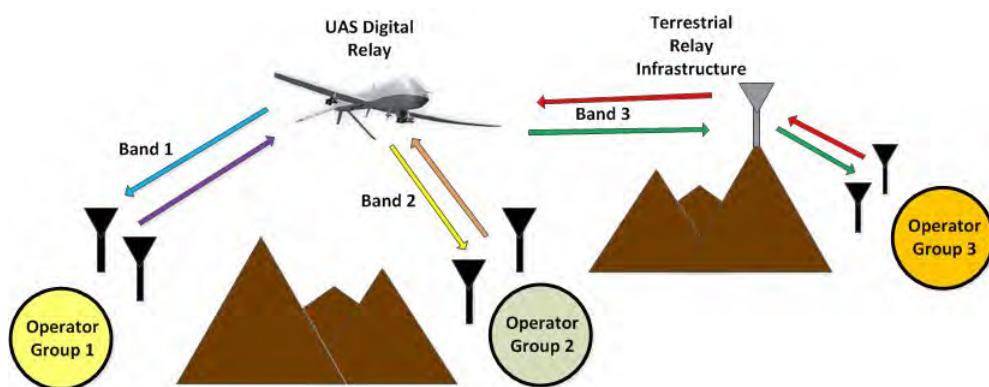

Figure 1. Diagram of proposed concept of operations

were available, they lacked ability to dynamically allocate and translate channels with diverse frequency and bandwidth attributes as required by the sponsor. This SDRD effort has attempted to overcome this limitation by developing computationally efficient polyphase channelizer signal processing techniques into a low-power field-programmable hardware platform.

Project

Signal Processing Overview

The polyphase channelizer signal processing approach was chosen for its computational efficiency in processing multiple narrowband channels simultaneously. The input communications band with bandwidth, ΔB, is digitized at a sufficiently high sampling frequency to obey the Nyquist rate, fs, where fs ≥ 2ΔB. Figure 2 displays a graphical depiction of a communications band with multiple channels spaced uniformly at Δf.

In analyzing a communications band of interest, a prototype filter is chosen with desired spectral characteristics to sufficiently channelize the incoming signals. A finite impulse response (FIR) filter is chosen in order to maintain linear phase performance over the entire pass, transition, and stop bands, which is

useful in a majority of communications applications. A low-pass prototype FIR filter, $H(z)$, of order N, may be decomposed into a polyphase description of M-rows if the filter order is evenly divisible by M, as shown in Equation 1 (Harris 2004):

$$H(z) = \left| \sum_{n=0}^{N-1} h(n) z^{-n} \right.$$

$$= \left| \sum_{r=0}^{M-1} z^{-r} \right| \sum_{n=0}^{N-1} h(r+nM) z^{-nM}. \tag{1}$$

More generally, the signals of interest are band-pass rather than low-pass. In the discrete time domain, a band-pass filter, $G(z)$, may be expressed as a simple heterodyne of low-pass filter coefficients in the z-transform domain, as expressed in Equation 2,

$$G(z) = H\left(e^{-j\theta_k} Z\right), \tag{2}$$

where θ_k is the complex frequency rotation phasor of the kth band-pass filter center, in radians. If the M channels are uniformly spaced, then the sampling frequency may be selected so the channel spacing corresponds to the sampling frequency divided by M, as shown in Figure 2. This criterion corresponds in the sampled data domain to centering each of the kth band-pass filter centers as the kth multiples of $2\pi/M$ radians. Under this condition, Equations 1 and 2 may be combined as
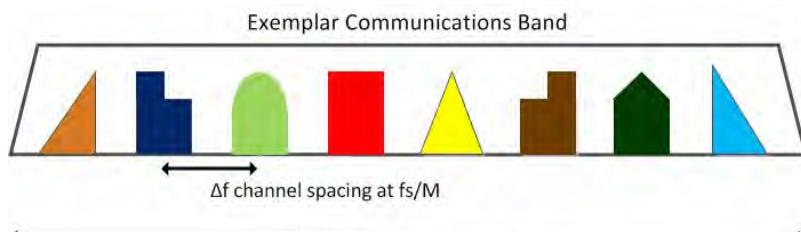

Figure 2. Exemplar communications band
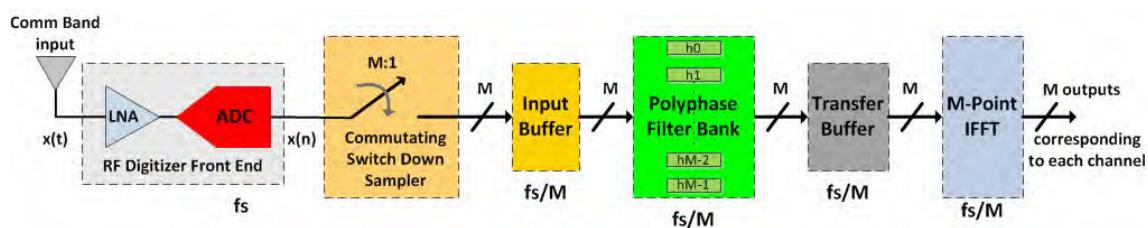
Figure 3. Polyphase analysis channelizer block diagram

$$G(z) = H\left(e^{-j\theta_k} z\right)$$

$$= \left| \sum_{r=0}^{M-1} e^{j\frac{2\pi kr}{M}} z^{-r} \right| \sum_{n=0}^{N-1} h(r+nM) z^{-nM},$$

(3)

where $\theta_k = 2\pi k/M$.

Using this particular choice of the band-pass filter (channelizer bin) center spacing, the complex phasor heterodyne on each row of the polyphase filter corresponds to an inverse fast Fourier transform (IFFT) applied to the polyphase filter bank output. The delay elements corresponding to each row are implemented using a commutating down-sampling switch. The associated signal processing block diagram is shown in Figure 3.

All of the M channels are simultaneously available for processing at the down-sampled rate fs/M. Placing the commutating down-sampling switch at the input of the filter bank reduces the filter order by M in each row of the polyphase bank by equivalence of the Noble Identity (Harris 2004). This reduction in filter order creates the significant computational savings as the number of channels, M, increases. While the down-sampling operation before the filter bank incurs aliasing, the aliasing is M-fold and unique to each row due to each delay element, z^{-r}. The unique M-fold aliasing is removed by application of the IFFT at the filter bank output. The IFFT computational workload is proportional to $(M/2)(\log_2 M)$ complex multiplications and $M(\log_2 M)$ complex additions (Proakis 2007).

Once the M down-sampled channel outputs are obtained after the IFFT block, each of these signals may be individually selected and translated into different channel assignments. This flexibility is essential to meet the dynamic channel allocation needs of the aerial relay system operational requirements for large and diverse user groups. For sampled input spectra that are relatively large and straddle multiple communication bands, this technology presents the capability to cross-band signals to overcome traditional spectral limitations. Figure 4 displays a graphical example of channel selection and translation using a polyphase channelizer.

The spectral translation occurs within a channel mapping switch signal processing block. For retransmission, the new channel assignments must be heterodyned, filtered, combined, and up-sampled before being converted back into an analog signal for broadcast. The polyphase synthesizer channelizer performs these functions as the dual of the polyphase analysis channelizer previously discussed and is displayed in Figure 5. Figure 6 is a block diagram of the entire relay system.
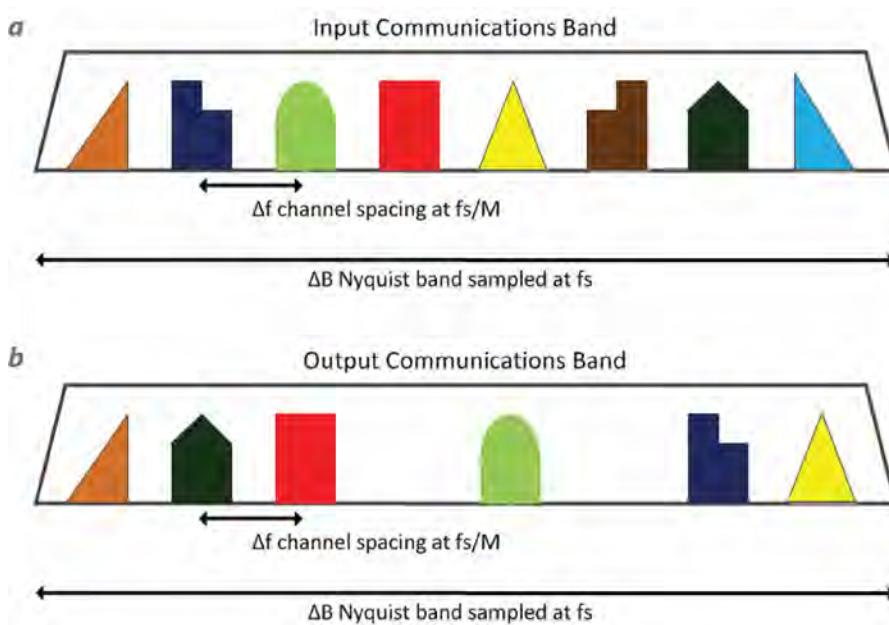

Figure 4. Polyphase channelizer (a) spectral input and (b) output graphic. Colored shapes represent different communications channels, which can be translated independently (i.e., no particular order), and may even be nulled (cancelled).
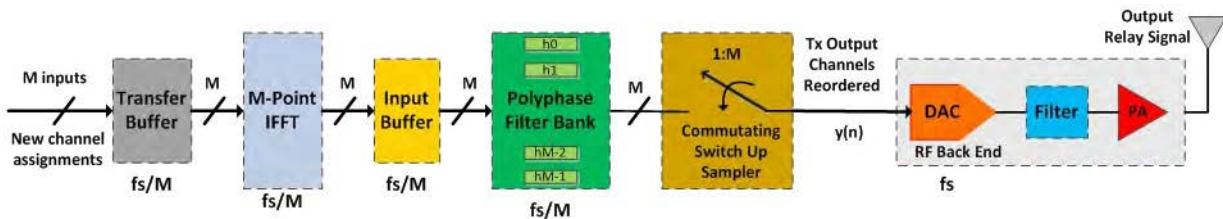
Figure 5. Polyphase synthesis channelizer block diagram
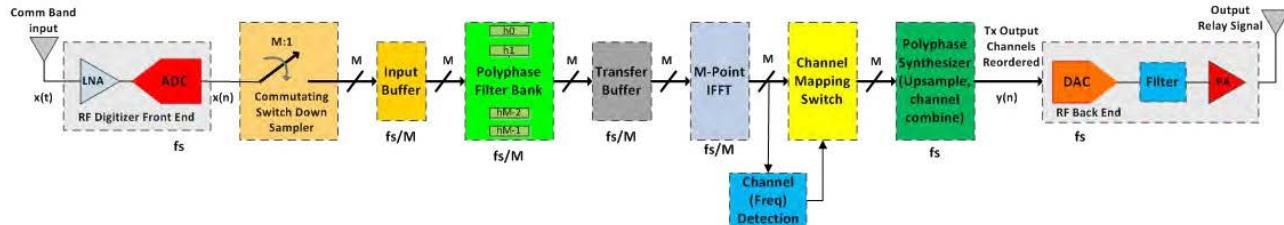
Figure 6. Relay system signal processing diagram

Perfect Reconstruction Filter Bank Investigation

For the generalized scenario featuring varying channel allocations and bandwidths, the polyphase analysis channelizer must be capable of processing signals across more than one channelizer bin while preserving baseband content. Spectral translation and reconstruction of the signal across the multiple channelizer bins must be accurate enough to minimize any perceivable errors. A filter with such characteristics is known as a perfect reconstruction filter bank. The primary attribute of the perfect reconstruction filter bank is the symmetrical overlap of the filter's transition band about the half magnitude point such that the waveform energy is conserved; this attribute is also known as a Nyquist filter (Harris 2004). Figure 7 depicts the frequency response (red dashed lines) across the multiple channelizer bins.

Various techniques were investigated for prototyping the analysis channelizer, ranging from using the Parks-McClellan exchange method (Harris 2004) to a windowed sinc function. The most successful Nyquist filter effort was developed using a Kaiser Bessel window with a beta factor of 8. The FIR filter was originally designed with 251 taps with the Kaiser Bessel
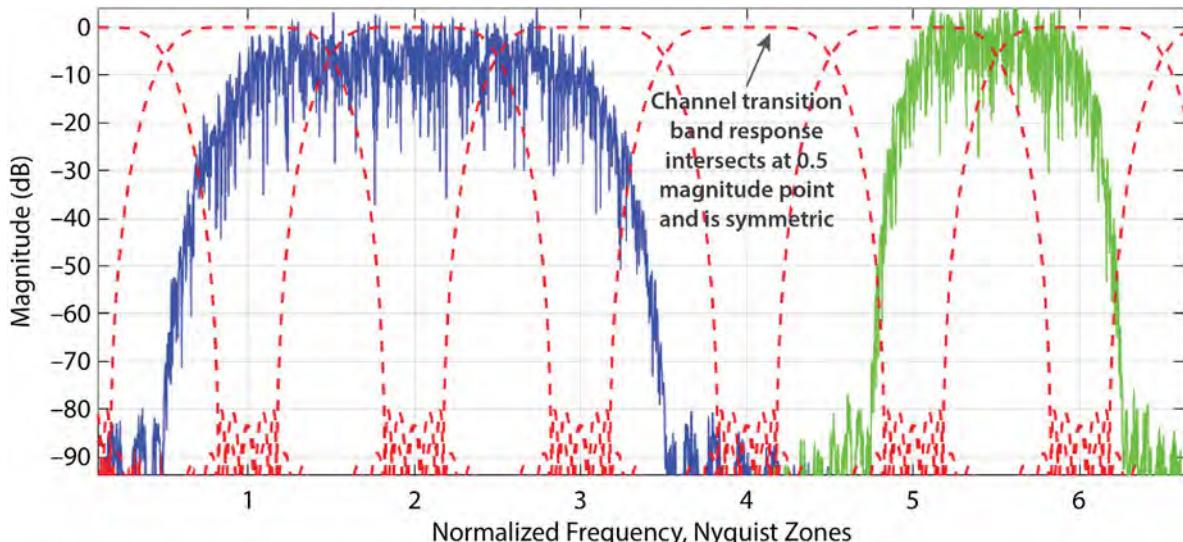
Figure 7. Perfect reconstruction filter bank frequency response across analysis channelizer input bins

window; the odd number of taps maintained alignment of the zero crossings spaced at increments of 25 counts. The filter was then padded with three leading zeros and two trailing zeros for a total of 256 taps for polyphase decomposition (32 rows × 8 columns); the filter response is plotted in Figure 8.
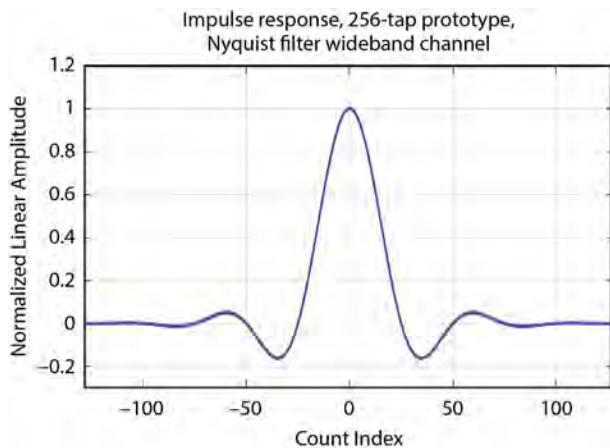
Figure 8. FIR prototype filter response for analysis channelizer

Decimation Rate Investigation

The decimation rates for filter bank operation were also examined. Maximally decimated (fs/M) perfect reconstruction filter banks demonstrate problems with spectral aliasing occurring across adjacent channelizer bins, as these adjacent channelizer bins overlap at the folding frequency. When significant input energy is present in the transition bands of adjacent channelizer bins, it ends up aliasing within that bin after down-sampling, as demonstrated in the middle row of plots in Figure 9.

By oversampling an integer multiple of the maximally decimated rate, (n × fs/M), the equivalent bandwidth is compressed by a factor n, and the spacing between adjacent Nyquist zones is subsequently increased by n. The bottom row of Figure 9 shows the decimation rate of 2 × fs/M, in which the folding frequency corresponds to the center of the adjacent channelizer bin, where the filter has reached its full stop-band attenuation, preventing aliasing from occurring. When operating the filter bank as non-maximally decimated, additional adjustments must be made to properly align the IFFT coefficients. Oversampling by a factor of 2 allows for convenient state machine alignment of these coefficients (Harris 2004; Chen 2014) and was chosen for the final design implementation.

Polyphase Synthesis Channelizer Properties

The polyphase synthesis channelizer performs the dual operation of the analysis channelizer. Initially the baseband channels are heterodyned through an IFFT, then processed through a synthesis filter bank where they are up-sampled by (M/n × fs) through a commutating switch for re-transmission at a Nyquist sample rate. For perfect reconstruction, the composite response of the analysis and synthesis filter banks must form a Nyquist channel (Chen 2014),

$$H(z)G(z) = H^{NYQ}(z). \qquad (4)$$

The analysis channelizer, $H(z)$, can perform channelization more effectively if it is selected as a Nyquist filter. Subsequently, the synthesis filter, $G(z)$, must be designed with near-unity response (minimal pass-band ripple) over the analysis filter pass and transition bands, as illustrated in Figure 10. The synthesis filter must also attenuate the adjacent Nyquist zones from the analysis channelizer, also shown in Figure 10.

In order to meet these criteria, the synthesis channelizer filter was designed using the Parks-McClellan algorithm for minimal pass-band ripple (less than 10^{-3} dB) as a 320-tap FIR filter.

Channelizer Results

MATLAB simulations were completed for an exemplar polyphase channelizer (32 channels) as illustrated in Figure 11, with signals of varying bandwidths and spacings. After being processed through the analysis channelizer, the baseband channels were then re-mapped and processed through the synthesizer channelizer for re-transmission.

After the signal frequencies were translated, the input and output baseband time domain waveforms were compared to ensure accuracy during the perfect reconstruction; two channels are plotted in Figure 12.
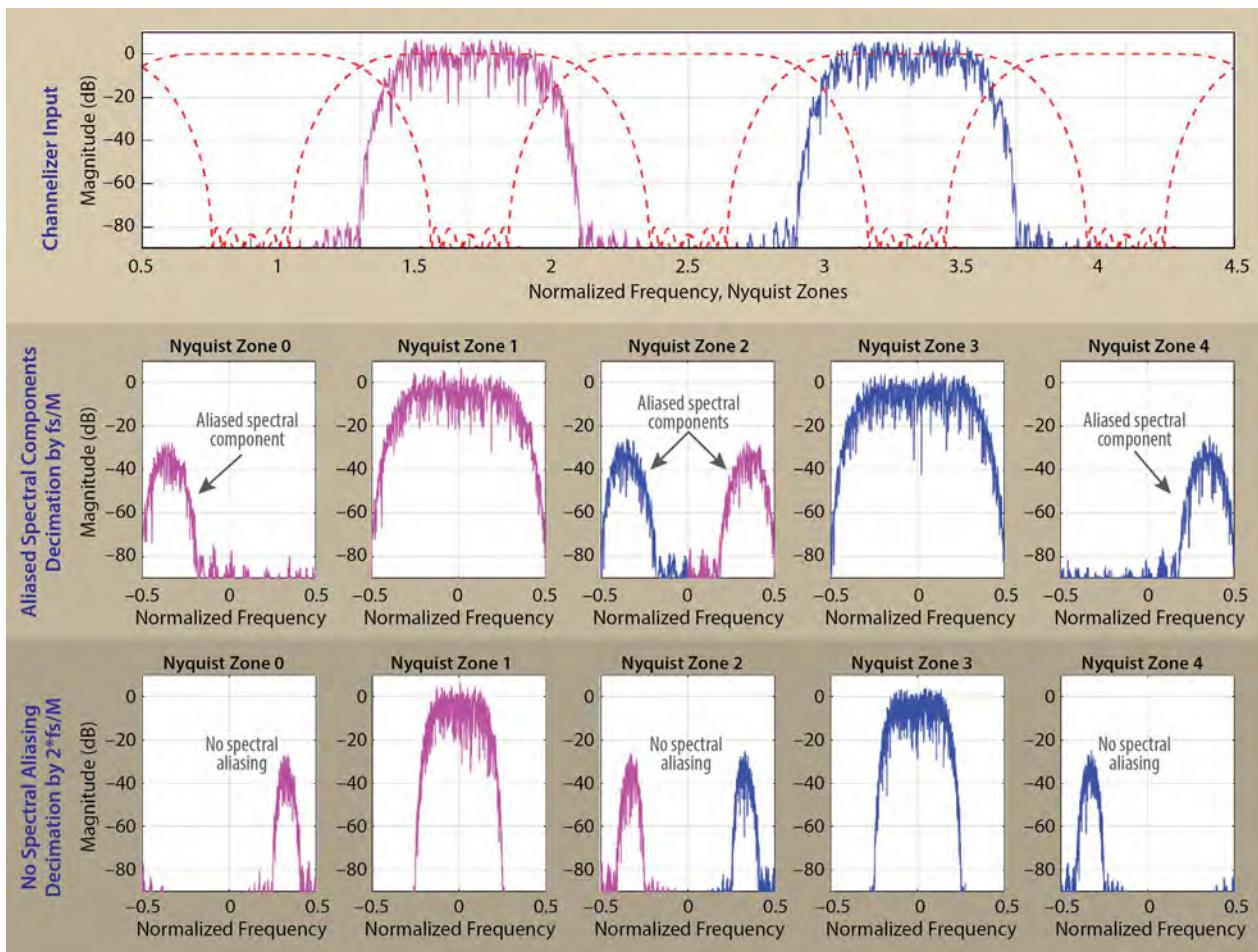
Figure 9. Channelizer decimation rates and Nyquist bin performance. The middle row displays aliased spectral components as a result of significant input energy present in the transition bands of adjacent channelizer bins for the maximally decimated channelizer. The bottom row shows no spectral aliasing when decimation has been further reduced by a factor of 2, since the adjacent bin energy has been fully attenuated.
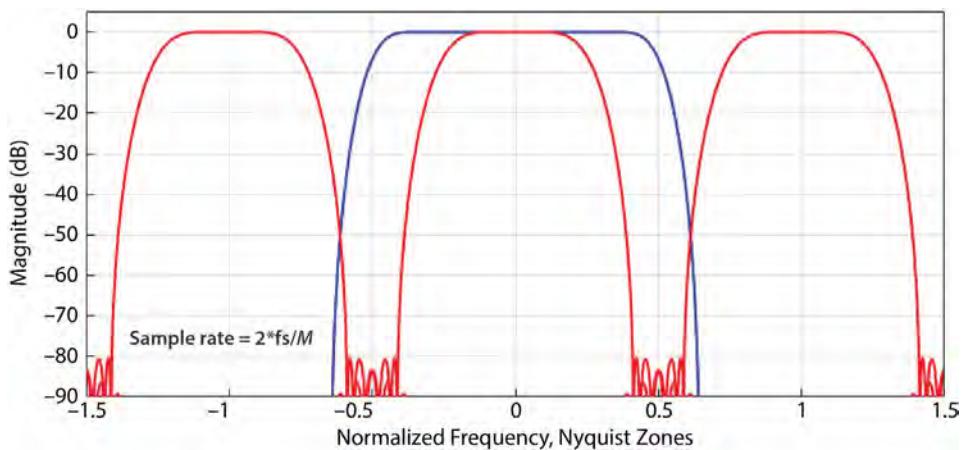
Figure 10. Polyphase synthesis filter characteristics. The synthesis filter (blue) must have minimal pass-band ripple and must also attenuate the adjacent Nyquist zones (red) from the analysis channelizer.
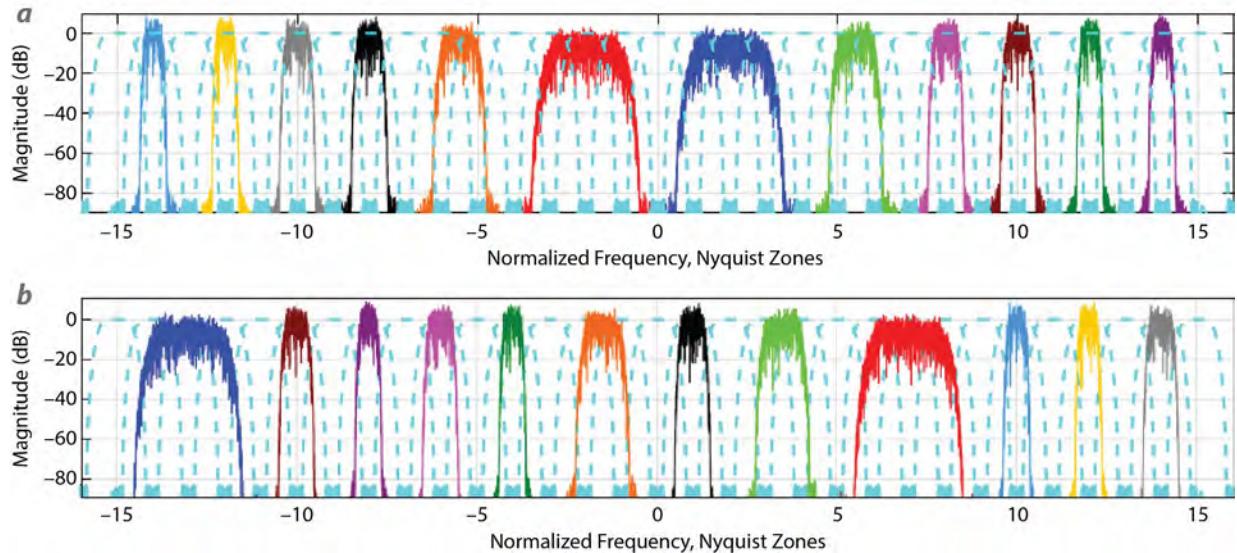
Figure 11. Polyphase channelizer spectral translation showing (a) analysis input signal spectra and (b) synthesis output signals after the signals have been translated through the channelizer. Each of the signals spectral shapes have been maintained, although they have been moved in frequency.
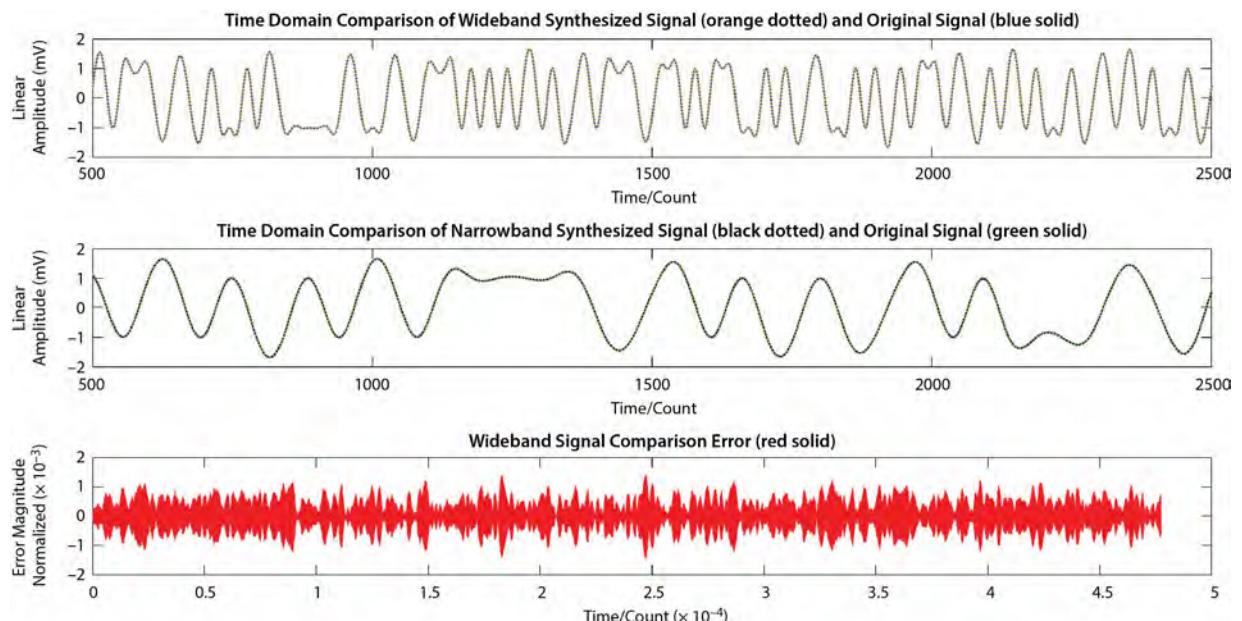
Figure 12. Time domain reconstruction of wideband and narrowband signals. The wideband signal comparison error indicates improvements can be made in the analysis channelizer filter transition band design.

In the wideband signal reconstruction example, errors were maintained within approximately 10^{-3}. Signals with band centers located at the channelizer band edges were observed to have up to 10% error, indicating future improvements can be achieved in the analysis channelizer filter transition band design.

Conclusion

A non-maximally decimated polyphase channelizer was developed with perfect reconstruction capabilities in order to perform dynamic channel allocation and spectral translation for a UAS relay application. Design trade-offs were thoroughly examined, and

an exemplar 32-channel design was completed in MATLAB. Implementation of the design into firmware on a Xilinx Zynq 7000 programmable-system-on-chip (PSoC) platform began at the end of the project. Future efforts should focus on completing firmware implementation for demonstrating the bounds of channelizer complexity vs. latency for the relay application.

Acknowledgment

References

Chen, X., F. Harris, E. Venosa, B. Rao, "Non-maximally decimated analysis/synthesis filter banks: Applications in wideband digital filtering," *IEEE Trans. Signal Process.* **62**, 4 (February 2014) 852–868.

Harris, F., C. Dick, M. Rice, "Digital receivers and transmitters using polyphase filter banks for wireless communications," *IEEE Trans. Microw. Theory Techn.* **51**, 4 (April 2003) 1395–1412.

Harris, F. J., *Multirate Signal Processing for Communications Systems*, Prentice Hall, Upper Saddle River, New Jersey, 2004, 135–149, 227–239.

Proakis, J. G., D. G. Manloakis, *Digital Signal Processing: Principles, Algorithms, and Applications*, 4th edition, Prentice Hall, Upper Saddle River, New Jersey, 2007, 540–541.

X-Ray Doppler Velocimetry

LO-004-16 | Continuing in FY 2017 | Year 1 of 3

Jeffrey A. Koch,[1,a] Eric C. Dutra,[a] Richard R. Freeman,[a] Michael J. Haugh,[a] and James A. King[a]

We describe a novel technique for measurement of bulk fluid motion in materials that is particularly applicable to very hot, x-ray–emitting plasmas in the high-energy density physics (HEDP) regime. This x-ray Doppler velocimetry (XDV) technique relies on monochromatic imaging in multiple wavelength bands near the center of an x-ray emission line in a plasma and utilizes bent imaging crystals. Shorter wavelength bands are preferentially sensitive to plasma moving toward the viewer, while longer wavelength bands are preferentially sensitive to plasma moving away from the viewer. Combining multiple images in different wavelength bands allows for reconstruction of the fluid velocity field integrated along the line of sight. Extensions are also possible for absorption geometries, for example, soft x-ray backlit radiography in subcritical implosion experiments. We describe the technique and present the results of simulations performed in the first year of the project to benchmark the viability of the technique for HEDP plasma diagnosis. In the second year of the project, we will focus on proof-of-principle experiments to demonstrate the XDV concept, ideally at the Sandia National Laboratories Z machine, where we can modify an existing crystal imaging experiment configuration to fit XDV. We will also continue with the back-analysis of XDV image data, optimizing our ability to infer velocity maps from multiple monochromatic images.

[1] kochja@nv.doe.gov, 925-960-2525

[a] Livermore Operations

Background

After several years of focused effort, the National Ignition Campaign at the National Ignition Facility (NIF) (Miller 2004) ended in 2012 without achieving the goal of ignition and thermonuclear burn in the laboratory (Lindl 2014). The reasons for this failure are not understood, and a variety of possible explanations have been proposed, but it is likely that at least part of the explanation is bulk fluid motion in the compressed hot spot (Spears 2014). This bulk motion serves as an energy sink, trapping implosion kinetic energy that could otherwise transfer to thermal heating and neutron production. Currently, no diagnostics can measure the degree of bulk fluid motion in the hot spot, and this gap between needs and capabilities motivated the x-ray Doppler velocimetry (XDV) project.

Astronomers have long utilized multispectral imaging at radio frequencies to measure bulk motion of gas clouds, for example, in distant galaxies (Shu 1982). An example of the power of this technique is shown in Figure 1. There, Doppler frequency shifts of the 21 cm hyperfine transition in neutral hydrogen provide information on motion of the emitting atoms. Combining spectroscopy and imaging (multispectral imaging) allows a map of gas cloud motion to be generated that shows bulk rotation.

An analogous instrument that can measure Doppler wavelength shifts of x-rays emitted by plasmas, locally in imaging mode, would allow bulk motion in the plasma to be diagnosed. We propose to accomplish

NGC 4449, white-light visible map
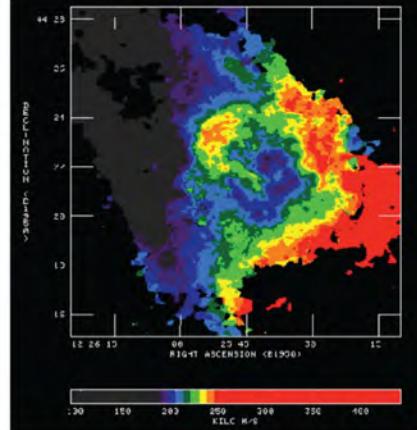
NGC 4449, multispectral microwave map

Figure 1. (a) White-light telescope image of galaxy NGC 4449 compared with (b) a multispectral color-coded microwave image of the same galaxy. The multispectral image shows large-scale rotation of gas, suggestive of an ancient merger between counter-rotating galaxies, which is important information that is not present in the white-light image.

this using near normal–incidence spherical, toroidal, or ellipsoidal bent crystals that are already widely used for quasi-monochromatic x-ray imaging applications (Pikuz 1995, Aglitskiy 1998, Uschmann 2000, Koch 2003, Akli 2011, Stoeckl 2012). These systems can provide very large collection solid angles when the angle of incidence is close to normal and the crystal quality is high, and can be very efficient when used with narrowband emission line sources (Koch 1998). Use of multiple crystals, each tuned to a slightly different wavelength band, can in principle allow a map of fluid velocity (averaged along the line of sight) to be generated; this is the essential concept behind XDV.

Project

The basic geometry of XDV is shown in Figure 2. Five identical bent imaging crystals, with the same interplanar spacing d, are arranged to view a plasma along a near-common line of sight (LOS), and each is configured with a slightly different Bragg angle f_B. The Bragg equation $\heartsuit = 2d\sin f_B$ implies that the center bandpass of each crystal falls at a slightly different wavelength $\heartsuit$. If we configure the range of wavelengths to run from the red wing to the blue wing of the unshifted center of an x-ray emission line from the plasma, then five different quasi-monochromatic images will be generated. Each image will emphasize velocities
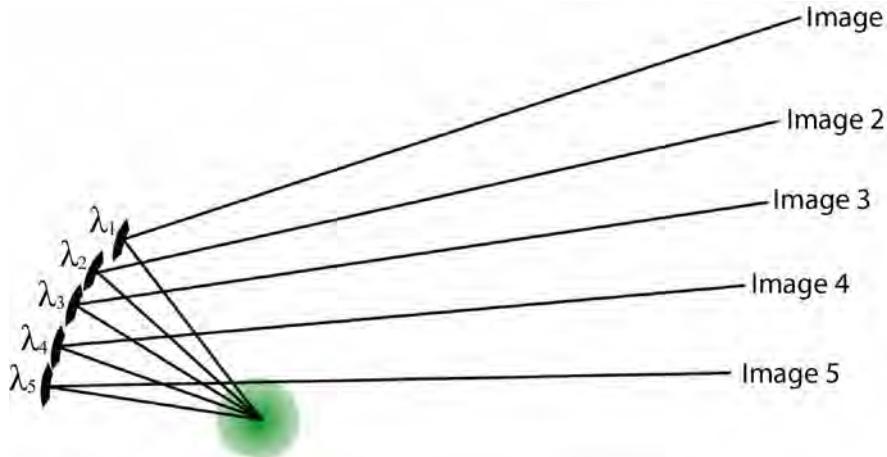
Figure 2. Sketch of one possible implementation of XDV. Here, five identical imaging crystals project five separate images of the source onto a detector. Each crystal is sensitive to different x-ray energies in closely spaced bands near the center wavelength of an emission line from the source. Combining the images, for example, by color-coding, would result in a multispectral image similar to that shown in Figure 1b.

corresponding to the Doppler shifts of the centers of the pass bands of the five crystals. This is shown schematically in Figure 3. Here, the number of crystals is arbitrarily chosen to be five. A lower bound is two crystals, the minimum necessary to show differences between images, while an upper bound will be limited by the complexity of the instrument and ultimately by view differences between LOSs, necessary due to the non-zero dimensions of the crystals and mounting fixtures.
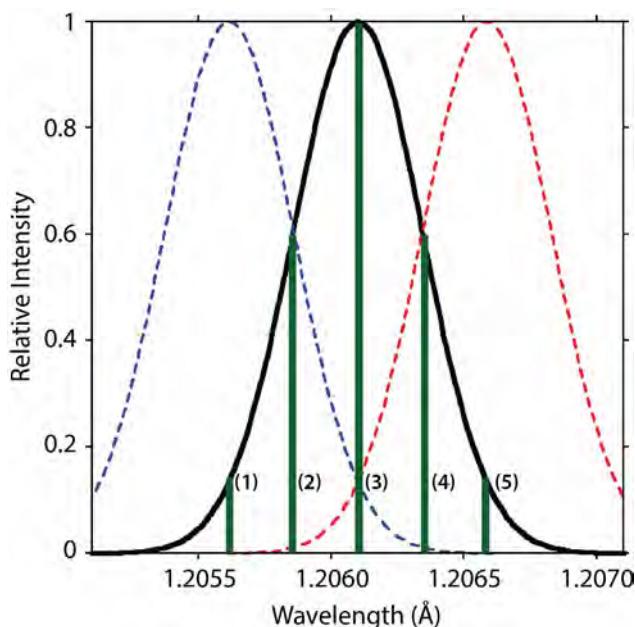

Figure 3. Sketch of the center wavelength distribution of the crystals shown in Figure 2. An unshifted line would appear brightest in the middle crystal (3). If the source was moving toward the crystal, the line would shift to the left and the source would appear brightest in the blue-tuned crystal (1); if the source was moving away from the crystal, the source would appear brightest in the red-tuned crystal (5).

In order to evaluate the diagnostic potential of XDV as applied to an experiment at the NIF, we used a 3-D Hydra (Marinak 1996) post-shot simulation of a NIF implosion (NIF shot N130927, convergence ratio of 33) and post-processed the results to generate a series of simulated XDV images. For a variety of LOSs, at a variety of times during the implosion, we generated 2-D moment maps integrated through the depth of

the plasma under the assumption that the plasma was uniformly doped with germanium that emitted an optically thin He-α line at an x-ray energy of 10.28 keV. The moments were integrated LOS intensity <I>, intensity-weighted fluid velocity <IV>, and intensity-weighted square of fluid velocity <IV^2> at each 1×1 μm pixel in the 2-D plane. Using the equations for the Doppler shift and the definition of the root-mean-square, we then calculated a normalized intensity, a spectral line center wavelength, and a spectral line width (due to fluid flow) at each pixel. Convolving the fluid motional broadening with an assumed thermal broadening consistent with a 4 keV ion temperature yielded our source objects for subsequent instrument ray tracing. We note that peak depth-averaged fluid velocities exceed 200 km/s in these post-processed moment maps, which is nearly the peak implosion velocity. This indicates that, in 3-D, some portions of the plasma retain their peak implosion velocities even at the time of peak compression, whereas in a 1-D approximation, the plasma should be stagnant.

The instrument ray trace was developed as part of this SDRD project, and is a custom Fortran Monte Carlo code that maps an arbitrary source to an image plane in full 3-D, using source and geometry information as well as crystal properties (d spacing, bandwidth, surface figure). It is a modification of ray trace code used for many crystal imaging applications over the past 20 years (Koch 1998). We assume quartz (0,7,1), bent to a 390 mm spherical radius of curvature with a 2.8 mm circular aperture diameter, and we choose five center wavelengths spanning an energy range of 10.284 to 10.776 keV. This range corresponds to $\pm$120 km/s motional velocities toward and away from the crystal. The bandwidths vary slightly depending on the Bragg angle, because the apertures are assumed to have a fixed diameter, and range from 0.9 to 2.5 eV. This is small compared with the spectral line widths of >6 eV FWHM.

Figure 4 shows simulated time-snapshot XDV images of this implosion from each of the five crystals, assuming a polar (0,0) LOS (LOS 1), at the time of peak compression. For comparison, a simulated pinhole
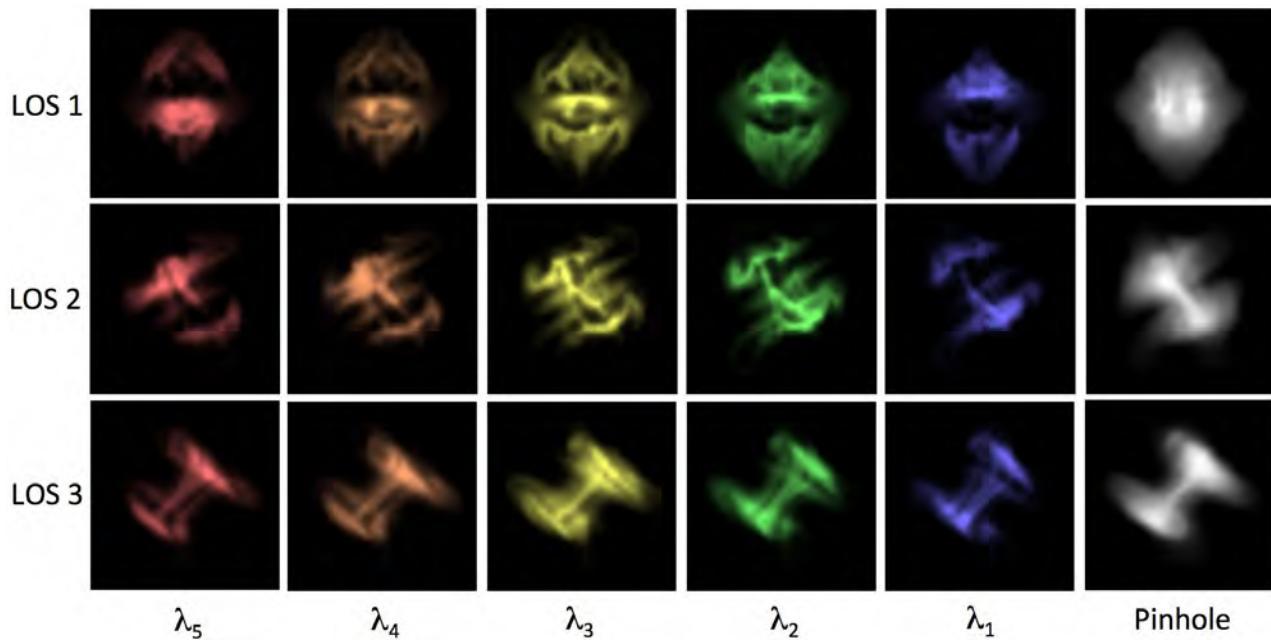
Figure 4. Simulated XDV images in five wavelength bands (λ_1–λ_5) ranging from red-center to blue-center, from three different LOSs (LOS 1 = (0,0), LOS 2 = (90,315), LOS 3 = (90,78)) compared with simulated pinhole camera images from the same LOSs (grayscale images). All images are instantaneous time snapshots at the time of peak emission intensity. The dramatic differences between XDV images, and the differences compared with pinhole camera images, show the power of the XDV concept to diagnose fluid flow in plasmas.

image with very broad bandwidth and no fluid velocity sensitivity is also shown; this would also correspond to an image obtained with a metal or multilayer-mirror instrument such as a Kirkpatrick-Baez or Wolter microscope. We see dramatic differences among the XDV images, indicative of hundreds of km/s fluid velocities toward and away from the crystal, and we also see that all XDV images are dramatically different from the simulated pinhole image. Observing XDV images like these would be a significant step forward in high-energy density physics (HEDP) implosion plasma diagnostic capabilities.

Different LOSs show similar differences among XDV images but with varying levels of sensitivity. Figure 4 also shows two of these alternative LOSs, both equatorial ((90,315) and (90,78)). This suggests that the choice of LOS matters, so the LOS should be chosen to correspond to the direction where maximal fluid velocities would be expected. This is likely to be the polar LOS along the hohlraum axis in a NIF indirect-drive implosion, based on the symmetry of the experiment.

Sensitivity studies with realistic image noise indicate that we could scale the peak velocities down by a factor of 20, to 10 km/s, and still retain sensitivity to fluid motion at that level with the same instrument. An important additional constraint is the required time resolution of the detector. In order to address this question, we generated intensity-weighted time-integrated images in the two extreme channels to approximate what we would observe with time-integrated detectors at these image locations. Figure 5 shows the results, indicating that at least for this simulated implosion and XDV configuration, we would still see dramatic differences among the XDV channels even using time-integrated detectors. Fast time-resolved cameras, essentially x-ray movie cameras with ~30 ps or better time resolution, would significantly extend the capabilities of the XDV diagnostic.

In 2016, we explored two options for proof-of-principle experiments. The first is the Z facility at Sandia National Laboratories (SNL). SNL collaborators have developed two-channel crystal imaging capabilities near 3.1 and 7.2 keV (argon and cobalt He-α lines, respectively),

Broadband Pinhole

XDV Blue
Plasma moving toward you

XDV Red
Plasma moving away from you
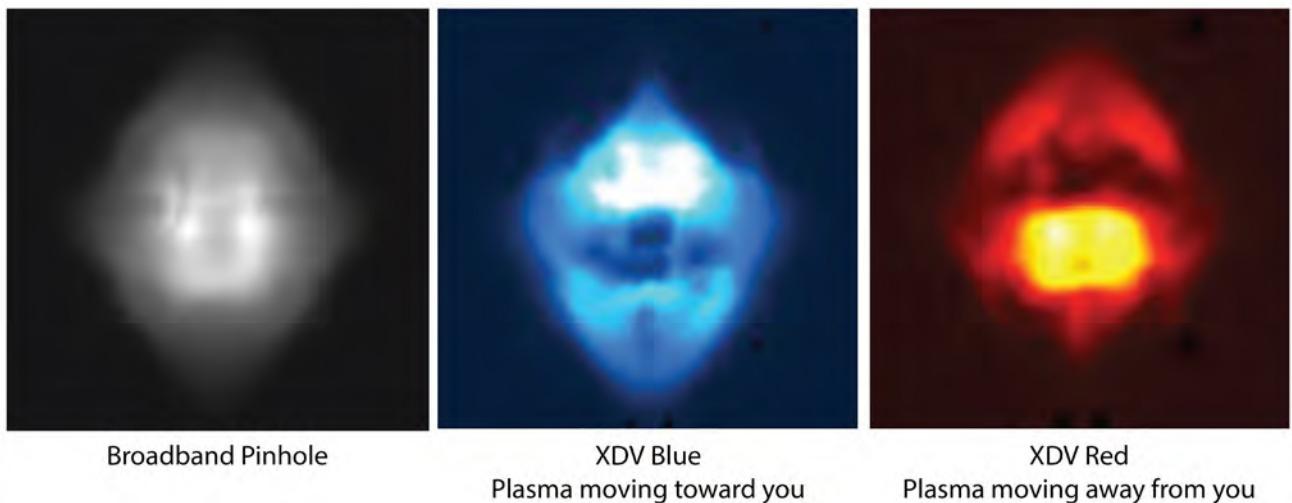
Figure 5. Simulated time-integrated XDV images (blue and red, from crystals 1 and 5, respectively, in Figure 2) compared with a broadband time-integrated pinhole image from the same LOS. The sensitivity of XDV to fluid flow is retained in this example even with no time resolution.

and simple modifications (narrowing the pass bands and moving them closer together by changing the Bragg angles) would allow a two-channel XDV system to be tested. The second is the Nevada Terrawatt Facility at the University of Nevada, Reno (UNR). UNR collaborators have developed single-crystal imaging capabilities, and multichannel extensions would be straightforward albeit complex. We hope to field proof-of-principle demonstration experiments at one or both facilities in 2017.

Conclusion

We have described a novel technique for measurement of bulk fluid motion in materials that is particularly applicable to very hot, x-ray–emitting plasmas in the HEDP regime. This XDV technique relies on monochromatic imaging in multiple wavelength bands near the center of an x-ray emission line in a plasma and utilizes bent imaging crystals. Shorter wavelength bands are preferentially sensitive to plasma moving toward the viewer, while longer wavelength bands are preferentially sensitive to plasma moving away from the viewer. Combining multiple images in different wavelength bands allows for a reconstruction of the fluid velocity field integrated along the LOS. Extensions are also possible for absorption geometries, for example, soft x-ray backlit radiography in subcritical implosion

experiments. We have described the technique and presented the results of simulations performed in the first year of the project to benchmark the viability of the technique for HEDP plasma diagnosis.

In FY 2017, we will focus on proof-of-principle experiments to demonstrate the XDV concept. The most promising option is the Z facility at SNL, where multiple-crystal imaging has been implemented and could be modified to an XDV configuration. A second option is the Nevada Terawatt Facility at UNR. Both options would view a pulse-power implosion, either a gas puff or laser plume or a wire array. A third option we will explore is an experiment at the Omega Laser Facility, possibly an inter-penetrating planar plasma collision. We also expect to make progress on back-analysis of XDV image data, optimizing our ability to infer velocity maps from multiple monochromatic images.

We have submitted one Technology Abstract on the XDV concept, "Method for imaging bulk motional velocities in plasmas" (3/16/15). The concept was awarded a provisional patent and has been submitted to the U.S. Patent and Trademark Office as a full patent application (Koch 2016). The work was presented at two inertial confinement fusion diagnostic workshops at Los Alamos and Lawrence Livermore National Laboratories, and will be presented as a technical

seminar at DOE Headquarters in FY 2017. An invited talk will also be presented at the Radiative Properties of Hot Dense Matter 2016 conference in Santa Barbara.

Acknowledgments

References

Aglitskiy, Y., et al., "High-resolution monochromatic x-ray imaging system based on spherically bent crystals," *Appl. Opt.* **37** (1998) 5253–5261.

Akli, K. U., et al., "A novel zirconium Kα imager for high energy density physics research, *Rev. Sci. Instrum.* **82** (2011) 123503.

Koch, J. A., et al., "High-energy x-ray microscopy techniques for laser-fusion plasma research at the National Ignition Facility," *Appl. Opt.* **37** (1998) 1784–1795.

Koch, J. A., et al., "4.5- and 8-keV emission and absorption x-ray imaging using spherically bent quartz 203 and 211 crystals," *Rev. Sci. Instrum.* **74** (2003) 2130.

Koch, J. A., "Methods and systems for imaging bulk motional velocities in plasmas," U.S. Patent Application 15/090,408, filed April 4, 2016, following U.S. Provisional Patent 62/142,985.

Lindl, J., O. Landen, J. Edwards, E. Moses, NIC Team, "Review of the National Ignition Campaign, 2009-2012," *Phys. Plasmas* **21** (2014) 020501.

Marinak, M. M., R. E. Tipton, O. L. Landen, T. J. Murphy, P. Amendt, S. W. Haan, S. P. Hatchett, C. J. Keane, R. McEachern, R. Wallace, "Three-dimensional growth factor simulations of Nova high growth factor capsule implosion experiments," *Phys. Plasmas* **3** (1996) 2070.

Miller, G. H., E. I. Moses, C. R. Wuest, "The National Ignition Facility," *Opt. Engin.* **43** (2004) 2841.

Pikuz, S. A., V. M. Romanova, T. A. Shelkovenko, T. Pikuz, A. Ya. Faenov, E. Förster, "Use of higher-order reflection from mica crystals in x-ray spectroscopic investigations at 0.1–0.3 nm," *Quantum Electronics* **25** (1995) 16.

Shu, F. H., *The Physical Universe: An Introduction to Astronomy*, University Science Books, Mill Valley, California, 1982.

Spears, B. K., et al., "Mode 1 drive asymmetry in inertial confinement fusion implosions on the National Ignition Facility," *Phys. Plasmas* **21** (2014) 042702.

Stoeckl, C., G. Fiksel, D. Guy, C. Mileham, P. Nilson, T. C. Sangster, M. J. Shoup, W. Theobald, "A spherical crystal imager for OMEGA EP," *Rev. Sci. Instrum.* **83** (2012) 033107.

Uschmann, I., K. Fujita, I. Niki, R. Butzback, H. Nishimura, J. Funakura, M. Nakai, E. Förster, K. Mima, "Time-resolved ten-channel monochromatic imaging of inertial confinement fusion plasmas," *Appl. Opt.* **39** (2000) 5865.

Ultra-High-Speed Velocimetry Using Dispersive Frequency Modulation Interferometry
STL-055-16 | Year 1 of 1

Jason Mance,[1,a] Brandon La Lone,[a] Bruce Marshall,[a] and Dale Turley[a]

The goal of this work was to develop a method for measuring velocities that are typically outside of the range available using standard photonic Doppler velocimetry (PDV) techniques. Present-day oscilloscopes can record as fast as ~70 GHz, limiting measurement velocities to ~70 km/s using standard PDV methods. The proposed technique optically stretches the PDV signal before it reaches the detector, reducing the beat frequency of the signal and bypassing the bandwidth limitations imposed by the detectors and oscilloscopes. Initial measurements using laser-driven foils demonstrate a stretch factor up to 10 times, which would theoretically increase the maximum measurable velocity to ~700 km/s. Further optimization of the system could result in a larger stretch factor if desired.

[1] mancejg@nv.doe.gov, 805-681-2266
[a] Special Technologies Laboratory

Background

In high-energy density science, there is a need to precisely measure velocities on the order of 10^1 to 10^2 km/s. VISAR has been successfully implemented in these applications for some time; however, a VISAR system has a large footprint, requires a high signal return that can cause problems with sample interrogation and low signal-to-noise levels, and cannot detect multiple velocities simultaneously. For speeds in the km/s range and below, it is often more suitable to employ the photonic Doppler velocimetry (PDV) technique because it takes up less space, is built with low-cost fiber components, is less sensitive to signal return levels, and can detect multiple velocities simultaneously. However, at high velocities, PDV signal frequencies exceed the measurement speeds of current detection systems. This work addresses a need for PDV systems capable of recording higher velocities. In particular, a recent assessment at the National Ignition Facility (NIF) calls for the integration of advanced high-speed PDV technologies (Frayer 2016).

At high velocities, PDV measurement capabilities become limited by insufficient oscilloscope or detector bandwidth. The beat frequency on a PDV signal is

$$F = \frac{2\upsilon}{\lambda}, \tag{1}$$

where υ is velocity and λ is wavelength. At υ = 50 km/s and λ = 1.5 μm, the beat frequency is 67 GHz. Currently, the fastest oscilloscopes are ~70 GHz and are very expensive, as are fast photodetectors. A new velocimetry technique is presented here that extends the measurable upper velocity limit by reducing the beat frequency of the PDV signal before detection. The technique, referred to here as high-speed PDV (HSPDV), is similar to traditional PDV in the sense that it measures the velocity by interfering a Doppler-shifted signal with a reference beam and recording the beat frequency on a photodetector/oscilloscope. However, unlike standard PDV approaches that use a continuous wave (CW) laser, the HSPDV's signal is recorded onto a chirped laser pulse, which is then stretched in time
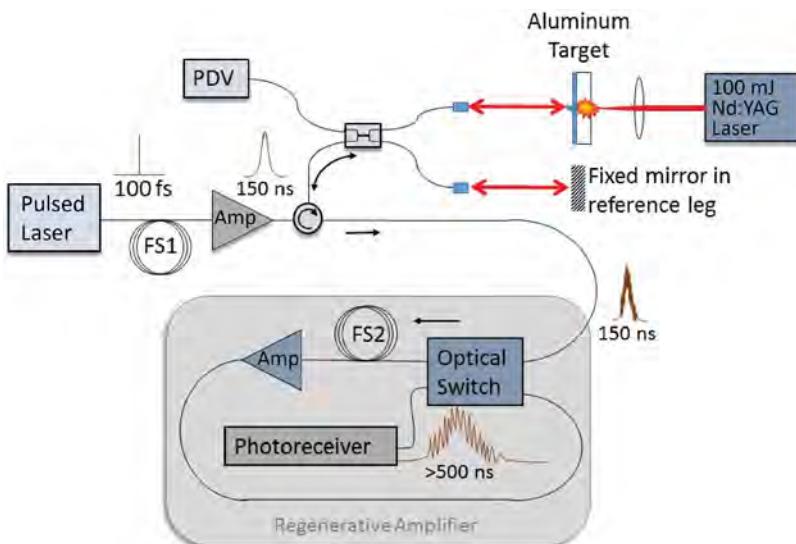
Figure 1. Schematic of an HSPDV system. A 100 fs laser is sent through a highly dispersive fiber spool (FS1) and amplified to make up for losses in the spool. FS1 stretches the pulse to 150 ns. The Doppler shift is encoded onto the pulse, and it is mixed with a reference pulse to obtain the PDV beat frequency. The pulse is then stretched further by multiple passes through another dispersive fiber spool.

before being detected. The temporal stretch reduces the beat frequency, effectively increasing the upper velocity limit.

Project

A simplified schematic of the HSPDV system is shown in Figure 1.

The entirely fiber-based system starts with a 100 ps Menlo System T-Light laser that is passed through a highly dispersive fiber spool (FS1). After two passes through FS1, the 100 fs pulse is chirped and stretched to ~150 ns. In order to make up for losses in the fiber, the pulse is amplified. The details of the fiber spools and amplifiers are reserved for a more detailed description later in this report. The amplified 150 ns pulse passes through a circulator, where it is split so that 90% is directed to the target on the "signal" line and 10% to the reference leg. The reference leg path length is set equal to the path length of the signal line and is fine-tuned with an adjustable delay stage. Once the Doppler shift is encoded onto the signal pulse, the signal line and reference leg pulses are recombined and sent through another dispersive spool (FS2). To obtain large amounts of dispersion and make up for losses, the pulse is multi-passed in a regenerative amplifier configuration where it is effectively trapped and amplified. The optical switch timing can be adjusted for any desired number of passes through FS2. The signal is then recorded with a fast photodiode/oscilloscope.

In order to test the system, a laser-based projectile launcher was built. The system used a Big Sky laser that outputs a 100 mJ, 10 ns, 1064 nm laser pulse focused onto an aluminum foil sample with a 75 mm focal length lens. When the foil sample was mounted in air, breakdown occurred in the air before the sample, and the subsequent loss of laser energy resulted in little or no projectile velocities. The back of the aluminum sample also reflected much of the laser energy. The breakdown issue was alleviated by mounting the sample on a 12 mm thick BK7 glass plate, which can handle more power than air at 1064 nm. The aluminum foil was glued to the plate with an epoxy mixed with fine carbon powder in order to increase the absorption of the back side at 1064 nm. The sample was placed on an adjustable stage and translated into the focus to increase pulse intensity and, subsequently, the velocity of the foil projectiles. This proved to be a fairly reliable method for creating projectiles with velocities up to around 2 km/s, at which point the BK7 substrate cracked and dispersed the laser light, resulting in a rapid decrease in projectile velocity with increasing pulse fluence. The velocity as a function of pulse fluence was recorded and is shown in Figure 2. Breakdown in the BK7 sample began occurring when the pulse fluences exceeded ~350 J/cm^2. Higher velocities may be obtainable by mounting the foil sample in a vacuum to avoid breakdown.
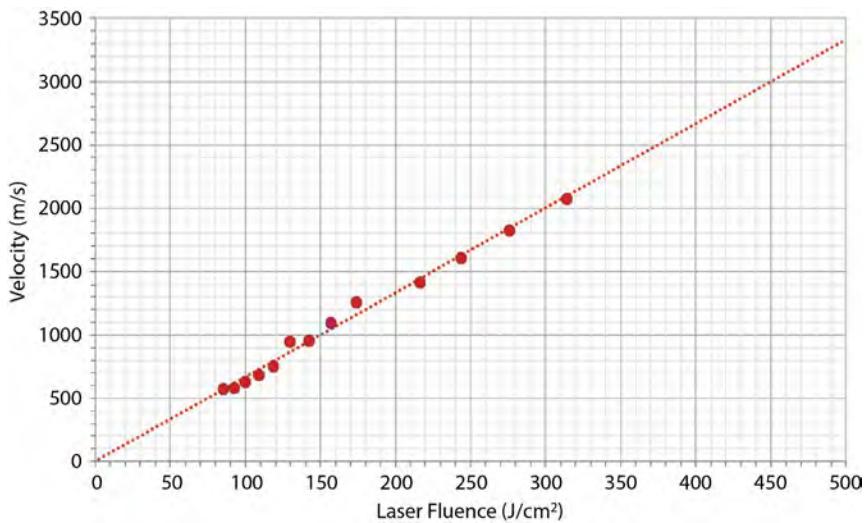
Figure 2. Projectile velocities of aluminum foil vs. laser fluence. Circles are data and dotted line is a linear fit.
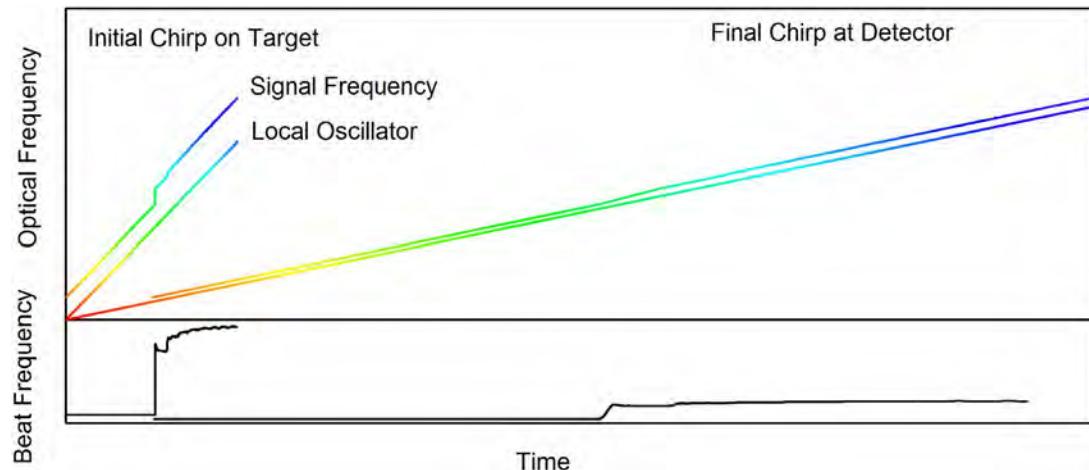
Figure 3. (upper) Illustration of dispersive pulse stretching technique used for HSPDV measurements. A velocity profile is encoded onto an initially chirped pulse, then the pulse is dispersed further to reduce the signal frequencies to a measurable range. The recorded signal (lower) is the beat frequency (difference frequency) between the Doppler-shifted "signal" pulse and a "reference" pulse.

The HSPDV system's method of stretching pulses and example of resulting beat frequency are shown in Figure 3. In frequency vs. time space, the initial transform-limited 100 fs pulse would appear as a vertical line. After dispersion, the pulse appears as a line with a slope proportional to the amount of dispersion in the pulse. Group velocity dispersion (GVD) contributes a linear shift with frequency while third order dispersion (TOD) contributes a quadratic shift. While it is important to consider TOD in the system, the effect is small enough that the illustration in Figure 3, which shows a line rather than a parabola, is an accurate approximation. Measurements of the dispersive properties of the fiber spools are presented later in this report. In Figure 3, the signal and reference pulses are chirped identically, then the Doppler shift is encoded onto the signal pulse. The lower traces depict the difference frequency, i.e., the PDV signal that is proportional to the target velocity. Further dispersion of the pulse therefore stretches the PDV signal in time and reduces the beat frequency as shown on the right side of the plot. By adjusting the number of passes

in the regenerative amplifier, the desired amount of dispersion can be added to the PDV signal. The stretch factor can be determined by measuring the dispersion in the fiber spools.

Calculating Velocity

Dispersion causes a change in phase with frequency. Relative to some frequency ω_0, and accounting for dispersion up to the third order, the phase after propagating through a medium of length L can be written

$$\varphi = \overbrace{\beta_0 L}^{\text{Initial Phase}} + \overbrace{\beta_1 L(\omega - \omega_0)}^{\text{Propagation}} + \overbrace{\frac{1}{2}\beta_2 L(\omega - \omega_0)^2}^{\text{GVD}}$$

$$+ \overbrace{\frac{1}{6}\beta_3 L(\omega - \omega_0)^3}^{\text{TOD}}. \tag{2}$$

The transit time is

$$t = \frac{\partial \varphi}{\partial \omega} = \beta_1 L + \beta_2 L(\omega - \omega_0) + \frac{1}{2}\beta_3 L(\omega - \omega_0)^2, \tag{3}$$

(Agrawal 2001, Xia 2010), which can be solved for ω to give

$$\omega = \omega_0 + \frac{1}{\beta_2 L}(t - \beta_1 L) + \frac{1}{2}\frac{\beta_3 L}{(\beta_2 L)^3}(t - \beta_1 L)^2 + O(t^3). \tag{4}$$

For the system shown in Figure 1, the signal and reference pulses travel through the first fiber spool (with length denoted as L_1), then the signal pulse is Doppler shifted such that the new frequency is $\omega_D = \omega_{SIG}(1 + 2\upsilon/c)$. Next, the reference pulse and Doppler-shifted signal pulse are recombined and travel through a second fiber spool of length L_2. The net transit time for the signal at frequency ω_D (on the detector) is then

$$t_{SIG} = \beta_1 L + \beta_2 L_1(\omega_{SIG} - \omega_0) + \frac{1}{2}\beta_3 L_1(\omega_{SIG} - \omega_0)^2$$

$$+ \beta_2 L_2(\omega_D - \omega_0) + \frac{1}{2}\beta_3 L_2(\omega_D - \omega_0)^2, \tag{5}$$

where $L = L_1 + L_2$ and it was assumed that both fiber spools were made of the same material (with the same β_n values). Using $\upsilon \ll c \rightarrow \omega_{SIG} \approx \omega_D (1 - 2\upsilon/c)$, this gives

$$t_{SIG} = \beta_1 L + \beta_2 L_1\big(\omega_D(1 - 2\upsilon/c) - \omega_0\big)$$

$$+ \frac{1}{2}\beta_3 L_1\big(\omega_D(1 - 2\upsilon/c) - \omega_0\big)^2 \tag{6}$$

$$+ \beta_2 L_2(\omega_D - \omega_0) + \frac{1}{2}\beta_3 L_2(\omega_D - \omega_0)^2.$$

The transit time of the reference pulse is straightforward:

$$t_{REF} = \beta_1 L + \beta_2 L(\omega_{REF} - \omega_0) + \frac{1}{2}\beta_3 L(\omega_{REF} - \omega_0)^2. \tag{7}$$

At the output of the second fiber spool, the signal of both pulses, overlapped in time, is recorded on a photodiode. The instantaneous relationship between the frequency of the reference beam and the Doppler-shifted signal beam is obtained by setting $t_{SIG} = t_{REF}$ in Equations 6 and 7 and solving to get

$$\omega_{REF} = \omega_D\left[1 - \frac{L_1}{L}\frac{2\upsilon}{c}\right]. \tag{8}$$

The photodetector sees a modulation from the difference frequency

$$\Delta f = \frac{1}{2\pi}(\omega_D - \omega_{REF}) = \frac{\omega_D}{2\pi}\frac{L_1}{L}\frac{2\upsilon}{c} = \frac{L_1}{L}\frac{2\upsilon}{\lambda}, \tag{9}$$

which is the traditional PDV beat frequency from Equation 2 reduced by the scaling factor L_1/L. Interestingly, the simple scaling factor is valid, even with TOD and higher dispersion terms, unlike the optical ranging data where the TOD and higher terms have to be corrected for in the analysis. Thus, in order to determine the velocity, one can simply multiply the time axis in the scope data by L_1/L then proceed with standard PDV analysis. This approximation assumes that the interferometer remains well balanced throughout the measurement so that there is negligible time shift between the signal and reference pulses because a time delay will also contribute a beat frequency in the data. Furthermore, it is sufficient to use a single value for λ throughout the analysis since the spectral bandwidth is small compared to the laser wavelength (e.g., s = 1550 ±15 nm), which allows one to simply input this data into a standard PDV algorithm after rescaling the time axis. In practice, the HSPDV signals

were within 1% of the PDV signals with the simple L_1/L scaling and assuming a constant λ. In principle, corrections for the changing wavelength and interferometer time delay could be applied if higher accuracy is desired, but this was not done in this project.

Dispersion Characterization

The dispersive properties of the fiber spools were measured using the method presented in Dorrer (2004). The lengths were 21.389 and 10.225 km for FS1 and FS2, respectively (Figure 1). The dispersion was measured with an unbalanced (10.96 ps delay) interferometer after a double pass through the spool. The spectrum was then recorded on an optical

spectrum analyzer and the temporal waveform was recorded on an oscilloscope. The beat pattern caused by interference served as a marker to map between the frequency and time domains. Figure 4 shows the pulse in the time and frequency domains after double passing the 21 km module. The dispersion parameters were obtained by extracting the time and frequency of the interference maxima in both domains and fitting the data to a second order polynomial, similar to Equation 3. The fit and extracted dispersion parameters are shown in Figure 5.

Amplifier Considerations

Commercially available erbium-doped fiber amplifiers (EDFAs) were used in conjunction with in-house built Raman amplifiers to provide broadband amplification of the signal. The Raman amplifiers consist of several CW laser diodes having wavelengths of 1460 and 1480 nm and output powers of ~200 mW. The spectrum of the EDFA and Raman amplifier gains are shown in Figure 6 along with the laser spectrum for reference.

While the combined gain spectrum of the Raman amplifier and EDFA is fairly broad and appears to cover the entire bandwidth of the laser pulse, after multiple passes through the regenerative amplifier, the gain
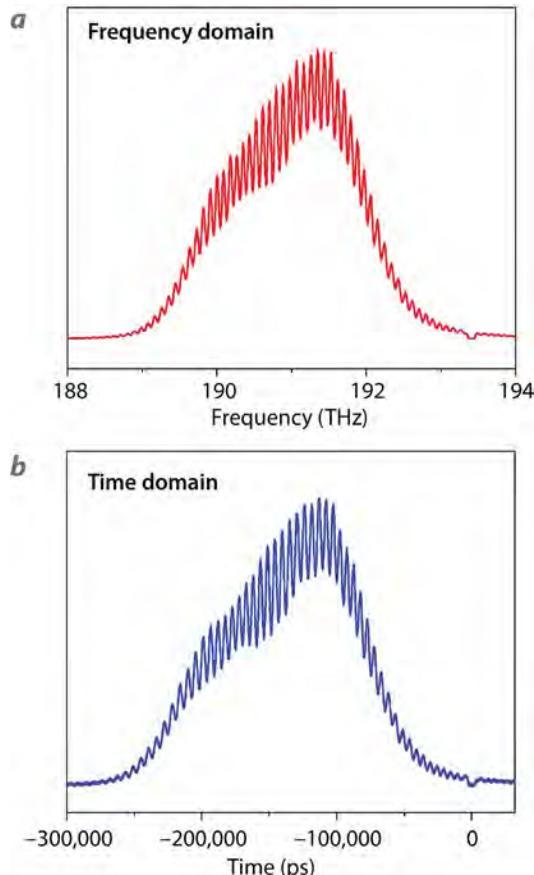
Figure 4. Data for measuring dispersion properties. (a) Pulse spectrum measured with a spectrum analyzer. (b) Pulse temporal profile measured with a photodiode and oscilloscope. The notch in the spectrum at t = 0 is a marker placed using a 1550 nm notch filter.

$$t = 2\pi\beta_2 L(f - f_0) + 2\pi^2\beta_3 L(f - f_0)^2$$
$$\beta_2 L = 8644 \text{ ps/THz}$$
$$\beta_3 L = -50.80 \text{ ps/THz}^2$$
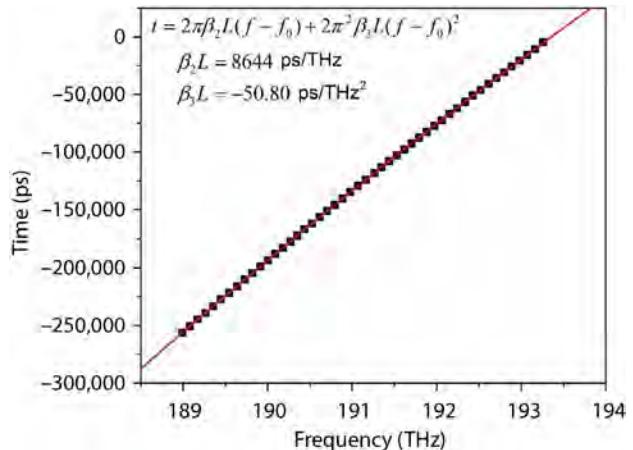
Figure 5. Optical frequency vs. time of dispersed pulses shown in Figure 4. A fit to the equation shown gives the GVD and TOD parameters. Measurement is for two passes through a 21.4 km length of highly dispersive fiber. Dispersion is relative to 1550 nm/193.415 THz.
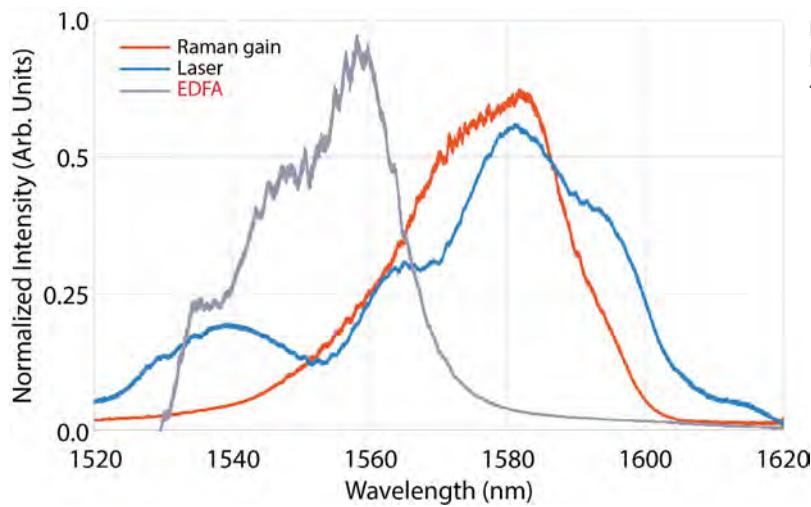
Figure 6. Single-pass gain spectra of Raman amplifier and EDFA along with the laser spectrum

spectrum narrows significantly and data are lost. With these amplifiers significant data loss occurs beyond ~30 passes. More passes could be obtained, without losing signal quality, by engineering an amplifier with a flat gain curve throughout the bandwidth of the laser pulse.

Measurements

Velocity measurements were made using a variety of amplifier and fiber spool configurations. The pulse width before the sample can be increased by using longer fiber lengths in FS1, which increases the permissible recording time of the experiment with the trade-off that more amplification is required in FS2 to retain the stretch factor. In the data shown here, the

100 fs pulses are double-passed through FS1, which has a single-pass length of 21.389 km. A 10.225 km spool is then used for FS2, which is passed 11 times in the regenerative amplifier. The total lengths are then L_1 = 42.778 km and L = 155.253 km, which gives a stretch factor of L_1/L = 3.629. The HSPDV and PDV velocity measurements are shown in Figure 7.

It is apparent from Figure 7 that the HSPDV signal has been stretched in time and that the beat frequency is lower as a result. After dividing the HSPDV time data by 3.629, the spectrogram frequencies were converted to velocity (Equation 1), and an extraction algorithm was used to isolate the peaks in the FFT data. The two measurements are overlaid in Figure 8. The velocity calculations agree to within 1%.
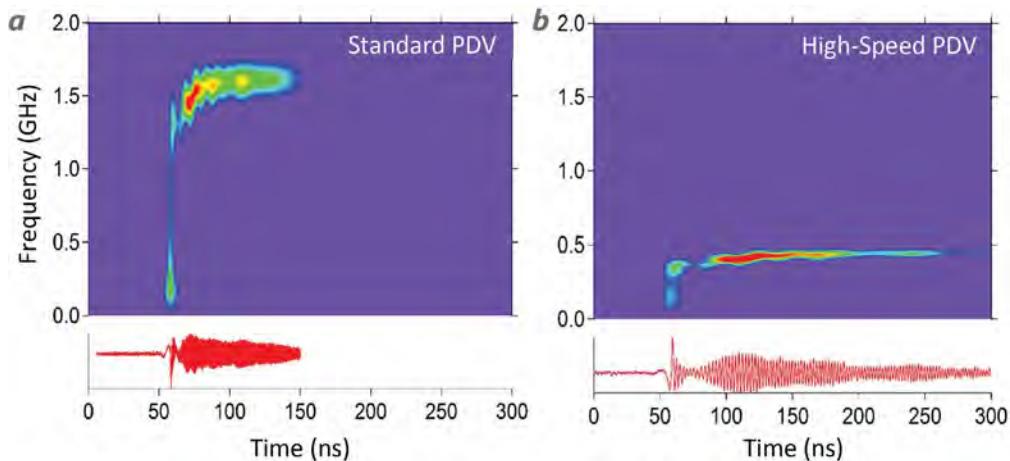
Figure 7. (a) PDV and (b) HSPDV spectrograms; the HSPDV pulse is stretched in time to create a lower beat frequency
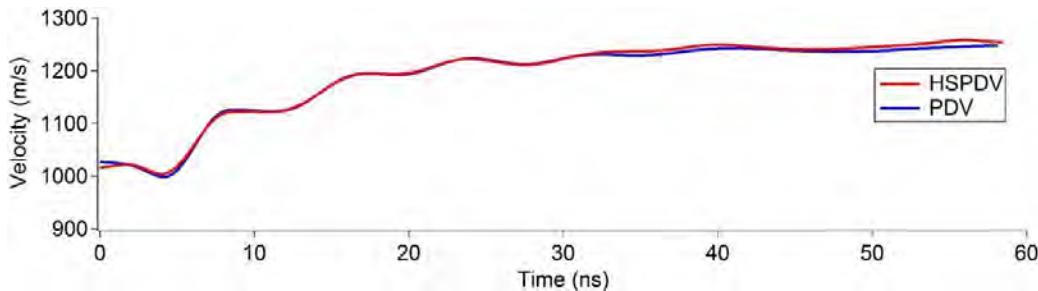
Figure 8. Velocity curves calculated from PDV and HSPDV measurements

### Quasi-CW Mode Operation

Several timing complications can arise using the HSPDV system as described thus far. Because the PDV signal is written onto a pulse instead of a CW laser, the pulse must be precisely timed to coincide with the target motion. This can be difficult because most high-bandwidth, transform-limited pulses are mode-locked and cannot be triggered on an external event. Additionally, obtaining continuous records longer than the pulse width (~150 ns) may be desirable. If it is possible to trigger the experiment on the laser pulse, as was done here, and the recording times are sufficient, the technique works well. In order to make measurements of arbitrary length and solve the trigger problem, a "quasi-CW" technique can be used. A quasi-CW laser can be created by increasing the length of FS1 until dispersion has stretched the pulses far enough that they overlap in time. Once the pulses are overlapped, there are no longer any time segments where data cannot be recorded, and thus the experiment can be

triggered at any point in time and can record for as long as permitted by the oscilloscope. A velocity measurement was made using the quasi-CW configuration, and the data are shown in Figure 9.

Each of the negatively sloped lines in Figure 9 are spectrograms of a single pulse, and at a given time there are two to three pulses present, leaving no gap in time where data would be missed. The slope on the pulses is an important part of the experimental arrangement of the system. Without this slope, the pulses would run together on the spectrogram, and there would be no way to differentiate the signal written onto neighboring pulses. The slope is obtained by adding a delay stage to one leg of the interferometer that offsets the reference and signal pulses by a small delay time τ. This results in a beat frequency

$$\Delta f = \frac{1}{2\pi} \left[\frac{1}{\beta_2 L} - \frac{\beta_3 L}{(\beta_2 L)^3} t \right] \tau, \tag{10}$$
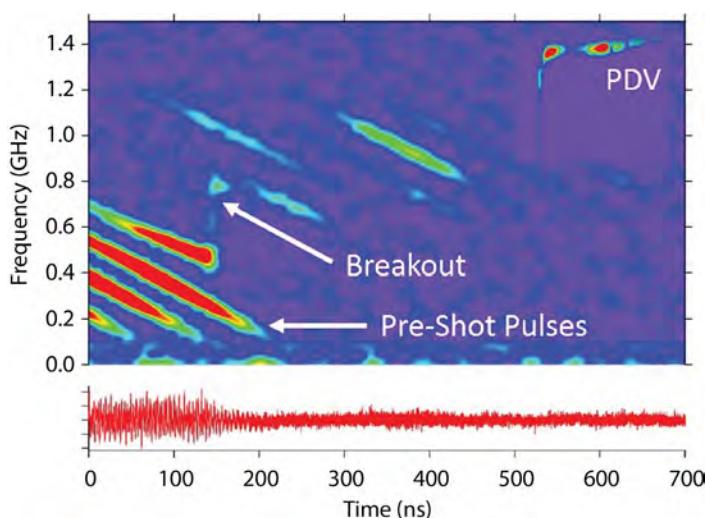

Figure 9. Velocity measurement results using a "quasi-CW" configuration where the pulses have been stretched until they overlap in time prior to the measurement. PDV data were recorded simultaneously and are shown in the upper right corner for comparison.

where the time t is in the laser pulse reference frame and $t = 0$ is defined relative to a reference frequency f_0 (e.g., $t \equiv 0$ at 1550 nm). The slope is apparent in the second term of Equation 10. In order to differentiate between the pulses, a significant slope must be added, and it becomes impractical to achieve a sufficient slope simply by increasing τ because the first term in Equation 10 also increases with τ. Thus, a pulse with sufficient slope has a baseline beat frequency that may exceed the bandwidth of the oscilloscope. The slope must be created without adding a large baseline frequency, as is the case in Figure 8 where the offsets of the sloped lines are just enough to keep the beat frequency above zero. This can be achieved by adding a large enough dispersive delay to the pulse such that it overlaps with a neighboring pulse in the train. The beat frequency can then be written

$$\Delta f = \frac{1}{2\pi}\left[\frac{1}{\beta_2 L} - \frac{\beta_3 L}{(\beta_2 L)^3}t\right]\left[\frac{T_N}{\beta_1}t - \tau\right],$$ **(11)**

where T_N is an integer multiple of the period of the pulse train and τ is the relative delay of the overlapped pulses ($\tau = 0$ when a pulse and its Nth neighbor arrive at the detector coincidentally). In this case, addition of the extra length adds to the slope of Δf without adding a constant offset. An offset can then be added by adjusting τ to ensure the lowest beat frequency is still above zero. The data in Figure 9 were obtained by adding about 1.5 km of SMF 28 optical fiber to one leg of the interferometer and τ was adjusted with two stages: a low-precision stage with ~2 m of travel and a high-precision (~10 fs/step) stage.

In terms of the optical frequency f, the beat frequency is

$$\Delta f = \frac{L_1}{L}\frac{2\upsilon}{c}f + \frac{l}{L}f,$$ **(12)**

where $l = (T - \tau)/\beta_1$ is the net added path length. Equation 12 reveals that the beat frequency has two distinct components

$$\Delta f = \Delta f_{\upsilon \neq 0} - \Delta f_{\upsilon = 0}.$$ **(13)**

The detected beat frequency is the sum of the initial beat frequency (velocity = 0) and the beat frequency associated with the Doppler shift (velocity ≠ 0). If the initial time varying beat frequency is subtracted from the data in the frequency domain, the remainder will give the PDV spectrogram. Fortunately, a map of the initial beat frequency across the pulse envelope is recorded in the pre-shot pulses. The velocity extraction was not performed here, but the spectrogram shown in Figure 9 demonstrates that the quasi-CW technique is possible.

Conclusion

Using the HSPDV technique, the measurements presented here increase the maximum measureable velocities obtainable using traditional PDV by a factor of ~3.6. Velocity measurements not shown here resulted in stretch factors of 10 without significant loss in signal quality. Factors well beyond 10 would likely be achievable with the development of a broadband amplifier with a flat gain curve. Calculations of the stretch factor are derived based on dispersion properties in the fiber spools, and it is relatively simple to account for the time stretch in the data analysis and determine the velocity. Some limiting factors of the technique are timing constraints imposed by mode-locked lasers, which can make triggering challenging if the laser must be triggered on the experiment, and a recording time limited by the duration of the pulse (on the order of 150 ns here). An alternate variation of this method is presented that removes both of these constraints, though the data analysis is more complicated.

This technique is an especially well suited alternative diagnostic to traditional PDV when measuring velocities >10 km/s with recording times in the hundreds of ns. In particular, this speaks to a recent assessment calling for the integration of PDV technologies with higher velocity measurement capabilities at NIF (Frayer 2016).

References

Agrawal, G. P., *Nonlinear Fiber Optics*, Academic Press, Inc., San Diego, 2001.

Dorrer, C., "Chromatic dispersion characterization by direct instantaneous frequency measurement," *Opt. Lett.* **29**, 2 (2004) 204–206.

Frayer, D. K., D. Fratanduono, "Considerations for a PDV diagnostic capability on the National Ignition Facility," *Proc. SPIE* **9966** (2016) 99660D.

Xia H., C. Zhang, "Ultrafast and Doppler-free femtosecond optical ranging based on dispersive frequency-modulated interferometry," *Optics Express* **18**, 5 (2010) 4118–4129.

This page left blank intentionally

Multi-Frame X-Ray Imaging Using a Streak Camera with a Patterned Photocathode

LAO-008-16 | Continuing in FY 2017 | Year 1 of 2

Daniel Marks,[1,a] Jeffrey A. Koch,[b] Roderic Tiangco,[b] Jonathan O'Connor,[b] and Mark Raphaelian[b]

We developed a new time-resolved x-ray imaging system based on compressed ultrafast photography (CUP) (Gao 2014) to achieve multi-frame imaging for energies in the 1–10 keV range with a frame rate between 1 to 10 frames per nanosecond depending on the sweep time. A patterned gold photocathode was constructed for use with an existing Kentech x-ray streak camera. Significant work in reconstruction algorithms was performed to enable reconstructions of data that are much less sparse. These algorithms were tested with optical streak camera CUP data acquired at NSTec Livermore Operations. In addition, we designed a new compressed imaging method and simulated its performance using a LiSens imaging technique (Wang 2015) with a streak camera. In the course of this project, a new compressed imaging technique was developed for high-speed imaging using a rotating disk to impose a pattern on an image acquired with a slow camera. Multiple high-speed frames can be reconstructed from a single image. We constructed this rotating disk system and tested it at slow speeds, but the system should be capable of imaging at over a million frames per second and could work for x-ray imaging as well. In FY 2017 we will acquire x-ray data on MagLIF experiments at Sandia National Laboratories using both CUP and LiSens. We will also take new data with our rotating disk camera to demonstrate higher speeds.

[1] marksdg@nv.doe.gov, 505-663-2093
[a] New Mexico Operations–Los Alamos, [b] Livermore Operations

Background

The fastest existing multi-frame x-ray imager is the DIXI camera (Gao 2014) that uses a time-dilating chamber and variable-voltage photocathode strips to achieve <10 ps images. Because a separate pinhole is used for each image, parallax issues exist. At the National Ignition Facility (NIF), DIXI is limited to five frames, which constrains the useful continuous time window. Furthermore, the DIXI camera is an expensive, complicated, heavy instrument that incorporates large magnets. There are many applications where such a camera would be impractical or impossible to use. A simpler, fast multi-frame imaging system using compressed ultrafast photography (CUP), such as we are developing, would be less costly and easier to field and is likely to be in high demand.

CUP is an emerging compressed sensing technique that compresses a time sequence of images onto a single streak camera image. In their original CUP research, Gao et al. (2014) demonstrated compression of very sparse images onto a single streak camera sweep using a patterned mask to impose fixed high-frequency content onto an image. The full image is streaked using a wide-open streak camera slit. We developed in-house and demonstrated an improved version of CUP in simulations during the FY 2015 effort of the multi-year SDRD project "Ultrafast All-Optical Framing Technology" (Frayer 2016). We acquired the original source code used by the Gao team and found that multiple image copies allow the reconstruction of

images that are much less sparse; we determined that this technique shows promise for capturing data from time-varying phenomena of interest to DOE missions.

Project

The work for this project was divided into developing the x-ray camera, algorithm development, optical streak camera experiments, LiSens streak camera imaging, and developing and testing the rotating disk camera.

Developing the X-Ray Camera

Before any work on this project could be accomplished, an x-ray streak camera had to be found that could be modified to have a patterned photocathode. Fortunately, we were able to find an unused Kentech low-magnification x-ray streak camera at the Lawrence Livermore National Laboratory, which we borrowed. This camera is capable of sweep speeds between 15 and 900 ps/mm. Associated hardware and missing parts were located, including a vacuum tank and high-voltage cables. A mount was constructed for attaching a CCD to the camera. The camera is now fully assembled and awaits testing to ensure proper operation.

There were several options for imposing a pattern on the input image to the streak camera. An external absorbing mask could be used, but if the mask was too thin, it would have penetration issues, or if it was too thick, angular restrictions. In either case, the image formation process would be much more complicated and difficult to model, and an exact model of the system is absolutely necessary for performing the CUP reconstructions. We considered using gold or cesium

iodide (CsI) to form the patterned photocathode. CsI has a much greater efficiency than gold, but degrades in the presence of air and so would allow us only limited testing. Gold is easy to pattern with photolithography, whereas CsI would require deposition through a stencil, which would be much less precise and probably lead to variable material thickness.

We decided to use a gold photocathode measuring 5 × 30 mm with a pattern formed by 70 × 70 μm and 140 × 140 μm squares. The larger square sizes are used on the horizontal edges where the spatial resolution is substantially worse. An additional line of gold is located at the edges, which can be used like a regular 1-D streak camera, possibly for collecting a record of the total x-ray flux over the whole image if this line is not blocked by a pinhole but instead views the entire source image (Figure 1).

Algorithm Development

Gao (2014) used the two-step iterative shrinkage/thresholding (TwIST) algorithm for reconstructions,

$$G_{i+1} = G_i + \lambda \, \Psi[G_i + K^T\{D - K(G_i)\}], \tag{1}$$

where D is the measured data, which consists of streak images; G_i is the object reconstruction; K is a projection operator, which generates simulated images from G_i; K^T is the back-projection operator; Ψ is a smoothing operator; and λ is a dampening constant. The smoothing operator chosen was a total variation constrained smoothing.

We acquired the source code and raw data from the authors of the original CUP paper and found problems immediately. The code produced severe image artifacts; these, as mentioned by Gao (2014), could
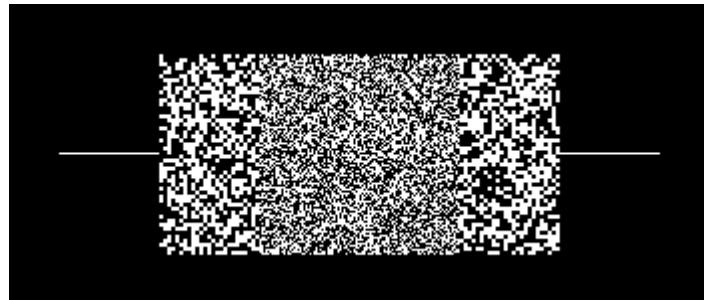

Figure 1. Pattern for gold photocathode. The smaller squares are 70 × 70 μm and the larger squares are 140 × 140 μm. White areas have 50 nm thick gold deposited on an aluminum and polyimide substrate.
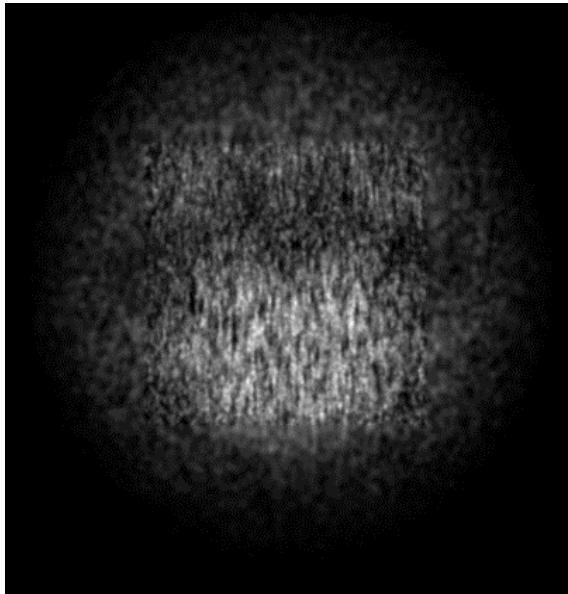
Figure 2. Simulated CUP data representing x-ray Doppler velocimetry data for NIF

be corrected by thresholding the images so only the very brightest pixels were seen. This gave presentable results for very sparse images, such as a moving blob of light, but was fatal to more complex images.

We collaborated with Prof. Richard Baraniuk at Rice University to develop better reconstructions. He improved the TwIST algorithm through better adjustment

of the dampening constant and also started the reconstructions at coarser resolution before proceeding to finer resolution reconstructions. He also introduced us to the D-AMP algorithm, which provided additional benefits.

$$G_{i+1} = \Psi[G_i + K^T\{Z_i\}]] \tag{2}$$

$$Z_i = D - K^T\{G_i\}] + Z_{i-1} \ \Psi[G_{i-1} + K^T\{Z_{i-1}\}]/m \tag{3}$$

Using the D-AMP algorithm we were able to perform significantly better reconstructions, particularly for complex objects. In Figures 2 and 3, we see simulated x-ray Doppler velocimetry data and a frame from the reconstruction using the D-AMP algorithm, respectively.

Optical Streak Camera Experiments

We acquired data with an optical streak camera using a setup close to that used by Gao in his original research (Gao 2014), including using a digital-micromirror-device to impose the pattern on the image. The imaging system is shown in Figure 4, the object scene generator is shown in Figure 5, the acquired data are shown in Figure 6, and the reconstructed image is shown in Figure 7.
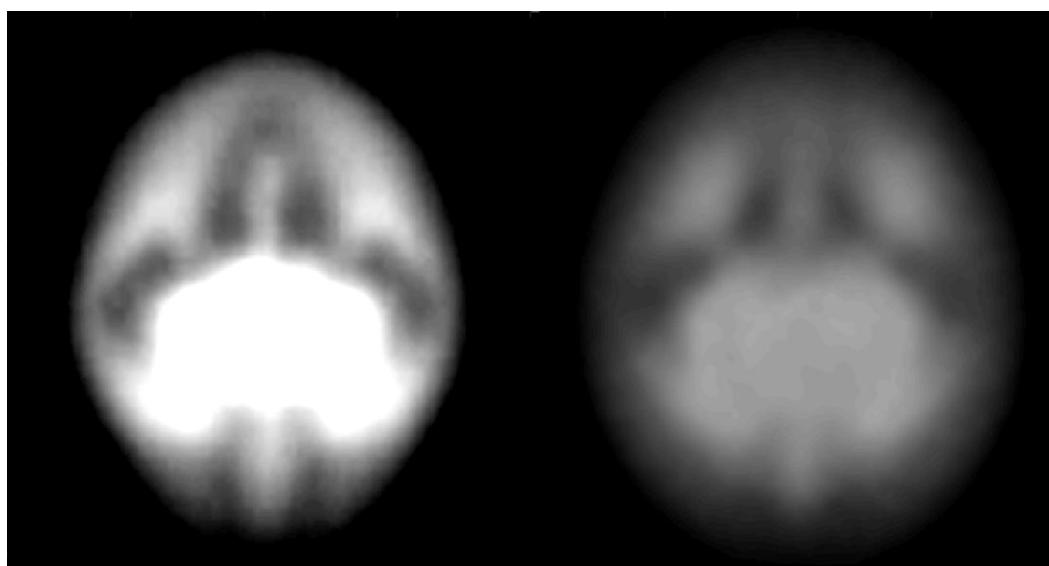

Figure 3. Reconstructions from the data shown in Figure 2. The left image is a single frame from the true object, and the right image is a single frame from the reconstruction.
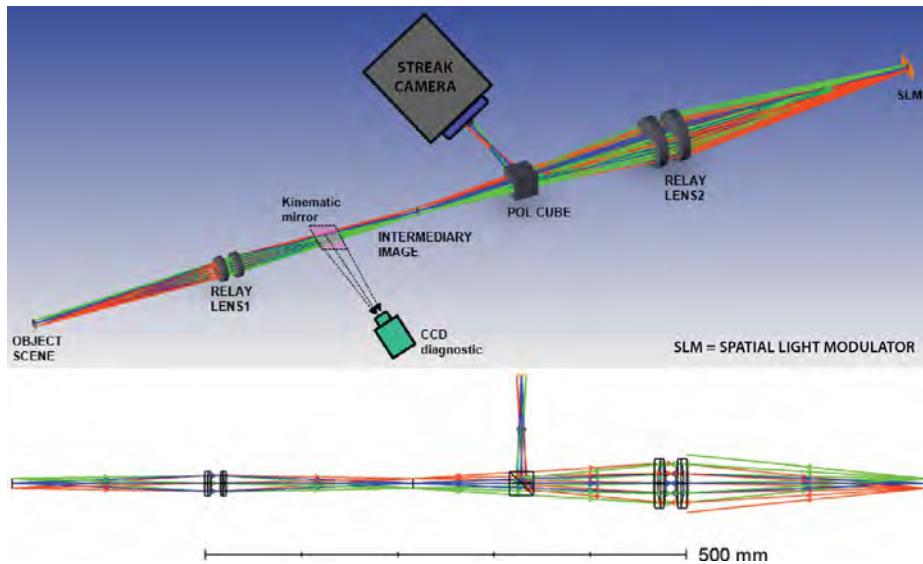
Figure 4. Optical diagram of optical streak camera data collection
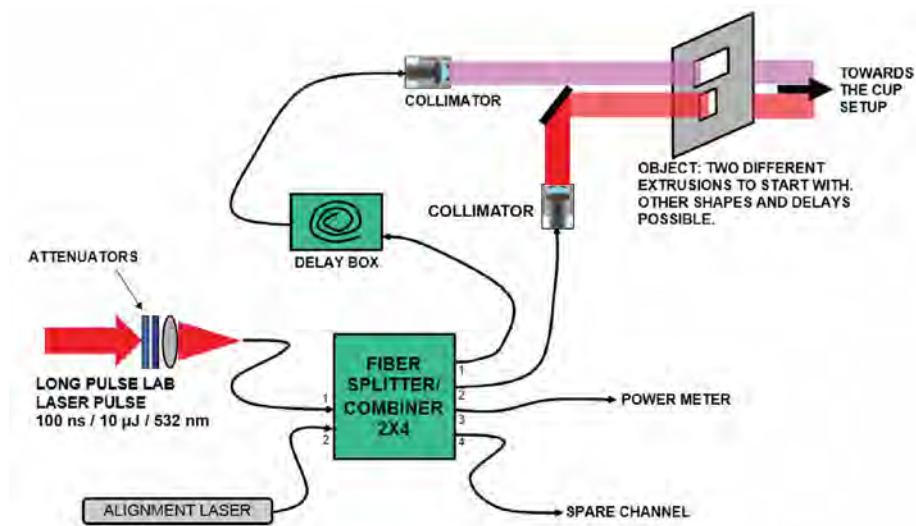
Figure 5. Laser and fiber arrangement used to generate the object scene, which consisted of square and rectangular objects delayed by different amounts through optical fibers

LiSens Streak Camera Imaging

When analyzing the simulated data, we discovered quickly that CUP is severely limited in the number of frames that can be reconstructed from a single streak camera image. Additionally, bright frames can overwhelm dim frames, and if data continue past the end of the streak it is almost impossible to get a good reconstruction. We hoped to use our camera for imaging x-ray emission from laser-heated plasmas for MagLIF experiments at Sandia National Laboratories. However, CUP, as originally conceived, would not be suitable for these experiments, because its time

resolution is not capable of hundreds of frames and the data continue long after the streak camera would be finished.

To meet the needs of the MagLIF experiment, we devised an alternative compressed imaging method that compresses a full 2-D image on a single line. The method is similar to the LiSens method developed for optical imaging (Wang 2015), except that with LiSens multiple images with different patterns are used to build up a single 2-D image. This LiSens system is shown in Figure 8b. Instead of patterning the photo-cathode, an absorbing pattern is inserted directly in
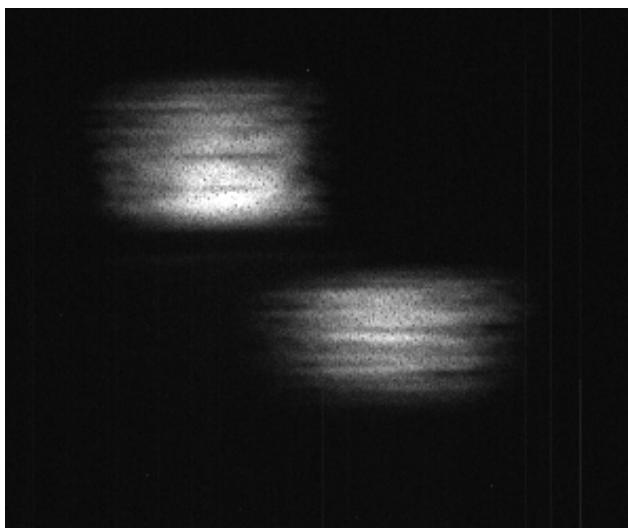
Figure 6. Raw data acquired using a 63 ns laser pulse

Figure 7. Two frames from the reconstruction, showing the (a) upper and (b) lower pulses

front of the experiment. Instead of an imaging pinhole, an imaging slit is used. A regular 1-D streak camera is used, so each pixel in the camera samples a patterned line from the object. From the data, as we have shown in simulations, a 2-D image can be reconstructed from a single line. Each line in the streak camera then encodes an independent 2-D image, and there is no longer any trouble with bright images interfering with dim images and hundreds of low-resolution images can be recorded.

Rotating Disk Camera

A new method for high-speed imaging using a patterned rotating disk was also developed and tested. This method involves placing a patterned rotating disk

at an image plane in order to impose a time-varying structure onto the image. This can be done with x-rays by placing the rotating disk near the image sensor, or it can be done optically by placing the rotating disk at an intermediate image plane as illustrated in Figure 9. Reconstruction is performed using the TwIST algorithm given in Equation 1.

We constructed a prototype rotating disk system using an optical chopper with a patterned Mylar sheet taped to it. The optical chopper can spin up to 60 rotations per second. The pattern on the Mylar sheet is composed of 40 × 40 µm squares. Theoretically this should allow imaging at more than a million frames per second for a limited number of frames. The resolution of the reconstructed images decreases as more frames are reconstructed.
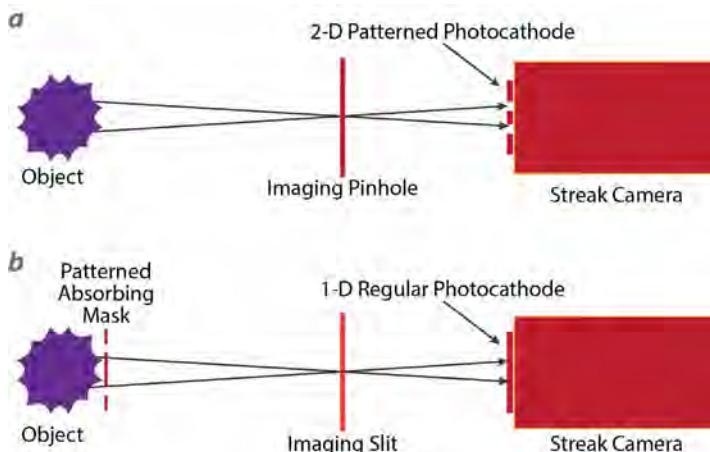
Figure 8. Diagrams of (a) CUP and (b) LiSens setup. The LiSens system uses multiple images with different patterns to create a 2-D image.
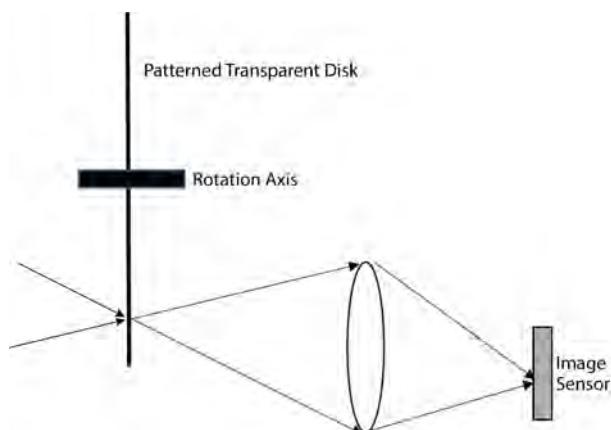
Figure 9. High-speed imaging using a patterned transparent disk to impose time-varying structure on an image. The image sensor takes a single picture from which multiple high-speed images are reconstructed.
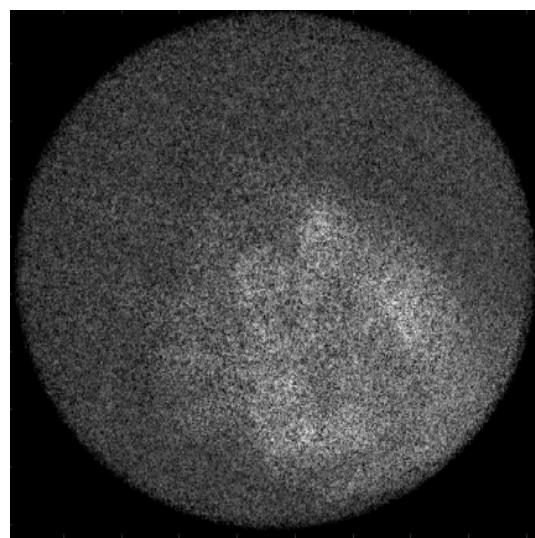
Figure 10. Raw image from rotating disk high-speed camera
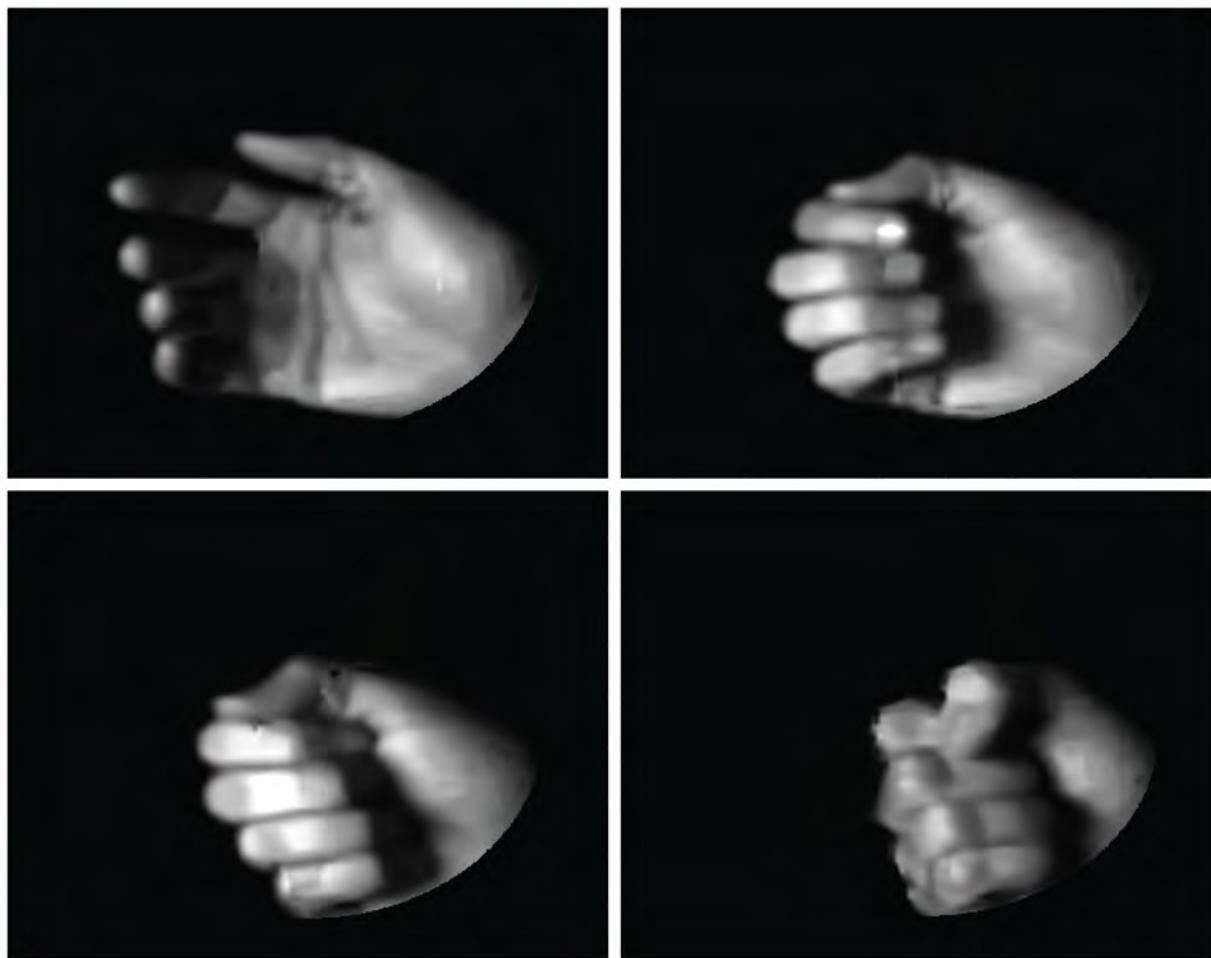
Figure 11. Four images out of 16 reconstructed images taken from the raw image shown in Figure 10

We acquired a slower image of a hand moving to verify the system performance for a complex object. The CCD image was 2000 × 2000 pixels, and 16 frames were reconstructed at 500 × 500 pixels each. The raw data are shown in Figure 10, and four frames from the reconstruction are shown in Figure 11.

Conclusion

During this year we assembled the parts and constructed a new photocathode for our x-ray streak camera, demonstrated the CUP technique with an optical streak camera, developed a new compressed imaging technique based on a LiSens system and developed a completely novel high-speed imaging system based on a rotating disk. A technology abstract was submitted for the rotating disk camera and a patent will be written. During our second year we plan to collect data on MagLIF experiments at Sandia National Laboratories, perform time-resolved imaging of the spot shape of a Platts x-ray source, and take higher-speed data with our rotating disk camera. We expect at least two publications to result from these experiments. While this project was originally conceived as a two-year effort, we may submit a FY 2018 proposal to continue testing and development, pending FY 2017 results. There is continued interest in using CUP and LiSens on future beam diagnostics for radiography machines.

Acknowledgments

We would like to thank Daniel Frayer for introducing us to the CUP technique and allowing us to do some initial development under his SDRD project. Thanks also go to Kathy Opachich, Jesus Castaneda, and Duane Smalley for their assistance.

References

Frayer, D., G. Capelle, D. Marks, A. Bernstein, "Ultrafast all-optical framing technology," in *Site-Directed Research and Development*, FY 2015, National Security Technologies, LLC, Las Vegas, Nevada, 2016, 205–211.

Gao, L., J. Liang, C. Li, L. V. Wang, "Single-shot compressed ultrafast photography at one hundred billion frames per second," *Nature* **516** (December 4, 2014) 74–77.

Wang, J., M. Gupta, A. C. Sankaranarayanan, "LiSens—A scalable architecture for video compressive sensing," 2015 IEEE International Conference on Computational Photography, April 2015, 1–9.

This page left blank intentionally

Dynamic Surface Tracking for Velocimetry Systems

STL-008-16 | Year 1 of 1

E. Kirk Miller,[1,a] Gene Capelle,[a] Tom Keenan,[a] Mike Grover,[a] Kevin Lee,[a] and Rachel Posner[a]

We have developed novel optical probes that adjust their focus dynamically during the experiment to continually collect maximum light from the surface as it moves, thereby optimizing the recorded signal-to-noise ratio. We demonstrated improved collection on dynamic experiments using an electro-optically refocusing lens. We also investigated an all-optical solution in which a polymer lens is refocused under stimulus from a laser that is not part of the core velocimetry system; our solution for this includes a custom-drawn plastic fiber doped with a dye that absorbs the pump wavelength but transmits the probe wavelength.

[1] millerek@nv.doe.gov, 805-681-2237
[a] Special Technologies Laboratory

Background

Shock physics experiments often create physical conditions that challenge the dynamic range of optical velocimetry systems. Fixed-focus probes can remedy this by returning more light over a limited travel distance, whereas collimating probes return less light but can track a surface over many centimeters. Dynamic experiments may generate dense clouds of ejecta in front of the shocked surface, interfering with optical velocimetry measurements of the occluded surface. Significant improvement in dynamic range for surface velocity can address this problem.

Project

Electrically Actuated Lens

We identified the dynamically refocusing graded-index (GRIN) lens from TAG Optics, Inc., as the option with the highest resonant frequencies and thus the best candidate for dynamic shock experimentation. These lenses are cylindrical liquid cells, driven on-resonance by a piezoelectric element in the housing. The resulting time-varying density profile creates a cylindrically symmetric profile in the index of refraction; this index profile creates a lensing effect that alternates between focusing and defocusing. For the IR-transmitting lens model HP-β, the resonant frequencies are typically 140, 180, 220, 260, 300, and 350 kHz, where higher frequencies correspond to higher-order modes with both higher optical power and smaller effective apertures. Excellent descriptions and resources are available on the company's website (www.tag-optics.com), and detailed analyses of the behavior of these lenses are found in McLeod (2007) and Duocastella (2013).

Our initial intent was to use a low-frequency resonance and slew the phase of the drive at shot time to track the surface as it moves toward the probe optics. For many experiments under consideration, even the lowest resonant frequency, 140 kHz, is too fast to track the surface in this way for more than a few microseconds. A custom-built lens with lower resonant frequency, on the order of 20 kHz, would be possible but much bulkier to field. As a result, we chose instead to operate the off-the-shelf lens at a higher resonant frequency, 220 kHz, and let it slew through focus

Table 1. Performance of TAG HP-β lens

| Resonant Frequency (kHz)	Effective Aperture (mm)	Maximum Optical Power (m⁻¹)
140	4.0	±0.8
220	2.4	±2
350	1.6	±4
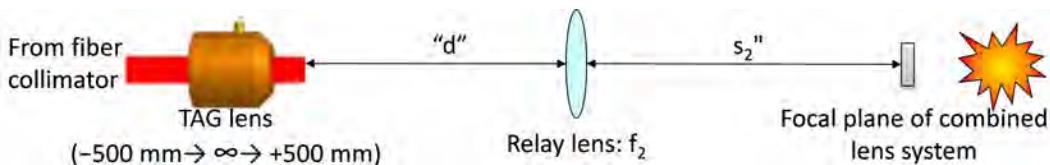
Figure 1. Optical system used for TAG demonstration experiments. The relay lens, of focal length f_2, is located a distance d from the TAG lens; the optical system focuses at a distance s_2'' from the relay lens.

repeatedly during the demonstration experiments. Performance data for the lens we used are shown for three resonance frequencies in Table 1.

We set up the TAG lens with a 100 mm relay lens so that it could be stood off from the experiment while still providing the necessary optical modulation. The system is diagrammed in Figure 1. The distance at which the experiment will be in focus, called out as s_2'', is the distance from the final lens to the focal point of the system.

For the 220 kHz resonance with an optical power of ±2 (focal length of ±500 mm), we can calculate s_2'' as a function of the TAG lens optical power to determine the range of distances over which the experiment will be in focus at different phases of the drive signal. Results for the 100 mm relay lens are illustrated in Figure 2. This calculation was done to select the relay lens and the appropriate TAG-to-lens separation for our demonstration experiments that have a total travel of ~40 mm. The range of s_2'' is just about right, ranging from 80 to 120 mm.

To determine the collection efficiency of the dynamically focusing probe, we performed ray-tracing simulations using the FRED optical code. The GRIN lens was modeled as a simple, second-order index contour; this is valid because the central maximum of the Bessel-function index gradient is much larger than the collimated light beam into the lens, so the variation in index profile sampled by the beam is dominated by
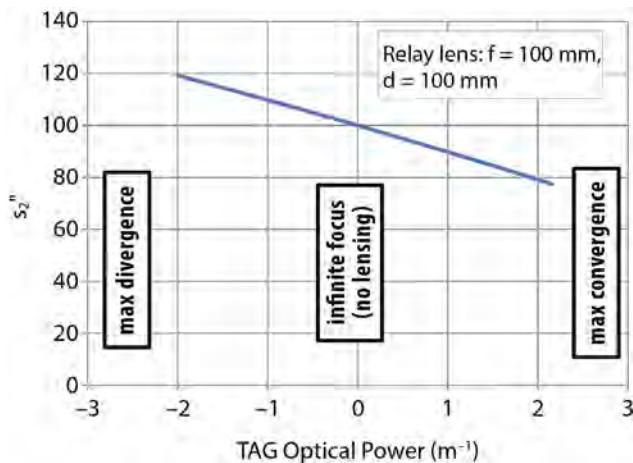
Figure 2. s_2'' vs. TAG optical power with 100 mm lens from the relay lens

the quadratic term. Collimated light from a 400 μm diameter source (fiber-optic GRIN collimator) was propagated through the lens system to a series of analysis planes at distances from 80 to 120 mm, in 10 mm increments. The FRED model of the system is shown in Figure 3. The index profile is of the form

$$n^2(r) = n_0^2 \times \left(1 \pm \left(n_2 \times r\right)^2 + \ell\right), \tag{1}$$

where n_0 = 1.3 for the TAG HP-β, and $|n^2|$ = 0.008 at peak to match the optical power of 2 at 220 kHz.

The efficiency at each plane was measured as the fluence through a 200 μm diameter region at the center of the analysis plane. While this is not ideal, in that it only measures light going in one direction, it is valid due to the time-reversal symmetry of the optical
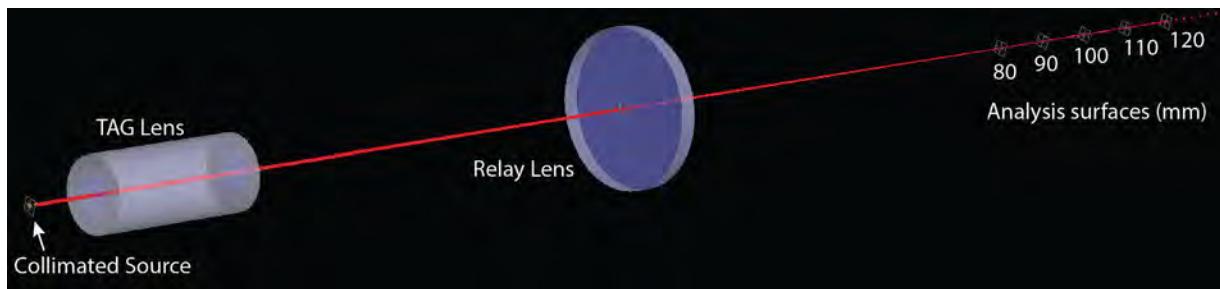
Figure 3. FRED model of TAG lens system used in demonstration experiments
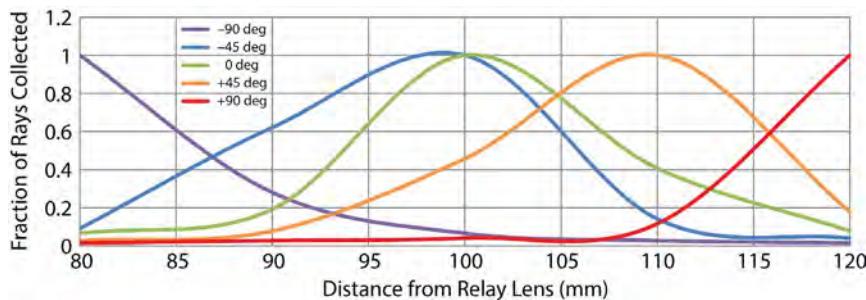
Figure 4. Results from ray-tracing for collection efficiency vs. distance for five different drive phases. Collection efficiency peaks at different distances from the relay lens for different phases of the drive signal, thus allowing us to collect light efficiently over the full experimental range on each cycle of the drive.
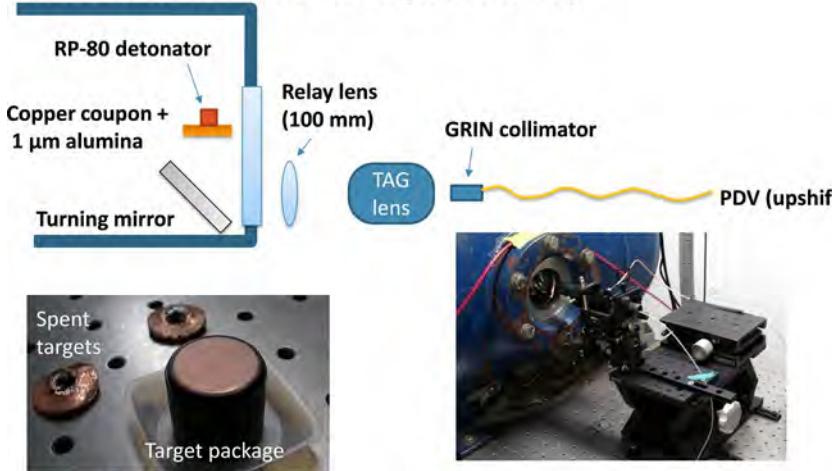
Figure 5. Diagram and photos of configuration for demonstration experiments at STL

system. It is also much faster than a two-way propagation due to the universally poor collection efficiency ($\sim 10^{-4}$) of photonic Doppler velocimetry (PDV) probes, and thus the need to propagate $\sim 10^5$ rays to achieve statistically useful results. The efficiency results are shown in Figure 4 for five different drive phases, spanning the full range of optical powers generated by the lens. The asymmetric efficiency curve at zero degrees is in qualitative agreement with a curve produced using purely geometrical arguments to estimate the efficiency before the full ray-tracing results had been calculated.

For our demonstration experiment, we used a shot package developed to characterize dynamic range on PDV systems in the past: a copper coupon coated with 1 μm alumina powder and driven with an RP-80 detonator. This package is known to generate a velocity of ~800 m/s for the copper; also, a cloud of ejecta that runs in front of the surface slows due to air resistance and is then swept up by the copper. Details of the dynamics can be found in La Lone (2015). The package was configured inside the small-explosives enclosure at the Special Technologies Laboratory (STL),
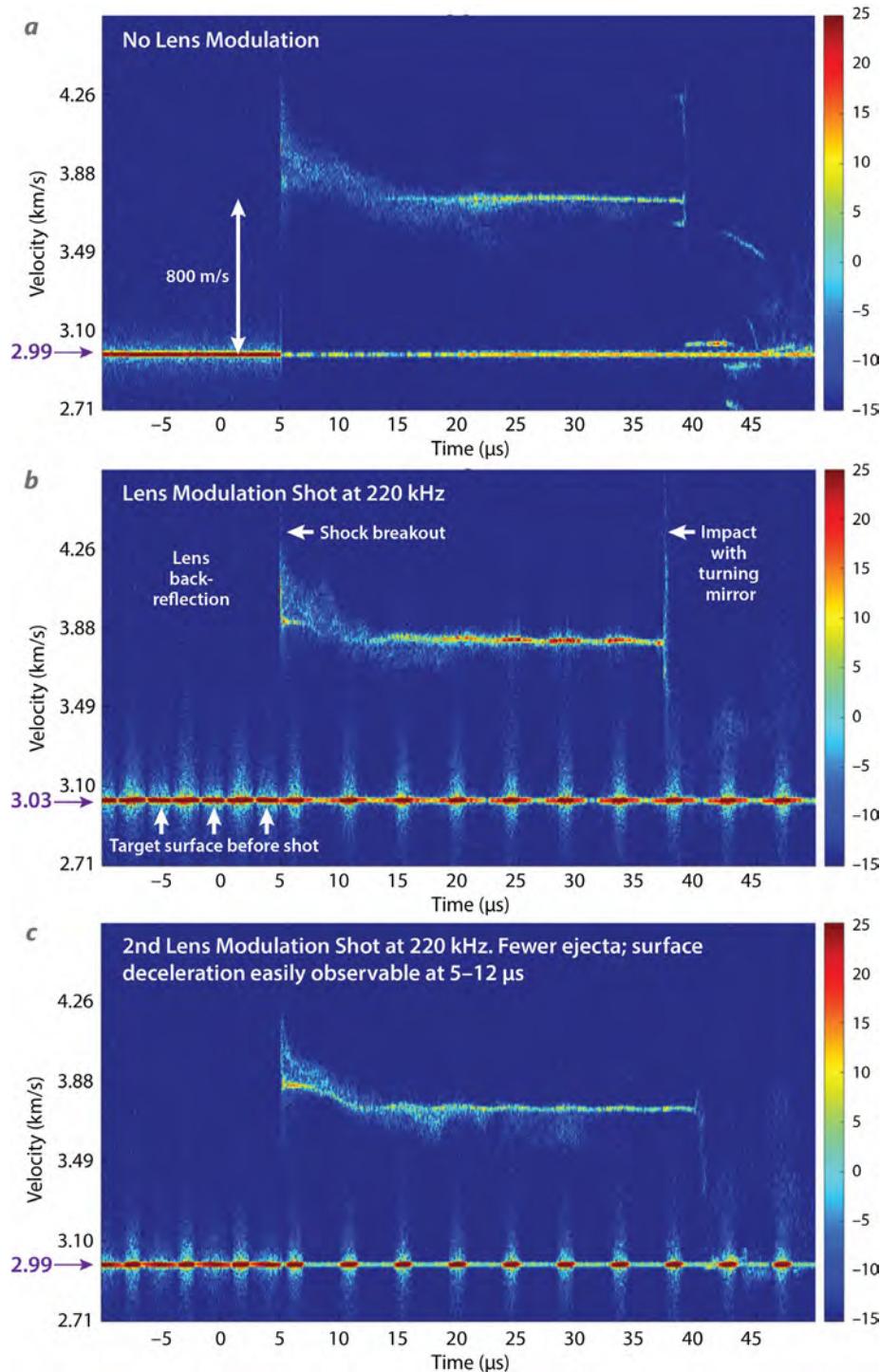
Figure 6. Velocity spectrograms from three TAG lens shots, showing (a) no modulation, and (b, c) two with 220 kHz modulation. Figure 6c shows fewer ejecta; surface decelerations are easily observable from 5 to 12 μs.

commonly referred to as the Boom Box. The PDV was brought in through the sapphire window in the side of the chamber and directed onto the experiment using a disposable aluminum mirror on a plastic substrate. The experimental setup is shown in Figure 5.

The PDV system used with the TAG lens was configured with an upshift, meaning that zero velocity occurs at approximately 4 GHz (or approximately 3 km/s on the velocity spectrograms below). One shot was done with no lens modulation, and the other two shots use lens
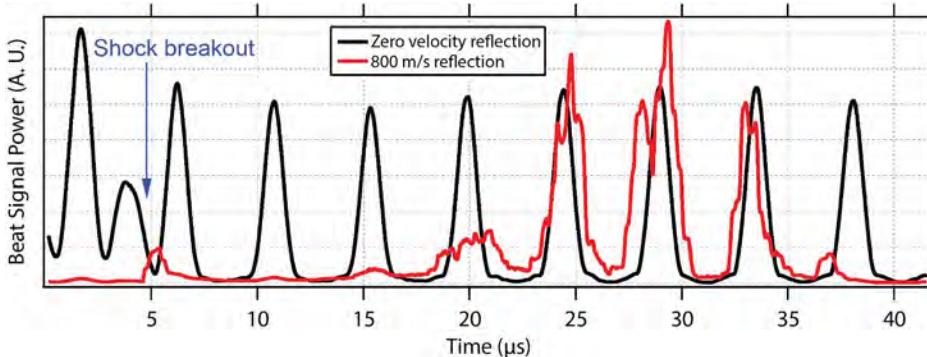
Figure 7. Beat frequency power vs. time for the first lens modulation shot (Figure 6b). Note the shifting of phase of the red trace (800 m/s) relative to the black trace (zero velocity) as the surface moves through the focal range of the system.

modulation at 220 kHz, giving optical power of ±2 at the extremes of the drive phase (Figure 6). Before the shock breakout at approximately 5 μs, the modulated spectrograms are dominated by two reflections that are out of phase, implying they come from different distances. By blocking the beam, we can assign one of the reflections to the TAG lens itself; that reflection continues at zero velocity after the shock breakout. The other reflection, which disappears from the zero velocity line after shock breakout, is the sample surface.

Comparing the second and third spectrograms (Figures 6b and 6c), we see that there is apparently a significant variation in how much the ejecta occludes the surface. The spectrogram in Figure 6c, in particular, seems to have fewer ejecta, so the surface can be seen decelerating from approximately 5 to 12 μs. This deceleration feature is familiar from earlier campaigns where control samples with no alumina powder were also shot, and it appears to be the normal behavior for these copper coupons driven with the RP-80 detonators. We assume that the surface is behaving similarly behind the ejecta clouds in the first two spectrograms.

The second spectrogram shows how the improved surface return shifts in time as the surface approaches the lens system. Near 20 μs, the peak surface return lags the zero velocity return from the lens; two cycles later, at 34 μs, the peak surface return leads the zero velocity return from the lens.

To better visualize the shifting of phase as the surface moves through the focusing range of the optical system, we can plot the beat frequency (electrical) power vs. time for both the zero velocity line (which gives the phase of the drive) and the 800 m/s line. The data, plotted in Figure 7, show the slewing of phase as the surface (red trace) moves through the focal range of the lens system.

While using the TAG lens, we discovered that back-reflections from the lens cause significant artifacts in the data, including multiple path lengths between the fiber probe and the target. Scans made using the Luna optical backscatter reflectometer (OBR), plotted in Figure 8, show the multiple back-reflections in the TAG lens and the effect on the sample return. Reducing the back-reflections could possibly be done
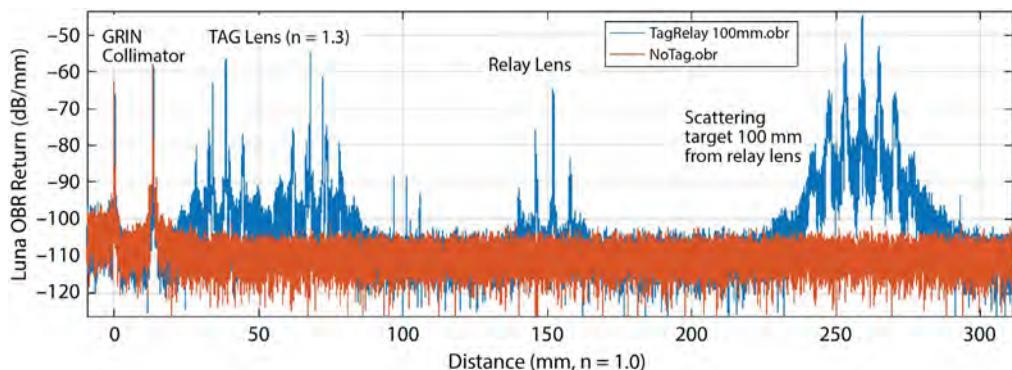
Figure 8. Luna OBR scans of the TAG system. The red trace is taken with only the fiber collimator; the blue trace includes the TAG lens, relay lens, and a scattering target 100 mm from the relay lens.
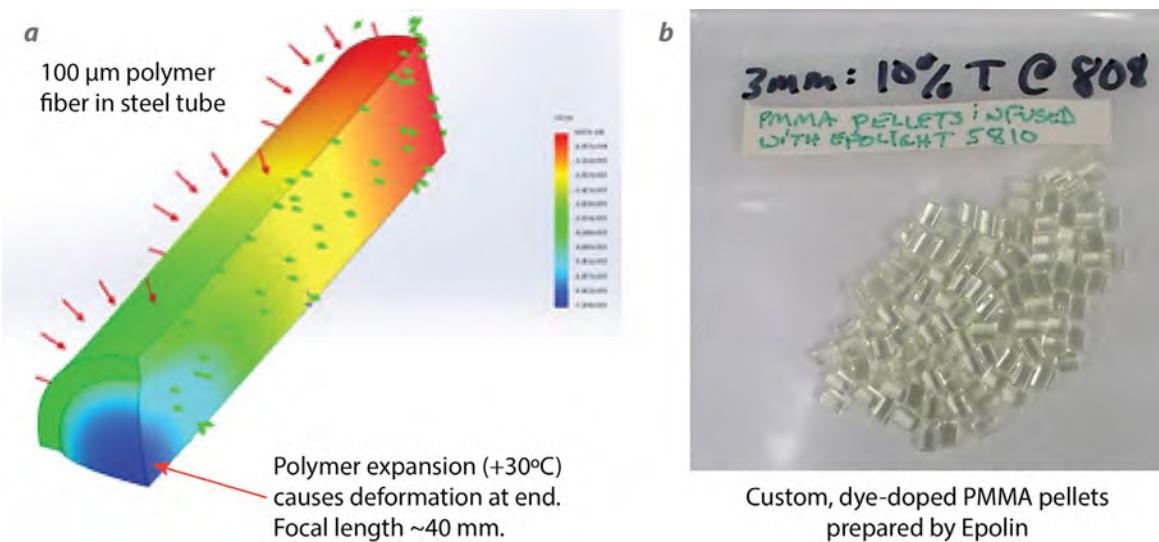
Figure 9. (a) FEA analysis results showing deformation of the ends of a polymer fiber heated inside a steel tube, and (b) dye-doped pellets for the optically actuated lens scheme

by better anti-reflection (AR) coating of the windows to (a) match the air-glass interface specifically for the PDV wavelength of 1550 nm and (b) match the glass-fluid interface at the same wavelength. The standard TAG lens windows are AR-coated for a wide range of IR wavelengths including 1064 nm. Because the TAG lens is a long-path, cylindrically symmetric lens, simply detuning the angle at which the collimated light strikes the window would likely degrade the performance of the lens.

The following observations may guide future work with these TAG lenses:

- Back-reflections need to be reduced by modifying or redesigning the windows of the liquid cell.

- For PDV, the beam size is small enough that a smaller-diameter liquid cell (with smaller effective aperture) might be tolerable; this might enable even higher resonant frequencies.

- Larger apertures and higher optical powers are available for visible-light lenses, so future imaging applications may be able to dynamically refocus with these other lenses.

Optically Actuated Lens

Our second approach to dynamically refocus the PDV probe sought to develop an optically actuated scheme that could be addressed through the transport fiber. We did numerical calculations to determine the feasibility of refocusing based on the following effects:

- Thermo-optic effect

- Photorefractive effect

- Photo-induced absorption/refraction (semiconductors and polymers)

- Microelectromechanical micro-mirrors

- Thermal expansion of polymers

Our calculations showed that the scheme with the best combination of response time, power requirement, and simplicity was the thermal expansion of a polymer monofilament (fiber with no cladding). We performed finite element analysis (FEA) of a system defined as a 100 μm diameter polymer fiber glued into a steel tube. For a 30°C temperature rise, we found that the end faces of the polymer should deflect to create a lens with 40 mm focal length. The FEA results are shown in Figure 9, together with the custom dye-doped pellets

Lab Data: Static Heating

Plastic fiber in brass chuck and heater

Collimated light from fiber

PMMA fiber glued into brass holder

Brass holder fits into Thorlabs lens heater

63 °C
54 °C
44 °C
34 °C
23 °C

Decreasing spot size
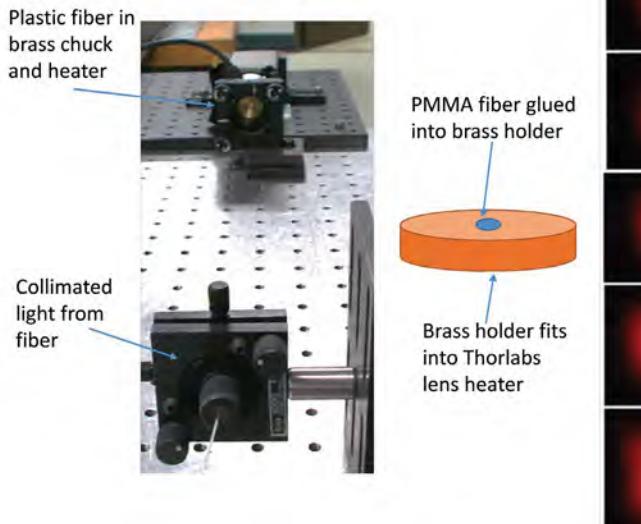
Figure 10. Static heating experiment of plastic fiber. The far-field spot size decreases as the temperature of the fiber increases, indicating a positive lensing effect due to mechanical deformation of the fiber ends.

fabricated by Epolin, Inc., for this project, which were drawn into monofilament fibers by Paradigm Optics, Inc.

As a preliminary proof of concept, we glued plastic fibers of different diameters into brass holders with precision-drilled holes, heated them while illuminating the fiber with collimated red light, and recorded the far-field spot size. The setup and results are shown in Figure 10.

Conclusion

We have developed two techniques based on novel optical probes to dynamically refocus a PDV system during a dynamic shock experiment to improve light collection. Our dynamic experiments demonstrated improved collection using an electro-optically refocusing lens. We also conducted proof-of-principle experiments to demonstrate the feasibility of an all-optical solution in which a polymer lens is refocused under stimulus from a laser that is not part of the core velocimetry system. The polymer lens system is covered under a patent (Miller 2016). Dynamically refocused probes could enable higher dynamic range on future experiments in which the collection efficiency of conventional, collimated probes is insufficient to deliver high-quality data in cases where particle clouds obscure a moving surface.

References

Duocastella, M., C. B. Arnold, "Transient response in ultra-high speed liquid lenses," *J. Phys. D* **46** (2013) 075102.

La Lone, B. M., B. R. Marshall, E. K. Miller, G. D. Stevens, W. D. Turley, L. R. Veeser, "Simultaneous broadband laser ranging and photonic Doppler velocimetry for dynamic compression experiments," *Rev. Sci. Instrum.* **86** (2015) 023112.

McLeod, E., C. B. Arnold, "Mechanics and refractive power optimization of tunable acoustic gradient lenses," *J. Appl. Phys.* **102** (2007) 033104.

Miller, E. K., G. Capelle, T. Keenan, D. Frayer, USPTO Provisional Patent #62/347,024, "Dynamically refocused fiber-optic probe," filed June 7, 2016.

This page left blank intentionally

Laser-Generated Ultra High–Energy Density Plasma for Fast Neutron Pulse Production and Neutron Diagnostic Developments

LAO-04-15 | Continued from FY 2015, Continuing in FY 2017 | Year 2 of 3

James Tinsley,[1,a] Alden Curtis,[b] and Jorge Rocca[c]

We are developing a pulsed neutron source using intense femtosecond laser pulses to generate an ultra high–energy density plasma that is rich in deuterium. Plasma densities that approach that of solid material are obtained through the interaction of the laser with arrays of aligned nanowires. We have measured yields as high as 3.6×10^6 neutrons per 1.6-joule laser pulse. This is an order of magnitude higher specific yield than has been reported elsewhere. Measurements of the plasma's deuteron energy spectrum compare fairly well with those from particle-in-cell simulations. In FY 2017 we plan to upgrade the laser system so that we can achieve a yield of at least 1×10^8 neutrons per pulse.

[1] tinslejr@nv.doe.gov, 805-681-2282
[a] Special Technologies Laboratory; [b] New Mexico Operations –Los Alamos; [c] Colorado State University

Background

This project is based on work done at Colorado State University (CSU), in which Professor Jorge Rocca and his collaborators have produced hot high-density plasmas through the interaction of high-power density laser pulses and aligned arrays of metal nanowires. The interaction of powerful lasers and solid materials is limited by the barrier to further light penetration that occurs when the critical electron density has been reached. This limits the laser penetration to a thin surface layer and the plasma density to (typically) 0.1% of the solid density. By replacing a solid material surface with an array of nanowires, a much stronger coupling of the incident laser radiation and the target material is possible.

Researchers at CSU and their collaborators have reported electron densities approximately 100 times that of the critical density, multi-keV temperatures, extremely high degrees of ionization, and gigabar pressures using this technique. By substituting highly deuterated polyethylene (CD_2) nanowires for the metals, we produce fast, intense pulses of neutrons through deuterium-deuterium (D-D) fusion.

This project supports a variety of project needs for subcritical experiments and high-energy density physics (HEDP). Specifically, neutron-diagnosed subcritical experiments (NDSE) need a fast neutron source for detector calibration. Additionally, NDSE will benefit from diagnostic development for improved time-of-flight (TOF) and neutron discrimination measurements, which will be necessary for the plasma characterization. HEDP experiments at the National Ignition Facility and the Z machine will benefit similarly from the development of a diagnostic that can be used for studying neutron burn as well as TOF and neutron discrimination.
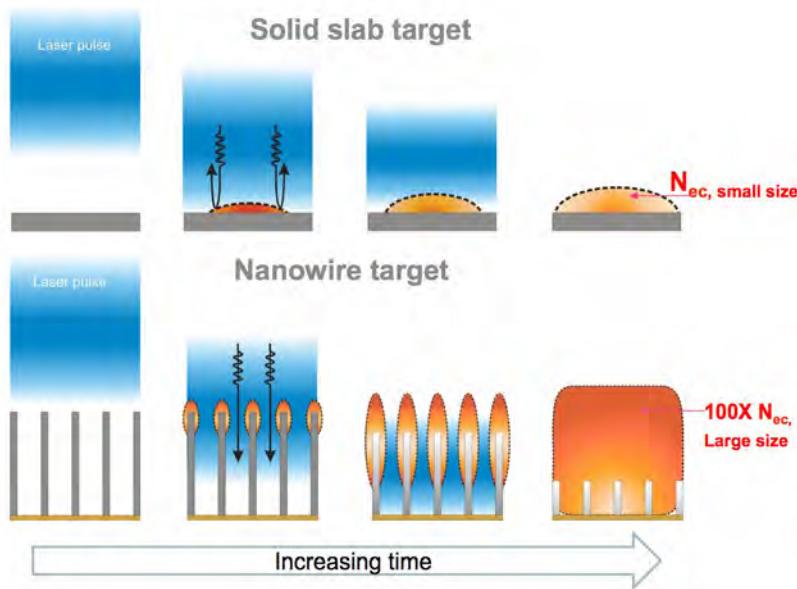
Figure 1. The difference between laser interaction with a solid surface and with a bundle of nanowires (Purvis 2013)

Project

The central concept in this project is illustrated in Figure 1. In contrast to a laser pulse hitting a flat surface, a pulse incident on an ordered array of nanowires is able to couple to a much larger volume of material before the free electron density becomes so high that it reflects any further incident laser energy. This makes possible plasmas that have densities close to that of the solid material, very high ionization levels, and gigabar pressures produced with 0.5–0.6 J laser pulses (Purvis 2013). Under such conditions, a plasma is created that contains a sufficient number of deuterons with sufficiently high energies to produce a useful number of neutrons in a pulse on the order of 1 ps duration.

In the first year of this project (Tinsley 2016), much of the effort was put into target fabrication, building new diagnostics, and conducting experiments to establish what needed to be done to ensure success in acquiring the data necessary to prove the concept. One unexpected discovery is that in producing CD_2 plasmas, we also generate a significant number of x-rays with energies approaching, and some even exceeding, 1 MeV. Some of these are undoubtedly caused by neutron interactions with matter inside the chamber, but many correspond in time to the laser-target interaction.

To isolate the neutron signals from most of the x-ray background, we set each neutron detector in a housing of lead, with 10 cm thick walls in front and 5 cm thick walls on the sides, top, and bottom. This shields the detectors from most of the x-rays they would otherwise be exposed to as well as other radiation that enters tangentially after scattering from nearby materials. Some x-ray response at varying signal strengths is still seen in many laser shots. We attribute this to the fact that some number of very high–energy x-rays are produced as part of the process, and these (or daughter x-rays from Compton scattering in the lead) have sufficient probability to penetrate the shielding and reach the detector in many of the events.

The elastic cross section for neutron interactions is sufficiently low that most neutrons will pass through the shielding unimpeded, and even those that scatter do so mostly by small angles. The inelastic cross section is substantially lower: only about 1 in 3,000 neutrons incident on the shielding is lost. Thus, the lead shielding does not materially affect our detection of neutrons.

Neutron detector signals from a few of the first direct measurements of neutrons due to a laser pulse interaction with nanowire targets are shown in Figure 2. The narrow signals at the left edge of each image are due to x-rays that penetrate the shielding, as discussed
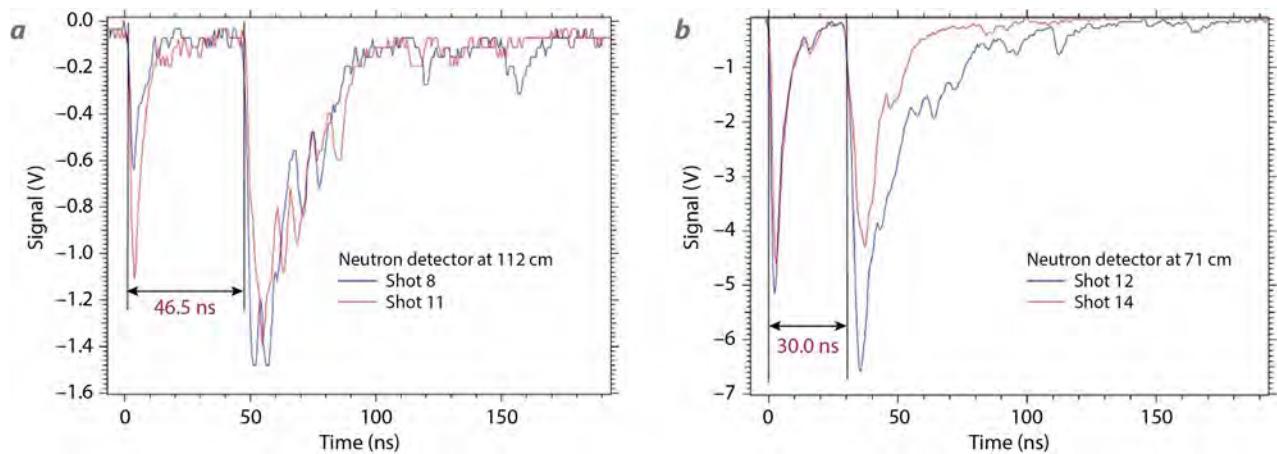
Figure 2. Signals from neutron detectors showing x-ray response (near left edge) and neutron response at a time that corresponds to the velocity of 2.45 MeV neutrons

above. The broad peaks to the right of those are due to neutron interactions. With the neutron detector set 112 cm from the laser/target interaction point, the separation between the x-ray and neutron peaks is precisely the expected correspondence between x-rays and 2.45 MeV neutrons. To confirm that we were truly seeing neutrons, we moved the detector assembly 41 cm closer to the target. The expected time shift in the neutron peak relative to the x-ray peak (and corresponding increase in neutron signal amplitude) was seen (Figure 2b).

There are two primary reasons for the time spread of the neutron signal. First, some of the neutrons emitted from the target will elastically scatter in the matter between the target and the detector (target chamber walls, shielding, etc.). This slightly lessens the neutron energy and increases its path length between target and detector. Both of these things lengthen the time for the neutron to reach the detector. Second, some deuterons are moving *toward* the detector when they interact with another deuteron, which adds center-of-mass momentum to any neutron emitted in that direction; such a neutron will arrive slightly sooner than it would have otherwise. The opposite is true for neutrons detected from interactions in which a deuteron was moving *away from* the detector. These variations (analogous to Doppler spreading) result in a spread in the neutron detection time that increases with the distance of the detector from the target.
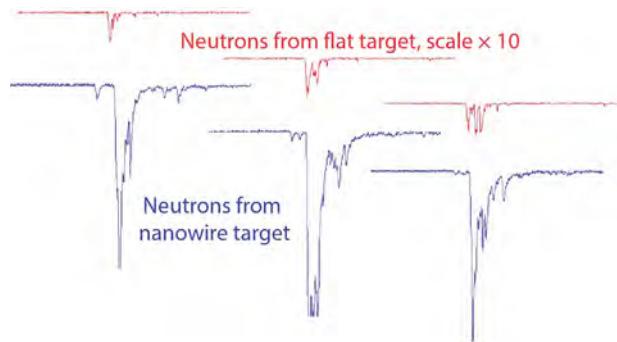
Figure 3. Neutron signals from laser shots on flat (red) and nanowire (blue) CD_2 targets

We also hit solid CD_2 targets with the same laser energy as used on the nanowire targets. A comparison of oscilloscope traces from one neutron detector in response to laser shots on a solid target (in red) and on nanowires (in blue) is shown in Figure 3. The response from the nanowire targets is 2–3 orders of magnitude greater. As expected, we see no neutron signal when hitting solid or nanowire targets made with polyethylene (CH_2).

Nanowire Targets

In the first year of this project, a significant effort went into making nanowire targets whose wires are straight, uniformly separated from each other, and not covered by extraneous material. This year, the process continued with nanowires made using alumina molds, which permit nanowire diameters of 200 nm and smaller. The polycarbonate molds used initially restricted us to
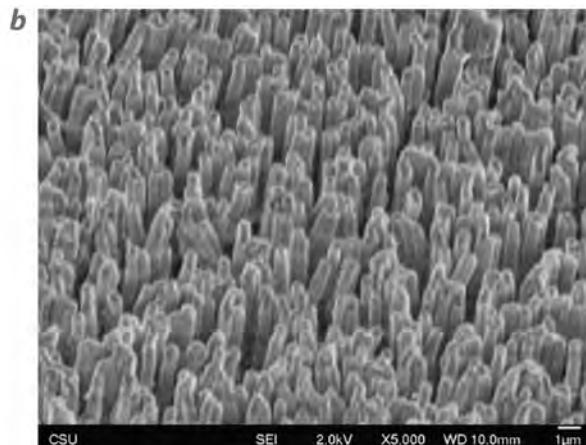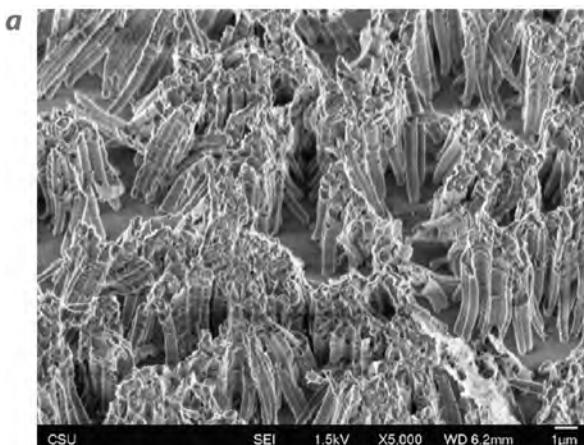
Figure 4. SEM images of nanowire arrays (a) before and (b) after an electrostatic charge has been applied to de-lump the individual wires
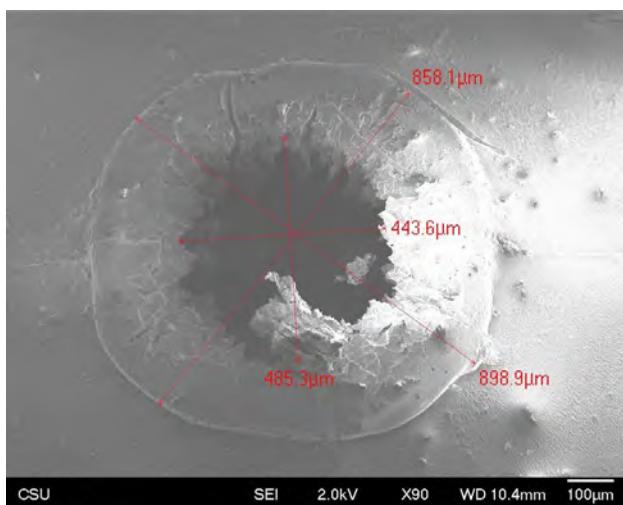
Figure 5. SEM image of a nanowire target after it has been exposed to a laser pulse shows a damage radius of at least 1 mm in diameter. The magnification is too low to resolve individual wires.

Figure 6. Next-generation target holder with nanowire arrays mounted in holes to isolate the laser damage

400 nm diameter wires. We also changed vendors for the CD_2 stock material, from Polymer Science to Sigma Aldrich. Although material from the latter is more expensive, it appears to be of better quality (more like conventional CH_2) and is easier to work with.

A new tactic this year is to apply an electrostatic charge to newly made targets to de-clump the wires, as shown in the scanning electron microscope (SEM) images in Figure 4. Another is to change the way that the targets are mounted in target holders. The targets are fabricated in 1.27 cm disks mounted on an aluminum holder. Previously, these holders were directly mounted on a framework that held eight of them, which was then mounted on an X,Y,Z-stage in the target chamber. Each of these targets were hit with the laser in a rectangular pattern with 1–2 mm separations, which is larger than the extent of the *visible* damage to the target.

After gaining some experience with these targets, we began to suspect that perhaps the targets were damaged at even greater distances than could be seen

by eye. One observation was that the first shot on a fresh target would produce a good response, and then a second shot at a short distance from the first would give a noticeably poorer result. To test this, we hit a target with only one laser pulse, and obtained SEM images of this target so that we could judge the extent of the damage (Figure 5). As can be seen in the image, the damage radius is at least 1 mm in diameter.

To minimize the collateral damage to the surrounding material from a laser shot, we adopted a target holder that isolates small nanowire targets from adjacent material. Small pieces of nanowire array are mounted on washers that are then mounted in holes in a metal plate (Figure 6). The thickness of the plate shields adjacent targets from the blast produced by the laser interaction.

Diagnostic Calibrations

This year we calibrated two of the primary diagnostics that were fabricated last year: the neutron detectors and the Thomson spectrometer.

The neutron detectors consist of a very fast plastic scintillator from Eljen, EJ-228, coupled to a Hamamatsu H2431 photomultiplier tube (PMT). Some of the neutrons passing through the scintillator will collide with protons in the material and transfer energy to them; the energetic protons then induce scintillation that is captured and amplified by the PMT. We began the year with two such neutron detectors. These were calibrated using NSTec's D-D dense plasma focus (DPF) machine, which is capable of producing in excess of 10^{10} 2.45 MeV neutrons per pulse.

The flux from the DPF is such that it was necessary to set the detectors at 17.5 m from the source and to bias the PMT at −1200 V, as distinct from the −2000 V generally used for our laser experiments. These conditions prevented the signals from overwhelming the recording system used to acquire the data. The difference in PMT gain between the two bias voltages was measured in the lab using known sources to excite the detectors and applied to the measurements to obtain the calibration values.

Later in the year, two more neutron detectors of the same design were fabricated and cross-calibrated against the first two. The addition of these detectors reduces the statistical variation in the measurements. It also makes it possible to detect any anisotropy in the generated neutron flux through the careful placement of the detectors around the target chamber.

The Thomson spectrometer consists of a drift tube with parallel electric and magnetic fields applied across it to separate ionized particles according to their charge and momentum (Cobble 2011). The results are captured at the image plane using a microchannel plate (MCP) to amplify the signal, which is then read out using a CCD camera. Each ion of a given charge-to-mass ratio falls along a parabolic line, the position on that line being a function of its energy (Figure 7). By this technique we
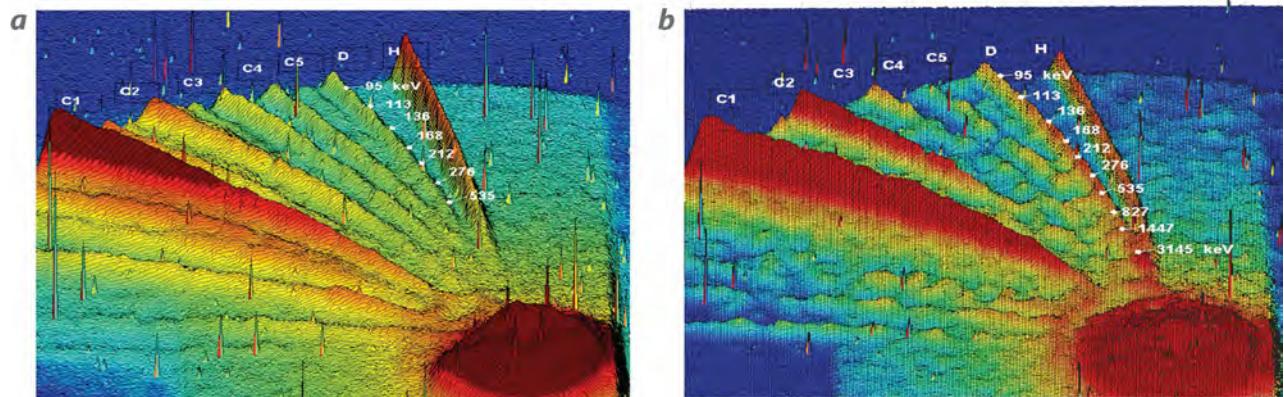

Figure 7. 3-D image of the carbon, deuteron, and proton ion distribution on the Thomson spectrometer image plane for (a) a flat target and (b) a nanowire target
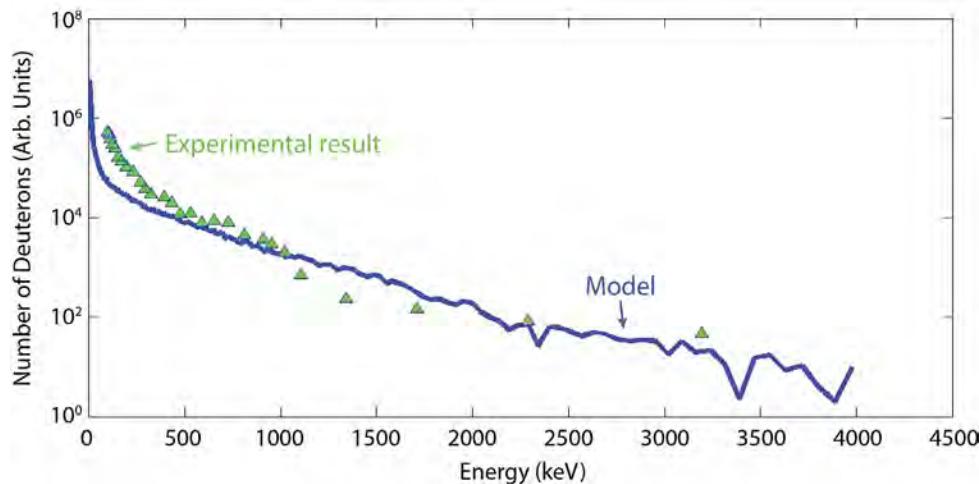
Figure 8. Comparison of a measured deuteron energy spectrum at 8×10^{19} W/cm^2 with that predicted by a PIC simulation. Aside from over-predicting the magnitude in the 1–2 MeV region, the model spectrum matches the measured spectrum reasonably well.

can analyze the constituents of the plasma generated by the laser pulse. We are especially interested in the energy spectrum of the deuterons and how it relates to the target conditions, the parameters of the laser pulse, and the flux of the detected neutrons.

The deuteron energy as a function of position on the image plane was measured using a fast pulser to gate the imager's MCP on at various intervals following the arrival of the laser pulse at the target. For a given MCP "turn on" time, there is a point on the deuteron ion line where the signal is cut off; this corresponds to the highest velocity ions that reach the MCP just as it is gated on. The velocity is then used to calculate the energy that corresponds to that location. A number of energy calibration points are shown in Figure 7.

Note that the trajectory corresponding to deuterium is the same as for C^{6+}, as they have equal charge-to-mass ratios. Images taken from laser shots on CH_2 targets show no signal at that location, indicating that no appreciable quantity of C^{6+} is produced. We therefore attribute all of the signal along this trajectory to deuterium. The proton line seen in the CD_2 data is from water vapor that is absorbed by the target. Targets that have been kept in vacuum between the time they are made and when they are loaded into the target chamber show much less proton signal.

Data Analysis

Images from the Thomson spectrometer were analyzed to produce the energy spectra of the deuteron ions from shots made with various laser intensities. These spectra were compared with particle-in-cell (PIC) model simulations corresponding to the same intensities. One such example for a laser intensity of 8×10^{19} W/cm^2 is shown in Figure 8. The model spectrum matches the measured spectrum reasonably well, except for over-predicting the magnitude in the 1–2 MeV region.

Neutron flux measurements were made over a range of laser intensities using a variety of targets. From these measurements we found a systematic trend in which
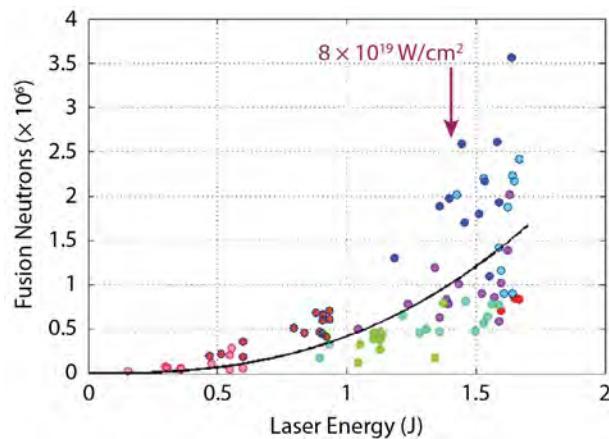
Figure 9. Measurements of neutron yield vs. laser intensity. The curve represents a dependence on intensity to the 2.28th power. Differently colored data points represent different targets.

the flux increases superlinearly with increasing laser intensity. A plot made from a set of measurements taken with the same experimental conditions, other than laser intensity, to avoid confounding interpretations for the results, is shown in Figure 9. The variations in measured flux at a given laser intensity are due to variations in the targets (nanowire diameter, etc.), variations in target quality, and neutron detection variations. By variations, we mean variations in the signal strength due to a particular neutron's interaction in the detector and in the statistical variation in the number of neutrons (typically several dozen) that hit a given detector in a single shot. The data points of a given color correspond to a particular target. From this we determine the relative performance of the various targets.

The curve shown in Figure 9 represents a fit to the neutron flux data of the form Flux = A × $I^{2.28}$, where A = amplitude and I = laser intensity.

This functional form has no theoretical basis but is a useful way to describe the increase in flux with laser intensity.

The significant gains in neutron flux as laser intensity increases can be understood by noting how the energy spectrum of the deuteron ions in the plasma changes as the input energy is increased. The deuteron ion energy spectra obtained from

PIC simulations of four laser intensities (3×10^{19}, 8×10^{19}, 2×10^{20}, and 5×10^{20} W/cm^2) are shown in Figure 10. The 8×10^{19} W/cm^2 curve (red) is the same as that shown in Figure 8. The *shape* of the spectrum changes with increasing input energy so that the fraction of ions with energies of several hundred keV or higher increases more rapidly than the energy.

The vast majority of D-D fusions occur between energetic deuterons from plasma entering the surrounding CD_2 and interacting with deuterons at rest. We can predict the effect of the deuteron energy spectrum on the generated neutron flux using the known energy-dependent cross section for D-D fusion and the rate of energy loss of the ions in the bulk material ($\partial E/\partial x$), which can be calculated. The latter is inverted to give the distance of travel through the material for a given energy loss ($\partial E/\partial x$). Integrating the product of the distance traveled per amount of energy loss, ΔE, and the average cross section between E and ΔE over all energies up to a particular initial energy gives the probability that a deuteron with that energy will undergo a fusion in the material. The results of this calculation for deuteron energies up to 10 MeV is given in Figure 11.

By integrating each of the ion spectra shown in Figure 10, with each energy bin weighted by the relevant fusion probability from Figure 11, we arrive at the relative neutron flux that can be expected for the
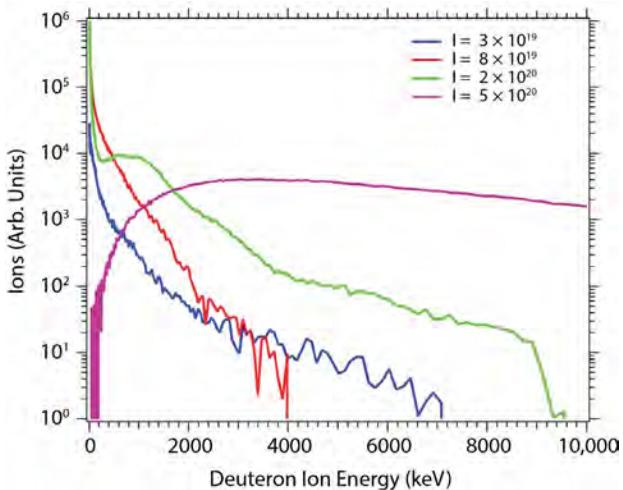
**Figure 10. Predictions of deuteron ion energy spectra for several laser intensities**
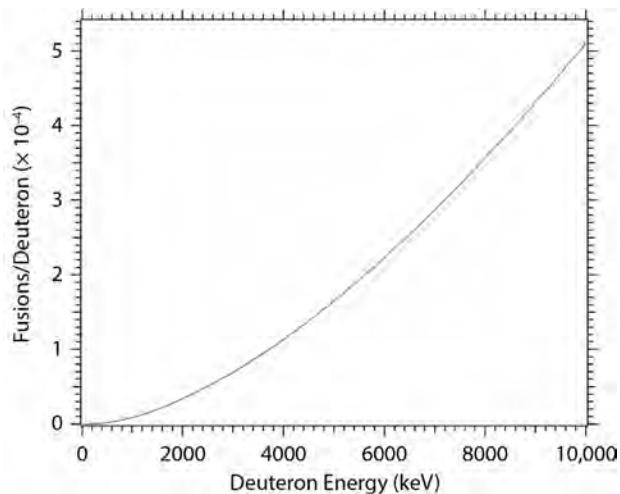
Figure 11. Calculation of the probability of D-D fusion as a function of deuteron energy
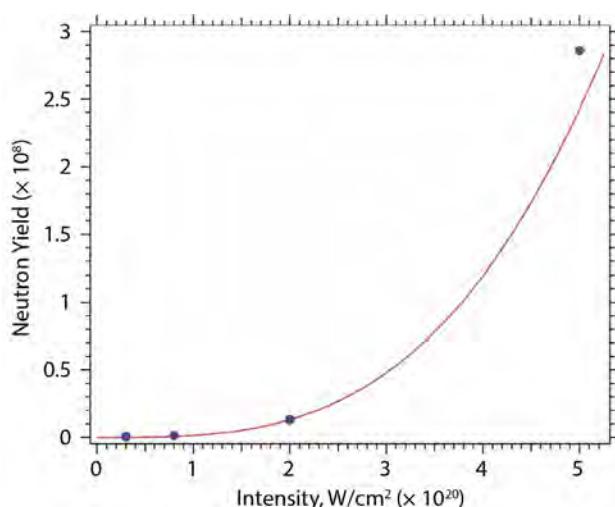
Figure 12. Calculated predictions of relative neutron yield vs. laser intensity, normalized to 1.5×10^6 at 8×10^{19} W/cm^2

corresponding laser intensity. These results, normalized to 1.5×10^6 neutrons at 8×10^{19} W/cm^2, which is representative of our measured values, are presented in Figure 12. From this, we predict that increasing the laser intensity to 5×10^{20} W/cm^2 will result in neutron fluxes in excess of 10^8. This assumes that the actual deuteron ion energy spectra continue to approximate the PIC calculations as well as they have thus far.

Laser System Upgrade

To achieve this goal, an upgrade of the laser beam line components has begun that will enable us to increase the laser intensity on the target by about an order of magnitude. To better couple the trigger laser pulse to the amplification stages, an acousto-optic modulator has been acquired and installed. Larger gratings are needed for beam pulse time compression, as are larger mirrors and a doubling crystal for the conversion from 800 to 400 nm. This is because the gratings can withstand only so much power density, so an increase in laser power means that the beam diameter must be increased. The increase in beam diameter, in turn, requires a larger target chamber with ports large enough for the beam to pass through. Finally, larger off-axis parabolic mirrors are needed to focus the beam onto the target. These upgrades will be implemented by the second quarter of FY 2017.

Conclusion

This year we have unambiguously demonstrated that we can generate 2.45 MeV neutrons from D-D fusion and have established the dependency of the yield on incident laser energy. We have also measured the energy spectrum of the deuterons in the plasma and have seen that it matches predictions made by the PIC simulations. Using these simulations, we expect that in the next year we will be able to generate neutron fluxes equal to, or greater than, 10^8 neutrons per laser pulse after we have implemented the upgrade described above.

A talk was given at this year's APS Division of Plasma Physics Annual Meeting on the results obtained thus far. A paper to be submitted to *Physical Review Letters* is also in preparation.

Acknowledgments

References

Cobble, J. A., K. A. Flippo, D. T. Offermann, F. E. Lopez, J. A. Oertel, D. Mastrosimone, S. A. Letzring, N. Sinenian, "High-resolution Thompson parabola for ion analysis," *Rev. Sci. Instrum.* **82** (2011) 113504.

Purvis, M., et al., "Relativistic nano-photonics for ultra-high energy density plasma physics," *Nature Photonics* **7** (2013) 796–800.

Tinsley, J. R., A. Curtis, J. Rocca, "Laser-generated ultra high–energy density plasma for fast neutron pulse production and neutron diagnostic development," in *Site-Directed Research and Development*, FY 2015, National Security Technologies, LLC, Las Vegas, Nevada, 2016, 227–233.

Site-Directed Research and Development

Appendixes

SDRD Performance Metrics

National Security Technologies–Operated Sites

Acronyms and Abbreviations

This page left blank intentionally

In the SDRD program we continue to use quantifiable metrics to gauge the performance of our R&D investment. Metrics such as intellectual property, technology transfer to our programs, and addressing R&D requirements are some of the most common types of measureable outcomes. We also consider the importance of other factors, such as follow-on programmatic or external funding received, new methods developed that effectively save costs, and overall enhanced staff capabilities. These are further indicators of innovation productivity and are also a direct measure of investment return. SDRD provides our staff with opportunities to explore and exercise creative motivations that ultimately lead to new knowledge and realized technologies. The traditional metrics we have used over the past years are tabulated below and are a broad measure of R&D performance.

Invention Disclosures

Invention disclosures are the first step in our intellectual property pursuit and are often followed by patent applications when deemed appropriate. SDRD has generated well over half of all inventions disclosed company-wide since FY 2002 and continues to do so to this day. On average about one-third of our projects generate new invention disclosures, which is a reasonably high ratio given that projects can vary widely from basic concept, low technical readiness, to much higher more applied development efforts. In fact, our programs benefit from a high rate of technology utilization precisely due to this diverse project mix.

	FY06	FY07	FY08	FY09	FY10	FY11	FY12	FY13	FY14	FY15	FY16
Number of projects	50	37	27	23	25	26	24	24	25	28	27
Invention disclosures	11	9	6	11	9	7	8	7	7	6	5
	22%	24%	22%	48%	36%	27%	33%	29%	28%	21%	19%

Technology Transfer

A relatively high percentage of projects, roughly 40%, produce technology that is subsequently adopted by a direct NNSS program. Another measure of program effectiveness and alignment with missions is how well projects address technology needs as identified in the annual NNSS *Technology Needs Assessment*. The ratio of needs addressed to total projects is also indicative of a trend that aligns efforts strategically with the NNSS mission. In addition, a number of projects, but still a small percentage, are targeting the emerging fields (of the *Needs Assessment*) that are new initiatives intended to incorporate higher risk and seek to explore opportunities for enhanced mission outside of traditional NNSS areas of expertise.

	FY06	FY07	FY08	FY09	FY10	FY11	FY12	FY13	FY14	FY15	FY16
Number of projects	50	37	27	23	25	26	24	24	25	28	27
Technology adopted by programs	8	8	8	10	10	9	10	9	10	11	10
	16%	22%	30%	44%	40%	35%	42%	38%	40%	39%	37%

We continue to strive to have SDRD effectively contribute new technology into key programmatic efforts as quickly as possible. New strategic efforts are also providing greater emphasis on forward-looking needs efficiently coupled with long-term visionary goals. As always, SDRD looks to be "ahead of our time by design" and push for SDRD innovations to intersect future and evolving missions with the most impact possible.

Needs Addressed

The NNSS *Technology Needs Assessment* document continues to be an effective tool for proposal submitters and reviewers. It provides a roadmap and guidance for technology gaps and challenges facing mission areas. As mentioned, our directed research emphasis areas were similar to last year, and they targeted key investment needs, including nuclear security, information security/assurance, high-energy density physics diagnostics, integrated experiments, advanced analysis, and safeguarded energy. The *Needs Assessment* is developed from a broad base of input from the national security complex, including laboratories, NNSA, and other external agencies. Significant revisions to the assessment were made again this year; most notably the "Emerging Areas and Special Opportunities" and "Blue Sky" sections were expanded, as were sections on new challenges and "Breaking Barriers" in cyber security, advanced radiography, energy security, and materials in the extremes. The *Needs Assessment* itself is now in the twelfth year of revision, and its utility and effectiveness continues to improve year to year.

	FY06	FY07	FY08	FY09	FY10	FY11	FY12	FY13	FY14	FY15	FY16
Number of projects	50	37	27	23	25	26	24	24	25	28	27
Gap or need addressed*	17	18	15	15	13	13	11	14	11	10	10
	34%	49%	56%	65%	52%	50%	46%	58%	44%	36%	37%
"Emerging Area & Special Opportunity" effort*	--	--	--	--	--	--	--	3	5	5	3
	--	--	--	--	--	--	--	13%	20%	18%	11%

*per NNSS R&D Technology Needs Assessment

Publications

Publications are another indicator of R&D output and provide an archival record of the investments made, which are then available to the broader scientific and technical community. We have placed a strong emphasis on high-quality, high-impact journal publications and many are highlighted in annual reports past and present. We are actively targeting about half of all SDRD projects will publish in a given year; an increase in follow-on publications has been noted and expectations are that publication numbers will grow in time.

	FY06	FY07	FY08	FY09	FY10	FY11	FY12	FY13	FY14	FY15	FY16
Journal publications	2	7	3	6	6	5	7	9	8	7	7

Livermore Operations (LO)
P.O. Box 2710
Livermore, California 94551-2710

Nevada National Security Site (NNSS)
P.O. Box 98521
Las Vegas, Nevada 89193-8521

New Mexico Operations (NMO) (Los Alamos and Sandia offices)
2900 East Road
Los Alamos, New Mexico 87544

North Las Vegas (NLV)
P.O. Box 98521
Las Vegas, Nevada 89193-8521

Remote Sensing Laboratory–Andrews (RSL-A)
P.O. Box 380
Suitland, Maryland 20752-0380
(Andrews Air Force Base)

Remote Sensing Laboratory–Nellis (RSL-N)
P.O. Box 98521
Las Vegas, Nevada 89193-8521
(Nellis Air Force Base)

Special Technologies Laboratory (STL)
5520 Ekwill Street
Santa Barbara, California 93111-2352

This page left blank intentionally

1-D	one-dimensional
2-D	two-dimensional
2DEG	2-D electron gas
2DHG	2-D hole gas
3-D	three-dimensional

A

ADC	analog-to-digital converter
AFB	Air Force Base
AFRL	Air Force Research Laboratory
Al	aluminum
AlB_4C	aluminum boron carbide
AlGaN	aluminum gallium nitride
AlN	aluminum nitride
ALS	Advanced Light Source
AlTaC	aluminum tantalum carbide
Am	americium
AmBe	americium-beryllium
AMS	Aerial Measuring System
AO	adaptive optics
AOTF	acousto-optic tunable filter
APD	avalanche photodiode
API	application program interface
APS	Advanced Photon Source
Ar	argon
AR	anti-reflection
ASIC	application-specific integrated circuit
AT-bus	advanced technology-bus
ATAK	Android Tactical Assault Kit
Au	gold

AuM	gold M x-ray
AVID	Advanced Visualization and Integration of Data

B

$Ba_2TiSi_3O_8$	fresnoite
bcc, BCC	body-centered cubic
bct, BCT	body-centered tetragonal
Be	beryllium
BeCu	beryllium copper
BET	Brunauer-Emmett-Teller
Bi	bismuth
BI	back-illuminated (camera)
BLE	Bluetooth low energy
BOFPs	bulk optic Fabry–Pérot interferometers

C

C^{6+}	carbon atom in the 6+ ionization state
C K	carbon K x-ray
Ca	calcium
Caltech	California Institute of Technology
$CaMoO_4$	calcium molybdate, powellite
CaO	calcium oxide
$CaWO_4$	calcium tungstate, scheelite
CCD	charge-coupled device
CD_2	deuterated polyethylene
CERN	Conseil Européen pour la Recherche Nucléaire, or European Organization for Nuclear Research
^{252}Cf	californium-252
CH_2, C_2H_4	polyethylene
^{35}Cl	chloride-35
ClK	chlorine K x-ray
CLYC	$Cs_2LiYCl_6{:}Ce_{0.5\%}$
CMOS	complementary metal oxide semiconductor
CMS	Compact Muon Solenoid (detector)
c_n^2	index of refraction structure constant
^{60}Co	cobalt-60
COTS	commercial off-the-shelf

cps	counts per second
CPU	central processing unit
^{137}Cs	cesium-137
CsI	cesium iodide
CSU	Colorado State University
Cu	copper
CUP	compressed ultrafast photography
CW	continuous wave
CZT	cadmium-zinc-telluride

D

DAC	diamond anvil cell
D-AMP	denoising-based approximate message passing (algorithm)
DAQ	data acquisition
DARPA	Defense Advanced Research Projects Agency
DC	direct current
D-D	deuterium-deuterium
DFT	density functional theory
DMD	digital-micromirror-device
DOE	U.S. Department of Energy
DOF	degree(s) of freedom
DPF	dense plasma focus
DSP	digital signal processing
D-T	deuterium-tritium
Dy	dysprosium
DyL	dysprosium L x-ray

E

EBAPS	electron-bombarded active pixel sensor (camera)
EDFA	erbium-doped fiber amplifier
EMCCDs	electron-multiplied
ENF	excess noise factor
EOS	equation of state
ESR	equivalent series resistance

F

FAA	Federal Aviation Administration
FCC	face-centered cubic
FEA	finite-element analysis
FFP	fiber Fabry–Pérot interferometers
FFP-TF	fiber Fabry–Pérot-tunable filter
FFT	fast Fourier transform
FI	front-illuminated (camera)
FIR	finite impulse response
FMCIO	FPGA Mezzanine Card IO
FOV	field of view
FP	Fabry–Pérot (interferometer)
FPGA	field-programmable gate array
FSR	free spectral range
FWHM	full width at half maximum
FY	fiscal year

G

GaAs	gallium arsenide
GADRAS	gamma detector response analysis software
GaN	gallium nitride
GBW	gain bandwidth
GGC	gamma gross count
GNSS	Global Navigation Satellite System
GPS	global positioning system
GRIN	graded-index
GS	global shutter
GVD	group velocity dispersion

H

^{1}H	hydrogen-1
H_2	hydrogen
He	helium
^{3}He	helium-3
^{4}He	helium-4
HE	high explosive

HEDP	high-energy density physics
HEP	high-energy physics
Hg	mercury
Ho	holmium
HoL	holmium L x-ray
HoM	holmium M x-ray
HPCAT	High Pressure Collaborative Access Team (Carnegie Science)
HS	high sensitivity
HSPDV	high-speed photonic Doppler velocimetry
HV	high voltage

I

ICCD	intensified CCD
ICP-AES	inductively coupled plasma-atomic emission spectroscopy
IFFT	inverse fast Fourier transform
i.i.d.	independent and identically distributed
ILC	International Linear Collider
IMU	inertial measurement units
$In_{12}Ga_{88}N$	indium-gallium-nitride
IO	input/output
IoT	internet of things
IR	infrared
IS	integrating sphere
ISO	International Organization for Standardization
ISR-2	Intelligence and Space Research (LANL)
IT	information technology

K

K	potassium

L

LA-ICP-AES	laser ablation-inductively coupled plasma-atomic emission spectroscopy
LANL	Los Alamos National Laboratory
LED	light-emitting diode
LET	linear energy transfer
LHC	Large Hadron Collider

^{6}Li	lithium-6
lidar	light detection and ranging
LiF	lithium fluoride
LoRa	long range (radio)
LOS	line of sight
LRE	L-rolled edge
LSF	line spread function

M

MCMC	Markov Chain Monte Carlo (code)
MCP	microchannel plate
MHD	magneto-hydrodynamic (code)
Mo	molybdenum
MO_3	(M = Mo, W)
^{98}Mo	molybdenum-98
^{99}Mo	molybdenum-99
mosfet	metal oxide semiconductor field-effect transistor
MPDV	multiplexed photonic Doppler velocimetry
MQTT	MQ Telemetry Transport (an ISO standard publish subscribe–based lightweight messaging protocol for use on top of the TCP/IP protocol; it is designed for connections with remote locations where a small code footprint is required, or the network bandwidth is limited)

N

NaCl	sodium chloride
NaI	sodium iodide
NaI:Tl	thallium-doped sodium iodide
NaK	sodium K x-ray
NASA	National Aeronautics and Space Administration
NDSE	neutron-diagnosed subcritical experiments
NEA	negative electron affinity
NGC	neutron gross count
NH_4NO_3	ammonium nitrate
Ni	nickel
NIF	National Ignition Facility
NIR	near infrared
NIST	National Institute of Standards and Technology

NNSA	National Nuclear Security Administration
NNSS	Nevada National Security Site
NRAT	Nuclear Radiological Advisory Team
NSCRAD	nuisance-rejection spectral comparison ratio anomaly detection
NSTec	National Security Technologies, LLC
NTF	Nevada Terawatt Facility
NVGs	night-vision goggles
N-ZERO	Near Zero Power RF and Sensor Operations (DARPA program)

O

OBR	optical back-reflectometer
OOASK	on-off amplitude shift keying
op amp	operational amplifier
OS	operating system

P

^{32}P	phosphorous-32
PC	personal computer
PCA	principal component analysis
PCB	printed circuit board
PCS	Poisson Clutter Split (algorithm)
PDV	photonic Doppler velocimetry
PIC	particle in cell
PMMA	poly(methyl methacrylate)
PMT	photomultiplier tube
PN	projected Newton
PPF	photons per frame
PSD	power spectral density (O'Neill)
PSD	pulse shape discrimination
PSF	point spread function
PSI	Physical Sciences, Inc.
PSoC	programmable system-on-chip
Pu	plutonium
PuBe	plutonium-beryllium
PZT	piezoelectric

Q

QE — quantum efficiency

R

R&D — research and development

RAP — Radiological Assistance Program

RGB — red/green/blue

RF — radio frequency

ROM — reduced order modeling

RS — rolling shutter

RSL — Remote Sensing Laboratory

S

^{35}S — sulfur-35

SBC — single-board computer

SCMOS — scientific CMOS

SDR — software-defined radio

SDRD — Site-Directed Research and Development (Program)

SEM — scanning electron microscope

Si — silicon

SiO_2 — silica

SiPM — silicon photomultiplier

SKIROC — Silikon pin Kalorimeter Integrated ReadOut Chip

SN — sensor network

SNL — Sandia National Laboratories

SNR — signal-to-noise ratio

SO_2 — sulfur dioxide

SOF — Special Operations Forces

SOI — silicon on insulator

SPIDER — Streaked Polar Instrumentation for Diagnosing Energetic Radiation

SSL — secure socket layer

STL — Special Technologies Laboratory (NSTec)

sUAS — small unmanned aircraft system

S(W) — substitutional tungsten

SWaP — size, weight, and power

T

Ta	tantalum
TaC	tantalum carbide
^{99}Tc	technetium-99
^{99m}Tc	metastable technetium-99
Tc	technetium
TCP/IP	Transmission Control Protocol/Internet Protocol
TEAMS	Technical Evaluation Assessment and Monitoring Site (Defense Threat Reduction Agency)
TEC	total electron content
TEM	transmission electron microscope
TES	transition edge sensor
TF	tunable filter
Ti	titanium
TI	technology integration
TOD	third order dispersion
TOF	time of flight
TRL	technology readiness level
TSS	tangential signal sensitivity
TTL	transistor-transistor logic
TwIST	two-step iterative shrinkage/thresholding (algorithm)

U

UAS	unmanned aerial system
UAV	unmanned aerial vehicle
UNLV	University of Nevada, Las Vegas
UNPE	underground nuclear proliferation experiment
UNR	University of Nevada, Reno
USAF	U.S. Air Force
USB	universal serial bus
UV	ultraviolet

V

V	vanadium
VASP	Vienna *ab initio* simulation package
VIS	visible
VISAR	velocity interferometer system for any reflector

VLSI	very large–scale integration
VTOL	vertical takeoff and landing

W

W	tungsten
WFS	wavefront sensor
WSMR	White Sands Missile Range

X

XDV	x-ray Doppler velocimetry